On the Surface Restructuring of Highly Dilute Alloys and its Effects on Catalytic Performance

by

Konstantinos G. Papanikolaou

In partial fulfilment of the requirements for the degree of

Doctor of Philosophy

at

University College London

Supervised by

Dr. Michail Stamatakis & Prof. Angelos Michaelides

Department of Chemical Engineering

UCL

I, Konstantinos G Papanikolaou confirm that the work presented in this thesis is my own. Where information has been derived from other sources, I confirm that this has been indicated in the thesis.

…….

Dedicated to the memory of my father Ioanni,
to my sister Marieta
and my mother Kalliopi.

Abstract

Recent studies have shown that highly dilute alloys of platinum group metals (PGMs: Pt, Rh, Ir and Pd) with coinage metals (Cu, Au, and Ag) serve as highly selective and coke–resistant catalysts in a number of important chemical reactions. These materials are composed of trace amounts of a PGM or Ni, whose atoms are embedded in a coinage metal surface, and their catalytic behaviour is governed by the size and shape of the surface clusters of PGM atoms. Therefore, establishing a means of control over the topological architecture of highly dilute alloy surfaces is crucial to achieving catalytic performance tailored to a specific application. This Thesis employs density functional theory, kinetic Monte Carlo and microkinetic modelling in order to investigate ways of manipulating the surface architecture of a number of dilute alloy surfaces towards optimal performance for key catalytic reactions. The latter include the direct dissociations of NO, CO_2 and N_2, and the reverse events, which are important in, among others, emission control technologies. Also examined is the potential of a Ni/Cu dilute alloy for the NO + CO chemistry, and it is demonstrated that the selectivity toward the desired products can be manipulated by tuning the size of the Ni clusters in the ensemble. The results can guide future theoretical, surface science and catalysis studies on highly dilute alloys, towards the development of superior catalysts that can efficiently accelerate chemistries of industrial significance.

Impact Statement

The total worldwide revenues of the chemical industry in 2019 were USD 3.94 trillion, which represented around 18 % of the total GDP of the United States of America. Approximately 90 % of bulk and specialty chemicals are prepared through catalytic processes, whereby a solid, liquid or gas substance (the catalyst) is employed in order to accelerate the conversion of raw materials into valuable products. Catalysts are used in a wide spectrum of important applications being the cornerstone in the synthesis of numerous everyday products (e.g. fertilisers, pharmaceuticals, plastics etc.), in petroleum refining and in the reduction of noxious gases that cause severe environmental issues. Along these lines, it would not be an overstatement to claim that catalytic materials are at the centre of a multi–trillion–dollar industry.

Among all catalyst types, solids (or heterogeneous catalysts) are the most widespread, and this is because of the associated benefits of using solid materials in a chemical process (e.g. easy separation from the reaction mixture, possibility for regeneration). A large number of industrial catalysts in the chemical and automotive sectors are based on platinum group metals (PGMs: Rh, Pt, Pd, Ir), and unsurprisingly, these two sectors are those with the highest demand in such metals. PGMs exhibit excellent catalytic performance for many industrial chemistries, but they are very expensive and scarce. These challenges can be circumvented by, the non–trivial task of, developing PGM–free catalysts that have equally good performance to PGMs.

This Thesis investigates a new class of bimetallic materials that have recently drawn the attention of the catalysis community and are known as *highly dilute alloys*. The latter contain trace amounts of a PGM or Ni, which are embedded in coinage metal (Ag, Au and Cu) surfaces. Although small, or no, amounts of PGMs are utilised, such materials exhibit resistance to common poisons, excellent selectivity, activity and stability for a number of reactions of practical interest. On this basis, they show strong potential in replacing conventional PGM–based materials. Given the exceptional catalytic performance of highly dilute alloys, their use in the industry may bring about a number of

benefits. These include the synthesis of products of high purity that comply with strict regulations (e.g. substances used in the pharmaceutical industry), the reduction of the complexity of the chemical process (and particularly the separation train), and the reduction of the associated capital and operating costs thereof, just to name a few.

Importantly, scientific research has shown that the catalytic performance metrics of dilute alloys depend on the arrangement of the atoms of the two constituent metals in the surface of the material. Therefore, establishing a means of control over the topological architecture of highly dilute alloy surfaces is crucial to optimising their catalytic performance with regard to the application of interest. The work presented in this thesis takes the advantage of sophisticated computational methods and identifies highly dilute alloys that can catalyse chemistries of central importance to emission control catalysis. This computational approach is employed in order to screen for the most promising materials for the catalytic reduction of noxious gases (e.g. N_2O, NO), thereby minimising the cost, time and resources required by experiments that may rely on cumbersome trial and error techniques. Markedly, the findings suggest that dilute alloys, which are composed of inexpensive metals, with a specific surface structure are promising for the aforementioned applications (e.g. reduction of pollutant emissions from road vehicles). Furthermore, this work provides guidance in developing pretreatment strategies in order to prepare the aforementioned structures. Thanks to their simplicity, these strategies have the potential to be applied in an industrial scale, and accordingly this thesis contributes to the ongoing efforts toward the successful commercialisation of highly dilute alloy catalysts.

Acknowledgment

I would like to express my great appreciation to my PhD supervisor Prof. Michail Stamatakis for his continuous support and excellent guidance throughout these 3.5 years. If there is something I feel truly lucky about, this is that I was supervised by Michail! My admiration for him gave me strong motivation to work hard and complete this Thesis in the best way I could. I feel extremely happy that I was given the opportunity to work within the Stamatakis group, and of course, I will welcome any opportunity for collaboration in the future.

I extent thanks to my second supervisor Prof. Angelos Michaelides. Unfortunately, we met only a few times during my PhD studies, but even under these circumstances, he gave me excellent advice, which was very beneficial to my work. Additionally, I would like to thank Prof. Charlie Sykes. Thanks to him and his feedback, I learnt and understood many aspects in relation to single atom alloy catalysts. I am grateful that I had the chance to work with him and his research group on exciting projects.

Special thanks are given to my colleague Dr. Matt Darby who helped me to do my “first steps” in density functional theory calculations and kinetic Monte Carlo simulation. I thank him for his enthusiasm on these topics and for the numerous and fruitful discussions. Moreover, I thank the UCL CPSE lab members Giannis D. Savva, Sai Yadavalli, Dr. Romain Réocreux, Dr. Julia Schumann, Dr. Shrikanth Divi, Dr. Pedro Ivo De Oliveira Filho and Dr. Arun Pankajakshan for being always willing to help and give a piece of advice.

I am also grateful to my dear friends Ronis, Harry, Antonis, Eldi, Andreas, Kleopatra, Madalin, Nikos, Olga, Dimitris Gkritzalis and Bessy, to my cousins Dimitris and Vasilis, and to my childhood friends Dimitris Tselentis, Dimitris Ntoulias, Ilias, Loukas, Marios, Panos and Tzortzis. I thank them for their encouragement throughout my PhD studies and life.

Last but certainly not least, I would like to thank my mother Kalliopi, my sister Marieta, my grandmother Vasiliki and my beloved Zeynep. They supported and helped me in many ways in carrying my PhD studies out.

List of Publications

i. **K. G. Papanikolaou**, M. T. Darby and M. Stamatakis (2018). "Adlayer Structure and Lattice Size Effects on Catalytic Rates Predicted from KMC Simulations: NO Oxidation on Pt(111)". *The Journal of Chemical Physics* 149(18): 184701.

ii. **K. G. Papanikolaou,** M. T. Darby and M. Stamatakis (2019). "CO-Induced Aggregation and Segregation of Highly Dilute Alloys: A Density Functional Theory Study". *The Journal of Physical Chemistry C* 123(14): 9128-9138. *Featured on the cover of The Journal of Physical Chemistry C.*

iii. **K. G. Papanikolaou**, M. T. Darby and M. Stamatakis (2020). "Engineering the Surface Architecture of Highly Dilute Alloys: an *ab initio* Monte-Carlo Approach". *ACS Catalysis* 10: 1224-1236. *Featured on the cover of ACS Catalysis.*

iv. **K. G. Papanikolaou** and M. Stamatakis (2020). "On the Behaviour of Structure-Sensitive Reactions on Single Atom and Dilute Alloy Surfaces". *Catalysis Science &Technology* 10: 5815-5828. *Featured on the cover of Catalysis Science &Technology.*

v. **K. G. Papanikolaou** and **M. Stamatakis** (2020). "Toward the Accurate Modeling of the Kinetics of Surface Reactions Using the Kinetic Monte Carlo Method". Book chapter in *Computational Modelling of Nanomaterials, Volume 18* by Elsevier.

vi. Y. Wang, **K. G. Papanikolaou**, R. T. Hannagan, D. A. Patel, T. A. Balema, L. A. Cramer, P. L. Kress, M. Stamatakis and E. C. H. Sykes (2020). "Surface facet dependence of competing alloying mechanisms". *The Journal of Chemical Physics* 153: 244702.

vii. M. Ouyang, **K. G. Papanikolaou,** A. Boubnov, A. S. Hoffman, G. Giannakakis, S. R. Bare, M Stamatakis, M. Flytzani-Stephanopoulos, E. C. H. Sykes (2021). "Controlling Reaction Pathways via in situ Tuning of Active Site Ensemble Size; Effect of CO on PdAu Single-Atom Alloy Catalysts". *Nature Communications* 12: 1549.

viii. **K. G. Papanikolaou** and M. Stamatakis (2021). "The Catalytic Decomposition of Nitrous Oxide and the NO + CO Reaction over Ni/Cu Dilute and Single Atom Alloy Surfaces: First-principles Microkinetic Modelling". *Catalysis Science &Technology*:10.1039/D1CY00011J.

Table Contents

Chapter 1

1. Thesis background

This Thesis focuses on the effects of the adsorbate layer structure and the surface morphology on the reactivity of pure metal and alloy catalysts. Therefore, in this chapter we introduce fundamental concepts and review the pertinent literature. We further present the objectives of our study and give an outline of the Thesis.

1.1. Heterogeneous catalysts

Solid catalysts are used to accelerate chemical reactions, which would not be proceeding at a considerable rate in a gas or a liquid phase.[1] The role of heterogeneous catalysts is central to the manufacturing of over 85% of everyday products currently on the market. These materials are composed of a porous support (a metal oxide, e.g. Al_2O_3, MgO etc.), whereon the active phase (one or more transition metals) is dispersed and often "organised" into nanoparticles (NPs) – (see e.g. Figure 1). In turn, NPs expose several different facets that provide the loci for the reactant species to interact with each other, and undergo chemical transformations. A number of industrial chemistries that have a large impact upon our everyday life, are catalysed by heterogeneous materials. Typical examples include the synthesis of ammonia (Fe catalyst), the production of ethylene oxide (Ag catalyst), the reduction of nitric oxide (NO) – (Rh catalyst), and the catalytic cracking of crude oil (zeolites).[1] Therefore, the discovery and development of materials with optimal catalytic properties has been a very active area of research during the last decades.

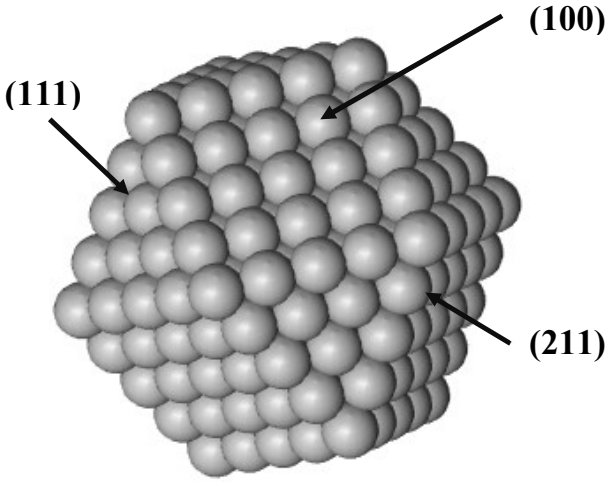

Figure 1. A cuboctahedral NP that exposes the most common low–index facets for face centred cubic metals (i.e. (100) and (111) surfaces) connected along edges, which can be modelled by a (211) step edge.

1.2. Predicting and tuning the reactivity of heterogeneous catalysts

An important, but challenging, step toward the understanding of chemical reactions over solid surfaces is to establish models that are capable of predicting the reactivity of solid catalysts. A widely employed model of this kind is the so–called *d* band model, which was developed by Hammer and Nørskov.[2] This model is a powerful tool that can help us rationalise reactivity trends among pure metal and alloy surfaces (the latter surfaces are those composed of more than one metal),[3] and it is briefly introduced in the following text.

As noted in section 1.1, gas–phase molecules adsorb on catalytic surfaces whereon they interact with other adsorbates that are within their close vicinity. According to the *d* band model, the adsorption energy of an adspecies (e.g. A*, where * indicates that the species is adsorbed on a surface) can be decomposed into the *sp* electron contribution, and the interaction between the adsorbate states and the *d* electrons of the metal[4]

$$E_{ads}\left(\mathrm{A}^*\right) = E_{sp} + E_d , \tag{1}$$

where E_{sp} and E_d represent the interactions between the electrons of the *sp* and *d* bands and the adsorbate states, respectively. The *sp* and *d* bands are formed from the corresponding *s*, *p* and *d* electrons of individual metal atoms. These electrons become delocalised in solid surfaces, and are therefore able to "travel" throughout the material. In general, the *sp* band is much broader than the *d* band, which is more localised and closer the highest occupied state (i.e. the *Fermi level*). As a result, one may expect a more significant *sp* contribution than *d* contribution to the adsorption energy.[5] Yet, the broad features of the *sp* bands result in a contribution that is similar for all the transition metals that are employed as heterogeneous catalysts, and accordingly the *d* band model relies on the assumption that reactivity differences between transition metals are by and large owing to E_d.[6]

Upon the interaction of the metal's *d* states with the states of an adsorbate, there is the formation of bonding and antibonding states similar to the bonding and antibonding orbitals of gas–phase molecules. The strength of the chemical bond between the adsorbate and the metal surface depends on

the position of the antibonding states relative to the Fermi level,[7] and the position of the latter states is determined by the position of the metal's *d* states. On this basis, the reactivity of metal surfaces can be described by the *d* band centre (ε_d), which is the first moment of the *d* density of states (DOS)[6]

$$\varepsilon_d = \frac{\int_{-\infty}^{\infty} \varepsilon \cdot \rho(\varepsilon) d\varepsilon}{\int_{-\infty}^{\infty} \rho(\varepsilon) d\varepsilon}, \quad (2)$$

where $\rho(\varepsilon)$ and ε are the electronic DOS distribution and the energy, respectively, and the integration proceeds over the filled states (i.e. states below Fermi level). In general, the higher the *d* band centre of a surface, the more reactive the surface is expected to be.

The *d* band centre is a descriptor of the variation of the binding strength of adsorbates over metal surfaces and can be used to explain reactivity trends. For example, from right to left across a series of the periodic table, the *d* states of metals move to higher energies (i.e. higher *d* band centre), thereby "shifting" the anti–bonding states to higher levels as well. In this manner, the antibonding states become increasingly unoccupied entailing a strong adsorbate–surface interaction. Therefore, the *d* band model predicts that transition metals on the left of the periodic table (e.g. Ru, Re, Fe etc.) interact with adsorbates more strongly than metals on the right (e.g. Au, Ag etc.). This trend is congruent with experimental findings, and also gives rise to the traditional activity volcano plots,[8] which "teach us" that the highest catalytic activity is achieved when adsorbates bind to the surface strong enough to undergo a chemical transformation, but weak enough so that the surface is not poisoned (i.e. an intermediate binding strength is optimal).

It follows that the catalytic performance of a material can be tuned by changing its *d* band centre, and this task may be achieved by: (1) modifying the surface structure; (2) introducing strain effects; and (3) alloying.[6] Regarding the first point, the *d* band of surfaces with low coordination number (e.g. (211)) tend to be narrower as compared to that of a densely packed surface (e.g. (111)), thereby lifting the *d* band centre to higher energy levels.[9] Consequently, stronger adsorbate binding is

anticipated on more open and undercoordinated surfaces. Moreover, strain effects are associated with changes to the lattice constant of a material. Mavrikakis et al. have shown that tensile strain (i.e. increase in lattice constant) induces a loss of electronic overlap between neighbouring metal atoms, thereby increasing the reactivity of the surface, whilst the opposite holds for compressive strain (i.e. reduced lattice constant).[10] Finally, alloying is another strategy to modify the structure of the *d* band, and therefore to change the position of the *d* band centre. In this regard, Kitchin et al. demonstrated that the dissociative adsorption energies for H_2 and O_2 over Pt(111) can be drastically altered by "intercalating" a layer of a 3*d* transition metal between the surface and subsurface layers of a Pt(111) slab.[11] The authors explained the simulated changes in the H_2 and O_2 dissociative adsorption energies over these "skin alloys" based on the structure of the *d* band and the position of ε_d.[11]

These three are ways to manipulate the reactivity of a surface, but it should be noted that a reactive surface is not necessarily catalytically active. This is because strong absorbate–surface interactions may result in the poisoning of the active sites. As indicated earlier, the optimal catalytic activity is found for intermediate adsorbate binding. This is the Sabatier principle,[8,12] which is displayed through the, common in catalysis, volcano plots (Figure 2 (a)). A volcano plot shows how the activity of a catalyst varies as a function of an activity descriptor (e.g. the adsorption energy of an intermediate surface species),[13] which is specific to the reaction under consideration.

Identifying a catalytic descriptor is useful for assessing the catalytic performance of heterogeneous catalysts in an efficient manner. Moreover, this concept can be used in conjunction with the so–called Brønsted–Evans–Polanyi (BEP) relations,[14] thereby providing a sophisticated framework that aids the discovery state–of–the–art catalysts based on a relatively small number of electronic structure calculations (see chapter 2).[8] The BEP relations belong to a class of scaling relations known as the linear transition state energy scaling relations,[15] and dictate that the activation barrier of a surface reaction correlates linearly to the reaction energy (i.e. the difference in energy between products and reactants) – (Figure 2 (b)). As it will be discussed in more detail in chapter 3 (see section 3.5.2), the

role of the BEP relation is central to kinetic simulations that take into account the interaction between adspecies.[16]

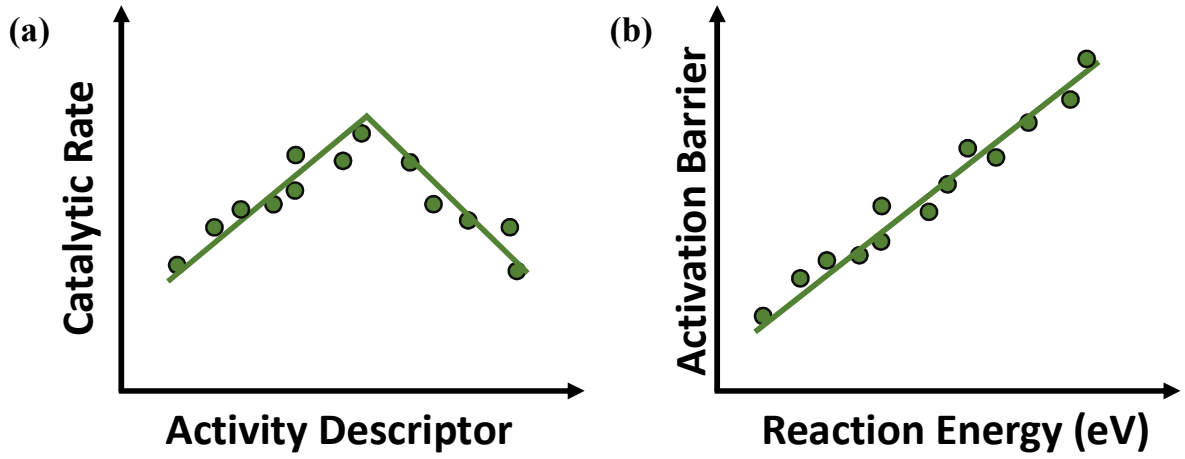

Figure 2. Panel (a) shows the shape of a volcano plot indicating that the maximum catalytic activity is observed for intermediate values of an activity descriptor; panel (b) shows a BEP plot where the reaction energy correlates linearly with the reaction energy. Each point on the two plots represents a catalytic surface.

The *d* band model and the linear scaling relations are tools that can facilitate the design of heterogeneous catalysts. However, it is not always true that these models provide accurate predictions in relation to the catalytic performance. For example, Xin and Linic showed that the *d* band model is incapable of predicting the trend of the binding strength of very electronegative adsorbates (e.g. OH*, F*, Cl*) on metal surfaces with almost fully filled *d* band.[5] Surprisingly, the authors demonstrated that for such adsorbate–surface systems stronger adsorbate bindings are accompanied by both lower (in energy) *d* band centres and, counterintuitively, larger adsorbate–surface bond distances. This unusual behaviour was explained by the magnitude of the repulsion between the *d* electrons of the metal surface and the renormalised states of OH*.[5] Along the same lines, there are certain classes of materials (e.g. dual–atom catalysts) that do not follow the linear scaling relations.[17] Yet, such a deviation may be beneficial because BEP relations pose a non–trivial constraint to the catalytic performance. This becomes apparent from Figure 2 (b), where one observes that low activation barriers are accompanied by strong product binding, which is the culprit for catalyst poisoning. As a result, a great amount of

ongoing research is dedicated to the discovery of materials that "break free" from the conventional BEP.[18]

This section has briefly reviewed some fundamental concepts and tools that may be employed upon the search for novel heterogeneous catalysts. These tools are powerful, but not always predictive owing to the very complex behaviour exhibited by chemical reactions on solid surfaces. In such cases, it is imperative to study surface reactions by considering their specifics in detail. This task can be accomplished by using elegant computational methods like density functional theory (DFT) – (see chapter 2), microkinetics (see chapter 6) and kinetic Monte Carlo (KMC) – (see chapter 3),[19] whose underpinnings and applications are briefly discussed in this Thesis.

1.3. The role of adsorbate – adsorbate interactions in catalytic reactions

A factor that adds to the complexity of catalytic reactions and requires particular attention is the interactions between adspecies on solid surfaces (these are known as *adsorbate–adsorbate* or *lateral interactions*).[20] The magnitude of these interactions may be significant (i.e. larger than 20 kJ/mol),[21] thereby affecting the macroscopic catalytic properties of the system. In particular, adsorbate–adsorbate interactions give rise to spatial correlation in the adsorbate layer (or adlayer – this is the layer formed by the adsorbed species on the solid surface), whereby ordered patterns may be formed and powerful microscopy techniques like scanning tunnelling microscopy (STM) may be employed to visualise them.[22] In turn, the adlayer structure impacts upon the reaction kinetics and thermodynamics, and a theory that is not capable of predicting the structure of the adlayer is essentially not able to accurately capture the behaviour of a surface reaction under a wide range of conditions.

Indeed, kinetic models that overlook adsorbate–adsorbate interactions often fail to capture the complexity of surface reactions.[23,24] Wu et al. modelled the oxidation of NO over Pt(111) and highlighted that the inclusion of long–range (i.e. interactions between adspecies that are not on neighbouring sites) and many–body interactions (i.e. interactions between more than two adspecies) were necessary in order to obtain O* coverages and reaction rates that are consistent with experimental

results.[16] Ovesson et al. parameterised KMC simulations based on DFT–derived energetics. Their computational work revealed that coverage effects control the direction of the oxidation reaction, and that small changes to O* coverage may result in dramatic changes to the production of NO_2.[25] It is true that the presence of spectator O* species even at moderate coverages can obstruct the O_2* dissociation reaction,[26,27] which is the rate–determining step (RDS) for the oxidation of NO on Pt(111). Finally, Schneider and co–workers demonstrated that there exists a considerable discrepancy between volcano plots of activity that take into account lateral interactions and those that do not.[28] This of course has strong implications in the search of optimal catalysts. In more precise terms, materials that appear on the top of the volcano plot in the absence of coverage effects may be, in practice, far from it and *vice versa*. Therefore, the inclusion of adsorbate–adsorbate interactions in kinetic models is often crucial. Unfortunately, conventional ways of modelling the kinetics of heterogeneous reactions (i.e., Langmuir-Hinshelwood type models) do not account for the aforementioned interactions. By contrast, the proper treatment of coverage effects is possible by employing elegant computational techniques like the KMC method (see chapters 3, 4 and 8).

1.4. Single atom alloys

Besides adsorbate–adsorbate interactions, the existence of numerous different active sites even within a single surface (crystal) is another source of complexity for surface reactions. Often two metals are combined in one catalyst (i.e. an alloy catalyst) in order to obtain superior performance as compared to that of the pure constituent metals. Indeed, the use of alloy catalysts is a common strategy to optimise the catalytic performance,[29] and such materials are being used in important large–scale applications such as naphtha reforming (Pt−Re alloy), and ammonia oxidation to nitric acid (Pt−Rh alloy). The disparate catalytic behaviour of alloy catalysts as compared to their monometallic counterparts is rationalised based on the *ligand* and *ensemble* effects.[30,31] The latter effects are related to the composition of the site whereon a species adsorbs,[32] while ligand effects are associated with compositional changes in the "surroundings" of the adsorption site, but not in the adsorption site itself.

An emerging class of bimetallic alloys that have lately attracted the attention of the catalysis community is the so–called single atom alloys (SAAs).[33] The latter contain a trace amount of a platinum group metal (PGM: Pt, Pd, Rh, Ir) or Ni embedded in a coinage metal surface (Cu, Au, Ag), and catalyse efficiently a number of chemistries.[34] The discovery of these materials is the result of continuous efforts toward the development of catalysts that are highly selective, resistant to poisons, and have the additional benefit of utilising minimal or no quantity of expensive PGMs.[35] The amount of the PGM (or dopant) is sufficiently small so that PGM atoms are atomically dispersed in the host surface (Figure 3 (a)). Under these circumstances, chemical bonds are activated on the reactive PGM, and this is followed by spillover to the coinage metal, whereon highly selective catalysis and efficient product removal are carried out.[36] In this way, one effectively combines the benefits of the two metals in one catalyst.

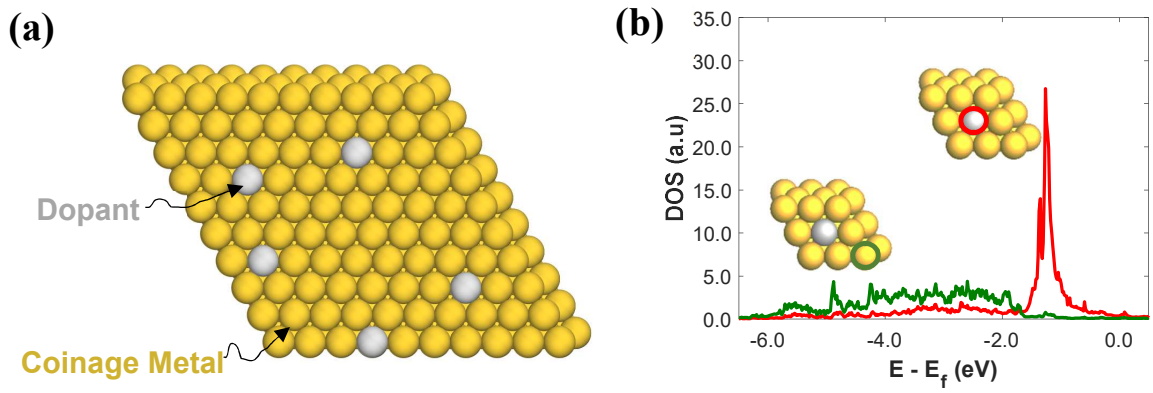

Figure 3. (a) An example of a SAA(111) surface where dopant atoms are isolated over a the host metal surface; (b) *d* DOS for a single Pd and an Au atom of Pd/Au(111) SAA. Pd and Au atoms are shown in grey and yellow, respectively.

As a result, SAAs catalyse selectively a number of reactions including hydrogenations,[37] C–H activation,[38,39] hydrogenolysis,[40] and catalytic oxidations.[41] Remarkably, recent studies by Xing et al.[42] revealed that SAAs have a great potential for replacing PGMs in emission control catalysis. In particular, the authors prepared a Pd/Cu SAA supported on Al_2O_3, and this catalyst was tested toward the NO + CO reaction. To better simulate the conditions under which an automobile catalytic converter functions, the authors tested the Pd/Cu SAA in the presence of O_2 and C_3H_6. The results not only

unveiled that the SAA catalyst is superior to its monometallic counterparts, but also that NO could be reduced to N_2 at relatively low temperatures (less than 250 ºC) and without the formation of by–products over the Pd/Cu surface.

The enhanced catalytic performance of SAA surfaces as compared to pure coinage metals is ascribed to the extraordinary electronic structure of isolated dopant atoms amid host metal atoms. Photoemission spectroscopy and DFT show that, for a number of SAA surfaces, the *d* band of the doped atom is very narrow, resembling that of a gas phase metal atom.[43,44] This electronic characteristic is a testament to the occasionally limited electronic interactions between the dopant atom and its coordination environment, and gives rise to the high reactivity of SAAs. For example, Figure 3 (b) shows the *d* DOS projected onto the isolated Pd atom and an Au atom of a Pd/Au(111) surface.[43,44] As seen, the *d* DOS of the isolated Pd atom exhibit a very sharp feature close to the Fermi level, while the *d* DOS of the Au atom are broad given its better interaction with its coordination environment.

The unusual electronic structure of SAAs is responsible for their unique catalytic behaviour. In particular, computational studies underscore that SAAs catalysts is another class of materials that "escape" from the conventional BEP relations (Figure 4),[45] and also that their reactivity cannot be understood based on the conventional *d* band model (see chapter 5).[43,46]

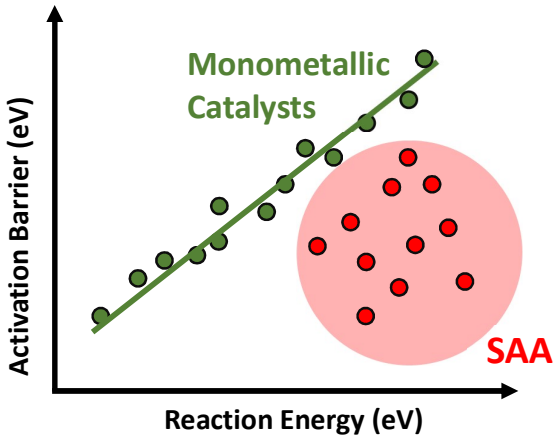

Figure 4. The use of SAAs is a strategy to break the traditional BEP relations, which are "convenient" but place a constraint to the catalytic performance.

According to studies dedicated to the activation of chemical bonds, SAAs break the traditional BEP relations because a dissociation reaction is activated on the dopant site, while the dissociation products may desorb from the surrounding host metal sites in a facile manner. On this basis, these remarkable materials bring us one step closer to the development of optimal heterogeneous catalysts.[47] On the other hand, the reasons why the reactivity of SAA surfaces cannot be rationalised by the *d* band model are not fully clarified yet, but they might be related to the repulsion between the adsorbate states and the localised *d* band of the isolated dopant.[5]

1.5. Highly dilute alloys – dopant clusters

The application of SAAs has been met with resounding success in the catalysis of numerous chemical processes; yet, their use is not ubiquitous. In some instances, dispersed dopant atoms are not capable of activating chemical bonds, with this task requiring contiguous active dopant metal sites like those seen in Figure 5.[48] The largest part of this Thesis is focusing on the catalytic properties of surfaces where dopants are organised in small clusters (e.g. dimers and trimers – Figure 5), but also on how to manipulate the morphology of such highly dilute alloys toward tailored catalytic performance for a specific application.

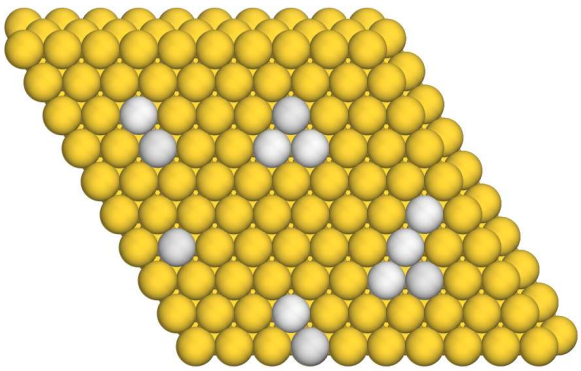

Figure 5. A (111) dilute alloy surface where dopant are organised in small clusters like dimers, trimers and tetramers. Host and dopant atoms are shown in yellow and grey, respectively.

There are several examples where the disparate catalytic behaviour between isolated dopant atoms and small dopant clusters on coinage metal surfaces has been reported. Goodman and co–workers studied the dehydrogenation of ethylene (C_2H_4) over a Pd/Au alloy supported on SiO_2, and

they argued that the reaction rate increases linearly with respect to the density of Pd dimer and trimer species on the catalyst surface.[49] Interestingly, in the absence of these Pd clusters, the reaction rate was poor, whereas at high densities of contiguous sites, the activity was excellent. Similarly, Gao et al.[50] examined the catalytic oxidation of CO over a Pd/Au(100) surface, and determined that isolated Pd atoms are incapable of dissociating O_2*, which is an essential elementary reaction in a number of oxidative chemical systems. The inability of isolated Pd atoms to dissociate O_2* has since been rationalised DFT calculations by Ham et al.[51] and their calculations have demonstrated that the activation barrier of the O_2* scission reaction is significantly lower on Pd dimers and Pd trimers as compared to single Pd atoms. The lower activation barrier of the reaction in the former configurations is attributed to the fact that Pd aggregates are only partially covered by CO* (e.g., a Pd dimer with only one CO* adsorbed thereon), thereby enabling O_2* to interact with the free Pd atoms of the small clusters for a sufficient amount of time and, therefore, dissociate.[51] The calculations of Kim and Henkelman on the same system (i.e. CO oxidation on Pd/Au alloys) highlighted that only clusters with more than three Pd atoms favour the adsorption of O_2 over CO adsorption, and on this basis the authors concluded that these are the active clusters for the catalytic CO oxidation.[52] Wang et al. demonstrated that Pd–Pd dimers on a Au host matrix exhibit optimal catalytic performance during the electroreduction of CO_2.[53] Qiu et al. proposed that Co trimers and tetramers on a Cu host are highly active and selective for the synthesis of CH_3OH via the hydrogenation of CO_2.[54] This is because CO_2* interacts strongly with the latter Co aggregates, and this strong interaction promotes its dissociation over desorption. McCue and Anderson studied the performance of Pd/Cu alloys toward the hydrogenation of acetylene (C_2H_2).[55] The surface composition of the Pd/Cu catalyst was quantified by means of Fourier–transform infrared (FTIR) spectroscopy, and the authors determined that surfaces whereon there is a significant fraction of Pd–Pd dimers are more active than that where the SAA phase prevails**.** Along the same lines, Stakheev et al.[56] conjectured that the SAA phase exhibits relatively low activity during the hydrogenation of diphenylacetylene over Pd/Ag alloys, while Vignola et al.[57]

argued that the oligomerisation of C_2H_2, which takes place as a side–reaction during its hydrogenation, could be prevented by clusters of two or three Pd atoms. Oligomerisation gives rise to detrimental coupled species that poison the active sites of the process catalyst, and therefore, using clusters that prevent this would be essential in catalytic process development.

These studies along with those referenced in the previous paragraph indicate that certain chemistries can be catalysed by materials with dopant atoms at high dispersion, whereas other chemistries require the presence of contiguous sites as found in dopant atom dimers, trimers, and islands. Therefore, it is important to define ways to control the topological architecture of bimetallic catalysts, and this is a topic of interest in this Thesis (Chapters 7 and 8).

Unsurprisingly, the restructuring of catalytic materials has been extensively researched, and a number of experimental and theoretical studies investigating the structure of alloy systems under vacuum[58,59] versus reactive conditions[55–57,60–63] (i.e., in the presence of adsorbates) have appeared in the literature. Since catalytic surfaces interact with gas–phase species during catalysis, it is reasonable to focus on catalyst restructuring under reactive conditions. The effect of numerous adsorbates (e.g. CO*, H*, O*, S*) on the structure of single crystal surfaces has been investigated.[64] Out of these adsorbates, CO* is of great interest because: (1) it is typically used as a probe molecule for specifying the properties of adsorption on solid materials; (2) it is a common molecule in many industrial chemistries; (3) it binds strongly on many transition metal surfaces, thereby causing considerable morphological changes to them.[55] Interestingly, the chemisorption of CO on metal surfaces gives rise to mobile surface species. Highly mobile carbonyl species on Pt– and Pd–doped Fe_3O_4(001) have been observed with scanning tunnelling microscopy (STM) after exposure of the surfaces to CO gas at low P_{CO} (e.g., 2×10^{-10} mbar); these species appeared to promote the formation of Pd and Pt aggregates over dopant dispersion. Additionally, the possibility of CO–induced surface manipulation has been demonstrated through diffuse reflectance infrared Fourier transform spectroscopy (DRIFTS) and FTIR studies on dilute Pd/Au and Pd/Cu alloys.[55,65] Both of these studies indicated that the exposure of the

alloy surfaces to CO gas caused the migration of Pd atoms from the bulk to the surface and the formation of dopant aggregates. The latter was evidenced by bands observed at relatively low wavenumbers of the FTIR spectra (ca. 2002 cm^{-1} see ref. 55) that correspond to CO* adsorbed on Pd atom clusters. CO–induced restructuring was further investigated in other experimental,[66] and computational studies,[67] and as mentioned earlier is the topic of chapters 7 and 8.

1.6. About this Thesis

Motivated by these studies, this Thesis examines the reactivity and surface restructuring of highly dilute alloys, while a small part of it is dedicated to the effect of adsorbate–adsorbate interactions on the adlayer structure and therefore on the rate of catalytic reactions. The presented investigations make use of sophisticated computational methods that improve our understanding with regard to atomic– and molecular–scale processes, and aid the development of heterogeneous catalysts. These methods are DFT and KMC and are reviewed at a relatively high level in chapters 2 and 3, respectively. However, the computational setup for the presented calculations is briefly described in the beginning of the corresponding chapter. In chapter 4, we explore coverage effects and their impact on reaction rates predicted by KMC simulations. To this end, we model the oxidation of NO on Pt(111). In Chapter 5, our focus turns to bimetallic alloys, and in particular to the performance of a number of dilute alloy surfaces toward association and dissociation reactions that are relevant to emission control technologies (e.g. NO dissociation, N_2 formation). We thus perform screening studies that highlight promising materials for the NO + CO reaction, and the most promising of these materials are assessed by additional first principles calculation and microkinetic modelling in chapter 6. Moreover, chapters 7 and 8 discuss strategies for the manipulation of dilute alloy surfaces. Finally, chapter 9 summarises the findings of the Thesis and provides directions for future research.

Chapter 2

2. Overview of density functional theory

The energy of gas–phase molecules, solid surfaces, and adsorbate overlayers can be obtained by electronic structure calculations. Use of these energies enables us to compute important parameters in relation to heterogeneous reactions (e.g. adsorption energies, activation barriers for "single–step" reactions), accordingly to identify the most favoured reaction paths for a chemical process, and parameterise kinetic simulations. This is an elegant bottom–up approach for modelling reactions on solid surfaces, and allows us to make a connection between the processes occurring at the atomistic and molecular scales to what is observed in the macroscale (i.e. catalyst and reactor scales). The most widespread electronic structure method in catalysis literature is the Kohn–Sham DFT.[68] The increasing popularity of the DFT method is attributed to its relatively low computational expense, as well as to the good agreement of predicted observables with experimental values for many systems. As this method is extensively employed in the remainder of this Thesis, the present chapter is dedicated to its fundamentals.

2.1. The Schrödinger equation

We start our discussion by describing the celebrated equation by Schrödinger (eq. (3)), which is used to study matter in the atomic and molecular levels within the framework of quantum mechanics. Its solution provides the wave function (Ψ) of any system, namely an entity that replaces the classical concept of the trajectory of a particle. Based on Ψ one calculates the probability of finding an electron in a point of certain coordinates within the system, but this function becomes extremely complex for systems with numerous nuclei and electrons. Given that the wave function contains the coordinates of every electron and nucleus (i.e. $\Psi = \Psi$ ($\mathbf{R_1}, \mathbf{R_2}, \ldots, \mathbf{R_{N+n}}$)), a system with N electrons and n nuclei entails an $3(n+N)$ dimensional problem. It follows that solving Schrödinger's equation for catalytic surfaces, which are essentially composed of several hundreds of atoms, will be an enormously complex, multidimensional problem. The time–independent Schrödinger equation in its succinct form is

$$\hat{H}\Psi(\mathbf{R}_1,.....,\mathbf{R}_{N+n}) = E\Psi(\mathbf{R}_1,.....,\mathbf{R}_{N+n}). \quad (3)$$

The Hamiltonian in eq. (3) is

$$\hat{H} = \left[-\frac{1}{2}\sum_{i=1}^{N}\nabla_i^2 - \frac{1}{2}\sum_{a=1}^{n}\frac{\nabla_a^2}{M_a} - \sum_{i=1}^{N}\sum_{a=1}^{n}\frac{Z_a}{|\mathbf{R}_i - \mathbf{R}_a|} + \frac{1}{2}\sum_{i=1}^{N}\sum_{j\neq i}^{N}\frac{1}{|\mathbf{R}_j - \mathbf{R}_i|} + \frac{1}{2}\sum_{i=1}^{N}\sum_{j\neq i}^{N}\frac{Z_a Z_\beta}{|\mathbf{R}_a - \mathbf{R}_\beta|} \right], \quad (4)$$

where the first two terms in the bracket are the kinetic energies of electron and nuclei, respectively; the third, fourth and last terms define the electron–nuclei, electron–electron and nuclei-nuclei interactions, respectively; M_a and Z_a are the mass and charge of nucleus α, respectively. The bracket term as a whole is the Hamiltonian operator that operates on Ψ. The last two terms are multiplied by ½ so that double counting is prevented.

The high complexity of eq. (3) can be reduced by making reasonable approximations. The first approximation relies on the fact that protons and neutrons are more than *1800* times heavier than electrons. Thus, one may treat the nuclei as stationary particles that create a field within which there

is a continuous motion of electrons. This is the *Born–Oppenheimer* approximation,[69] which enables the division of the electronic structure problem into two parts. These are the electronic and nuclear parts that can be solved independently, thereby reducing the dimensionality of the wave function from $3(n+N)$ to $3N$. Under these circumstances, the *electronic* Schrödinger equation is simplified to

$$\hat{H}_{elec}\,\Psi\left(\mathbf{R}_1,.....,\mathbf{R}_N\right)=E_{elec}\,\Psi\left(\mathbf{R}_1,.....,\mathbf{R}_N\right), \tag{5}$$

and the electronic Hamiltonian is simplified to

$$\hat{H}_{elec}=\left[-\frac{1}{2}\sum_{i=1}^{N}\nabla_i^2-\sum_{i=1}^{N}\sum_{a=1}^{n}\frac{Z_a}{\left|\mathbf{R}_i-\mathbf{R}_a\right|}+\frac{1}{2}\sum_{i=1}^{N}\sum_{j\neq i}^{N}\frac{1}{\left|\mathbf{R}_j-\mathbf{R}_i\right|}\right]. \tag{6}$$

The solution of eq. (5) provides the electronic energy based on which one may calculate the total energy of the system as

$$E_{total}=E_{elec}+\frac{1}{2}\sum_{i=1}^{N}\sum_{j\neq i}^{N}\frac{Z_a Z_\beta}{\left|\mathbf{R}_a-\mathbf{R}_\beta\right|}, \tag{7}$$

where the second term on the right appears in eq. (4) and represents the nuclei–nuclei repulsions. The ground state energy is expressed as a function of the position of the nuclei (i.e. $E_{total}(\mathbf{R_1}, \mathbf{R_2},\ldots, \mathbf{R_n})$). This function is known as the potential energy surface (PES) because the kinetic energy of the stationary nuclei is zero.

2.2. Density functional theory

Under the Born–Oppenheimer approximation, the dimensionality of Ψ is reduced; however, the task of solving the Schrödinger equation remains a formidable one. To be more specific, the electronic wave function is now a function of x, y and z coordinates of each electron in the system (i.e. $\Psi = \Psi\ (\mathbf{R_1}, \mathbf{R_2},\ldots, \mathbf{R_N})$). Therefore, even a small cluster of 10 Cu atoms (supported NPs usually contain thousands of atoms) will result in a Ψ with more than *870* dimensions. The situation is even worse owing to the complicated form of the electron–electron repulsion term (i.e. 3rd term in the bracket of eq. (6)).

At this point, we note that the electronic wave function is a mathematical construct that cannot be observed in an experiment. What one can measure instead, is the probability that *N* electrons will have a set of coordinates (e.g. $\mathbf{R}_1$, $\mathbf{R}_2$,…, $\mathbf{R}_N$), and a closely related quantity to this is the electron density, $\rho(\mathbf{r})$. This is a three–dimensional function that can be determined experimentally using X–ray diffraction.[70] The electron density provides a wealth of information (e.g. the average position of the electrons and the total number of electrons), which is essentially the same to what is obtained once the extremely complex $\Psi(\mathbf{R}_1, \mathbf{R}_2, \ldots, \mathbf{R}_N)$ "has been specified". This implies that instead of focusing on how to attain Ψ, our goal should be to solve for $\rho(\mathbf{r})$. To this end, one can employ the DFT method, namely an electronic structure method that focuses on the electron density instead of the full wave function, and it is widely applied thanks to its satisfactory accuracy and moderate computational cost. This theory is based on two mathematical theorems proved by Kohn and Hohenberg,[71] but also on a set of equations developed by Kohn and Sham in the mid–1960s. These aspects are briefly discussed in the following, beginning with the two theorems.

The 1st theorem by Kohn and Hohenberg states that: *The ground–state energy of Schrödinger equation is a unique functional of the electron density.* In other words, this theorem dictates that based on the ground state electron density, one can uniquely determine the ground state energy ($E[\rho(\mathbf{r})]$), i.e. the solution of the incredibly intricate eq. (5). The high importance of the 1st theorem emerges from the fact that the 3*N* problem of solving Schrödinger equation may be converted into a three–dimensional problem. The only difference is that, we simply express the ground state energy as a functional of $\rho(\mathbf{r})$ and not with respect to $\Psi(\mathbf{R}_1, \mathbf{R}_2, \ldots, \mathbf{R}_N)$.

Yet, the 1st theorem gives no information on how to obtain the electronic density that corresponds to the ground state energy. This is done in the 2nd theorem by Kohn and Hohenberg, which unveils an important property of $E[\rho(\mathbf{r})]$: *The electronic density* $\rho(\mathbf{r})$ *that minimises the energy* $E[$

$\rho(\mathbf{r})$] *of the ground state is the electron density that corresponds to the full solution of Schrödinger equation*. The exact functional exists and is unique (1st Hohenberg–Kohn theorem), but unfortunately its exact form in not known. Therefore, approximate forms are employed in practice, and the variational principle is applied (according to the 2nd Hohenberg–Kohn theorem) in order to find the $\rho(\mathbf{r})$ that minimises $E[\rho(\mathbf{r})]$.

The two Hohenberg–Kohn theorems in conjunction with the so–called Kohn–Sham (KS) equations lay the foundations of the DFT method.[68] In particular, the work of Kohn and Sham demonstrated that the electron density that gives the ground state energy can be found by solving a system of differential equations where each equation correspond to an electron (eq. (8)). These equations describe fictitious non–interacting electrons that still obey the Pauli principle and are defined so that they yield the same electron density as that of interacting electrons.[68]

$$\left[-\frac{\hbar^2}{2m}\nabla^2 + V_{eff}(\mathbf{r})\right]\psi_i(\mathbf{r}) = \varepsilon_i\psi_i(\mathbf{r}), \tag{8}$$

where $\hbar$ is the reduced Planck constant; m is the mass of an electron. Having obtained the single–electron wave functions (ψ_i), one may compute the kinetic energy, which is a functional of $\rho(\mathbf{r})$ (eq. (9)), but also $\rho(\mathbf{r})$ itself (eq. (10))

$$T[\rho(\mathbf{r})] = -\frac{1}{2}\sum_{i=1}^{N}\int \psi_i^* \nabla^2 \psi_i d^3r, \tag{9}$$

$$\rho(\mathbf{r}) = \sum_{i=1}^{N}|\psi_i(\mathbf{r})|^2. \tag{10}$$

Once $\rho(\mathbf{r})$ is computed, numerous properties of the systems can be derived. For example, the total number of electrons is obtained by simply integrating $\rho(\mathbf{r})$ [72]

$$N = \int \rho(\mathbf{r}) d^3r \qquad \rho(\mathbf{r}) > 0 \quad . \tag{11}$$

V_{eff} in eq. (8) is an effective potential that contains three terms

$$V_{eff}(\mathbf{r}) = V(\mathbf{r}) + V_H(\mathbf{r}) + V_{XC}(\mathbf{r}), \tag{12}$$

where $V(\mathbf{r})$ describes the interaction between the *i* electron and all the atomic nuclei; $V_H(\mathbf{r})$ is the Hartree potential and $V_{XC}(\mathbf{r})$ is the exchange correlation (XC) energy. The Hartree potential describes the repulsion between the explicitly considered electron in the KS equation and the total electron density, and is given as

$$V_H(\mathbf{r}) = e^2 \int \frac{\rho(\mathbf{r}')}{|\mathbf{r} - \mathbf{r}'|} d^3r'; \tag{13}$$

interestingly, the explicitly considered electron is also part of the electron density, thereby interacting with itself. This is resulting in an unphysical self–interaction error, which is lumped into the exchange and correlation potential defined as

$$V_{XC}(\mathbf{r}) = \frac{\delta E_{XC}(\mathbf{r})}{\delta \rho(\mathbf{r})}, \tag{14}$$

where δ represents a functional derivative.[73]

From the equations presented in this section, it appears that the KS equations can only be solved after computing V_{eff} (eq. (12)), while V_{eff} can be found after obtaining the electron density (eq. (10)), which is attained based on the solution of the KS equations (eq. (8)). This "circularity" indicates that the KS equations should be solved iteratively after providing an initial guess for $\rho(\mathbf{r})$. Then, V_{eff} is calculated, the KS equations are solved and $\rho(\mathbf{r})$ is updated (Figure 6). This procedure is repeated until the difference between the initial and updated $\rho(\mathbf{r})$ is negligible, that is, the KS equations are solved numerically and in a self–consistent manner (Figure 6).

2.3. A brief overview on exchange–correlation functionals

According to KS DFT, the ground state energy is given by eq. (15) where the first three terms on the right are found based on the KS single–electron wave functions, while the last term is the XC term. This term accounts for quantum mechanical effects not included in the other terms, and also for the difference between the kinetic energies of interacting and non–interacting electrons.[74] Unfortunately, the XC term is not known and in practice, one has to resort in approximate expressions in this regard.

$$E[\rho]=T[\rho]+V[\rho]+V_H[\rho]+E_{XC}[\rho]. \tag{15}$$

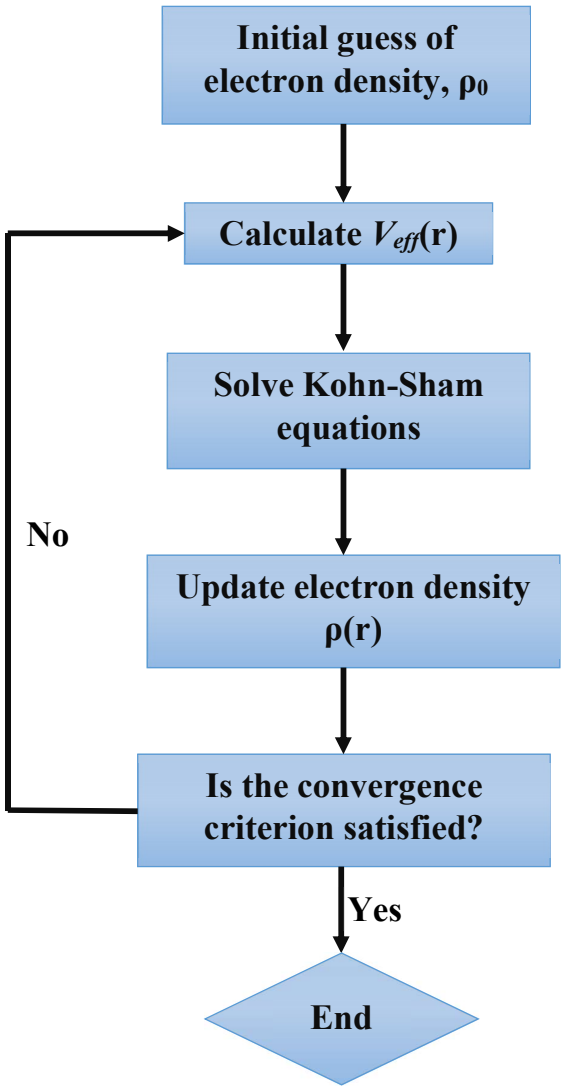

Figure 6. Iterative procedure for solving the KS equations in a self–consistent manner.

The largest portion of DFT error stems from the approximate nature of XC functionals that are currently in use, and the development of increasingly accurate XC functionals is a topic of ongoing research.[75] The following paragraphs provide a short description of commonly employed XC approximations.

The first, and simplest, approximation makes use of the local electron density to define the XC functional. This is the local density approximation (LDA), for which the $E_{XC}[\rho(\mathbf{r})]$ term is given by

$$E_{XC}[\rho(\mathbf{r})] = \int \rho(\mathbf{r})\,\varepsilon_{XC}^{unif}[\rho(\mathbf{r})]d^3r\,, \tag{16}$$

where ε_{XC}^{unif} is the exchange–correlation energy per electron in a uniform electron gas. This term can be divided into the exchange and the correlation terms, the former of which was derived by Dirac,[76]

$$\varepsilon_X^{unif}(\mathbf{r}) = -\frac{3\left(3\pi^2\right)^{\frac{1}{3}}}{4\pi}\rho(\mathbf{r})^{\frac{4}{3}}\,. \tag{17}$$

The analytical expression of the correlation term is unknown and differences between LDA functionals arise based on the way the correlation term is parametrised. Despite its simplicity, the LDA approximation works well in some occasions and turns out to correctly predict structural properties of solids.[77] On the other hand, LDA functionals become highly inaccurate when species either in an adsorbed state or in the gas–phase are present in the system that is being modelled. This is because under these conditions, the system deviates considerably from the uniform electron gas configuration. As molecular orbital (MO) theory states, a chemical bond is the result of accumulated electron density between two atoms as a result of the constructive interference of atomic orbitals.[78] In turn, this deviation gives rise to an inhomogeneous electron density, thereby deteriorating the accuracy of LDA.[77]

An improvement can be achieved by developing XC approximations that make use of more physical information than LDA. An example is the generalised gradient approximation (GGA), which considers the dependence of $E_{XC}[\rho(\mathbf{r})]$ on the density gradient and therefore

$$E_{XC}^{GGA}[\rho(\mathbf{r})] = \int \rho(\mathbf{r}) \varepsilon_{XC}^{GGA}[\rho(\mathbf{r}), \nabla\rho(\mathbf{r})] d^3r \,. \quad (18)$$

GGA functionals, and particularly the Perdew–Burke–Ernzerhof (PBE) functional, yield reliable results for processes that take place on solid surfaces.[79] For example, using a revised version of the PBE functional, Honkala et al. were able to determine the nature of the active site for NH_3 synthesis on Ru catalysts and to acquire insightful information about the reaction mechanism.[80] Additionally, GGA functionals predict adsorption energies over transition metal surfaces with a reasonable accuracy, since they provide values that typically differ by less than 0.2 eV as compared to experiment.[81] Along these lines, GGA functionals are the most widespread in the catalysis literature, and are also extensively employed in this Thesis.

Meta– and hyper–GGA are classes of functionals that include even more physical "ingredients" than GGA. Meta–GGA include information from $\rho(\mathbf{r})$, $\nabla\rho(\mathbf{r})$ and $\nabla^2\rho(\mathbf{r})$, while hyper–GGA include information from $\rho(\mathbf{r})$, $\nabla\rho(\mathbf{r})$ and describe the exchange by using a mixture of the exact exchange and the exchange of a GGA functional. These functional categories occupy higher rungs than GGA in the Jacob's ladder, which was used as a metaphor by Perdew co–workers for the classification of XC functionals (Figure 7).[82] The ladder leads to the "heaven" where the true XC functional "exists" and, on this basis, a DFT calculation gives the same result as the one obtained from the solution of the equation of Schrödinger (Figure 7).

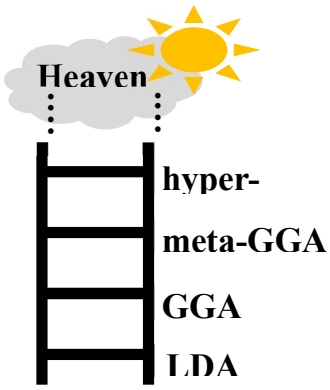

Figure 7. Jacob's ladder of density functional theory approximations for the XC energy.[82]

Yet, DFT functionals on higher rungs do not always provide better results as compared to that of lower rungs. For example, functionals on high rungs may be semi–empirical that have been developed based on specific experimental or *ab initio* data. Such functionals are expected to be fairly accurate for systems that are closely related to those in the selected training set, but they may fail to describe systems that exhibit significantly disparate behaviour.[83]

2.4. Practical aspects of DFT calculations on solid surfaces

Solid surfaces are composed of a very large number of atoms that form multi–layer structures, within which electrons can move freely. This results to a tremendously large number of occupied energy levels that are very close to each other, and therefore to the formation of energy bands instead of molecular orbitals like those of gas–phase species. Owing to the very large number of atoms involved in extended solid surfaces, one may expect that DFT calculations of solid surfaces will be a task that requires substantial computational effort. This is true, but fortunately, the computational cost can be alleviated by taking advantage of the periodicity encountered in crystal structures. A perfect solid structure (i.e. a structure that has no local defects) is a periodic configuration, where a finite part of the structure can be repeated to form the solid. This finite part is the unit cell and contains all the information one needs in order to define a periodic material with infinite extent. If this unit cell contains the minimum number of atoms that are necessary is the *primitive cell*.

For periodic surfaces, the solution of the Schrödinger equation satisfies Bloch's theorem according to which the wave functions of particles that experience a periodic potential in a lattice of spacing a (i.e. V(x+a) = V(x)), are given by eq. (19). We note that these solutions are only valid for periodic potentials.[84] As seen, the wave function is the product between two functions. $u_{\mathbf{k}}(\mathbf{r})$ is the *Bloch function* and has the same periodicity as the potential V. $\exp(i\mathbf{k}\cdot\mathbf{r})$ is a plane wave, and hence the name plane–wave calculations that is very often used for DFT calculations for extensive solid surfaces.

$$\psi_{\mathbf{k}} = \underbrace{\exp\left(i\,\mathbf{k}\cdot\mathbf{r}\right)}_{Plane\ wave}\ \underbrace{u_{\mathbf{k}}\left(\mathbf{r}\right)}_{Bloch\ function}, \tag{19}$$

where $u_{\mathbf{k}}\left(\mathbf{r}\right) = u_{\mathbf{k}}\left(\mathbf{r} + \mathrm{a}\right)$. The space of vectors **r** and **k** are called the real and the reciprocal space, respectively, and mathematical problems posed by DFT are often more conveniently solved in the **k** space than in the real space.[85] If $\mathbf{a}_1$, $\mathbf{a}_2$, and $\mathbf{a}_3$ are lattice vectors of the primitive cell in the real space, then the lattice vectors of the primitive cell in the reciprocal space (also known as *Brillouin zone* (BZ)) $\mathbf{b}_1$, $\mathbf{b}_2$ and $\mathbf{b}_3$ are defined so that $\mathbf{a}_i \cdot \mathbf{b}_j$ is 2π for i = j and 0 otherwise. The volumes of the two cells are related as shown by eq. (20),[85] and therefore larger vectors in the real space correspond to smaller vectors in the reciprocal space.

$$V_{BZ} = \frac{2\pi^3}{V_{cell}}, \tag{20}$$

where V_{BZ} and V_{Cell} are the volumes of the BZ and the primitive cell in the real space.

The periodicity of $u_{\mathbf{k}}\left(\mathbf{r}\right)$ suggests that the Bloch function can be expanded by means of a set of plane waves

$$u_{\mathbf{k}}\left(\mathbf{r}\right) = \sum_{\mathbf{G}} c_{\mathbf{G}}\ \exp[i\,\mathbf{G}\cdot\mathbf{r}], \tag{21}$$

where $\mathbf{G} = \mathrm{m}_1\,\mathbf{b}_1 + \mathrm{m}_2\,\mathbf{b}_2 + \mathrm{m}_3\,\mathbf{b}_3$ is a reciprocal lattice vector that satisfies $\mathbf{G}\cdot\mathbf{R} = 2\pi\mathrm{m}_i$, with m_i being an integer and **R** being a real space lattice vector.[85] By replacing eq. (21) into eq. (19)

$$\psi_{\mathbf{k}}\left(\mathbf{r}\right) = \sum_{\mathbf{G}+\mathbf{k}} c_{\mathbf{G}+\mathbf{k}} \exp\left(i\left(\mathbf{k}+\mathbf{G}\right)\mathbf{r}\right), \tag{22}$$

where $c_{\mathbf{G}+\mathbf{k}}$ is a plane wave expansion coefficient. Eq. (22) implies that for a system with infinite number of electrons, occupying infinite different states in **k** space, an infinite number of calculations will be required. In addition, it appears that in order to evaluate the solution even at a single point in **k** space, the summation of eq. (22) will have to go over an infinite number of possible **G** values. However, the electronic wave function is very similar on **k** points that are very close in the reciprocal

space. Moreover, when $\Psi_{\mathbf{k}}$ is expanded to infinity leads to solutions of a very high kinetic energy that have little meaning from a physical standpoint. This issue is resolved by setting a cutoff energy, E_{cut} ($E_{cut} = \left(\hbar^2 / 2m\right)\mathbf{G}_{cut}^2$), that truncates the summation in eq. (22)

$$\boldsymbol{\psi}_{\mathbf{k}}(\mathbf{r}) = \sum_{|\mathbf{k}+\mathbf{G}|<\mathbf{G}_{cut}} c_{\mathbf{k}+\mathbf{G}} \exp\left(i(\mathbf{k}+\mathbf{G})\mathbf{r}\right) \cdot \tag{23}$$

To find the cutoff energy that provides the desired accuracy, one has to converge the total energy (or the parameter of interest) with respect to E_{cut} . The same is true for the **k**–point mesh that is used to sample the Brillouin zone.[85]

2.5. Pseudopotentials

We conclude our discussion on DFT with a short introduction to pseudopotentials. According to our previous discussion, a large E_{cut} will be needed in order to take into account fast oscillating plane waves of high curvature. The kinetic energy operator $\hat{E}_{kin} = -\left(\hbar^2/2m\right)\nabla^2$, which appears in the equation of Schrödinger, contains a second derivative term. In general, the second derivative provides a measure of the curvature of a mathematical function. It follows that the larger the second derivative the sharper the function will be, and, in turn, the higher the kinetic energy of the particle. Core electrons are often characterised by a very high kinetic energy and consequently their wave functions show fast oscillations that are also large in amplitude. For an accurate description of these electrons, the summation in eq. (22) has to be expanded to a large extent, and that will significantly increase the computational cost of DFT calculations.

Nonetheless, core electrons have hardly had any effect on the physical properties of a material. The less tightly bound valence electrons are those that participate in chemical bonding, thereby determining the properties and behaviour of the material. Accordingly, it is reasonable to approximate the behaviour of core electrons so that the number of plane waves that should be added in the summation of eq. (22) is kept minimal. This task is accomplished by employing pseudopotentials,

which render plane wave calculations computationally tractable. In doing so, the electron density of a set of core electrons is simply replaced by an effective potential, which is a smooth function that properly describes the physical properties of the actual ionic core. DFT software packages often provide a library of pseudopotentials. Those that require high E_{cut}, are called hard, whereas those with a low E_{cut} are called soft pseudopotentials. A type of the latter is the ultrasoft pseudopotentials. Although a low E_{cut} is needed in this case, usually a number of empirical parameters has to be specified. An alternative way to approach pseudopotentials is the projector–augmented–wave (PAW) method,[86] which requires the use of no empirical parameters, and provides equally accurate results as ultrasoft pseudopotentials or even better for materials with high magnetic moment.[86]

2.6. Concluding Remarks

This chapter provided a high–level overview of the DFT method, by means of which one can obtain the electronic structure of catalytic surfaces covered with adsorbates, and investigate atomic–scale processes (e.g. bond breaking). As discussed, modern DFT relies on two theorems by Kohn and Hohenberg and on a set of equations known as the KS equations. Although DFT calculations are generally insightful, they disregard effects that are always present during an actual surface reaction. For example, DFT is a zero temperature approach, but surface reactions never happen at 0 K. Therefore, we proceed by discussing how DFT results may be used to parameterise models that account for such effects, thereby enabling the accurate description of heterogeneous reactions.

Chapter 3

3. Kinetic Monte Carlo

DFT has been playing a key role in the development of state-of-the-art catalytic materials (e.g. Ni_3Fe for the methanation of CO,[87] Co–doped MoS_2 for hydrodesulphurisation reactions[88]), and it is the most established electronic structure method within the computational catalysis community. Yet, this method is limited to small systems, under zero pressure and temperature conditions. To accurately model a surface reaction, one needs to take into account temperature, pressure and important entropy effects. This may be accomplished by parametrising KMC simulations based on DFT–derived energetics. The KMC method is a sophisticated statistical mechanics technique, which can deal with the highly complex nature of surface reactions. The following sections are dedicated to the theoretical foundation this method,[89] applications of which are presented in chapters 4 and 8. *The contents of this chapter have been published in Computational Modelling of Nanomaterials, Volume 17, 2020, pp. 95–125*.

3.1. The time scale problem and the KMC trajectory

During a chemical transformation, a system performs a "jump" from one basin (i.e. reactant state **A**) of the PES to another (i.e. the product state **B**). The two states are separated by an energy barrier, which is the difference between the energy of the transition state of the transformation minus the energy of the initial state (**A**). The energy barrier will be traversed only when sufficient momentum is possessed by the system. Until that time, the system may spend a lot of time wandering in the basin of the initial state, performing random vibrations.

Conventionally, one can follow the evolution of the system from state **A** to state **B** by adopting some variant of molecular dynamics (MD). The MD method is based on the numerical integration of Newton's 2nd law of motion with respect to time, thereby providing the full trajectory followed by the system upon the **A→B** transition. The reliability of the simulated MD trajectories depends on the accuracy of the calculation of the forces ($\mathbf{F}_i$) exerted on the participating atomic species, and in order to assure high accuracy and numerical stability during simulation, the selected time step in an MD simulation must be small enough to resolve atomic vibrations. As the latter occur in the picosecond scale,[90] typically employed MD time steps are in the order of femtoseconds.[91] Then, it comes as no surprise that the time scales accessible by the MD method is, at best (even by taking the advantage of modern supercomputers), in the order of microseconds.

Yet, in the field of catalytic reaction engineering, one is interested in reactive events (or rare events in MD parlance), which arise from barrier crossings. Reactive events may require seconds or even hours to happen, namely time scales that are not accessible by classical MD techniques (hence the term rare events). However, as mentioned earlier, the system can spend a significant amount of time in an initial state **A** undergoing random vibrations that do not alter its chemical state and therefore are not reactive events. To circumvent the problem of the large gap between the time–scale of a molecular vibration and a chemical reaction, we may resort to methods that focus on the coarse time–scale of barrier crossing and not on atomic vibrations that occur in the picosecond scale.

Thus, KMC is a method that bridges the time–scale gap between atomic vibrations and elementary reactive events, and can be adopted to study the kinetics of catalytic reactions. In a KMC simulation, our attention is focused on the statistics of barrier crossing, based upon which a stochastic trajectory is generated. Post–processing of this trajectory yields macroscopically observed quantities (e.g. surface coverage, turnover frequency, reaction order with respect to surface species, etc.) that can be directly compared to experimental observables.

Importantly, the information with regard to barrier crossing is coarse–grained in the so–called reaction rate constant (k_{ij}). This parameter is derived from the transition state theory (TST) and represents the average number of the occurring $i \rightarrow j$ events per unit time. In more precise terms, this parameter tells us that on average $k_{ij} \cdot d\tau$ events will happen within the time interval [$\boldsymbol{\tau}$, $\boldsymbol{\tau} + d\boldsymbol{\tau}$], per reacting species (or configuration, e.g. a pair of molecules on neighbouring lattice sites), while it gives no information on when a specific event will take place. One of the fundamental assumptions of TST is that the reactant state is Boltzmann–distributed.[92] This assumption appears to be in line with the extensive wandering of the system in the initial PES basin before the occurrence of the reactive event, which allows the initial state to reach quasi–equilibrium. Additionally, provided that the fundamental assumptions of the TST (e.g. Boltzmann distributed initial state, rare event occurrence, no quantum tunneling, etc.) are valid, and that k_{ij} is accurately calculated from a force–field, the overall reaction rates predicted by a KMC simulation will be identical to those of an MD simulation with the same force–field. However, the KMC results would have been obtained at a fraction of the computational cost of MD.

The principles of the KMC method and the corresponding KMC trajectory can be illustrated using a prototype model involving a CO molecule that is either adsorbed on a Ni(111) surface or exists in the gas phase. We assume that CO is initially adsorbed on the low–index Ni(111) surface (Figure 8 (a)). Then the temperature is increased gradually, causing the desorption of CO* (such an elementary event may take place in a Temperature–Programmed Desorption experiment). Figure 8 (a) shows the

PES for the desorption of CO* from Ni(111), where state **A** corresponds to the adsorbed state and state **B** corresponds to a gaseous (desorbed) state (Figure 8 (c)). The blue curly line in Figure 8 (a) represents a typical MD trajectory, and as observed the system undergoes extensive wandering within the basin of the adsorbed state, before traversing the energy barrier ($E_{barrier}$) and making a "jump" to the desorbed gas state (state **B**).

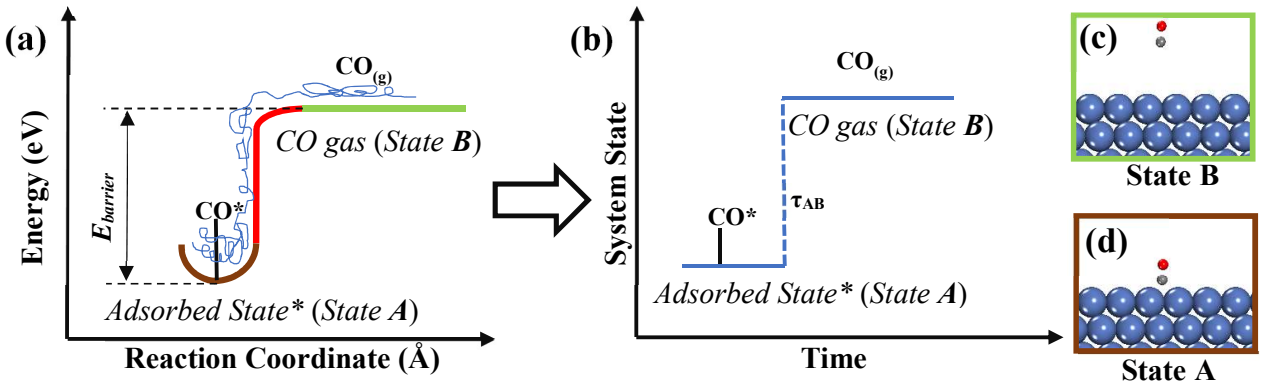

Figure 8. Panel (a) shows a schematic description of the PES for the desorption of CO* from a Ni(111) surface. The blue curly line shows a representative MD trajectory. CO in the desorbed state is assumed to be in a gas state; panel (b) shows a schematic of a KMC trajectory, indicating the state–to–state dynamics followed in a KMC simulation; panel (c) shows the desorbed state that corresponds to the right flat part of the PES in (a); the distance between CO and surface is sufficiently large, thereby ensuring small interaction between CO and the Ni surface; panel (d) shows the adsorbed state as found from DFT calculations. C, O and Ni atoms are shown in grey, red and blue, respectively.

On the other hand, the KMC method does not resolve these fast molecular motions that, as highlighted earlier, are not reactive events. The corresponding KMC trajectory is portrayed in Figure 8 (b), where one observes state–to–state dynamics. In simpler terms, in a KMC simulation, CO will be either adsorbed or in the gaseous state. The KMC trajectory emerges through a sequence of state–to–state hops that eventually allow us to simulate a large number of reactive events, and consequently to access time scales that are relevant to catalytic applications. We point out that the time interval spent in a particular state depends on the energetic features of the possible "escape pathways" from that state to others. This "lingering time" (more formally referred to as "waiting time" or "inter–arrival time") is dictated by the rate constant, k_{ij} (where i and j are the initial and final states), which quantifies the propensity (i.e. the probability of occurrence of an event per unit time) for a transition.

3.2. Fundamental concepts in KMC simulations

KMC simulations that model surface reactions are commonly lattice–based; thus, the catalytic surface is represented by a lattice, which is a collection of sites with translational symmetry, thereby forming a regular grid. Because of the translational invariance, the position of each site of the grid is defined by two linearly independent vectors, $\mathbf{A_1}$ and $\mathbf{A_2}$, which are the so–called *primitive vectors* and are not uniquely defined. For example for the low–index (100) surface, two possible pairs of primitive vectors would be: $\mathbf{A_1} = \alpha(1,0)$ & $\mathbf{A_2} = \alpha(0,1)$ or $\mathbf{A_1} = \alpha(-1,0)$ & $\mathbf{A_2} = \alpha(0,1)$ where α is the lattice constant of the metal. The points lying within the area spanned by the primitive vectors (essentially within the unit cell) are:

$$m_1 \cdot \mathbf{A_1} + m_2 \cdot \mathbf{A_2},$$

where $m_1, m_2 \in [0, 1)$. A unit cell may contain a single site (this corresponds to a Bravais lattice) or more than one site (this corresponds to a composite lattice), and by tiling it over space one gets the simulation lattice.

The lattice sites can be either occupied by an adsorbate or vacant (i.e. "occupied" by a "free site" pseudo–species). Each site has a site number (i.e. site identity) and an occupation variable pertinent to its state (i.e. vacant or occupied). Within the lattice–gas model formalism, when the latter index is 0 the site is vacant, whilst when this is 1 the site is occupied by an adsorbate. Furthermore, if the adsorbate layer is composed of more than one adspecies, additional indices, besides 0 and 1, have to be used in order to fully specify the state of a particular lattice site. By registering all the aforementioned indices into a two–dimensional matrix (i.e. the occupation matrix), one becomes aware of whether a site is free or occupied by an adsorbate, and in the latter case by which adsorbate. In this way, the state of the lattice is fully specified.

The concept of this simple matrix–grid representation of KMC lattices is highlighted in Figure 9 (a) and (b), where the adsorbate layer of the portrayed lattices are composed of CO*, O* and "free site" "pseudo–species". The latter species are represented by 2, 1 and 0, respectively. The

configuration in Figure 9 (a) can be directly mapped onto the occupation matrix, wherein each element describes the state of a site. A reactive event between an O* and a CO* species involves two sites, and can only happen if these two species exist in neighbouring sites. For instance, in the system portrayed in Figure 9 (a), a realisable CO* + O* → $CO_{2(g)}$ event involves sites 22 and 23 and its execution will bring about a change in the adsorbate layer and in the occupation matrix (Figure 9 (b)). Hence, a KMC event is simply modelled as a change in the occupation matrix.

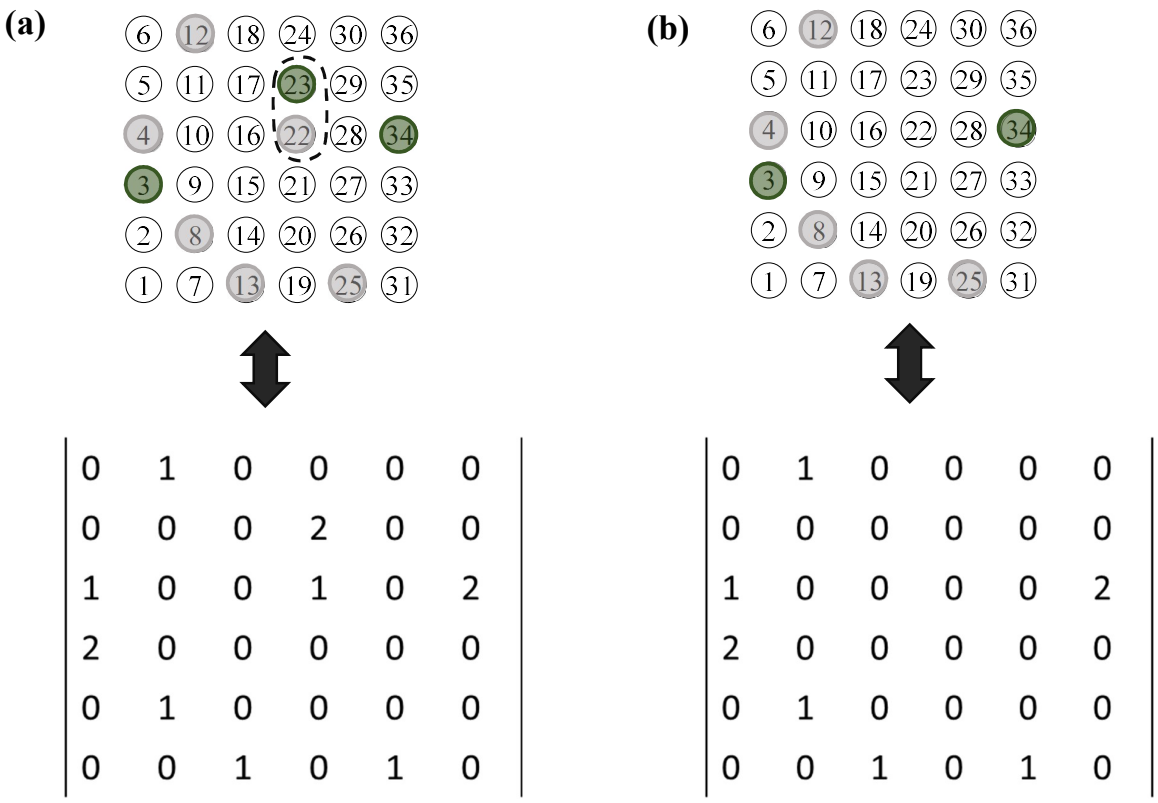

Figure 9. (a) A rectangular lattice whose adlayer pattern is mapped into the occupation matrix; (b) Same lattice as in (a) and the modified occupation matrix after the execution of a CO* + O* → $CO_{2(g)}$ event. Site numbers are shown in the centre of the circles in both (a) and (b). The white circles with thin black edges are vacant sites, the grey circles with grey edges indicate O* species and the green circles with thick green edges indicate CO* species.

We highlight that the connectivity between the lattice sites is a crucial property for the successful enlistment of possible events on the simulation. For the simple examples we just discussed, the site corresponding to element (m,k) of the occupation matrix, has the following four neighbours:

(m+1,k), (m,k+1), (m-1,k) and (m,k-1). Thus the detection of a reactive pattern, such as CO oxidation, amounts to checking that the "current" site (m,k) and one of its neighbours are occupied by CO* and O* respectively (Figure 9 (a)). For more complicated lattices, the lists of neighbours can be stored in the memory for efficient detection of such reactive patterns, but also for the detection of energetic interaction clusters (see section 3.6).

The site occupation can change because of the random (stochastic) execution of microscopic processes (i.e. KMC events). The latter can be adsorptions or desorptions of species, reactions (Eley-Rideal or Langmuir-Hinshelwood) and diffusions of adspecies from one site to another. Throughout the KMC simulation, a large number of events is executed, but only one event is simulated per KMC step. For instance, a diffusion and an adsorption cannot happen simultaneously, but only in two consecutive KMC steps.

To better illustrate this concept, we return to our exemplar system of section 3.1 (CO on Ni(111)). We assume that the Ni(111) surface is in contact with a gas species reservoir of $CO_{(g)}$ (Figure 10). In state **A** there is a $CO_{(g)}$ molecule that approaches the surface (Figure 10), and subsequently (in state **B**, Figure 10) it binds thereon as a result of electronic interactions with the Ni atoms on the solid surface. This process is modelled by the execution of a KMC elementary event, which changes the microscopic energy of the system. The two snapshots of the catalytic surface in Figure 10 (state **A** and state **B**) correspond to two basins of the PES that are visited by the system. We point out that it is likely, but not necessary, that the microscopic energy of the system will be different in two consecutive states visited by the system (e.g. as those shown in Figure 10). An example of a KMC event that causes no change to the microscopic energy of the system is the diffusion of a species from an atop site to another atop site on an empty lattice (i.e. in the absence of any spectator species). In this case, the initial state is equivalent to the final state by translational symmetry, and of course, the two states have identical energies.

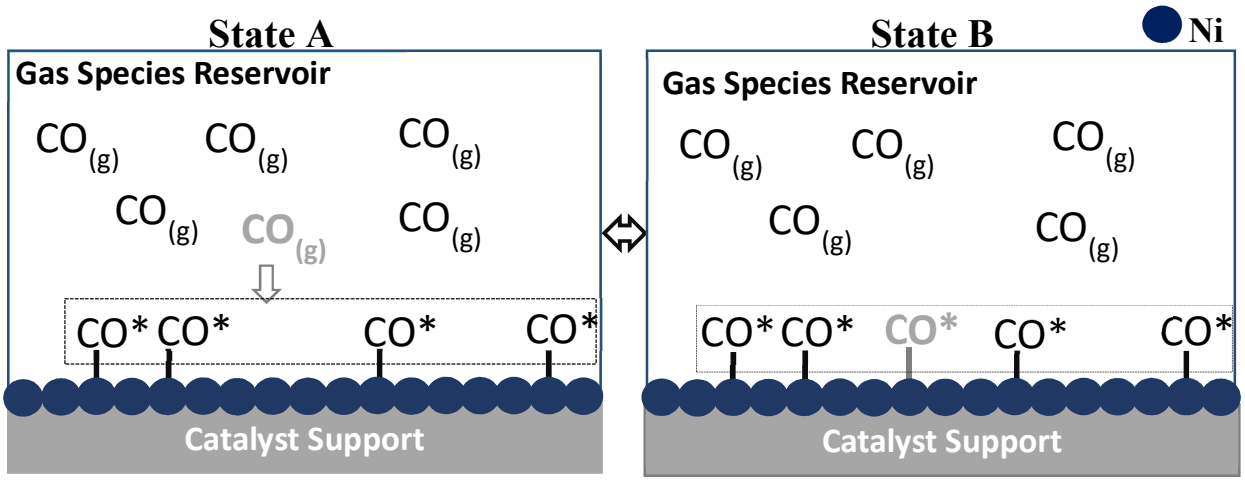

Figure 10. Illustration of an elementary process (CO adsorption on Ni(111)) that changes the adsorbate layer structure in a KMC simulation. The execution of this process corresponds to one KMC step. The species involved in the elementary process are shown in grey, the rest of gas phase species are shown in black, Ni atoms are shown as filled dark blue spheres, adspecies are shown with an * notation and the catalyst support is shown in grey**.** In both insets, the adspecies that compose the adsorbate layer are enclosed in dashed rectangles.

During a KMC simulation the occurrence of reactive events is random and satisfies the so–called *Markov property*,[93] which states that given the present state of the system, the probability of a transition to another state is independent of the past history. In addition, KMC simulations of physical systems of interest typically satisfy an additional property, which calls for *memoryless transitions*, or equivalently, exponentially distributed waiting (inter–arrival) times. This is justified as follows: as the system vibrates in the current PES basin (which corresponds to a KMC state) before the barrier crossing, momentum is continuously dissipated leading to quasi–equilibrium. The equilibration of the system in the current PES basin "breaks" any connection between the state visited prior to the current state and any state (basins) that will be visited next. These two properties (Markov and memoryless) are central to the formulation of the KMC framework.

As the system performs "jumps" from one basin of the PES to another, it passes through a large number of states. The collection of these states defines the state space, **Ω**, and a KMC simulation is nothing more than a random walk within **Ω**, emerging by the simulation of a sequence of elementary processes. Because of the Markovian nature of the KMC processes, we express the evolution of the

probability of finding the system in a particular state i, $P_i(\mathbf{t})$ where $i \in \mathbf{\Omega}$, by means of the Markovian Master equation:

$$\frac{dP_i(\mathbf{t})}{dt} = -\sum_{i \neq j} k_{ij} P_i(\mathbf{t}) + \sum_{i \neq j} k_{ji} P_j(\mathbf{t}), \tag{24}$$

where k_{ij} is the rate constant of the elementary event that brings about the transition from state i to another state j ($j \in \mathbf{\Omega}$) and k_{ji} is the rate of the reverse transition. If state j is not accessible from state i via a single elementary event, the corresponding rate constant is zero. The states i and j correspond to two different adlayer structures (see e.g. Figure 10).

Eq. (24) is simply a *loss–gain* equation: the first term on the right hand is the loss term that decreases $P_i(\mathbf{t})$ as a result of transition from i to j, and the second term is the gain term that increases $P_i(\mathbf{t})$ as the system moves from another state j to i. The numerical solution of the Master equation is a daunting task because of the very large number of states visited by the system in a KMC simulation. Nevertheless, one does not need to perform such a task. One needs to produce trajectories with statistics consistent with the Master equation instead, and this is what is done in KMC simulations.

Additionally, the Master equation imposes thermodynamic constraints that must be obeyed. In particular, under stationary conditions, the probability of finding the system at a state i has to be constant with respect to time (i.e. $\frac{dP_i(\mathbf{t})}{dt} = 0$), and from eq. (24) we write

$$\sum_{i \neq j} k_{ji} P_j^{eq} = \sum_{i \neq j} k_{ij} P_i^{eq}, \tag{25}$$

where P^{eq} is the time–independent probability of finding the system in a specific state under stationary conditions. Eq. (25) indicates that the total flux to state i from all other states j equals the flux from states i to state j at stationery conditions. Under thermodynamic equilibrium, there is an even stronger constraint imposed by the Master equation. This is the principle of *microscopic reversibility*, which is called principle of *detailed balance* when applied to non–elementary (i.e. reactions that involve several steps) chemical reactions. The principle of *detailed balance* dictates that, at thermodynamic

equilibrium, for each microscopic elementary process there is a reverse process occurring with the same rate as the forward process, namely

$$k_{ji}P_j^{eq} = k_{ij}P_i^{eq}. \tag{26}$$

To find an expression for the time–independent probability, we recall that a system at thermodynamic equilibrium has Boltzmann–distributed energies and therefore

$$P_i^{eq} \sim \exp\left(-\frac{\varepsilon_i}{k_B T}\right), \tag{27}$$

where ε_i is the microscopic energy of the system at state *i*, *T* is the temperature and k_B the Boltzmann constant.

A subtlety of KMC simulations needs to be discussed at this point. What we refer to as microscopic energy (ε_i) is actually the free energy of the PES basin corresponding to KMC state *i*; after all, KMC is essentially a coarse-grained approach. Thus, ε_i contains electronic and vibrational contributions of the adsorbate species as well as electronic, translational, vibrational and rotational contributions of the species in the gas reservoir:

$$\varepsilon_i = E_i + E_{vib,i} + E_{rot,i}^{gas} + E_{transl,i}^{gas} + E_{vib,i}^{gas} + E_i^{gas}, \tag{28}$$

where E_i and $E_{vib,i}$ are the electronic and vibrational energies of the current lattice configuration or state *i*; $E_{rot,i}^{gas}$, $E_{transl,i}^{gas}$, $E_{vib,i}^{gas}$ and E_i^{gas} are the rotational, translational, vibrational and electronic energies of the gas species. With regard to the vibrational contribution, if the bottom of the potential energy well is chosen as a reference, eq. (28) will require a zero–point energy correction as well. We point out that adsorbate–adsorbate lateral interactions (attractions or repulsions between adspecies on the lattice) affect the electronic energy E_i but have negligible effect on the vibrational modes of the adsorbates.[20] We return to this point in section 3.5, where we discuss ways of incorporating adsorbate–adsorbate (or lateral) interactions in KMC models.

From eq. (26), eq. (27) and eq. (28), we can now express the *detailed balance* principle as a ratio of two Boltzmann factors that contain the microscopic energy of the system at states *i* and *j*:

$$\frac{k_{ij}}{k_{ji}} = \exp\left(-\frac{\varepsilon_j - \varepsilon_i}{k_b T}\right) = \frac{Q_j}{Q_i}\exp\left(-\frac{\Delta E_{rxn}}{k_B T}\right), \tag{29}$$

where Q_i and Q_j are the partition functions of states *i* and *j*, respectively; these partition functions contain vibrational, translational and rotational contributions of the gas species and the vibrational contributions of the adsorbates. The numerator of the Boltzmann factor in eq. (29) represents the change in the electronic energy of the system due to the transition from state *i* to state *j*, ΔE_{rxn} (i.e. the reaction energy). Based on eq. (28), the reaction energy is expressed as

$$\Delta E_{rxn} = \left(E_j + E_j^{gas}\right) - \left(E_i + E_i^{gas}\right). \tag{30}$$

3.3. KMC spatio–temporal evolution

As mentioned earlier, in a KMC simulation we do not explicitly solve the Markovian Master equation. Instead, we generate stochastic realisations (trajectories) whose statistics follow this equation and by sampling these trajectories, we obtain the observables of interest. In generating these trajectories, a KMC algorithm needs to determine two things at each step: (i) the amount of time required for the transition from the current state to the new state and (ii) the state that will be visited next. While there are a few algorithmic variants for propagating the KMC simulation, the statistics of event occurrence have to be the same and in line with the Master equation, which contains all the information for the temporal evolution of the system.

3.3.1. Advancing the time in KMC simulations

In early KMC algorithms the time was advanced in an approximate way by multiplying the total number of KMC steps by an average time increment.[94] The time advancement in modern KMC algorithms relies on a more rigorous approach, which simulates the exact statistics of the Master equation.[95] The approach considers the possible events that may be executed from state *i*, thereby

bringing the system to a new state. The total escape rate from state *i* is defined as the sum of the rate constants of all the potential events that can alter the state of the system and therefore

$$k_{i\rightarrow} = \sum_{\substack{j\in\Omega \\ j\neq i}} k_{ij} \,. \tag{31}$$

As discussed in section 3.2, during the "inactive" period of thermal vibrations in the current PES basin, there is a "loss of memory" in the system, and as a result, the transition to another state is equally probable at every moment spent in the current state. This, in turn, gives rise to exponential decay statistics.[96] Along these lines, the cumulative probability of escape from state *i* to any other state $P_{i\rightarrow}(\tau)$, i.e. the probability that the system has escaped from state *i* at some time less than τ is given by:

$$P_{i\rightarrow}(\tau) = 1 - \exp\left(-k_{i\rightarrow}\cdot\tau\right). \tag{32}$$

The corresponding probability density for the same escape will be the first derivative of $P_{i\rightarrow}(\tau)$, which gives the following exponential distribution:[97]

$$P(\tau) = \frac{dP_{i\rightarrow}(\tau)}{d\tau} = k_{i\rightarrow}\exp\left(-k_{i\rightarrow}\cdot\tau\right). \tag{33}$$

In addition, each of the microscopic processes that brings the system from state *i* to another state *j* follows an exponential distribution as well. For a time–independent rate constant the probability for the *i*⟶*j* escape is:

$$P_{ij}(\tau) = k_{ij}\exp\left(-k_{ij}\cdot\tau\right). \tag{34}$$

Samples from this distribution can easily be obtained if a uniform random number generator (URNG) is available. If $\chi \in (0,1]$ is a sample from the uniform distribution, then a random waiting time for the *i*⟶*j* transition can be computed as:[95]

$$\tau_{trans}^{ij} = -\frac{\ln(\chi)}{k_{ij}}, \tag{35}$$

3.3.2. KMC algorithms

Having discussed the temporal evolution in KMC simulation, we proceed by describing the general structure of a KMC algorithm. The three widely implemented methods in computational codes for propagating the state of on–lattice KMC are: the random selection method, the direct method and the first reaction method. The underlying concepts of these methods along with their technical details can be found in the available literature,[95,98–102] but the general form of the KMC algorithm remains the same for all cases.

In preparation of a KMC simulation, one has to specify the simulation setup and parameters. The former includes the reaction mechanism (i.e. the elementary processes that can happen on the lattice), the energetics of the system, including the interaction between the surface and adsorbates, as well as adsorbate–adsorbate interactions, and the structure of the simulated lattice. The simulation parameters are the pressure, temperature and composition of the gas phase, which is in contact with catalytic surface, as well as all parameters relevant to the energetics and the kinetics of the system, i.e. energetic interaction parameters and kinetic constants, which can be parameterised e.g. by the Arrhenius equation. In the next step, the lattice is initialised. This can be done by either specifying an initial adsorbate configuration on the lattice or by choosing to start with an empty lattice. The latter corresponds to an adsorbate–free surface, whilst the former starts the simulation with a pre–covered surface. Stationary conditions may be reached fast, if one is aware of representative adlayer configurations under the simulation conditions, thereby initialising the lattice by seeding the adsorbates in such a configuration.[103]

In the next stage, the KMC algorithm scans the lattice and detects all the elementary processes that can happen thereon. Based on the detected events, a lattice process queue is constructed and the KMC algorithm selects the next process to be executed. Once the selected process is executed, the lattice and time are updated accordingly. Thus, processes that cannot happen anymore are deleted from the lattice process queue and substituted by newly enabled processes. For instance, when CO* desorbs

from a site, a diffusion of this previously adsorbed species on the neighbouring sites is no longer possible and such elementary events have to be deleted. Yet, neighbouring adsorbate species are now able to diffuse to the free site generated by the CO* desorption. The latter processes have to be added to the process list. In the next step, the time is advanced and the termination criterion is checked. If this criterion is fulfilled, the algorithm terminates, otherwise the process to be executed next is selected and the aforementioned updates happen anew. A stopping/termination criterion can be set based on clock time, simulation time or the number of the executed KMC steps. This general algorithm is shown, as a flow chart, in Figure 11. The way one "decides" (i) which process will happen next out of all the possible processes and (ii) when this process will happen, gives rise to variations (e.g. direct method, first reaction method) of this general algorithm.

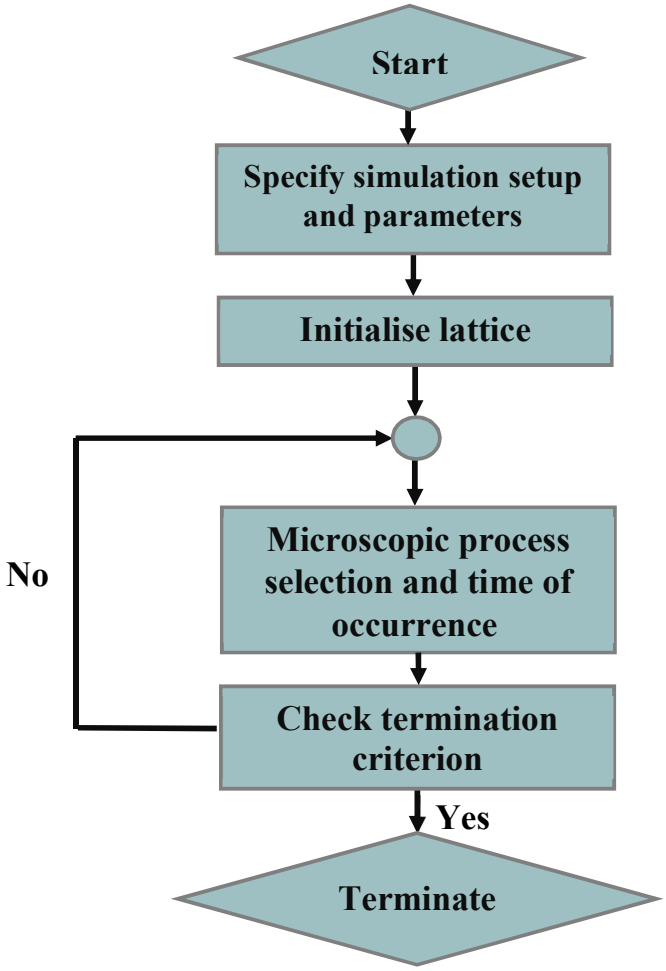

Figure 11. The general structure of a KMC algorithm presented in a flow chart.

3.4. The reaction rate constant from first principles

In line with our previous discussions, the selection of the next event and the waiting time for the occurrence thereof are determined by the KMC algorithm. Both decisions are heavily based on the computed reaction rate constants of the detected events. We will now demonstrate how the rate constant of a microscopic processes can be calculated from first principles.

The rate constant from TST is parameterised as follows:[92]

$$\mathrm{k_{TST}} = \frac{k_B T}{h} \frac{Q^{\dagger}}{Q_{\mathrm{R}}} \exp\left(-\frac{\mathrm{E}^{\dagger}}{k_B T} \right), \tag{36}$$

where $Q^{\dagger}$ and Q_{R} are the partition functions of the transition and reactant states and $\mathrm{E}^{\dagger}$ is the activation energy of an elementary event. In general, the term $\frac{Q^{\dagger}}{Q_{\mathrm{R}}} \exp\left(-\frac{\mathrm{E}^{\dagger}}{k_B T} \right)$ describes the relative probability of finding the system in the transition state over the reactant state, whereas the $k_B T/h$ term comes from the momentum of the system "moving" from the reactants towards the products region. Eq. (36) is retrieved based on the assumptions that thermal equilibrium has been reached between the initial and transition states, that the Bohr–Oppenheimer approximation holds, that quantum tunnelling is negligible and that there is no barrier recrossing.[92] The latter assumption implies that once the system has reached the transition state with a momentum toward the product region, it will necessarily react to form a product. Nonetheless, in several cases barrier "recrossings" happen frequently, thereby bringing back the system to the initial state and "cancelling" the reactive event. This effect leads to an overestimation of the rate constant by the TST, and in general $\mathrm{k_{exact}} < \mathrm{k_{TST}}$. In order to mitigate the overestimation of the rate constant, a dynamic correction coefficient can be introduced to eq. (36), which is always less than 1 such that

$$\mathrm{k_{exact}} = \kappa \frac{k_B T}{h} \frac{Q^{\dagger}}{Q_{\mathrm{R}}} \exp\left(-\frac{\mathrm{E}^{\dagger}}{k_B T} \right). \tag{37}$$

This factor κ is the so–called transmission coefficient and is calculated from MD simulations. For our calculations κ is set equal to 1 to avoid the computational cost associated with MD calculations.

Notice that both eq. (36) and (37) involve a Boltzmann factor and a pre–exponential term. The activation energy of a reactive event (entering the Boltzmann factor) is computed from DFT calculations combined with efficient methods in finding the saddle point between the reactant and product states. Such methods are the dimer method,[104] as well as the nudged elastic band (NEB) method, [105,106] the theoretical underpinnings of which can be found in ref. [107].

The pre–exponential terms in eq. (36) and eq. (37), contain partition functions which are also computed from first principles calculations. In general, Q contains all the information about the thermodynamic behaviour of a system (as it can be related to all thermodynamic potentials) and is defined as:

$$Q = \sum_{i\,states} e^{-\frac{\varepsilon_i}{k_B T}} = e^{-\frac{\varepsilon_0}{k_B T}} \left(\sum_{i\,states} e^{-\frac{\varepsilon_i - \varepsilon_0}{k_B T}} \right), \tag{38}$$

where ε_i is the energy of microstate i, the sum runs over all miscrostates, and ε_0 is the energy of the ground state. At very low temperatures one should expect $\to 1$ and at the limit of $T = 0$ K the partition function will be unity. Under these circumstances, only the ground state is populated. ε_i is the sum of the energy contributions of the different modes of molecular motion (i.e. translations, vibrations, rotations) and is

$$\varepsilon_i = \varepsilon_i^{translation} + \varepsilon_i^{rotation} + \varepsilon_i^{vibration} + \varepsilon_i^{electronic}, \tag{39}$$

By replacing eq. (39) into eq. (38), we factorise the partition function into different contributions as

$$\begin{aligned} Q = & \left(\sum_{i\ states} e^{-\frac{\varepsilon_i^{translation}}{k_B T}} \right) \left(\sum_{i\ states} e^{-\frac{\varepsilon_i^{rotation}}{k_B T}} \right) \left(\sum_{i\ states} e^{-\frac{\varepsilon_i^{vibration}}{k_B T}} \right) \left(\sum_{i\ states} e^{-\frac{\varepsilon_i^{electronic}}{k_B T}} \right) \\ & = Q^{translation} \cdot Q^{rotation} \cdot Q^{vibration} \cdot Q^{electronic} \end{aligned}, \tag{40}$$

and each of them can be examined separately.

We begin with the *electronic* excitation energies, which are typically much larger than the thermal energy, $k_B T$, and therefore $Q^{electronic} = 1$ for applications in catalysis. $Q^{electronic}$ is rarely not equal

to unity, and an exception is alkali metal atoms, where there is a degenerate ground state and $Q^{electronic} = 2$.

The *vibrational* modes are often the dominant modes of motion in surface reactions given that molecules and atoms are, at least partially, translationally and rotationally "constrained" on surfaces.[108] By assuming that a species performs harmonic vibrations, we imply that it is under the influence of a parabolic potential energy that upon substitution to the 1D Schrödinger equation gives

$$\varepsilon_i = \left(i + \frac{1}{2} \right) \hbar\omega \qquad i = 0,1,2,\ldots.., \tag{41}$$

where ω is the frequency of oscillation. By substituting eq. (41) into (38) we obtain

$$Q_m^{vibration} = e^{-\frac{\hbar\omega_m}{2k_BT}} \left(1 + e^{-\frac{\hbar\omega_m}{k_BT}} + e^{-\frac{2\hbar\omega_m}{k_BT}} + e^{-\frac{3\hbar\omega_m}{k_BT}} + \ldots \right) = \frac{e^{-\frac{\hbar\omega_m}{2k_BT}}}{1 - e^{-\frac{\hbar\omega_m}{k_BT}}}, \tag{42}$$

where $Q_m^{vibration}$ and ω_m are the partition function and the oscillation frequency of the m^{th} normal mode, respectively. The numerator of eq. (42) contains the zero–point energy factor $\frac{1}{2}\hbar\omega$. The total vibrational partition function is the product of all the partition functions that correspond to the different normal vibrational modes such that

$$Q^{vibrational} = Q_1^{vibrational} \cdot Q_2^{vibrational} \cdot \ldots \cdot Q_m^{vibrational} = \prod_{j=1}^{m} \frac{e^{-\frac{\hbar\omega_j}{2k_BT}}}{1 - e^{-\frac{\hbar\omega_j}{k_BT}}}. \tag{43}$$

For example for a CO molecule in the gas phase, there is only one mode of vibration to be included in eq. (43), the stretching of the CO bond, as this is the only mode that brings about a change to the energy of the system. Conversely, when CO is adsorbed on Ni(111) there are 6 modes of vibrations in total. The first two correspond to the stretching of the bonds between C and O, and C and Ni, respectively. The other four are frustrated rotations and translations.

Moving on to the *rotational* partition function, we find that its expression differs depending on the molecular symmetry. For rotating chemical groups around an axis, the rotation is 1D and the corresponding partition function is:[108]

$$Q^{rotation,1D} = \frac{2\pi}{h}\sqrt{2\pi\, I\, k_B\, T}\ . \tag{44}$$

On the contrary, for a rotating linear molecule (e.g. CO_2) the rotation is 2D and the corresponding partition function is:[108]

$$Q^{rotation,2D} = \frac{8\pi^2 I\, k_B\, T}{\sigma h^2}, \tag{45}$$

where σ is the symmetry number. The latter number is 2 for molecules with inversion centre such as H_2O, CO_2 and H_2. In both eq. (44) and eq. (45), I represents a moment of inertia which is

$$I = \sum_i m_i\, r_i^2\ , \tag{46}$$

where m_i is the mass of atom i and r_i is its distance from the rotating axis. For non–linear rotating molecules, after fixing the centre of mass of the molecule, we find three different moments of inertia, I_A, I_B, I_C and the partition function for rotation is

$$Q^{rotation,3D} = \frac{\sqrt{\pi}}{\sigma}\left(\frac{8\pi^2 I_A\, k_B\, T}{h^2}\right)\left(\frac{8\pi^2 I_B\, k_B\, T}{h^2}\right)\left(\frac{8\pi^2 I_C\, k_B\, T}{h^2}\right). \tag{47}$$

Finally, species attached to solid surfaces perform free *translations* only to a limited extent. The free translation area can be approximated by the size of the active site, which can in turn be approximated by the van der Waals radius of the metal atom. In contrast, for molecules in the gas phase, the free translation length is the volume of the container where the translation happens. The partition function $Q^{translation}$ is found following a similar procedure as for $Q^{vibration}$,[78] and

$$Q^{translation,3D} = \frac{V\sqrt{2m\pi k_B T}}{h}, \tag{48}$$

where m is the mass of the adsorbate and V is the volume of the container, wherein a molecule performs the translations. We note that, if the partition function for translation is to be calculated for a transition state, a 2D gas state has to be considered and

$$Q^{translation,2D} = A_{st} \cdot \frac{2 \cdot \pi \cdot m \cdot k_B \cdot T}{h^2}. \quad (49)$$

Using the equations presented in this section, in conjunction with the transition state theory expressions (36) or (37), one can find the rate constant of a microscopic process solely based on first principles calculations. The presence of spectator species in the vicinity of a reactive pattern (i.e. the presence of an adsorbed CO species next to a CO–O surface pattern, which can give CO_2) has negligible effect in the ratio of partition functions of eq. (37).[20] In other words, Q is presumed as a coverage–independent quantity and can be computed, independently of the local coverage of the configuration whereon a reactive event takes place, using the equations we have presented so far. This is not true, however, for the activation energies of elementary events, which may be substantially affected by coverage effects.[28,109,110]

3.5. Modelling adsorbate–adsorbate interactions in KMC simulations

3.5.1. The effect of adsorbate–adsorbate interactions on the adsorption energy

Lateral interactions have an important effect on the structure of the adsorbate layer, but also on the stability of the initial, final and transition states of reactions; therefore, they can markedly affect the rate of catalytic reactions. For instance, a directly observable effect of repulsive and/or attractive interactions between adsorbates is the formation of ordered patterns on catalytic surfaces.[22,111] There are several factors that give rise to these adsorbate–adsorbate interactions, including electrostatic interactions, indirect interactions through the surface material and overlap between the wave functions of two or more adsorbates that reside on neighbouring sites.[3] The latter effect is important when two adsorbed species are at small distances between each other (e.g. less than 2.5 Å).[112,113]

Owing to adsorbate–adsorbate interactions, the binding strength of an adsorbate on a surface decreases at increasing surface coverage, thereby occasionally preventing the reach of full monolayer

(ML) coverage.[16] To illustrate this effect, we define the surface coverage with respect to a specific adsorbate as

$$\Theta = \frac{N_{ads}}{N_{surf-atoms}}, \tag{50}$$

where $N_{surf\text{-}atoms}$ is the number of metal atoms on the surface layer of the catalyst, and N_{ads} the number of chemisorbed species thereon. The average adsorption energy of a species at different coverages can be computed from DFT, using the following expression:

$$E_{ads}^{average} = \frac{E^{N_{ads}+slab} - E^{slab} - N_{ads} \cdot E^{ads(g)}}{N_{ads}}, \tag{51}$$

where $E^{N_{ads}+slab}$ is the total DFT energy of the DFT slab with N_{ads} adsorbates on the surface, E^{slab} is the total DFT energy of the clean slab and $E^{ads(g)}$ is the DFT energy of the corresponding gas–phase species.

The effect of increasing coverage on $E_{ads}^{average}$ is shown in Figure 12, where less negative values of $E_{ads}^{average}$ are computed at increasing CO* coverage of a Ni trimer on a Ni/Cu(111) surface. In general, more negative values of $E_{ads}^{average}$ correspond to stronger CO* binding, and we indeed observe a weaker CO* binding at higher coverages (Figure 12). In particular, at 1/3 ML coverage we compute an average adsorption energy, which is less negative by ~0.13 eV as compared to the corresponding value computed at 1/9 ML coverage. This difference can be significant; in the presence of more than one type of surface species on the catalyst surface, binding energy differences on the order of 0.10 eV can lead to a surface almost fully covered by the species that binds stronger thereon (we assume an equimolar gas–phase composition).[114]

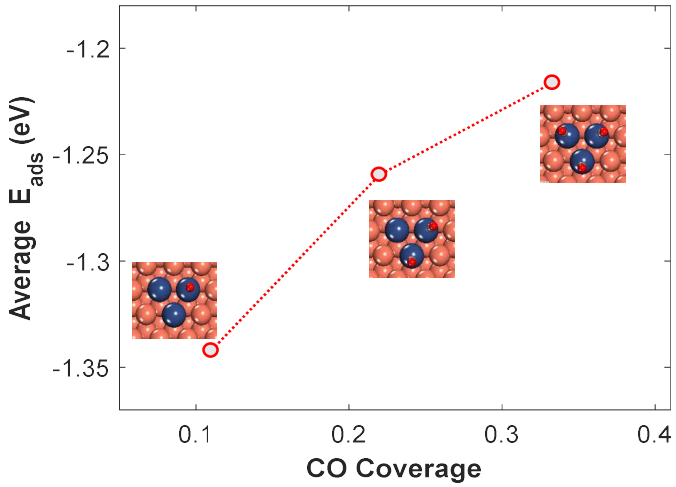

Figure 12. Effect of increasing CO* coverage to the average adsorption energy of CO* on the top site of a Ni trimer on a Ni/Cu(111) surface. The insets next to the points show the top view of the DFT slab used for the calculations, in the relaxed state. Ni atoms are shown in blue, Cu atoms are shown in orange, C atoms are shown in gray and O atoms are shown in red. For these calculations, a four–layer (3 × 3) slab with 9 atoms in the surface layer was used.

3.5.2. Effects of adsorbate–adsorbate interactions on the activation energy of elementary processes

Coverage effects are not only important to the adsorption energy of species on solid surfaces. Similarly, these effects impact upon the activation barrier of KMC events and therefore upon the computed rate constant. Note that an activation barrier for a surface process represents the energy difference between two adsorbed states, both of which are governed by the same physics and are affected by adsorbate–adsorbate interactions. Using eq. (37) we express the ratio of the forward and reverse rate constants of a reversible process as

$$\frac{\mathrm{k}_{\mathrm{TST}}^{fwd}}{\mathrm{k}_{\mathrm{TST}}^{rev}}=\frac{Q_{\mathrm{P}}}{Q_{\mathrm{R}}}\exp\left(-\frac{\Delta \mathrm{E}_{rxn}}{k_b T}\right)=\frac{Q_P}{Q_{\mathrm{R}}}\exp\left(-\frac{\mathrm{E}_{fwd}^{\dagger}-\mathrm{E}_{rev}^{\dagger}}{k_b T}\right), \tag{52}$$

where Q_{P} and Q_{R} are the partition functions of the product and the reactant states, respectively, $\mathrm{E}_{fwd}^{\dagger}$ and $\mathrm{E}_{rev}^{\dagger}$ are the activation energies of the forward and reverse reactions, respectively, and $\Delta \mathrm{E}_{rxn}$ is the reaction energy. The latter represents the energy difference between the initial and final states (Figure 13) and from eq. (52)

$$\Delta E_{rxn} = E^{\dagger}_{fwd} - E^{\dagger}_{rev}, \tag{53}$$

which is also dictated by the principle of microscopic reversibility (see section 3.2).

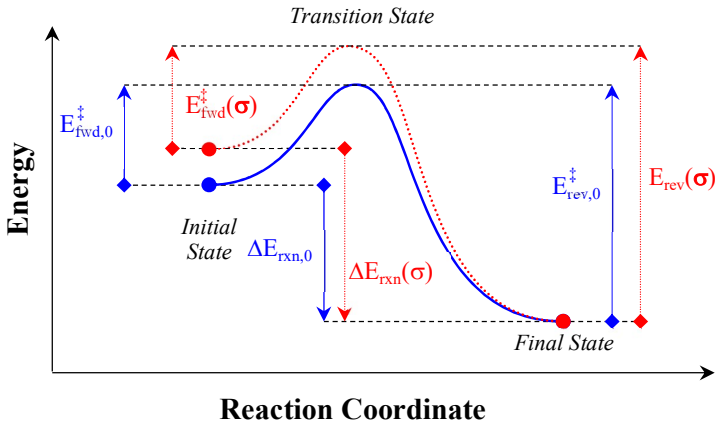

Figure 13. Energy profile of a reversible elementary KMC step (blue line), and energy profile of the same step with destabilized initial state (red line).

Lateral interactions between spectator and reacting species give rise to a change to the electronic energy of the initial and/or the final state, thereby altering the reaction energy (see eq. (30)). This is illustrated in Figure 13, where the red dotted line represents a destabilised initial state that changes the activation energy of the reverse reaction ($E^{\dagger}_{rev}$). Coverage–dependent activation energies can be modelled by the BEP relationship, which was briefly mentioned in section 1.2.[14] According to the BEP relation, the activation energy of an elementary process scales linearly with the reaction energy such that

$$E^{\dagger}_{fwd} = \alpha \Delta E_{rxn} + \beta, \tag{54}$$

$$E^{\dagger}_{rev} = (\alpha - 1) \Delta E_{rxn} + \beta, \tag{55}$$

where α and β are fitting parameters which can be obtained from first principles calculations.

The significance of the BEP relation is far–reaching in KMC,[115] eliminating the need of performing a large number of DFT calculations for the transition state energies in all the possible configurations of spectator species within the neighbourhood of the reaction. Instead, the effect of

lateral interactions between the reacting species and such spectators is quantified by this linear relation after fitting α and β from first–principles. This dependence of activation energy on the local coverage of spectators, eventually shapes the macroscopic performance of the catalyst in terms of the observed kinetics.

In the BEP representation, the only information required in order to compute the activation energy, consists of the energies of the final and initial states and the activation barrier at the zero–coverage limit. For the implementation of the BEP relation in KMC, the fitting parameters, α and β, are parameterised with respect to the forward and reverse activation energies, the reaction energy in the zero–coverage limit and the proximity factor ω.[116] The latter parameter defines how reactant– or product–like the transition state is with respect to the reaction coordinate and $0 \geq \omega \geq 1$.[117] The activation energy of an $i \rightarrow j$ reaction is

$$\mathrm{E}^{\dagger}_{fwd}\left(i \rightarrow j\right) = \max\left\{0,\ \Delta\mathrm{E}_{rxn}\left(i \rightarrow j\right),\ \mathrm{E}^{\dagger}_{fwd,0} + \omega \times \left(\Delta\mathrm{E}_{rxn}\left(i \rightarrow j\right) - \Delta\mathrm{E}_{rxn,0}\right)\right\}, \tag{56}$$

where $\mathrm{E}^{\dagger}_{fwd,0}$ and $\Delta\mathrm{E}_{rxn,0}$ are the forward activation barrier and the reaction energy at the zero–coverage limit, respectively. The max operator ensures a non–negative activation energy. In line with eq. (56) and eq. (53), the reverse activation energy will be given as

$$\mathrm{E}^{\dagger}_{rev}\left(i \rightarrow j\right) = \max\left\{-\Delta\mathrm{E}_{rxn}\left(i \rightarrow j\right),\ 0,\ \mathrm{E}^{\dagger}_{rev,0} - \left(1 - \omega\right) \times \left(\Delta\mathrm{E}_{rxn}\left(i \rightarrow j\right) - \Delta\mathrm{E}_{rxn,0}\right)\right\}, \tag{57}$$

where $\mathrm{E}^{\dagger}_{rev}$ is the reverse activation barrier at the zero coverage limit.

3.5.3. Modelling the lattice energetics: the cluster expansion Hamiltonian approach

According to our discussion in the previous section, coverage–dependent activation energies are calculated using the BEP relation, which is parameterised based on the energy of the final and initial states of the system. In turn, the latter energies can be computed by adopting a cluster expansion (CE) Hamiltonian approach, which enables the accurate modelling of lateral interactions on solid surfaces.

Early first principles–based KMC works employed only first nearest neighbour (1NN) pairwise interactions in the energetics model, whilst long–range and/or many–body interactions were neglected owing to the large computational cost incurred upon their incorporation in the reaction model. Nevertheless, inclusion of long–range and many–body interactions is often necessary in order to reproduce experimentally observed adlayer structures, surface coverages, catalytic rates and activation energies.[16,20] A versatile way to treat lateral interactions of any range and complexity is the aforementioned CE method.[118] This method has been extensively used to study the thermodynamics of adsorbate layers,[20,119,120] and the diffusion of atomic species on transition metals.[121] Importantly, Schneider and co–workers have recently applied the CE method for the prediction of catalytic rates.[16] Within the CE framework, the energy of a specific adsorbate (or lattice) configuration is represented by a sum of energy contributions of "clusters" or "figures", typical examples of which are seen in Figure 14 (a). Each cluster's contribution to the total energy can be calculated from first principles and is known as the effective cluster interaction (ECI) of that cluster. Based on the ECI parameters, of the different patterns defined in the energetics model, one can calculate the total energy of a lattice configuration as

$$H(\sigma) = \sum_{k=1}^{N_c} \frac{\mathrm{ECI_k}}{\mathrm{GM_k}} \mathrm{NOC_k}\,, \tag{58}$$

where N_c is the number of clusters incorporated in the energetics model; $\mathrm{ECI_k}$ is the effective cluster interaction of the cluster k; $\mathrm{NOC_k}$ is the number of times cluster k was detected on the lattice state σ and $\mathrm{GM_k}$ is a correction factor against cluster double–counting, known as graph-multiplicity factor. For instance, the 1NN cluster in Figure 14 (a) can be detected twice by the KMC algorithm because of symmetry: either as 6-12 or as 12-6. Therefore, we set a $\mathrm{GM_{1NN}}$ equal to 2. If the ECIs of the incorporated patterns in the energetics model are known, one can find the energy of any lattice configuration by applying eq. (58). For example, by assuming that the ECIs of the 1NN, 2NN and

single–body clusters in Figure 14 (a) are 2.0 eV, 1.5 eV and -2.0 eV, respectively, we calculate the energy of the adsorbate configuration shown in Figure 14 (b) as follows:

$$H(\sigma)=\left(\frac{-2.0eV}{1}\right)\times 5+\left(\frac{2.0eV}{2}\right)\times 2+\left(\frac{1.5eV}{2}\right)\times 4=-5.0\ eV\,.$$

The forward and reverse activation energies of a microscopic process depend on the local environment, wherein this elementary process takes place. This is because of the lateral interactions between the species that participate in the reaction and spectator species. In a BEP relation, the aforementioned energies are parameterised with respect to the reaction energy (see eq. (56) and eq. (57)), which is found by adopting the CE Hamiltonian approach as follows

$$\Delta E_{rxn}(\sigma\rightarrow\sigma') = H(\sigma') - H(\sigma) + \Delta E_{gas}\,, \tag{59}$$

where σ (initial) and σ' (final) are two consecutive lattice states visited by the system and ΔE_{gas} is the difference in the gas phase energy between the final and initial states. The reaction energy computed from eq. (59) is used in eq. (56) and eq. (57), thereby providing coverage–dependent activation energies.

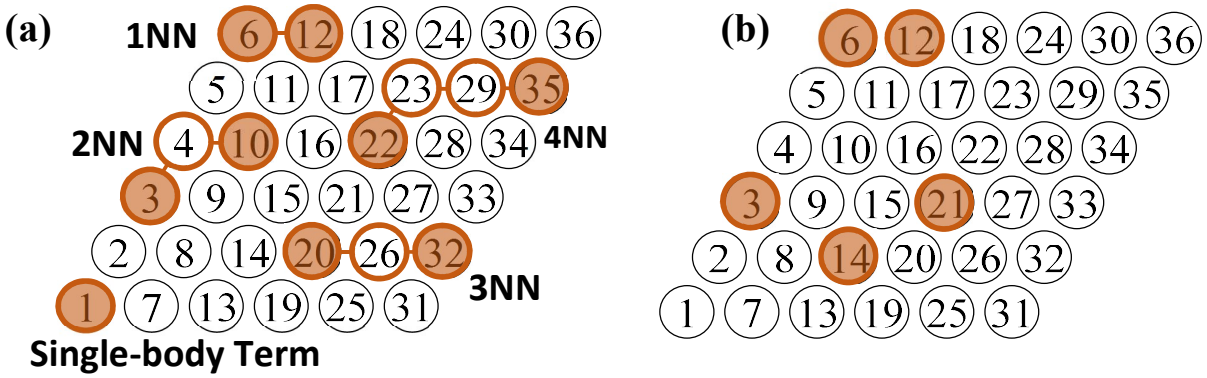

Figure 14. (a) Examples of graph patterns (or clusters) that may be taken into account in a Hamiltonian model; (b) an example of snapshot of the lattice during a KMC simulation. The orange circles indicate sites occupied by an adsorbate. The white circles with black edges are vacant sites and white circles with orange edges indicate sites that may or may not be vacant. Site numbers are shown in the centre of the circles in both (a) and (b).

The calculation of the Hamiltonian of a specific lattice state (eq. (58)) requires knowledge of the ECI parameters of the considered patterns in the CE. To find these parameters, one has to fit eq.

(58) to a DFT dataset, which includes a large number of adsorbate configurations (N_{conf}) and a least–squares approach is then adopted to minimise

$$\chi^2 = \frac{1}{N_{conf}} \sum_{i=1}^{N_{conf}} \left[H(\sigma_i) - E_{DFT}(\sigma_i) \right]^2 , \quad (60)$$

where σ_i is the lattice state of configuration i, $H(\sigma_i)$ is calculated from eq. (58) and $E_{DFT}(\sigma_i)$ is the formation energy of the i configuration calculated from DFT.

We note that any desired number of clusters can be added to the CE, but this could potentially require a large number of DFT calculations to fit the ECIs, which would be costly. Considering a large number of clusters in the CE may also result to overfitting issue,[108] since, besides the adsorbate–adsorbate interactions, the CE will also capture the DFT error. A remedy to overfitting is to truncate the CE to the "right" level, which can be determined based on statistical techniques, such as the leave–one–out cross–validation (LOOCV) method,[60,122] and Bayesian statistics.[123,124] In the former method, a configuration is left out from the DFT dataset and linear regression is performed to find the ECIs. Then based on the calculated ECIs, we compute the formation energy of the omitted configuration and compare it to the DFT–computed formation energy. This is done not only for one configuration, but for each configuration in the DFT data set, thereby calculating a cross–validation score (CV) by using eq. (61).

$$CV^2 = \frac{1}{N_{conf}} \sum_{i=1}^{N_{conf}} \left[E_{CE}(\sigma_i) - E_{DFT}(\sigma_i) \right]^2 , \quad (61)$$

where $E_{CE}(\sigma_i)$ is the CE–predicted formation energy for the configuration i. The CV score describes the predictive capability of the CE: the lower the CV value, the more probable is that the energy of an adsorbate configuration that may appear during the KMC simulation, but is not included in the DFT dataset, will be predicted correctly. On the other hand, in Bayesian model selection, one compares different interaction models, and each of them is assigned with a probability based on Bayes's theorem. The model with the highest probability is the one that is expected to be the most robust. An interesting discussion on the application of this method is provided by Jansen and Popa in ref. [124].

3.6. Handling more complex lattices and reactions

In section 3.2, we highlighted that the catalytic surface can be represented by a simple matrix–grid, which is a network of sites connected to each other. As discussed, the direct mapping of a simple matrix–grid lattice into an occupation matrix is a rather intuitive and simple. However, several complications arise when modelling surfaces with more complex geometry, than those seen in Figure 9 (a) and (b). A typical example is a (211) stepped surface, where the atoms on the edge are connected with 2 atoms on the (111) facet and 1 atom on the (100) facet.[125] A more rigorous and generic approach for the representation of the simulation lattice (including the connectivity of sites) and of the elementary events of realistic chemistries, is provided by the graph–theoretical KMC (GT–KMC) framework of Stamatakis and Vlachos.[126]

Early KMC works were based on the assumption that an adsorbate can occupy only one site and that a maximum two sites are involved in an elementary reaction.[127–129] In realistic chemistries, however, the existence of multi–dentate species that occupy more than one site (e.g. bidentate when occupying two sites) and the occurrence of elementary processes that involve more than two sites are common.[130–132] Then, the approach just noted (assuming "one adsorbate per site") cannot capture the complexity of the surface reaction. This can be achieved only by adopting a multisite approach.

Such an approach was first established by Hansen and Neurock in order to study the kinetics of ethylene hydrogenation on Pd.[133] Using a multisite KMC algorithm the authors could account for events that involve three sites and also capture bidentate species. This approach was later generalised by Stamatakis and Vlachos to arbitrarily complex chemistries, i.e. chemistries that include species with dentate number even larger than 2 and an arbitrary number of sites involved in elementary events, in the context of the GT–KMC framework.[126] Within this formalism one can deal with the high complexity of surface reactions, whilst keeping the computational expense comparable to the "one adsorbate per site" approach thanks to the use of efficient data structures.[126]

In the GT–KMC framework, the catalytic surface is represented as a two–dimensional lattice graph where vertices denote surface sites, and edges define the connectivity (neighbouring relations) between those sites (Figure 15 (a) and (b)). Similarly, to the rectangular lattices in Figure 9 (a) and (b), every lattice site has an identity label, which is known as the site index. The connectivity between the sites is shown in a table, where each row is dedicated to a specific site and includes all of its neighbouring sites.[126] The lattice may be periodic or non–periodic depending on the application. The former lattice type is used to describe sites that belong to an extended surface, precluding edge sites,[108] while non–periodic lattice may be used to model a reaction on an entire NP facet.[103] In GT–KMC each lattice site is represented by a three–element vector,

$$s_i \in \{1, 2, \ldots, \mathrm{S_T}\} \times \{x_1, x_2, \ldots, x_{S_L}\} \times \{y_1, y_2, \ldots, y_{S_L}\} \qquad \forall\, i \in \{1, 2, \ldots, \mathrm{S_L}\}\,, \tag{62}$$

where S_L is the number of sites and S_T is the number of site types. The first element of the vector denotes the site type, whilst the second and third elements give the x–coordinate and y–coordinate of the site. For instance, the representation of site 6 in Figure 15 (a) will be s_6 = (1; 7 Å; 2.2 Å), and an entire simulation lattice is given by a $3 \times S_L$ array

$$s \in \left\{\left(s_{i,j}\right)_{j=1}^{3}\right\}_{i=1}^{S_L}. \tag{63}$$

The state of each site is defined in a similar manner. Namely, it is given by a three–element vector such that

$$\sigma_i \in \{1,2,\ldots,\mathrm{S_L}\} \times \{0,1,\ldots,\mathrm{N_S}\} \times \{1,2,\ldots\mathrm{maxdent}\} \;\Rightarrow\; \sigma \in \left\{\left(\sigma_{i,j}\right)_{j=1}^{3}\right\}_{i=1}^{3}\,, \tag{64}$$

where N_S is the number of species bound to the surface. The first element provides the entity label, which is a unique integer that identifies an adsorbate (or an "empty–site" pseudo–adsorbate) on the lattice. The second element denotes the species that occupies site *i* (e.g. 0 for empty site, 1 for CO*, 2 for O* adatom etc.), and the third element is the dentate number of that adsorbate on site *i*. The latter is useful when multi–dentate species participate in the reaction, in which case one needs to specify the

orientation of the adspecies. Under these circumstances, N_S will be always less than S_L, while in the presence of mono–dentate species only and for a fully covered surface $N_S = S_L$.

Using a toy example, we present how the state of the system is specified within the GT–KMC formalism. In this toy model there are two mono–dentate adsorbates (reactants), A* and B*, that can react to give a bidentate product, AB**. The orientation of the latter species should be known (Figure 15 (a) and (b)). Figure 15 (a) shows the graph of a small periodic lattice, whereon all the aforementioned species exist. The state of the lattice (array σ in line with eq. (64)) is shown in Figure 15 (c). As noted, each AB** species occupies two sites; the site pairs occupied by AB** species are {2, 9} and {4, 11} in Figure 15 (a). Since sites 2 and 9 are occupied by the same species, they will have the same entity number (Figure 15 (c)) and the same species number. This is also the case for sites 4 and 11 (Figure 15 (b)).

Such a description not only provides information about the occupation of sites, but also clarifies the orientation of the multi–dentate species, thereby specifying unambiguously the state of the system. A change to the orientation of the two AB** adsorbates, as the one seen in Figure 15 (b), is effectively described by a difference in the states of the corresponding sites (Figure 15 (d)). In this case, sites 4 and 2 have the same entity number, as is true for sites 9 and 11.

Similarly, within the GT–KMC framework, the elementary events are represented as connected graphs with specified initial and final configurations.[126] It follows that the GT–KMC approach is heavily based on the detection of surface patterns. The latter are detected by solving a sub–isomorphism problem,[134] whose solution indicates whether an existing pattern in a graph is part of another graph as well. Accordingly, complex multisite reactions and intricate energetic patterns can be detected. We note that GT–KMC combined with the CE expansion method provide the framework toward the accurate modelling of highly complex surface reactions. The aforementioned combination is indeed powerful and has been applied to both dynamic (see chapter 4)[135,136] and equilibrium problems (see chapter 8).[63]

(a)

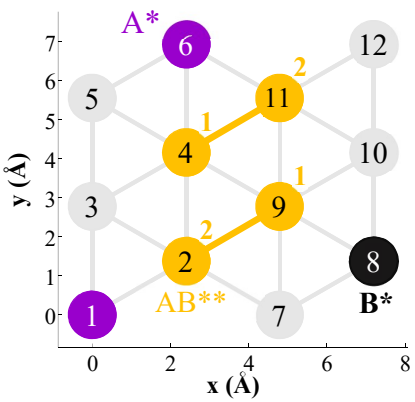

(b)

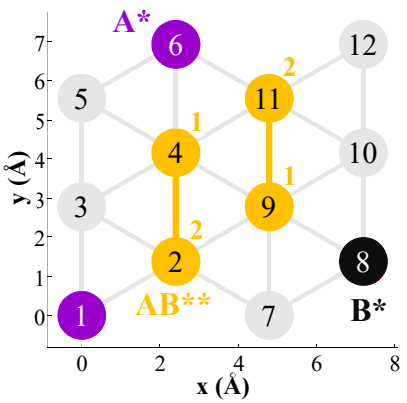

(c)

Site Number	Entity Number	Species	Dentate
1	1	1	1
2	***2***	3	1
3	3	0	1
4	***4***	3	2
5	5	0	1
6	6	1	1
7	7	0	1
8	8	2	1
9	***2***	3	2
10	9	0	1
11	***4***	3	1
12	10	0	1

(d)

Site Number	Entity Number	Species	Dentate
1	1	1	1
2	***2***	3	1
3	3	0	1
4	***2***	3	2
5	5	0	1
6	6	1	1
7	7	0	1
8	8	2	1
9	***4***	3	2
10	9	0	1
11	***4***	3	1
12	10	0	1

Figure 15. (a) and (b) show two small periodic lattices, whereon A*, B* and AB** species are adsorbed on lattice sites. A*, B* and AB** are shown in purple, black and yellow, respectively. Vacant sites are represented by grey circles and sites numbers are shown in the centre of the circles in both (a) and (b). (c) and (d) show the state (σ) arrays of the configurations shown in (a) and (b), respectively. The state of each lattice site is represented by a three–element vector as described in the main text. *Figure adapted from ref.* 126.

3.7. Concluding remarks

Having reviewed the underpinnings of DFT and KMC methods, we now proceed by presenting their applications in heterogeneous catalysis. As highlighted in this chapter, the strength of the KMC method is its ability to treat adsorbate–adsorbate in a systematic and detailed manner. The following chapter is dedicated to the effect of such interactions on the predicted rate of catalytic reactions in KMC.

Chapter 4

4. Studying the effect of adsorbate–adsorbate interactions on the structure of the adlayer and on KMC–predicted catalytic rates

This chapter demonstrates the effect of adsorbate–adsorbate interactions the catalytic rates predicted by KMC simulation to model. To this end, we model the catalytic NO oxidation on Pt(111). The interaction between the adspecies are treated by adopting a CE Hamiltonian approach, thanks to which we are allowed to incorporate interaction of increasing complexity to our model. The obtained data underline that CE models that include interactions of different range may yield disparate adsorbate layer structures, thereby resulting in disparate predicted catalytic rates as well. Additionally, it is found that energetics models that include long–range and three–body terms are more accurate in predicting the structure of the adsorbate layer than models that take into account only short–range interactions. On this basis, the results of this chapter highlight the key role of adsorbate–adsorbate interactions toward the accurate modelling of surface reactions. *The contents of this chapter have been published in J. Chem. Phys. 149, 184701 (2018).*

4.1. Computational details

Kinetic Monte Carlo. KMC simulations of NO oxidation on Pt(111) were performed within the GT–KMC framework,[126] as implemented in *Zacros* (version 2.0).[137] Adsorbate–adsorbate interactions were of high importance to our work and were accurately captured by a general CE approach incorporated in this framework. The simulation input was composed of the reaction conditions (temperature, pressure, gas phase composition etc.), the lattice structure that represents the catalytic surface, an energetics model where we specify the CE capturing the lateral interactions, and the reaction mechanism which defines all possible elementary events that can happen on the lattice. Optionally, one may also provide an initial adsorbate configuration on the lattice, otherwise the simulation is by default initialised with an empty lattice.

The frequency by which a particular event is executed during the simulation is proportional to its rate constant. The forward and reverse rate constants of each elementary event can be computed from eq. (36), but the activation energy in the Boltzmann factor is affected by lateral interactions (i.e. σ and σ). To account for the effect of lateral interactions on the reaction kinetics, the forward and reverse activation energies of each elementary reaction step were parameterised with respect to the reaction energy (ΔE_{rxn}) using a BEP relation (see paragraph 3.5.2).[14,16] The latter quantity was estimated for each lattice state, σ, detected during the simulation and required the calculation of the energy of configuration σ and of the succeeding state σ'. These configuration energies were in turn calculated using the CE Hamiltonian approach.[118] To determine the total energy, the lattice was scanned by *Zacros* and clusters defined in the energetics model were detected and enumerated (see paragraph 3.5.3).[116]

Finally, the catalytic rate is given by the turnover frequency (TOF) which is defined as the number of molecules of gas A produced per active site, per unit time. "A" is a representative gas species, which will be NO_2 in our case (see next section). To determine the TOF, we plot the number of molecules of gas A produced during the simulation versus time and filter out any initial transients

(whilst the system reaches steady state) before fitting using linear regression. Subsequently, we divide the slope by the total number of lattice sites as shown in eq. (65).

$$\mathrm{TOF} = \frac{n_A}{\sum \tau \times N_{sites}}, \tag{65}$$

where n_A is the number of A molecules produced, $\sum \tau$ is the simulation time and N_{sites} is the number of lattice sites.

Reaction mechanism and simulation details. This work is based on an original reaction model developed by Wu et al.[16] and adapted for KMC by Nielsen et al.[116] Three reversible elementary events (see eq. (66), eq. (67) and eq. (68)), from which the O_2 dissociation on Pt(111), eq. (67), is the RDS. Furthermore, it is assumed that the catalytic oxidation of NO proceeds via an Eley–Rideal mechanism, and that O* dominate the catalytic surface, in accord with the high efficiency of NO_2 in supplying the catalyst surface with O* atoms.[26,138] Moreover, the analysis is restricted to surface coverage below 1/2 ML, where the Pt surface is not reconstructed,[111] and O* populate three–fold fcc hollow sites only.[16,20,139]

$$\mathrm{NO} + \mathrm{O}* \underset{k_{rev}}{\overset{k_{fwd}}{\rightleftharpoons}} \mathrm{NO_2} + *, \tag{66}$$

$$\mathrm{O_2} + 2* \underset{k_{rev}}{\overset{k_{fwd}}{\rightleftharpoons}} \mathrm{O}* + \mathrm{O}*, \tag{67}$$

$$\mathrm{O}* + * \underset{k_{rev}}{\overset{k_{fwd}}{\rightleftharpoons}} \mathrm{O}* + *, \tag{68}$$

where * depicts a vacant fcc site. Eq. (66) represents the reversible Eley–Rideal NO oxidation, eq. (67) is the O_2 dissociation and eq. (68) is the surface diffusion of O* between neighbouring fcc lattice sites.

As noted earlier, the forward and reversible rate constants of each elementary events were computed based on eq. (36), while the corresponding activation energies were found using a BEP relation (see paragraph 3.5.2). The proximity factor (ω, defining the relative position of the transition state along the reaction coordinate) was set to unity for the dissociation of O_2 as the transition state is

molecular O_2 with an elongated O─O bond,[16] zero for the NO oxidation/reduction and 0.5 for O* diffusion.

In relation to the rate constants, there is a quasi–equilibrium where the dynamics of NO oxidation/reduction and O* diffusion are fast compared to O_2 dissociation, such that the latter is the RDS (based on the previous work by Schneider and co–workers).[16] Therefore the values of the pre–exponential terms for the NO oxidation/reduction and O* diffusion are set such that the rates of these elementary events are at least 50 times larger than the rate of the RDS, assuring the fast equilibration of the adlayer.[116,140] This method has been implemented in our previous work and for further details on the derivation and calculation of the rate constants the reader may consult ref. [116].

The simulations were performed using two types of lattices, with and without periodic boundary conditions. The shapes of the periodic lattices are equilateral parallelograms of dimensions m × m (containing a total of m^2 sites) and for the non–periodic ones we use equilateral parallelograms in addition to equilateral triangles of side length n (containing a total of $\sum_{i=1}^{N} i$ sites).

The reaction is modelled at a total pressure of 1 bar, and fixed partial pressures of NO, O_2 and NO_2. The NO_2 to NO pressure ratio is set to 0.37 in all simulations, thereby fixing the chemical potential of surface oxygen μ_{O*} (since reaction (66) is fast), and the partial pressure of O_2 is set to 0.1 bar. The reaction is carried out either at 480 K or 680 K temperatures and the lattice is always initialised with an O* adsorbate overlayer with the ° structure, which is a stable adlayer configuration when using short–range, 1NN lateral energetics at 1/3 ML coverage. Thus, the system is initially in a low energy state, though is allowed to reach stationary conditions before analysing the kinetics.

Lateral interaction models. We studied different CE models of varying complexity. In particular, we examined cases where the CE Hamiltonian contains 3, 5 and 8 figures (clusters) and the corresponding graph patterns are presented in Figure 16. Each Hamiltonian contains a constant term (which does not affect any of the results but included for compatibility with other Hamiltonian descriptions), and a

single–body term that models the adsorption energy of one O* adsorbate. In the 3–Fig. CE model, two–body interactions with adsorbate separation of up to 1NN are considered; these short-range interactions are often referred as hard interactions herein, as the lead to highly ordered adlayer structures (see next section). In addition to 1NN interactions, 2NN and 3NN two–body interactions are included in the 5–Fig. CE model (see Figure 16). Finally, the 8–Fig. CE model incorporates the clusters found in the 3–Fig. and 5–Fig. cluster expansions, as well as two–body terms at 4NN and 5NN separation in addition to a 3–body NN cluster (1–1–3 cluster). The terms included in each CE model along with their ECIs can be found in Appendix I.

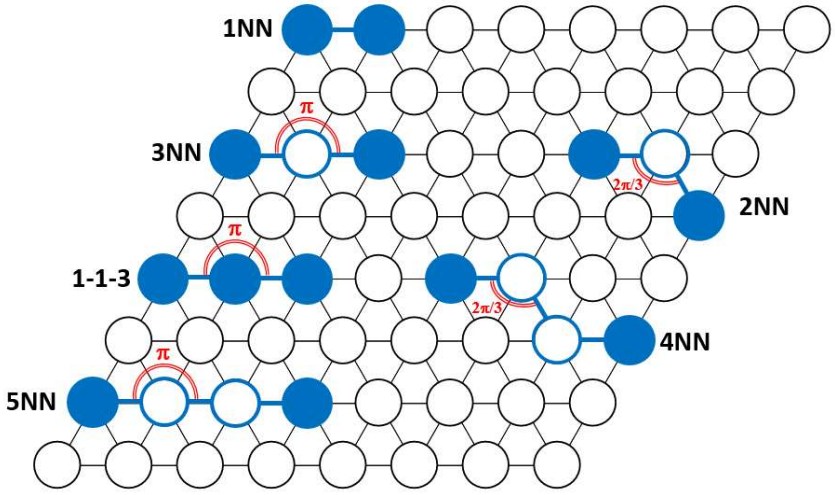

Figure 16. Graph patterns (or clusters) that are taken into account in 3–Fig., 5–Fig. and 8–Fig. CE Hamiltonian models. The blue circles indicate sites occupied by oxygen atoms. The white circles with black edges are vacant sites and white circles with blue edges indicate sites that may or may not be vacant.

4.2. Results and discussion

4.2.1. 3–Figure CE energetics

We first examine a 3–Fig. CE model where only 1NN interactions contribute to the energetics. To exclude lattice–boundary effects on the predicted catalytic rate, we run simulations on periodic equilateral lattices of various sizes at the two aforementioned temperatures (480 K and 680 K). The calculated TOFs on parallelogram lattices with number of sites ranging between 36 and 2500 (6 × 6 to 50 × 50) are plotted in Figure 17. For both temperatures, there is an oscillatory behaviour in the catalytic rate as the lattice size is increased. A regular pattern is observed by which certain lattice sizes

exhibit much higher activities than others; a difference which does not diminish even for relatively large lattices of more than 2000 sites. Upon further inspection, we note that lattices with a number of sites per side that is divisible by 3, exhibit a significantly lower TOF (ca. one order of magnitude lower) than those with sites non–divisible by this number.

According to our earlier discussion on the BEP relationship, the activation energy for a surface reaction is dependent on the configuration of neighbouring spectators in the adsorbate overlayer. It follows that this dependence is carried into the corresponding kinetic constant and indeed the catalytic rate. Thus, the variability in the values of TOF can be elucidated by studying the adlayer structures of different lattices giving high and low TOF. To this end, we use two representative lattice sizes, a 42 × 42 lattice (1,764 sites), whose number of sites per side is divisible by 3, and a 44 × 44 lattice (1,936 sites), for which this is not true. Snapshots of these lattices for simulations at 480 K are shown in Figure 18 (a) and (b), respectively.

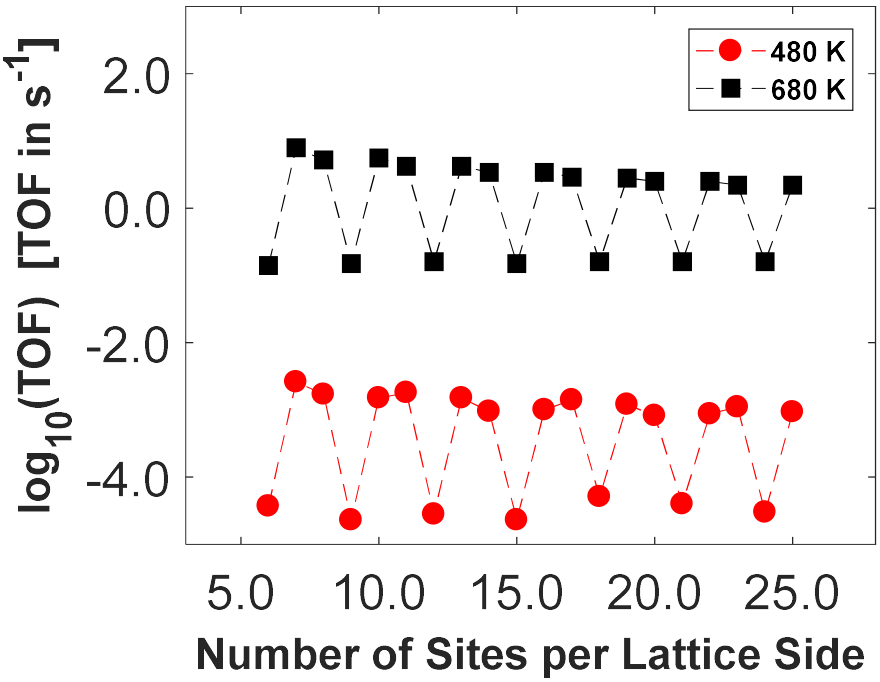

Figure 17. Computed TOFs of the 3–Fig. CE model for a range of lattice sizes at 480 K (red) and 680 K (black). P_{tot} = 1 bar, P_{NO_2}/P_{NO}=0.37 and y_{O_2} = 0.1 for all simulations.

In a representative configuration at stationary conditions on the 42 × 42 lattice, the O* adspecies are perfectly ordered in the ° structure, which minimises the 1NN repulsions exerted upon them (Figure 18 (a)). The ordered structure is, however, disrupted on the 44 × 44 lattice by the formation of anti–phase boundaries that appear to divide the adlayer into a number of perfect ° domains (Figure 18 (a)). As the 44 × 44 lattice has a number of sites per side that is not divisible by 3, it is impossible for the adlayer to organise into a perfect ° structure and instead forms line–defects: the observed anti–phase boundaries. That is to say that the size of the lattice is not commensurate to the stable ° adlayer structure. Closer examination of these defects reveals lower local coverage in the anti–phase boundary (Figure 18 (b), inset left) compared to the ordered ° domain (Figure 18 (a), inset). Even lower local O* coverages are detected on point–defect regions that are adjacent to anti–phase boundaries (Figure 18 (b), inset right), where remarkably, the pair of fcc sites covered by the cyan line is surrounded by just one neighbouring O* adatom.

The local coverage affects the activation barrier of the RDS (i.e. O_2 dissociation) because of the repulsion between O* adatoms. By the BEP relationship, the lower coverage of O* in the anti–phase boundary is expected to result in lower activation barriers on fcc site pairs thereon. The effect of the local coverage on the O_2 dissociation activation is shown in Figure 18 (c) and (d), where the snapshots found in Figure 18 (a) and (b), are colour–coded, respectively, according to the activation energy values of the dissociation of O_2. The presence of four 1NN O* adatoms around empty fcc site pairs in the ° phase domain considerably hampers the dissociation of O_2, by significantly elevating the activation barriers from 0.02 eV at the zero coverage limit to approximately 1.90 eV in this region. On the other hand, the lower local coverage in anti–phase boundary and point defect configurations results in lower values for the activation energy, between 1.20 and 1.60 eV at the former and less than 1.0 eV at the latter. Consequently, in these regions, high values of the O_2 dissociation rate constant are computed, making the RDS more probable to occur.

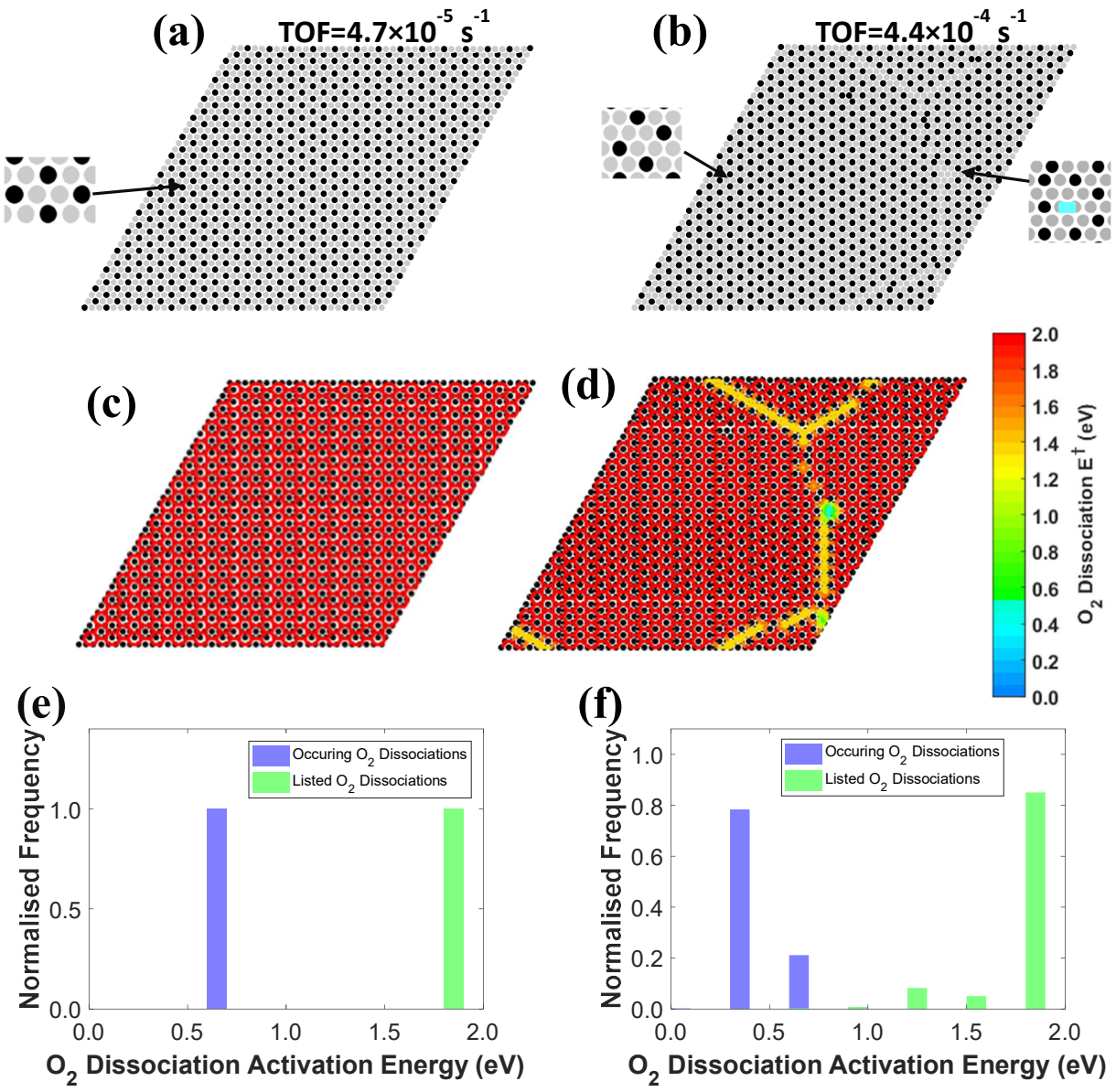

Figure 18. Representative lattice snapshots from KMC simulation at 480 K of a 3–Fig. CE energetics model. Panels (a) and (b) show the adlayer structure of a 42 × 42 and a 44 × 44 lattice, respectively; O* adatoms are represented by black circles and empty sites by grey circles. The close–up on the left of panel (a) shows a phase domain local configuration, while close–ups on the left and right of panel (b) indicate local anti–phase boundary and point defect configurations, respectively. Panels (c) and (d) show the same snapshots but coloured according to the local O_2 dissociation activation energy where low values and high values are shown in blue and red, respectively. Panels (e) and (f) show histograms of the distribution of O_2 dissociation activation energies of listed events by the KMC algorithm on (a) and (b) KMC snapshots, respectively (green) and of the actually executed adsorptions throughout the simulation (blue) on the 42 × 42 and the 44 × 44, respectively. The former are normalised to the total number of listed O_2 dissociations for the particular KMC snapshot and the latter to the total number of executed O_2 dissociations throughout the KMC simulation. P_{tot} = 1 bar, P_{NO_2}/P_{NO} =0.37 and y_{O_2} = 0.1 bar.

The different adlayer regions seen in Figure 18 (d) do not equally contribute to the catalytic rate. To identify the local configurations whereby oxygen adsorptions occur on each lattice, we plot a histogram of the distribution of O_2 dissociation activation energies on the 42 × 42 and 44 × 44 lattices in Figure 18 (e) and (f), respectively. The green bars in these histograms show the activation energy distribution of O_2 dissociation events that may occur on each lattice (Figure 18 (a) and (b)). These are possible events that may happen on vacant fcc site pairs and are listed in the event–queue of the KMC algorithm. As expected, in the 42 × 42 system all of these listed events have the same activation energy (ca. 1.90 eV) because of the ordered ° structure seen in Figure 18 (a). This is not true for the 42 × 42 lattice given the observed anti–phase boundaries. In this case, the majority of O_2 dissociations belong to the ordered ° phase, simply because this phase covers most of the lattice area, and have activation energies of 1.80 – 1.90 eV (tallest bar on the right of Figure 18 (f)). Events with activation energies between 1.20 and 1.60 eV correspond to adsorption processes on anti–phase boundary sites, while those below 1.0 eV correspond to O_2 dissociations on sites located in point defect regions. The normalised frequencies of possible dissociation events on anti–phase boundary and point defects are less than 19 % and 4 %, respectively, of that over the ordered domain.

On the other hand, the blue histogram shown in Figure 18 (e) and (f) correspond to O_2 dissociation events that actually occur (i.e. are executed by the KMC algorithm during the simulation) on the 42 × 42 and 44 × 44 lattices, respectively. To generate these histograms, we record the activation energies of all occurring O_2 dissociations *throughout the simulation*. Interestingly, on the 44 × 44 lattice no O_2 dissociation happens on ° and anti–phase boundary domains (Figure 18 (f)); instead, these events happen primarily at point defects adjacent to the anti–phase boundaries, with the largest portion of the lattice remaining inactive. The catalytic activity is dominated by defect–regions that contain fcc site pairs with two 1NNs or less, and the overall reaction appears to proceed in short “bursts” in these highly active but also highly ephemeral point defects. Thus, the absence of anti–phase boundaries in the 42 × 42 lattice, where all O_2 dissociations happen on rarely formed point defects with activation

barrier of 0.62 eV (Figure 18 (e)), explains the one order of magnitude lower TOF compared to that on the 44 × 44 lattice, as well as the fluctuations in the catalytic rate as shown in Figure 17.

4.2.2. NO oxidation on non–periodic lattices

To verify whether the discussed effects in the previous section are associated with the lattice periodicity, we have performed additional simulations using non–periodic equilateral parallelogram lattices. These lattices provide a better description of complete nanoparticle facets. By eliminating the periodic boundary condition, one breaks the connectivity between sites that belong to opposite sides of the lattice. Consequently, potential reaction patterns that involve O* (or vacant sites) located on two opposite sides cannot be detected by the algorithm in this case. Under these circumstances, there is no generation of anti–phase boundaries that disrupt the ° structure, and therefore, the catalytic rate is not subject to systematic changes at increasing lattice size as in Figure 17 (Figure 19 (a)).

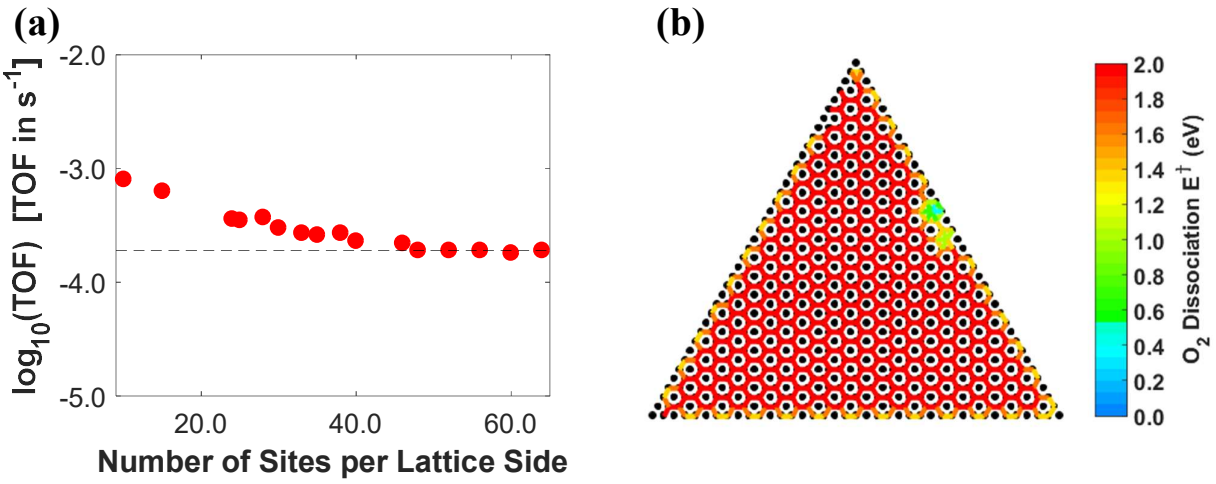

Figure 19. (a) TOF of various non–periodic parallelogram lattices at 480 K, y_{O_2} = 0.1 bar and P_{NO_2}/P_{NO} = 0.37 for 3-Fig. CE energetics; (b) typical snapshot of a KMC simulation using a triangular non–periodic lattice with 780 sites of a 3–Fig. CE energetics model at 480 K and colour–coded according to O_2 dissociation activation energy (low and high values are shown in blue and red, respectively). Conditions as in panel (a).

On the contrary, the computed TOF decreases with increasing number of lattice sites for lattices smaller than 46 × 46 (Figure 19 (a)). Beyond that point, the catalytic rate is practically constant and independent of the lattice size (Figure 19 (a)). After careful examination of the adlayer structure, it is noted that highly active point defects are now present on the lattice edges/corners throughout the KMC

simulation. Because of the non–periodicity, adspecies on edges/corners experience less repulsion compared to the inner phase adsorbates, as it may be true in a real nanoparticle facet. More specifically, the "curvature" at nanoparticle edges result in larger distances between adsorbates in neighbouring facets as compared to cases where these adsorbates are on a planar surface. In addition, edge adsorbates might be differently oriented than the adsorbates on conterminous facets,[141] and therefore the dynamics of non–periodic lattices may better represent those on the facets of a nanoparticle.

In line with the latter consideration, the catalytic oxidation is modelled on equilateral triangular (111) lattices that have the same shapes as facets encountered in perfect nanoparticle structures such as cuboctahedral and octahedral. Figure 19 (b) shows the results of such KMC simulations, revealing that O_2 dissociation is indeed more facile on edges/corners as compared to inner parts of the lattice, and therefore the catalytic activity emerges predominantly from such locations in our non–periodic 3–Fig. CE calculations.

The edge/corner sites are also characterised by a distinct electronic environment given their low coordination number, which is not taken into account in our simulations. What the latter show, is that, even in the absence of such electronic effects, there is a remarkably different physicochemical environment on edges/corners that is governed by geometry and lateral interaction strength, which results in the distinct behaviour of these sites compared to those in the inner part of the facet. It should, however, be noted that for a complete description of the chemistry towards highly accurate catalytic rate predictions on edge and corner sites, electronic effects have to be accounted for, in addition to the geometric effects shown here. The adsorption energy of O* at edges and terraces is often not the same.[142] This is verified by the higher TOF measured at larger Pt particle size, which implies that edge/corner sites might be poisoned in practice as a result of strong adsorbate binding.[143]

4.2.3. Beyond 1NN interactions

We proceed by investigating the effect of long–range interactions on the adlayer structure. We will first present the results for a 5–Fig. CE Hamiltonian model, that includes long–range adsorbate–

adsorbate interactions (2NN and 3NN) and leads to more accurate predictions than the 3–Fig. CE.[116] We instantly note significant differences between the results of these simulations (Figure 20) compared to those previously obtained with the 3–Fig. CE (Figure 18). We show simulation snapshots with colour–coded maps of the O_2 dissociation barriers, on a 44 × 44 non–commensurate periodic lattice at 480 K and 680 K (Figure 20 (a) and (b), respectively). There is a notable absence of well–defined anti–phase boundary regions in these cases, owing to the incorporation of 2NN and 3NN lateral interactions (Figure 20), and the adlayer distribution appears more random compared to that obtained by the 3–Fig. CE at 480 K (Figure 20 (a)). In turn, the calculated TOF is significantly higher because of the presence of several highly active configurations characterised by low local coverage, with O_2 dissociation activation barriers less than 1.0 eV (Figure 20 (a)).

At 480 K, we observe some ° islands in the O* adlayer, and the total O* surface coverage is around 0.34 ML. As seen from the colour–coded KMC snapshot in Figure 20 (a), the O_2 dissociation activation barrier on fcc pairs belonging to these ordered islands is approximately 1.40 eV. This lower activation energy compared to that of the 3–Fig. CE on identical adsorbate configurations (i.e. 1.90 eV, see Figure 18) reflects the "softening" of adsorbate–adsorbate interactions at higher order CEs. The distribution of activation energies for the executed O_2 dissociations at 480 K (Figure 20 (c) – blue bins) reveals that no oxygen adsorption occurs on ° islands. On the contrary, around 40 % of O_2 dissociation events happen with activation energies between 0.40 and 0.50 eV, in configurations with no more than two 1NN O* adatoms (for example the configuration highlighted by the cyan line in the inset above the blue bin at 0.40 – 0.42 eV in Figure 20 (c)).

Furthermore, at 680 K the O* adlayer appears mostly random, as it lacks any appreciably large ordered island (Figure 20 (b)). A lower average O* coverage (ca. 0.27 ML) and a greater degree of adlayer disorder compared to the previous case at T = 480 K, give rise to numerous local adlayer configurations of very low coverage, which encompass pairs of fcc sites without any 1NN O* adatoms. Unsurprisingly, the majority of O_2 dissociations happens therein and are executed with activation

energies below 0.10 eV (Figure 20 (c) – green bins). The occurrence of these low local coverage configurations in conjunction with the relatively high temperature result in higher TOF by two orders of magnitude as compared to 480 K. Instead of a "short burst" behaviour, as for the 3–Fig. CE (Figure 18), events are executed with a broader range of activation energies at both temperatures with a "widespread participation" of fcc site pairs in the catalytic rate (Figure 20 (c)).

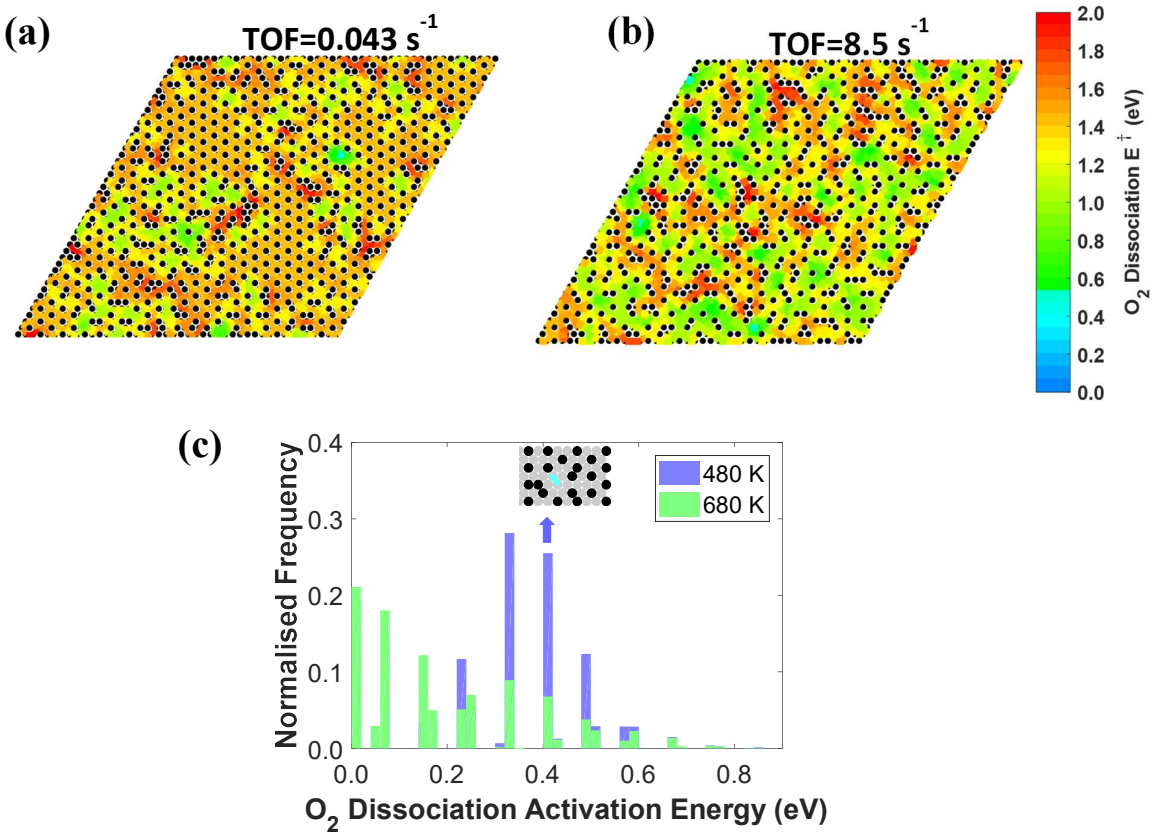

Figure 20. (a) and (b) show KMC snapshots of a 44 × 44 periodic lattice for 5–Fig. CE energetics at 480 K and 680 K, respectively. The snapshots are colour–coded according to the O_2 dissociation activation energy where blue and red correspond to low and high values, respectively. Panel (c) shows a histogram of the distribution of O_2 dissociation activation energies at 480 K (blue) and 680 K (green). P_{tot} = 1 bar, P_{NO_2}/P_{NO} =0.37 and y_{O_2} = 0.1 bar.

Plots of the computed TOFs at 480 K and 680 K for lattice sizes up to 2500 sites are given in Figure 21. A key difference is noted between the simulations at 680 K and 480 K; at 680 K there is near–constant TOF with increasing lattice size, whereas at 480 K there are systematic variations of the catalytic rate. These fluctuations at 480 K span a much narrower range as compared to those of 3–Fig. CE (see Figure 17) and are associated with the retained spatial correlation at this temperature. Upon

closer inspection, we also note that the predicted TOF on commensurate lattices at 480 K exhibits an increasing trend with increasing lattice size (Figure 21), though this trend fades for larger lattices, beyond 45 × 45 (Figure 21).

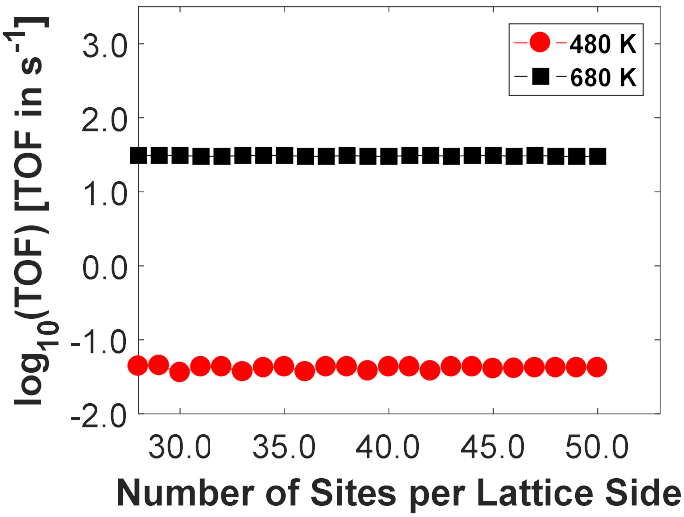

Figure 21. Calculated TOFs of the 5–Fig. CE model for a range of equilateral parallelogram periodic lattices at 480 K (red) and 680 K (black). P_{tot} = 1.0 bar, P_{NO_2}/P_{NO} =0.37 and y_{O_2} = 0.1 for all simulations.

To clarify the causes of the lower TOF on smaller commensurate lattices, within the size range of 6 × 6 to 45 × 45, we investigate the local adlayer configurations for O_2 dissociation events. Figure 22 (a) – (d) show the activation energy distributions of the executed O_2 dissociations on a 9 × 9, 12 × 12, 45 × 45 and a 48 × 48 lattice, respectively. It is important to point out that in this case, the histograms were constructed after processing the statistics of the activation barriers of all *occurring* O_2 dissociations. The main observation is that in all lattices this elementary event is executed at roughly the same activation energies (i.e. on the same local adlayer configurations). The activation barrier distributions of the two large commensurate lattices (45 × 45 and a 48 × 48 – Figure 22 (c) – (d)) are identical, and consequently, the two calculated TOFs are in excellent agreement.

Conversely, remarkable differences are noticed in the distributions of the two small lattices (i.e. 9 × 9, 12 × 12). As seen, on the 9 × 9 lattice around 53 % of O_2 adsorptions happen with an activation barrier less than 0.48 eV, whilst the corresponding normalised frequency of the next largest commensurate lattice (12 × 12) is higher by approximately 7 %. This difference suggests that local

low O* coverage configurations (i.e. configurations where O_2 dissociation can occur with activation energy of 0.48 eV or less) may be more frequently formed during the KMC simulation as compared to the 9 × 9 lattice, thereby explaining the discrepancy between the predicted catalytic rates on the two lattices (Figure 21).

To verify this speculation, we examine how the catalytic rate is affected by the frequency of configurations where O_2 can dissociate with barrier less than 0.48 eV. This normalised frequency is calculated by enumerating the KMC lattice snapshots where low O* coverage configurations have been detected and subsequently dividing this number by the total number of KMC snapshots taken throughout the simulation (i.e. by the total number of O_2 dissociations). The result for nine commensurate periodic lattices with up to 2916 sites is shown in Figure 22 (e). On lattices smaller than 45 × 45, the frequency of highly active configurations increases with the lattice size, whereas for larger lattices there is a convergence of this frequency value to ca. 0.85. Interestingly, the observed trend is in excellent agreement with the TOF trend in Figure 21, where constant catalytic rate values (TOF ≈ 0.042 s^{-1}) are reached on lattices larger than 42 × 42.

We finally present results of an 8-Fig. CE model where 4NN and 5NN pairwise interactions as well as a 3-body interaction are taken into account (graph patterns in Figure 16). At 480 K and under stationary conditions, a substantial part of the O* adsorbate layer adopts a 2 × 2 structure at surface coverage approximately equal to 0.28 ML (see the O_2 dissociation colour–coded KMC snapshot in panel (b) of Figure 23). Adsorbate–adsorbate interactions become "softer" as compared to 3 and 5–Fig. CE models. This is reflected in the fact that O_2 dissociations can happen on pairs of fcc sites encompassed by the ordered 2 × 2 phase with low activation energy being in the range 0.55 – 1.0 eV (Figure 23 (b)). Besides, we observe the formation of several 1–1–3 triplets in the adlayer that, to a limited extent, cause the development of a meandering phase with 2 × 1 O* domains (Figure 23 (b)). This structure becomes dominant at higher surface coverage (see Figure A1 in Appendix I) and therefore these triplets can be considered the precursor of the 2 × 1 O* phase.

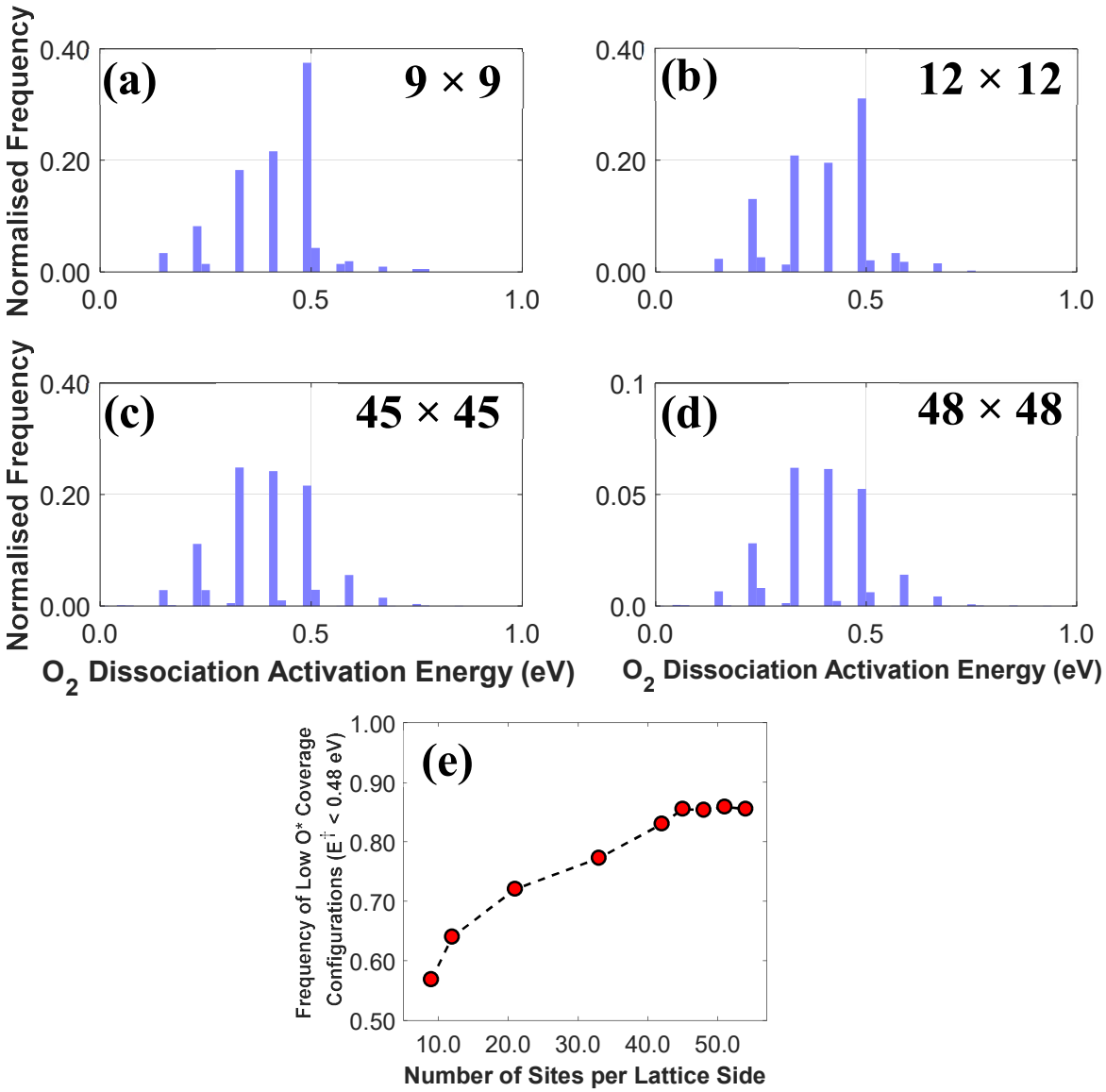

Figure 22. Panels (a) and (b) show the activation energy distributions of occurring O_2 dissociations for 5–Fig. CE on a 9 × 9 and a 12 × 12 periodic lattice, respectively; (c) and (d) show the same distribution for a 45 × 45 and a 48 × 48 periodic lattice, respectively. Panel (e) shows the frequency of appearance of highly active adlayer configurations for nine commensurate lattices. T=480 K, P_{tot} = 1 bar, P_{NO_2}/P_{NO} =0.37 and y_{O_2} = 0.1.

Importantly, because of the largely ordered adlayer at 480 K, the computed TOFs on periodic lattices with size in the range of 10 × 10 to 50 × 50 (Figure 23 (c)) show again an oscillatory behaviour similar to that observed in Figure 17. Commensurate to the 2 × 2 O* phase are now lattices with number of sites (per side) divisible by 2, and after thorough inspection of event–wise KMC snapshots of commensurate and non–commensurate lattices we find that there is no formation of well–defined anti–phase boundaries. To this end, the calculated TOFs on different lattices are on the same order of

magnitude (Figure 23 (c)), which was not true for the 3–Fig. CE model because of the existence of "hard" short range interactions and therefore anti–phase boundaries.

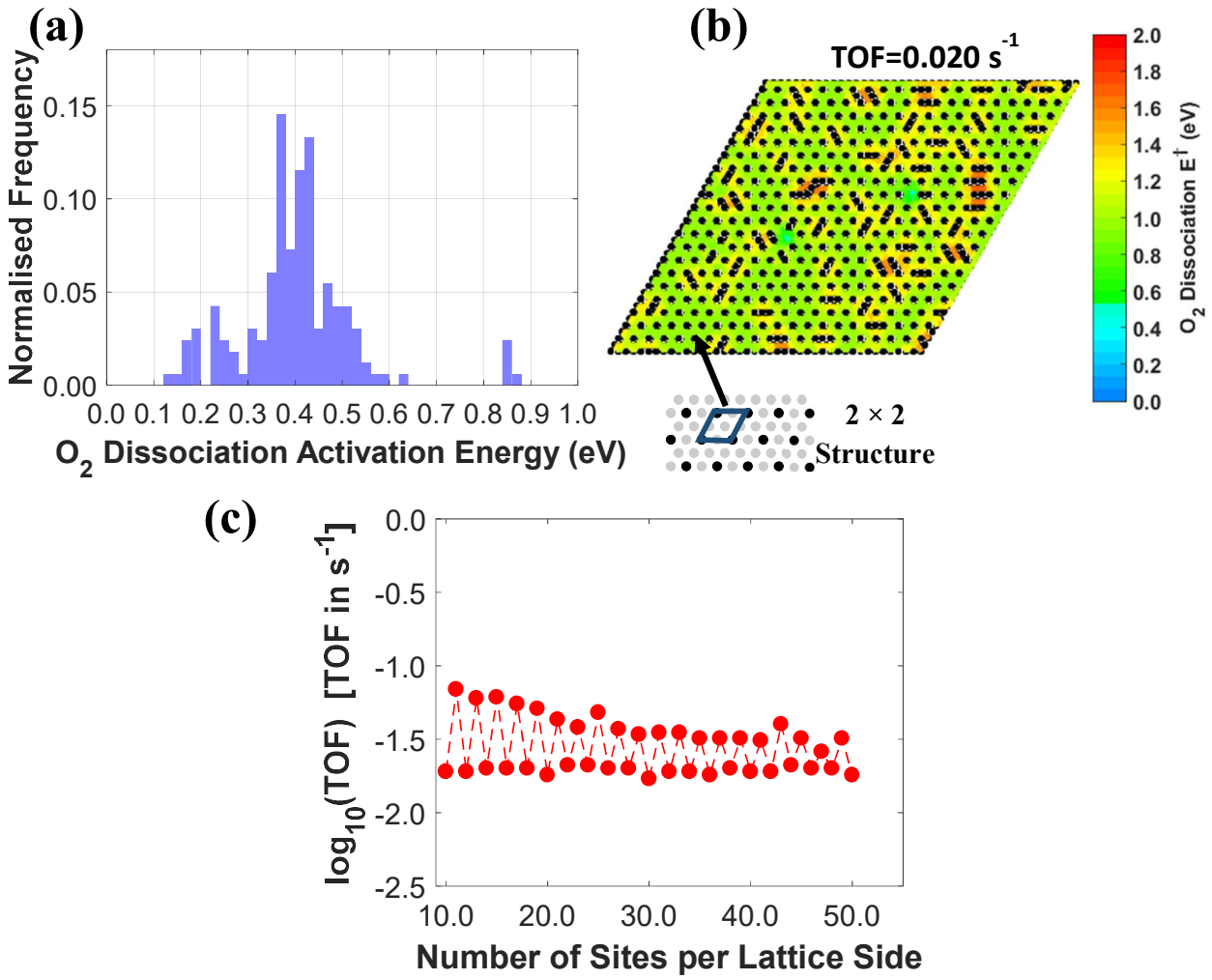

Figure 23. Panel (a) shows the O_2 dissociation activation energy distribution on a 42 × 42 commensurate periodic lattice. Panel (b) shows an O_2 dissociation KMC colour–coded snapshot of the 42 × 42 lattice for 8–Fig. CE energetics model. Panel (c) plots the computed TOF of the 8–Fig. CE model.

The two aforementioned adlayer patterns have been detected using STEM and low–energy electron diffraction (LEED) at similar coverages to those reported here,[111,138] and have also been reproduced in computational studies that employ equilibrium models.[20,27,144] This furnishes evidence that the O* – Pt(111) system, at least with regard to the adlayer structure, is more accurately described by an 8–Fig. CE energetics model than by the 3–Fig. CE and 5–Fig. CE models.

The formation of the 2 × 2 phase is explained by the very small energetic contribution parameter of 3NN clusters (0.012 eV) compared to other clusters in 8–Fig. CE models (see Appendix I), leading to the formation of numerous such patterns in the adsorbate layer (Figure 23 (b)). According to experimental studies the 2 × 2 O* phase remains inactive to the catalytic NO oxidation within the temperature range of 350 – 500 K at 1/4 ML surface coverage,[138] and this is further corroborated by our 8–Fig. CE simulations. In more precise terms, the activation barrier distribution of the executed O_2 dissociations on a 42 × 42 periodic lattice (Figure 23 (a)) reveals that less than 5 % of such events takes place with activation barrier of 0.55 – 1.0 eV. By contrast, we see that the vast majority of O_2 dissociation events happen with barriers below 0.50 eV (Figure 23 (a)). The contribution of fcc site pairs to the catalytic rate is even more widespread than in the simulations with the 5–Fig. CE. Yet, the overall reaction progresses in a similar manner in both cases with O_2 dissociations occurring for various adlayer configurations and not only on highly active point defects as for the 3–Fig. CE simulations. The calculated TOFs are in turn of the same order of magnitude, but not identical, owing to the fact that the adsorbate layer exhibits different structure in the two cases.

The analysis is finalised with a comparison between the apparent activation energy, $E_{app}^{\dagger}$, found by the 8–Fig. CE model and experimentally obtained values.[145] To determine , we calculate seven TOFs at different temperatures in the temperature range of 480 - 493 K where the differences in surface coverage are known to be small.[16] From the Arrhenius plot in Figure 24, we find $E_{app}^{\dagger}$ = 52.6 ± 4.0 kJ mol^{-1}, which is slightly greater than the reported value by Smeltz et al.[145] over Pt(111) single crystals under similar conditions (ca. 41 kJ mol^{-1}). Furthermore, we compute TOF = 0.013 s^{-1} at P_{NO_2}/P_{NO} = 0.56, y_{O_2} = 0.1 and 480 K. At these conditions, the experimentally reported TOF (ca. 0.15 s^{-1}) is found one order of magnitude larger.[145] This discrepancy is in accord with the larger computed , by 11 kJ/mol (0.1 eV), as compared to experiment.[145] More specifically, a larger activation barrier by 0.1 eV results

in a smaller rate constant by a factor of approximately 11 at 480 K. As noted in chapter 8, errors of around 0.1 to 0.2 eV are indeed expected for commonly used DFT functionals.[146]

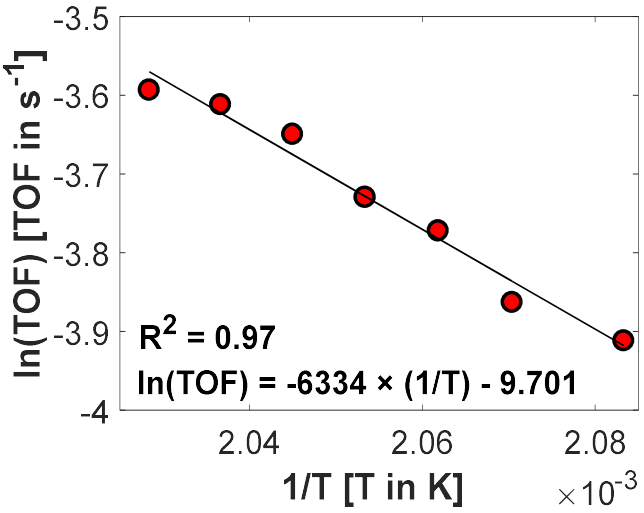

Figure 24. Arrhenius plot of the temperature dependence of the rate of NO oxidation on a 42 × 42 commensurate periodic lattice for 8–Fig. CE, y_{O_2} = 0.1 bar, P_{NO_2}/P_{NO}=0.37 and P_{tot} = 1 bar. Slope in K, k_B in eV/K and in eV.

4.3. Concluding remarks

Chapter 4 described the inhomogeneity of adsorbate layers that is caused by lateral interactions and adds to the complexity of surface reactions. KMC simulation in conjunction with CEs is an approach capable of dealing with this complexity. Catalytic reactions become even more complicated when they occur over alloy catalysts, which have a number of active sites with a dissimilar contribution to the total activity of the material. The remaining chapters of this Thesis examines the performance of chemical reactions on highly dilute alloys, and also the restructuring of these materials under reactive conditions.

Chapter 5

5. Structure sensitive reactions over single atom and dilute alloys

The present chapter focuses the behaviour of structure sensitive over dilute and single atom alloys. Recent theoretical and experimental studies corroborate that isolated dopant atoms on coinage metal surfaces exhibit *d* states that resemble that of a free metal atom (see section 1.4).[43,44] This finding gives rise to questions of paramount importance for future surface science and theoretical investigations: are isolated dopant atoms on the most common (111) and (100) surfaces equivalent in terms of reactivity? Do dopant atoms on different flat facets have comparable electronic structures? Could typically structure sensitive reactions (e.g. N─N,[147] C─O,[148] N─O[149] bond–breaking) exhibit similar behaviour on the two aforementioned flat surfaces? This chapter attempts to answer these questions by means of DFT calculations. It begins with an investigation on the adsorption of NO, N_2 and O adspecies over a number of SAA(111) and SAA(100) surfaces, and continues with simulations of structure sensitive association/dissociation reactions on the same surfaces. *The contents of this chapter have been published in Catal. Sci. Technol., 2020,10, 5815-5828.*

5.1. Computational details

Before discussing our results let us first describe the employed computational setup. Periodic DFT calculations were performed using the Vienna *ab initio* Simulation Package (VASP),[150,151] which solves the KS equations (eq. (8)) in an iterative manner.[68] The PAW method was employed to model the interaction between the core and valence electrons, and the kinetic energy cut–off was set at 400 eV (see sections 2.4 and 2.5).[152] Exchange and correlation effects were treated with the optB86b–vdW functional,[153–155] which accounts for dispersive van der Waals (vdW) interactions. Spin–polarised calculations were performed for gas–phase NO and O_2, but also for Ni surfaces and Ni–containing alloys; however on the latter surfaces, we noticed that the magnetic moment of Ni atoms was quenched during the simulation, which is consistent with previous works.[43,44] The low–index (100) and (111) surfaces were modelled by a 5–layer $p(3 \times 3)$ cell, and periodic images along the z–direction were separated by a vacuum of 10 Å. The presence of a small number of dopant atoms (i.e. up to three) on the surface layer of the highly dilute and SAA surfaces will, in all probability, have an unimportant effect on the lattice constant of the host material. Therefore, the lattice constant of the alloy materials was the optB86b–vdW computed lattice constant of the host metal (i.e. 3.608 Å, 4.077 Å and 4.127 Å for Cu, Ag and Au, respectively). During geometry optimisation, the three top layers of the DFT slab and any adsorbed species were allowed to relax, whilst the two bottom layers were fixed at the calculated lattice constant. The electronic self–consistency threshold was set to 10^{-7} eV, the Hellman-Feynman forces were relaxed to less than 10^{-2} eV/Å and the first Brillouin zones of the (111) and (100) surfaces were sampled with a $9 \times 9 \times 1$ Monkhorst–Pack k–point mesh. Our k–point convergence check shows that this simulation setup affords a good accuracy (see Figure A3 in Appendix II). In turn, this permits us to compare our computed activation barriers for the dissociation of CO_2 reaction on the (100) surface to those previously obtained on the (111) surface using a $13 \times 13 \times 1$ k–mesh (see Figure A4 in Appendix II).[45] The adsorption energy of a NO and N_2 species bound to the surface (E_{ads} (A*), where A* = NO* or N_2*) was calculated using the following expression:

$$E_{ads}(A*) = E_{tot}^{A*+slab} - E_{tot}^{slab} - E_{tot}^{A_{(g)}}, \quad (69)$$

where $E_{tot}^{A*+slab}$ is the DFT total energy of a slab with the adsorbed species thereon, E_{tot}^{slab} is the DFT total energy of the clean slab, and $E_{tot}^{A_{(g)}}$ is the DFT total energy of the adspecies in the gas phase. The corresponding adsorption energies of O adatoms on the different surfaces are computed relative to O_2 in the gas–phase:

$$E_{ads}(O*) = E_{tot}^{O*+slab} - E_{tot}^{slab} - \frac{1}{2} \times E_{tot}^{O_{2(g)}}, \quad (70)$$

where $E_{tot}^{O*+slab}$ is the DFT total energy of a slab with an O* thereon, and $E_{tot}^{O_{2(g)}}$ is the DFT total energy of O_2 in the gas phase.

The transition states (TSs) of the elementary reactions studied, were located using the dimer method,[104] and vibrational frequency analyses verified that each TS found was a first–order saddle point on the potential energy surface. The activation barrier (E_a) and the reaction energy (ΔE_{rxn}) of an elementary step are found from eq. (71) and eq. (72), respectively.

$$E_a = E_{TS} - E_{IS}, \quad (71)$$

$$\Delta E_{rxn} = E_{FS} - E_{IS}, \quad (72)$$

where E_{TS}, E_{FS} and E_{IS} are the DFT–computed energies for the TS, final state (FS) and initial state (IS), respectively.

5.2. Results and discussion

5.2.1. Adsorption energies on SAA (111) and (100) surfaces

The adsorption of CO* on the top dopant site has been explored over a number of Cu–, Ag–, and Au–based SAA surfaces.[67,125] A highlight of these works is that the binding strength of CO* on SAA (111) and (100) surfaces is almost identical,[125] thereby suggesting that isolated dopant atoms on flat facets exhibit very similar reactivity. To some extent, this phenomenon can be attributed to the limited electronic and spatial overlap between the dopant atom and its surrounding host metal atoms.[43,44]

First, we further investigate and compare the reactivity of SAA (100) and (111) surfaces by calculating the adsorption energy of other common adsorbates thereon. We compute and report the adsorption energies of N_2*, NO* and O* on the top dopant site of Cu–, Ag– and Au–based SAA (100) and (111) surfaces, with Pt, Pd, Rh and Ni as dopants. With regard to the most stable adsorption structure of the adsorbates under investigation, our DFT calculations show that both N_2 and NO prefer to adsorb in an upright linear configuration, with N being closer to the alloy surface for the latter species (i.e. the dopant atom).

Figure 25 (a) shows a parity between the computed adsorption energies of the three adspecies on the (111) and (100) SAA surfaces. For greater clarity, we do not show which alloy corresponds to which point in the plot, but a full list of the adsorption energy values is provided in Appendix II. A first observation is that there is a strong correlation between $E_{ads}(111)$ and $E_{ads}(100)$ for the SAA surfaces, with the vast majority of the plot points lying close to the parity line (Figure 25 (a)). We also observe that the binding strength is systematically stronger on the more open SAA (100) surfaces than on the SAA (111) surfaces, by ca. 0.10 eV on average (Figure 25 (a)). As noted earlier, one may expect a small electronic interaction between the PGM atom and its coordination environment.[44] Yet, the narrow dopant–host interactions do not rule out the transfer of charge between these two types of surface species.[44] Consequently, the observed disparate reactivity in Figure 25 (a) may be the result of dopant–host charge transfer, which occurs to a different extent on the SAA (100) and (111) surfaces, given their different geometry.

In chapter 1, it was discussed that the reactivity of pure metal and alloy surfaces is conventionally explained by the position of the *d* band centre (ε_d) relative to the Fermi level: the higher the *d* band centre the higher the reactivity of a catalytic surface.[6] In an effort to better understand the generally higher reactivity of the SAA (100) facet as compared to the SAA (111) facet, we compute the *d* band centres of the isolated PGM atoms on the examined SAA surfaces (Figure 25 (b)).

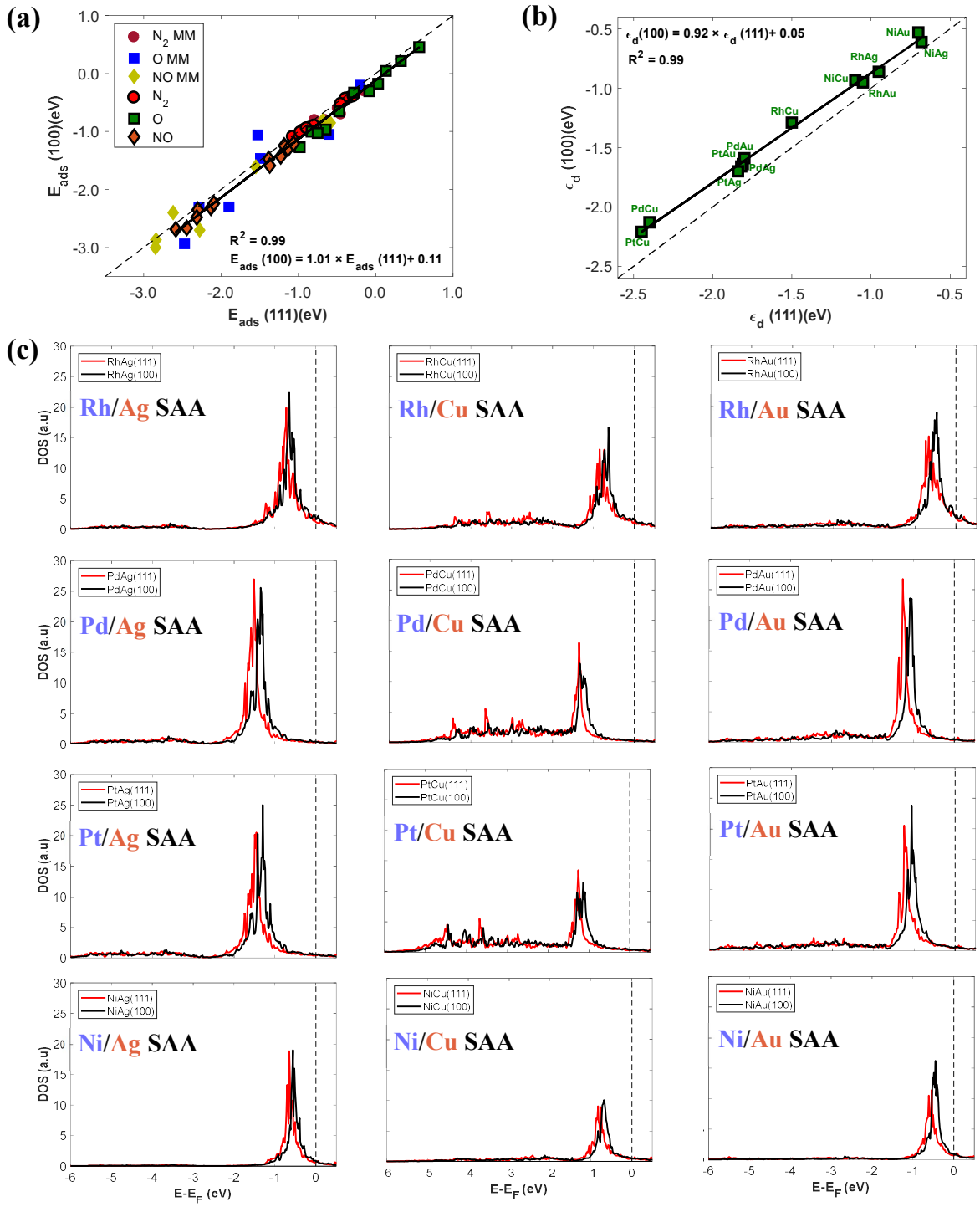

Figure 25. (a) Parity plot between $E_{ads}(100)$ and $E_{ads}(111)$ for the adsorption of N_2*, NO* and O* on the top dopant site of a number of SAA surfaces; for clarity, we also show the adsorption energies of the three species on the most stable adsorption site of the corresponding monometallic (MM) surfaces which include Pt, Pd, Rh, Ni, Ag, Au and Cu surfaces (points without outline). (b) Linear correlation between $\varepsilon_d(100)$ and $\varepsilon_d(111)$ of the dopant *d* states of the SAA surfaces. The parity line is shown as a dashed black line in panels (a) and (b); determination coefficients (R^2) and fitting lines are shown in both panels (a) and (b). In the linear fit in panel (a) only the SAA surfaces are considered (points with black outline). (c) *d* DOS plots for all the SAA (100) and (111) surfaces, whereby the DOS are projected onto the *d* states of the single atom.

Interestingly, the results reveal a strong correlation between $\varepsilon_d(100)$ and $\varepsilon_d(111)$. Additionally, one observes that the values of $\varepsilon_d(100)$ for the materials studied are always at higher energy than the corresponding values of ε_d (111), suggesting that the *d* band model can rationalise the disparate reactivity exhibited by different SAA facets. On the contrary, the same model cannot explain the reactivity of different SAA surfaces that belong to the same facet. As noted in chapter 1, the reactivity of SAAs cannot be explained by the *d* band model, and this is confirmed by a poor correlation between the adsorption energies of the investigated adspecies (i.e. $E_{ads}(O)$, $E_{ads}(N_2)$ and $E_{ads}(NO)$) and the *d* band centres of the PGM for a specific facet (Figure A5).

Next, we study the electronic structure of the dopant on the two low–index surfaces. To this end, we present the corresponding *d* projected DOS plots for a number of dopant atoms on coinage metal surfaces (Figure 25 (c)). As seen in Figure 25 (c), the *d* band of the single atom exhibits very sharp features close to the Fermi level for all Au– and Ag–based SAA surfaces for both low-index facets. Conversely, Cu-based SAA surfaces deviate, to some degree, from this behaviour, probably because of a better electron density mixing between the dopant and Cu atoms (Figure 25 (c)).[43] It is also noted that the DOS plots of SAA (100) surfaces are shifted slightly closer to the Fermi level as compared to those of SAA (111) surfaces (Figure 25 (c)). This shift in *d* DOS is consistent with the data displayed in Figure 25 (b), and implies a higher electron density available close to the Fermi level for the PGM atoms on SAA (100). The result is an enhanced interaction between the SAA (100) dopants and the adsorbate species (Figure 25 (a)).

5.2.2. Assessing the reactivity of SAA surfaces by calculating kinetic barriers

We continue by assessing the reactivity of SAA(100) and SAA(111) surfaces by means of TS calculations. We compute and report *effective* activation barriers with respect to the most stable initial states for three typically structure–sensitive reactions (for the definition of the effective barrier see Figure A6 in Appendix II), which include the direct dissociations of NO*, CO_2* and N_2*,[56,156–158] over the same SAA surfaces as before. The same barriers are computed over seven (100) and (111) pure

metal surfaces (i.e. Pt, Pd, Rh, Ni, Ag, Cu and Au surfaces). The dissociation of the aforementioned adsorbates may occur through different pathways over the dilute alloy surfaces. The goal is to identify and report the reaction barriers that correspond to the minimum energy path (MEP), which will be the most probable dissociation route during reaction (Figure 26).

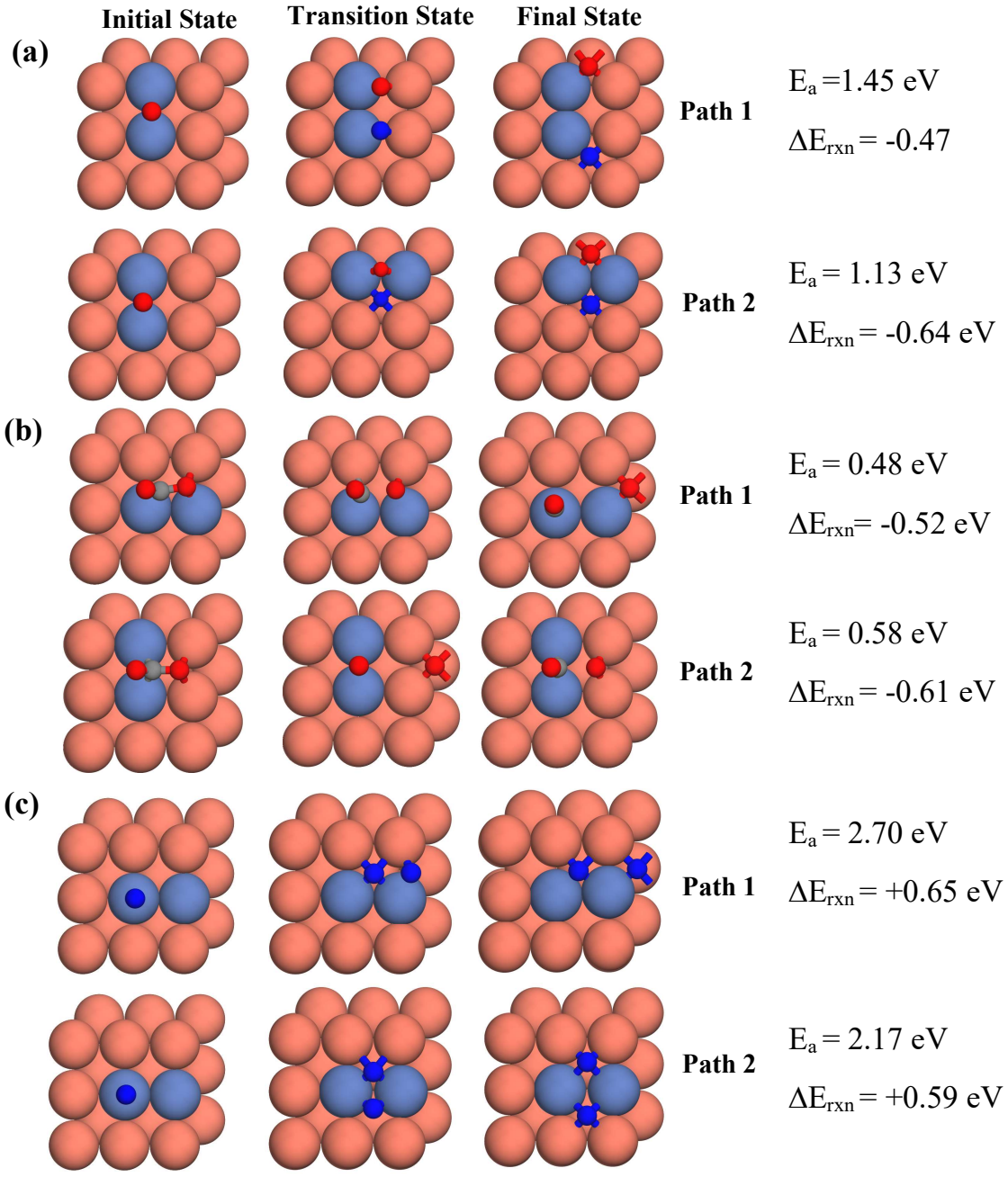

Figure 26. Examples of different reaction pathways for the dissociation of (a) NO; (b) CO_2 and (c) N_2. The computed barriers and reaction energies are shown on the side of each pathway. The images show the top view of the DFT slab and Cu, Ni, N, O and C atoms are shown in orange, purple, blue, red and grey, respectively.

Figure 26 shows examples of two alternative dissociation pathways for one of the examined surfaces, namely the $Ni_2Cu(100)$ where Ni atoms form 1NN dimers. Also shown are the computed E_a and ΔE_{rxn} for each path (Figure 26). Path 2, in which the bond cleavage occurs (nearly) above the bridge site of the Ni–Ni dimer, is the energetically favoured path for the diatomic adspecies (i.e. NO* and N_2*), while CO_2* prefers to dissociate along the dimer (Figure 26). Similar analysis for other SAA and cluster surfaces leads to the reported MEP barriers of Figure 27. It should, however, be noted that given the extreme complexity of the PES the existence of alternative paths to those identified cannot be precluded.

Moreover, to verify the reliability of our calculations, it is instructive to compare our results to data reported in the literature. The direct dissociation of NO* is underscored as a crucial step for the NO reduction with CO. According to theoretical and experimental studies, under some circumstances this reaction step is the RDS of the NO + CO reaction.[159,160] Among the commonly employed pure metal catalysts in three–way catalytic converters (i.e. Rh, Pt and Pd), Rh is the only metal that is capable of activating the N─O bond at low temperatures.[157] This observation is in line with our DFT calculations, which show that the activation barriers for the NO* dissociation reaction over Rh surfaces (i.e. E_a = 0.44 eV and 1.42 eV for Rh(100) and Rh(111), respectively) are considerably lower than those over Pd and Pt surfaces (E_a = 1.44 eV, 2.25 eV, 0.81 eV and 2.05 eV for Pd(100), Pd(111), Pt(100) and Pt(111), respectively) – (Figure 27 (a)). Based on our simulations, the initial state of this reaction involves a nitric oxide molecule, which is adsorbed in an upright linear configuration with the N atom closer to a hollow site (3–fold and 4–fold for (111) and (100) surfaces, respectively). The only exception to that is Rh(100), where we find that a different adsorption configuration, with NO almost parallel to the surface, is thermodynamically more stable than the upright linear adsorption structure. This is consistent with previous theoretical studies;[161] in addition, our computed NO dissociation barriers on Rh(100), Rh(111), Pd(100) surfaces are congruent with activation barriers reported in previous theoretical and experimental works.[157,162–166]

Regarding the dissociation of CO_2* on Cu(100), we compute E_a = 0.95 eV, namely a value which is in excellent agreement with the experimentally determined value by Chorkendorff and co–workers of $E_a = 0.96 \pm 0.05$ eV.[167] We also note that there is an excellent match between our calculated E_a for Ni(100) and Rh(100) surfaces and those reported by Liu et al. (Figure 27 (c)).[158] Furthermore, in Figure A7, we provide the activation barriers for the reverse reaction (i.e. CO* oxidation to CO_2*). Our data, in line with other studies, suggest that the catalytic CO oxidation is very facile on pure metal Ag and Au surfaces,[168] while relatively low activation barriers are calculated for Cu(111) and Cu(100) surfaces (0.48 eV and 0.73 eV, respectively).

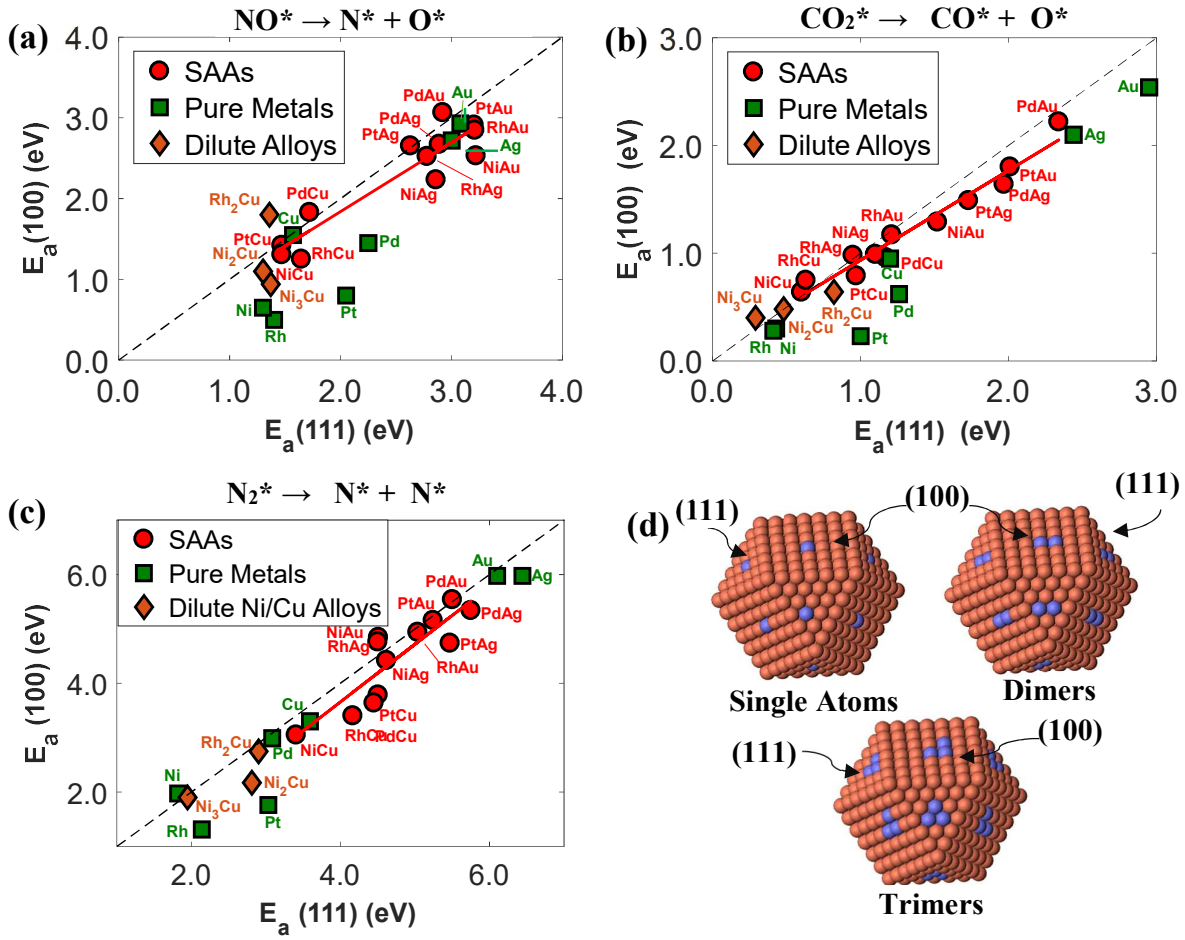

Figure 27. E_a(100) and E_a(111) parity for SAA surfaces (red circles), pure metal surfaces (green squares) and Ni clusterss on Cu (orange diamonds) for (a) the direct dissociation of NO*; (b) the dissociation of CO_2*, and (c) the dissociation of N_2*. (d) Cu nanoparticles whereon the geometry of Ni and Rh clusters (Ni_2Cu, Rh_2Cu and Ni_3Cu) on the (100) and (111) surfaces is highlighted. Cu and Ni or Rh atoms are shown in orange and purple, respectively. The red lines in panels (a), (b) and (c) are linear fits of only the SAA data (red circles).

An important observation in Figure 27 (a) – (c) is that all three dissociation reactions are, in most of the cases, more facile on (100) SAA and pure metal surfaces than on the corresponding (111) surfaces. Indeed, according to Liu and Hu,[112] one should expect more facile bond activation on more open surfaces and on those containing under–coordinated sites (e.g. steps and kinks). This is not true, however, for association reactions, which do not follow this trend.[112] In our results, the structure–sensitivity of reactions that involve N─O, C─O and N─N bond–breaking is clear for PGM surfaces (i.e. Pt, Pd, Rh and Ni), for which there is a significant scatter in the data (Figure 27 (a) – (c)). By contrast, the dissociation barrier differences between the (111) and (100) SAA surfaces are relatively small, and noticeably less accentuated in comparison to monometallic PGM surfaces (Figure 27 (a) – (c)). The same is true for coinage metal surfaces as well.

In order to quantify the average difference between the computed kinetic barriers on the two low–index surfaces, we define the following metric, $\overline{D_k}$:

$$\overline{D_k} = \frac{1}{N_k}\sum_{i=1}^{N_S}\left|E_{a,k,i}(100) - E_{a,k,i}(111)\right|,$$

$$k \in \{SAAs, PGMs, Coinage\ Metals, All\ Pure\ Metal\ Surfaces\} \quad (73)$$

where N_k is the number of surfaces in group k (where $k \in$ {SAA surfaces, PGM surfaces, coinage metal surfaces, all pure metal surfaces}), $E_{a,k,i}$ are the computed activation barriers for surface i that belongs to group k, and N_S is the total number of surfaces in group k. Thus, for each catalyst group k, $\overline{D_k}$ is indicative of the average extent by which the dissociation barriers computed for (111) surfaces deviate from those for the more open (100) surfaces.

Table 1 summarises values of $\overline{D_k}$ for the dissociations of NO*, CO_2* and N_2*. We note that $\overline{D_{SAAs}}$ and $\overline{D_{Coinage\ Metals}}$ show similar values for the three dissociation reactions, and an average $\left|\overline{D_{SAAs}} - \overline{D_{Coinage\ Metals}}\right|$ of just 0.11 eV (Table 1). Along these lines, bond scission processes seem to exhibit low structure sensitivity on both pure coinage and SAA low–index surfaces. On the other hand,

we find that the deviation between $E_a(100)$ and $E_a(111)$ for PGM surfaces is, on average, larger by ca. 0.38 eV than that for SAA surfaces. Accordingly, it appears that a significant "part of the structure sensitivity" of dissociation reactions is diminished on SAA surfaces as compared to the PGM surfaces, and this is an important observation from a surface science standpoint. The "retained structure sensitivity" of SAAs can be ascribed to two factors: (i) the slightly different electronic *d*–band structure of the dopant on SAA (100) and (111) (see Figure 25 (b) and (c)); and (ii) geometric effects that arise as a result of the extended nature of the TS structure. Indeed, the TS geometries for the N_2* and NO* dissociations are quite extended, and involve mainly mixed metal sites (e.g. see Figure 28 for SAA (100) surfaces).[169] Yet, the scission of the C─O bond of CO_2* appears to happen closer to the top dopant site, hence the relatively small for this reaction (see Figure 28 and Table 1).

Table 1. $\overline{D_k}$ values for SAA and pure metal surfaces for the three examined dissociation reactions.

Reaction	$\overline{D_{SAAs}}$ (eV)	$\overline{D_{PGMs}}$ (eV)	$\overline{D_{Coinage\,Metals}}$ (eV)	$\overline{D_{All\,Pure\,Metals}}$ (eV)
1. NO* → N*+O*	0.27	0.94	0.15	0.60
2. CO_2* → CO* + O*	0.13	0.42	0.33	0.39
3. N_2* → N* + N*	0.39	0.55	0.36	0.49

Finally, the group *All Pure Metals* (Table 1) includes all the pure metal surfaces (i.e. PGM and coinage metals). Although this group contains the coinage metal surfaces, which do not exhibit pronounced structure sensitivity for the bond cleavage reactions, we compute $\overline{D_{All\,Pure\,Metals}}$ values that are always larger than $\overline{D_{SAAs}}$ and an average $\left|\overline{D_{SAAs}} - \overline{D_{All\,Pure\,Metals}}\right|$ over the three reactions of ca. 0.23 eV.

5.2.3. Highly reactive Ni and Rh clusters on Cu-based alloys

Another noteworthy feature of Figure 27 is that Cu–based SAAs show considerably lower dissociation barriers as compared to Ag– and Au–based SAA surfaces (Figure 27 (a) – (c)). The high

activity of Cu–based SAAs toward numerous chemical reactions has been experimentally confirmed.[40,42,170] We determine that, among the Cu–based SAAs, Ni/Cu and Rh/Cu bimetallic alloys exhibit the lowest dissociation barriers. The most facile bond cleavage reactions are predicted to occur on Ni/Cu surfaces (Figure 27 (a) – (c)). This behaviour may be explained by: (1) the more localised *d* states of the isolated Ni atom on Cu as compared to the broader *d* states of Rh, Pt and Pd atoms on the same host metal (Figure 25 (c)), and (2) the closer position of the *d* DOS peak of Ni on Ni/Cu to the Fermi level than the corresponding Pt and Pd peaks on Pt/Cu and Pd/Cu, respectively (Figure 25 (c)).

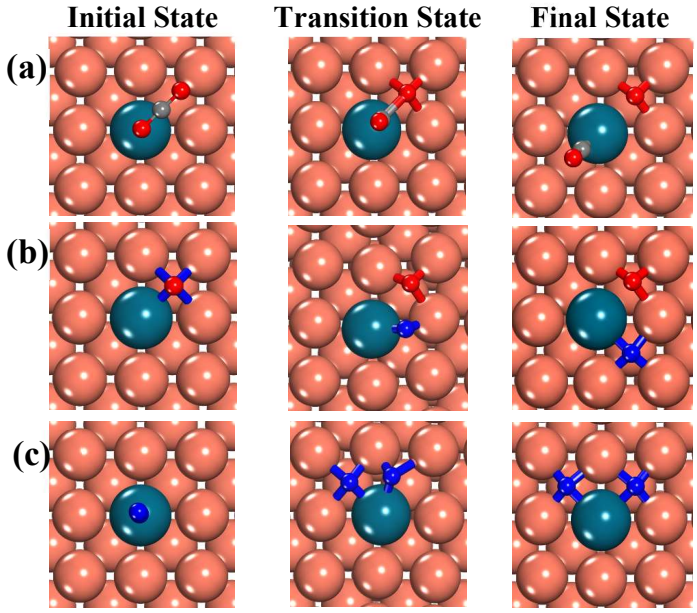

Figure 28. Top view of representative IS, FS and TS structures on SAA(100) surfaces for the (a) dissociation of CO_2*; (b) dissociation of NO*; and (c) dissociation of N_2*. Dopant and host metal atoms are shown in dark green and orange, respectively. N, O and C atoms are shown in blue, red and grey, respectively. The structures of this figure correspond to the Pd/Cu(100) system, but they are representative for the majority of the SAA(100) surfaces.

Yet, our simulations show that the computed kinetic barriers on pure metal Ni and Rh surfaces are always lower than those of the Ni/Cu and Rh/Cu SAA surfaces (Figure 27 (a) – (c)). For example, the activation barriers for the direct dissociation of NO* on Rh (111) and (100) surfaces are 1.42 eV and 0.44 eV, respectively, while on Ni/Cu (111) and (100) SAA surfaces are 1.47 eV and 1.07 eV (Figure 27 (a)). Along the same lines, the dissociation of CO_2* appears to be more facile on Rh(100) – (E_a = 0.28 eV) than on Ni/Cu(100) – (E_a = 0.64 eV) – (Figure 27 (b)). Finally, the same trend holds

true for the dissociation of N_2* for which our computed barriers for SAA surfaces are very large (i.e. $E_a > 3.0$ eV), and large for pure metal surfaces (i.e. $E_a > 2.0$ eV) – (Figure 27 (c)).

In an effort to circumvent the "kinetic barrier gap" between SAA and pure metal surfaces, we explore the reactivity of small PGM clusters (i.e. dimers and trimers), on Cu surfaces. PGM clusters embedded on coinage host surfaces have recently drawn the attention of the catalysis community (see chapter 1). Herein, we focus our attention on Ni and Rh clusters on a Cu host (i.e. Ni–Ni dimers and Ni trimers, which will be denoted as Ni_2Cu and Ni_3Cu, and Rh dimers Rh_2Cu) – (Figure 27 (d)). This is because Ni/Cu and Rh/Cu SAA surfaces demonstrate the highest capability of activating chemical bonds (Figure 27 (a) – (c)), and because Ni/Cu alloys are composed of relatively inexpensive metals and therefore are attractive from a practical standpoint. Regarding the Rh/Cu dilute alloys, we examine the performance of Rh–Rh dimers on Cu, as *ab initio* Monte Carlo studies indicate that the SAA phase on Rh/Cu exhibits high thermodynamic stability under both vacuum and reactive conditions.[63] Along these lines, we assume negligible formation of clusters larger than Rh–Rh dimers at low concentration of Rh over these surfaces.

Our data suggests that the kinetic barriers for NO* or CO_2* dissociation on Rh–Rh dimers are closely comparable to or higher than those on the Rh/Cu SAA surfaces (Figure 27 (a) and (b)). On the contrary, the breaking of N─O, C─O and N─N bonds is easier on Ni clusters than on isolated dopant atoms on coinage metals (Figure 27 (a) – (c)). Therefore, the presence of small Ni aggregates on the catalytic surface appears to be beneficial for the catalytic activity toward dissociation reactions. Remarkably, Ni_2Cu, Ni_3Cu surfaces perform almost equivalently to commonly employed PGMs in catalysis, such as Ni, Pt and Rh (Figure 27 (a) – (c)). For the direct dissociation of NO*, which is a key reaction step for the NO + CO reaction,[159] $Ni_2Cu(111)$ and $Ni_3Cu(111)$ demonstrate moderate kinetic barriers of 1.30 eV and 1.37 eV, respectively. These barriers are lower than the corresponding barriers for Rh(111) ($E_a = 1.42$ eV) as well as than that for Pd(111), Pt(111) ($E_a = 2.25$ eV and 2.08 eV, respectively) – (Figure 27 (a)). Additionally, the desorption energies of NO* from Ni dimers and

trimers are larger (within the range of 2.7 eV – 3.1 eV for both low-index surfaces; see Appendix II) than the corresponding NO* dissociation kinetic barriers, indicating a high probability for NO dissociation over Ni clusters. This dissociation probability will also be large on the Ni(111) surface (where we find E_a = 1.29 eV and a desorption energy of NO of 2.84 eV; see Appendix II), but not that large for pure Cu(111) whereon the NO* dissociation barrier (E_a = 1.57 eV) is almost identical to the corresponding desorption barrier (1.55 eV). Finally, it should be mentioned that on the (100) surface the lowest kinetic barrier is observed for Rh(100) (E_a = 0.44 eV), justifying the extensive use of Rh in catalytic converters.

Moreover, the cleavage of the C─O bond is quite facile on Ni_3Cu and Ni_2Cu surfaces (E_a < 0.50 eV for both Ni cluster surfaces). Regarding their pure metal counterparts, our calculations imply that the desorption of CO_2 will be preferred to its dissociation over Ni(111), Cu(111) and Cu(100) (see Appendix II). Remarkably, the same is not true for Ni–Ni dimers and trimers, where we compute CO_2* desorption energies that are larger than the CO_2 dissociation barriers on these surfaces (see Appendix II). Accordingly, we conclude that CO_2 dissociation will be generally favoured against CO_2 desorption over that Ni cluster surfaces. The only exception to that is the $Ni_2Cu(111)$ surface for which the dissociation and desorption energies are 0.47 eV and 0.37 eV, respectively.

The better efficiency of Ni_2Cu and Ni_3Cu in cleaving chemical bonds compared to the Ni/Cu SAA, can be rationalised by the electronic structure of these systems (Figure 29). Based on the IS and TS structures of the examined dissociation reactions, we realise that, with the exception of the $Ni_3Cu(111)$ surface, the adsorbate species mainly interact with mixed sites on the Ni/Cu surfaces (i.e. sites that are surrounded by both Cu and Ni atoms) – (e.g. see Figure 28). These mixed sites, whereon the bond breaking occurs, are composed of three and four surface atoms for (111) and (100) dilute alloy surfaces, respectively, and are displayed in the insets on the right of Figure 29 for the Ni/Cu dilute alloy and SAA surfaces.

Also shown in Figure 29 (a) and (b) are the *d* DOS projected onto the atoms of the mixed active sites of SAA and dilute alloy surfaces. Almost all DOS plots exhibit bimodality; the *first* peak on the right (between 0.0 eV and -1.30 eV) is related to the *d* states of the embedded Ni atoms, while the broader peak on the left (between -1.50 eV and -4.50 eV) corresponds to the *d* states of Cu atoms (Figure 29 (a) and (b)). On the other hand, the $Ni_3Cu(111)$ surface is hardly bimodal, and this stems from the fact that the active site for the dissociation thereon is composed only of Ni atoms (Figure 29 (a)).

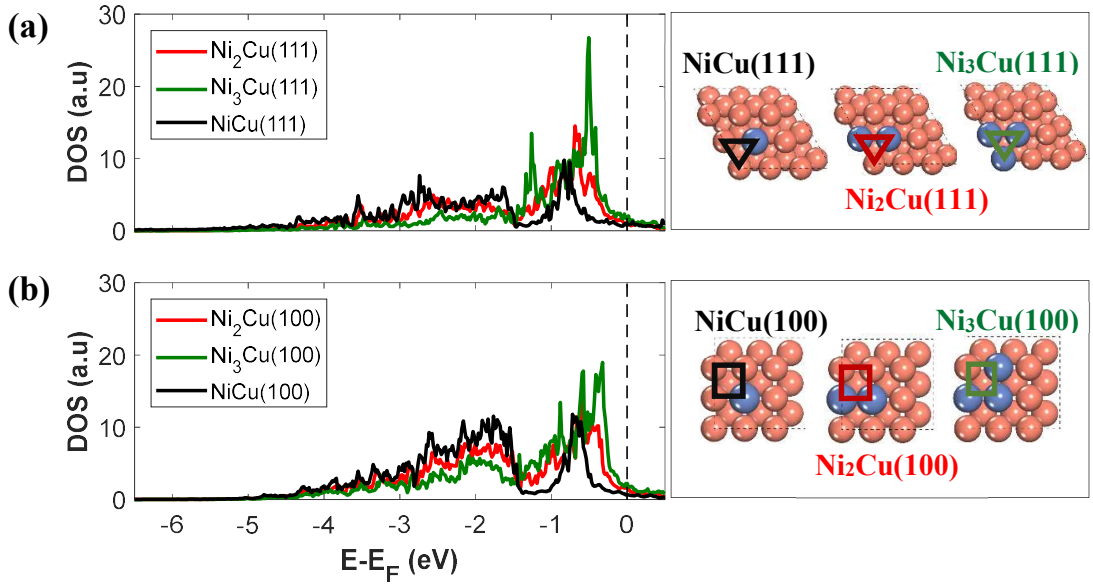

Figure 29. *d* DOS plots for the Ni/Cu SAA and dilute alloy (a) (111) and (b) (100) surfaces, whereby the DOS are projected onto the *d* states of the mixed active sites shown on the right inset of each DOS plot. The mixed active sites are highlighted in the same colours as those of the corresponding DOS curves.

Importantly, it is noted that the right DOS peaks of Ni_3Cu and Ni_2Cu exhibit higher intensity and are closer to the Fermi level than the corresponding peaks of the two SAA low–index surfaces (Figure 29). Along these lines, one may expect that electron back–donation from the mixed active site of the former surfaces to the antibonding orbitals of the adsorbates will be more pronounced compared to that on the Ni/Cu SAA surfaces. Charge transfer in this direction leads to the formation of dissociation precursors (e.g. during CO_2* dissociation),[158] and thus is a crucial process in bond breaking reactions. This observation explains the generally higher efficiency of small Ni clusters (i.e. dimers and trimers) than isolated Ni atoms in activating chemical bonds (Figure 27 (a) – (c)).

5.2.4. On the performance of Ni and Rh clusters in association reactions

Our discussion in the previous section implies that small Ni, and Rh to a smaller extent, clusters on Cu surfaces show promising performance in relation to the activation of chemical bonds. The next step is to examine the performance of the Rh_2Cu, Ni_2Cu and Ni_3Cu surfaces toward association reactions, which are often equally important to dissociation reactions. We focus on the reverse reactions to those presented in Figure 27, namely the formation of NO*, N_2* and CO_2*. Besides the aforementioned highly dilute alloy surfaces, we also investigate the performance of pure Cu, Ni and Rh surfaces, as these catalysts are the monometallic counterparts of the dilute alloys. Before proceeding to our results, we briefly discuss some fundamental principles with regard to association reactions. This discussion will help us in deciphering the observed trends in our simulation data.

In general, the barrier of an association reaction (e.g. A* + B* ↔ AB*) can be decomposed into terms that are associated with the geometric and electronic effects on the kinetic barrier as follows:[113]

$$E_a^{as} = E_{TS}^{as} - E_{IS}^{as} = \underbrace{\left(E_A^{TS} + E_B^{TS}\right) - \left(E_A^{IS} + E_B^{IS}\right)}_{Electronic\ effects} + \overbrace{E_{int}^{TS} - E_{int}^{IS}}^{Geometric\ effects}, \quad (74)$$

where , E_A^{TS}, E_B^{TS}, E_A^{IS} and E_B^{IS} and are the chemisorption energies of A and B in the TS and IS positions, respectively, E_{int}^{TS} and E_{int}^{IS} account for the interactions between the reactants A and B in the TS and IS, respectively.[171] The latter terms are often positive as a result of repulsive interactions between the two reactants.

The chemisorption energies in eq. (74) are strongly related to the local electronic environment (i.e. the position of the *d* band centre) of the surface whereon the reactant species are bound to. These terms may be considerably different for chemisorption on under–coordinated sites (e.g. steps, kinks) than for chemisorption on flat surfaces (e.g. sites on the (111) surface), and quantify the contribution of the electronic effects to the association barrier.[112] Importantly, a large number of association reactions, including these examined here, exhibit early TSs. In such cases, the IS structure closely

resembles the TS structure (e.g. see panels in Figure 28 in the reverse order), thereby rendering E_A^{TS} and E_B^{TS} similar to E_A^{IS} and E_B^{IS}, respectively. On this basis, it is generally true that the contribution of electronic effects to the structure sensitivity of association reactions is small,[112] but not necessarily negligible.

Furthermore, the contribution of the geometric effects to E_a^{as} is described by E_{int}^{TS} and E_{int}^{IS},[112] which quantify the interactions between the two reactants in the TS and in the IS. These interactions arise due to: (i) bonding competition effects;[172] and (ii) the direct Pauli repulsion between the reactant species.[113] The former effects are important when the reactants are bonded to the same metal atom in the TS and/or IS structures.[113] A good example is the activation of CH_4 over a Pt/Ag(111) SAA surface, where CH_3* and the activated H adatom share the top Pt site in the TS.[45] Accordingly, we expect that bonding competition effects will be alleviated for the NO*, N_2* and CO_2* formation reactions on Rh, Cu, Ni, Rh_2Cu Ni_2Cu and Ni_3Cu (100) and (111) surfaces, for which in the TS and IS, the reactants are located in different hollow sites and are not competing for the same metal top site (see Figure 30 (c)).

Regarding the direct Pauli repulsions, we note that these effects are important when the distance between the reactant species is less than 2.5 Å.[113] Within this range of distance there will be a direct overlap between the wave functions of the reactants.[3] Figure 30, panels (a) and (b) summarise these distances ($d_{A\text{-}B}$) for the three studied reactions on dilute and pure metal surfaces for the TS and IS structures, respectively. It is observed that for all the ISs $d_{A\text{-}B} > 2.5$ Å, while for all the TSs the opposite is true and in the vast majority of the cases $d_{A\text{-}B} < 2.0$ Å. Therefore, the magnitude of direct Pauli repulsions in the IS will be small, and E_{int}^{IS} in eq. (74) will be approximately zero.[112,113] Conversely, Pauli repulsions will be significant in the TSs and the magnitude of a computed association barrier will be heavily dependent on E_{int}^{TS}.

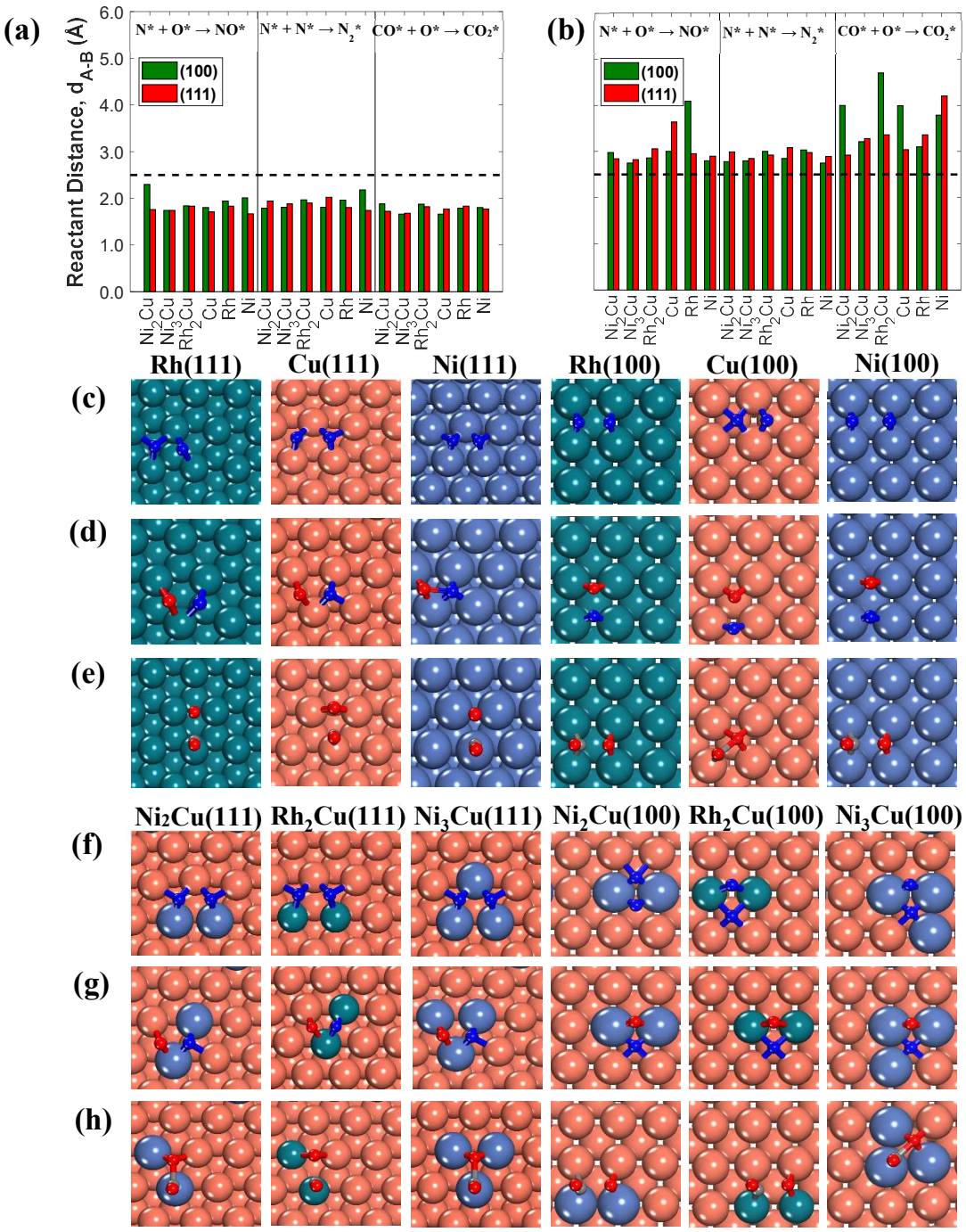

Figure 30. Reactant distances in the (a) TS and (b) IS structures for the three association reactions on the dilute alloy and pure metal (111) and (100) surfaces. The dashed line marks the 2.5 Å distance, below which Pauli repulsions become significant. Top view of the TS structures for the three reactions on the (111) and (100) pure metal surfaces (panels (c) – (e) for N_2, NO, CO_2, respectively) and dilute alloy surfaces (panels (f) – (h) for N_2, NO, CO_2, respectively). O, N and C atoms are shown by red, blue and grey, respectively. Ni, Cu and Rh atoms are shown in purple, orange and dark green, respectively.

Our computed barriers for the formation of N_2*, NO* and CO_2* are shown in Figure 31 (a), (b) and (c) from where one sees that these association reactions exhibit significant structure sensitivity.

This behaviour can be loosely attributed to the fact that, in many cases, the reaction intermediate species reside in high coordination sites (i.e. threefold and fourfold sites) – (Figure 30 (c) – (h)).[173] The lowest structure sensitivity is seen for the oxidation of CO*, where CO* and O* in the TS are always bound to low coordination sites (i.e. top and bridge sites) – (Figure 30 (e) and (h)).[173] Importantly, for all the association reactions, we observe that the Cu and dilute alloy surfaces follow the same trend by which the computed barriers on the (111) surfaces are lower than those of the corresponding (100) surfaces. The exact opposite trend is observed for Rh surfaces (Figure 31 (a), (b) and (c)). These trends are associated with the extent of the direct Pauli repulsions between the reactants in the TS on these surfaces (we discuss this in the following paragraphs).

Particular attention is paid to the formation of N_2* as this reaction is a crucial elementary step for the NO reduction by CO because of the following reasons: (i) this association reaction frees up active sites that can catalyse subsequent surface reactions; and (ii) it is the RDS for the NO + CO reaction at high temperatures.[159] The IS of this reaction involves two N adatoms on hollow sites, whilst in the FS, N_2* is vertically adsorbed on a top site.[149,174] In order to verify the reliability of our data, we compare our computed kinetic barrier on Rh(111) – (E_a = 1.84 eV) to the value reported by Ishikawa and Tateyama for the same reaction pathway of N_2 formation (E_a = 1.78 eV),[159] and we find a reasonable agreement.

Our simulations show that the N_2* association reaction proceeds with similar kinetic barriers on the Rh_2Cu(100), Ni cluster (100) – (i.e. Ni_2Cu & Ni_3Cu), Cu(100) and Rh(100) surfaces (Figure 31 (a)). These barriers are large, being within the range of 1.50 eV – 2.00 eV, and the lowest values are observed for Rh(100) and Ni_2Cu(100) (1.50 eV and 1.57 eV, respectively) – (Figure 31 (a)). We also find a very large association barrier on Ni(100) (E_a = 2.82 eV), whereon the formation of N_2 will be an extremely rare event.

Interestingly, the formation of N_2* is dramatically more facile on Ni e clusters, Rh–Rh dimers and Cu (111) surfaces as compared to the Rh(111) and Ni(111) surfaces. For example, the kinetic

barrier for the $Ni_2Cu(111)$ surface (E_a = 0.62 eV) is lower than that for Rh(111) (E_a = 1.85 eV) by 1.23 eV and that for Ni(111) (E_a = 1.54 eV) by 0.92 eV (Figure 31 (a)). This observation, along with the ability of Ni clusters to dissociate the N─O bond, and the relatively low CO* oxidation barriers of Cu surfaces (Figure 31 (c)), make us envision a bifunctional Ni/Cu alloy suitable for the reduction of NO. On this alloy catalyst, Cu atoms may be the active sites for the oxidation of CO*,[175] while Ni clusters will provide the sites for the N─O bond cleavage and the formation of N_2*.

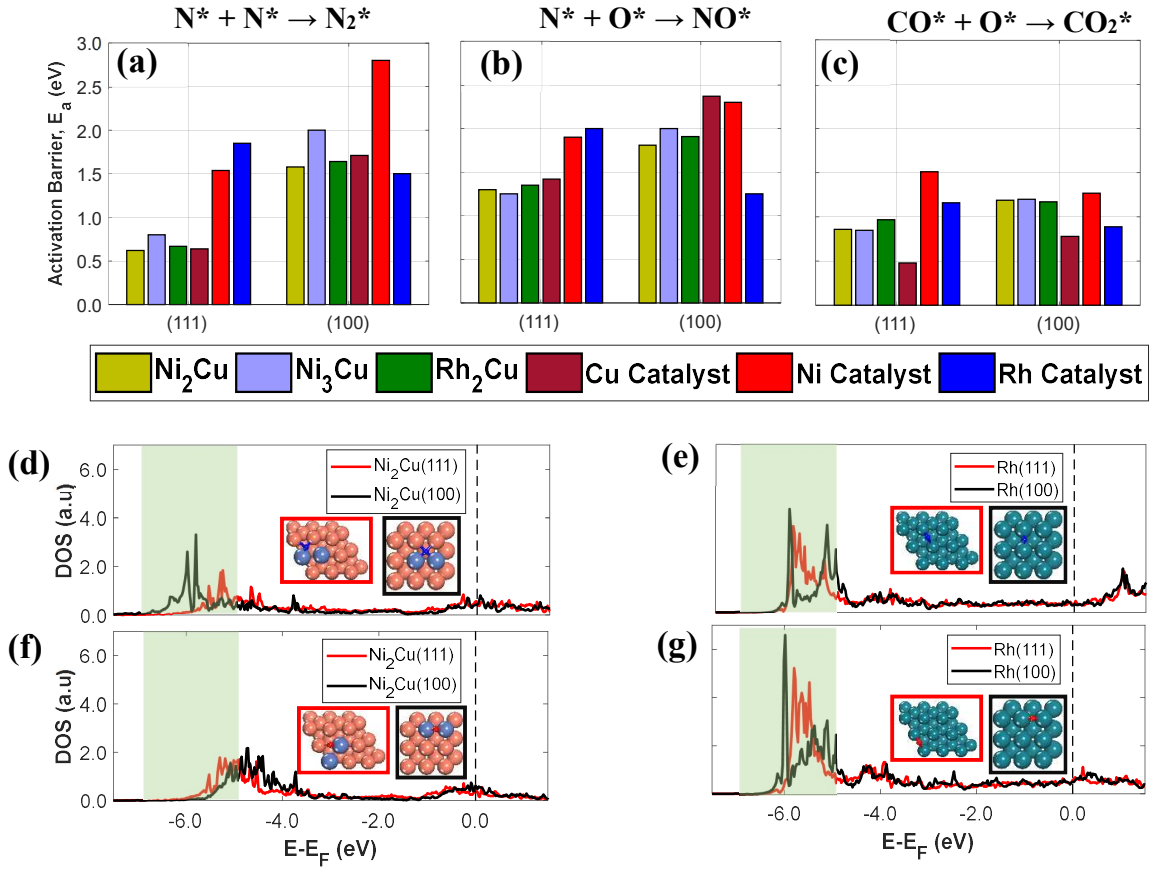

Figure 31. Computed barriers for the formation of (a) N_2; (b) NO and (c) CO_2 on different (100) and (111) dilute alloy and pure metal surfaces (colour coding shown in the legend below the bar charts). Panels (d) and (e) show the 2p–projected DOS of an N atom adsorbed on Ni_2Cu and Rh surfaces, respectively. Panels (f) and (g) show the 2p–projected DOS of an O atom adsorbed on Ni_2Cu and Rh surfaces, respectively. The insets in panels (d), (e), (f) and (g) show the top view of the DFT slabs where the positions of the adatoms (N and O) is highlighted. Cu, Ni, Rh, O and N atoms are shown in orange, purple, dark green, red and blue, respectively. The area shaded in green in panels (d), (e), (f) and (g) is the *p-d* bonding area.

As pointed out earlier, an interesting observation is that the kinetic barrier for the formation of N_2* for Rh(100) is lower than that for Rh(111) (i.e. $E_a(111) > E_a(100)$), while the opposite trend is true for the rest of the examined surfaces (i.e. $E_a(111) < E_a(100)$) – (Figure 31 (a)). This is true for the

other association reactions as well (Figure 31 (b) and (c)), namely bond formation is more facile on the most densely packed dilute alloy (111) surfaces (Ni_2Cu, Ni_3Cu and Rh_2Cu).

According to our previous discussion, the preponderant contribution to the computed association barriers stems from the direct Pauli repulsion between the reactants in the TS. Qualitative insights into the magnitude of the Pauli repulsion can be provided by the local DOS of the reactant species in the TS position.[113] To this end, we analyse the N 2*p*–projected DOS of a single N atom adsorbed on the same position as in the TS structure for the following four surfaces: $Ni_2Cu(111)$, $Ni_2Cu(100)$, Rh(111) and Rh(100) – (Figure 31 (b) and (c)). The former two surfaces are representative of the $E_a(111) < E_a(100)$ trend, while the latter two follow the $E_a(111) > E_a(100)$ trend. Our DFT calculations show that the TS position for the N* atom is near a bridge site for Rh(100), Rh(111) and $Ni_2Cu(111)$ surfaces and near a mixed 4–fold site for $Ni_2Cu(100)$ – (Figure 30 (c) and (f)).

The DOS plots are displayed in Figure 31 (d) and (e), and the main difference between the DOS curves is observed in the region between –7.0 eV and –5.0 eV; this is the region where the *p* orbitals of the N adatom mix with the *d* states of the catalytic surface (i.e. the *p–d* bonding region). We realise that the 2*p*–projected DOS in the *p–d* bonding region of the $Ni_2Cu(100)$ surface has much higher intensity and appears more localised than on the $Ni_2Cu(111)$ surface (Figure 31 (e)). Therefore, we expect a larger Pauli repulsion between the N adatoms on $Ni_2Cu(100)$ than on $Ni_2Cu(111)$, thereby explaining the large difference in the computed barriers (E_a = 1.57 eV and 0.62 eV for $Ni_2Cu(100)$ and $Ni_2Cu(111)$, respectively). Similarly, the N* 2*p*–projected DOS for Rh(111) and Rh(100) show an overall higher density of states in the *p–d* bonding region for the former surface than for the latter (the total areas below the DOS curves in the *p-d* bonding region are 1.62 for Rh(111) and 1.35 for Rh(100); Figure 31 (e)). However, in this case the intensity of the peaks is similar (Figure 31 (e)), and consequently there is no dramatic difference in the barriers exhibited by the two surfaces (E_a = 1.85 eV and 1.50 eV for Rh(111) and Rh(100), respectively).

The observed trends for the formation of NO* can be understood along the same lines as for the formation of N_2*. We find that for the former reaction $E_a(100) > E_a(111)$ on the three dilute alloy surfaces, and that the TS structures on both $Ni_2Cu(111)$ and $Ni_2Cu(100)$ facets involve an O adatom on a mixed bridge site (Figure 30 (g)). By analysing the 2*p*–projected DOS of the O adatom in the mixed bridge sites of the two aforementioned surfaces, we note that the DOS peaks in the *p*-*d* bonding area are similar in terms of intensity and width (Figure 31 (f)). This may be an indication that the observed differences between the barriers of the NO* formation on (111) and (100) dilute alloy surfaces arise largely from the disparate electronic structure of the N* atoms on these surfaces (Figure 31 (d)), and not from both reactants. Accordingly, the barrier differences between the (111) and (100) surfaces for the association of NO* are much smaller than that for the formation of N_2* (Figure 31 (a) and (b)). Finally, Figure 31 (g) shows the 2*p*–projected DOS of an O adatom on Rh(111) and Rh(100) surfaces. The O* DOS on Rh(111) exhibit a higher intensity and are more localised than the DOS for Rh(100), thereby explaining the $E_a(100) < E_a(111)$ trend in Figure 31 (b).

5.3. Concluding remarks

As a final remark, regardless of the showcased capability of Ni clusters to perform facile N_2* formation and N─O bond scission, we acknowledge that further studies are required to establish Ni/Cu dilute alloys as promising NO reduction catalysts. In particular, additional reaction steps that take place during the NO + CO reaction have to be examined (e.g. the formation of N_2O).[176–178] Moreover, in the presence of CO, the formation of harmful $Ni(CO)_4$ species is a common problem for Ni–based catalysts, and this would also have to be taken into account. Finally, KMC simulations, which account for adsorbate–adsorbate interactions, should be performed in order to unveil phenomena occurring at the mesoscale. This will also enable an accurate comparison between the Ni/Cu dilute alloy and currently employed metals in catalytic converters (Pd, Pt and Rh). Some of these factors are considered in the next chapter, while the rest could be future research.

Chapter 6

6. The decomposition of N_2O and the NO + CO reaction over Ni/Cu dilute alloys

A key conclusion of the previous chapter was that bond cleavage reactions exhibit reduced structure sensitivity on low–index facets that prevail on NPs of fcc metals. This result implies that studies over the (111) SAA facet may give insight into the behaviour of the (100) SAA facet, and vice versa, thereby accelerating the development and design of optimal SAA catalysts. Additionally, the presented screening study revealed the potential of Ni/Cu dilute alloys, whereby Ni atoms form small clusters, for the NO + CO reactions. The catalytic reduction of NO by CO is a crucial reaction for controlling automobile emissions, and Rh is underlined as the most promising PGM for this reaction.[179] By and large, this is because Rh can activate the N─O bond at relatively low temperatures,[46,157,180] and also because of its high resistance to common poisons (e.g. sulphur).[181] Therefore, Rh is extensively used in the automobile three–way catalysts (TWCs), whereon noxious gases (nitrogen oxides (NO_x), CO, unburned hydrocarbons) are converted into environmentally benign products (e.g. N_2). Yet, there are two important shortcomings in relation to Rh: (1) it is very expensive; and (2) it is scarce.[179] Unsurprisingly, these downsides have turned the attention of the catalysis community into the search of TWCs that are either PGM–free[182–191] or utilise minimal amounts of PGMs.[42,192–194] The present chapter contributes to these efforts by investigating the performance of Ni/Cu(111) dilute alloys for the catalytic reduction of NO by CO. As the formation and decomposition of nitrous oxide (N_2O) are parts of the NO + CO reaction, we begin by studying these reaction steps by means of DFT. Then, the obtained energetics are used to parametrise a microkinetic model for the entire NO + CO reaction. Along with the Ni/Cu dilute alloys, the aforementioned reactions are also modelled on Cu(111) (i.e. the host metal surface), as well as on Rh(111), which is used for benchmarking. *The contents of this chapter have been published in Catal. Sci. Technol., 2021.*[195]

6.1. Computational details

The DFT setup for the calculations of this chapter is identical to the one employed in the previous chapter (see section 5.1). The microkinetic model for the NO + CO reaction included 16 reaction steps for Cu(111), Ni/Cu(111) single atom alloy (SAA), and $Ni_2Cu(111)$ surfaces and 14 reaction steps for Rh(111) – (see Table 3). On the monometallic surfaces there was only one site type, while in the bimetallic surfaces there were Cu and Ni sites, denoted as Cu* and Ni*, respectively. Therefore, for the latter surfaces, we define the "local" coverages as follows:

$$\theta_i^{(m)} = \frac{N_i^{(m)}}{N_{sites}^{(m)}}, \tag{75}$$

where $N_i^{(m)}$ is the number of molecules of adsorbate species *i* that are bound to sites of type *m* (either Cu* or Ni*); and $N_{sites}^{(m)}$ is the number of sites of type *m*. We further define the *total* coverage of adsorbate *i*, θ_i, as:

$$\theta_i = \sum_{m=1}^{N_{st}} x_m \theta_i^{(m)}, \tag{76}$$

where N_{st} is the total number of site types; the summation index *m* runs over these site types (for the bimetallic surfaces the two types are: Cu* and Ni*; for monometallic surfaces there is only one site type which can be either Cu* or Rh*); and x_m is the fraction of sites *m* on the surface, given as:

$$x_m = \frac{N_{sites}^{(m)}}{\sum_{1=1}^{N_{st}} N_{sites}^{(1)}}. \tag{77}$$

All reactions were considered reversible, and the forward/reverse rates were given by the typical mass–action law expressions used in microkinetic models, which contain the partial pressures of gas–phase species (considered as constants) and the surface coverages. The gas–phase species taken into account were NO, CO, N_2, CO_2, N_2O, while the surface species were O*, CO*, N*, NO*, CO_2*, N_2* and N_2O*, as well as the vacant site pseudo–species denoted as *. Regarding the N_2O* species, three different

adsorption geometries were taken into account (see the next section). The transitions from one adsorption geometry to another could happen through *transformation reactions* that were included in the reaction mechanism (see R10 – R11 in Table 3). The forward rate for reaction *j* on site–type *m* is formulated as follows:

$$R_{fwd,j}^{(m)} = k_{fwd,j}^{(m)} \prod_{g \in \mathrm{R}_j^{gas}} \left(P_g\right)^{-\nu_{gj}} \prod_{i \in \mathrm{R}_j^{surf}} \left(q_i^{(m_{ij})}\right)^{-\nu_{ij}} . \tag{78}$$

In the above equation, R_j^{gas} is the set of gas–phase reactant species of reaction *j*; P_g is the partial pressure of gas species *g*; and ν_{gj} is the stoichiometric coefficient of that gas phase species in reaction *j*. By convention, stoichiometric coefficients are negative for reactants and positive for products; if a species does not appear in a certain reaction, the corresponding stoichiometric coefficient is zero. Moreover, R_j^{surf} is the set of surface reactant species of reaction *j*; ν_{ij} is the stoichiometric coefficient of that surface species *i* in reaction *j*; and $q_i^{(m_{ij})}$ is the local coverage of surface species *i* on sites of type m_{ij}. The latter term may or may not be equal to *m*, since, a reaction that is said to happen on site *m* (e.g. Ni*), may well involve another species adsorbed on a neighbouring site type (e.g. Cu*). For instance, when reaction R9 of Table 3 (NO* + N* ↔ N_2O* $\eta 2NbNt$ + *) happens on a Ni site, NO* is found on the Ni site, while N* is on Cu; therefore, the rate would be:

$R_{fwd,9}^{(\mathrm{Ni}^*)} = k_{fwd,j}^{(\mathrm{Ni}^*)} q_{\mathrm{NO}^*}^{(\mathrm{Ni}^*)} q_{\mathrm{N}^*}^{(\mathrm{Cu}^*)}$.

For further information on the considered reactant configurations for events that involve two sites see Appendix III. Similarly, the reverse rate for reaction *j* on site–type *m* is formulated as follows:

$$R_{rev,j}^{(m)} = k_{rev,j}^{(m)} \prod_{g \in \mathrm{P}_j^{gas}} \left(P_g\right)^{\nu_{gj}} \prod_{i \in \mathrm{P}_j^{surf}} \left(q_i^{(m_{ij})}\right)^{\nu_{ij}} . \tag{79}$$

Note that P_j^{gas} and P_j^{surf} denote sets of products of reaction *j*, and the stoichiometric coefficients appear with their "original" positive signs, because of the convention mentioned earlier.

The rate constant calculations for the surface reactions ($k_{fwd,j}^{(m)}$ and $k_{rev,j}^{(m)}$) are calculated after invoking the widely used transition state theory approximations. If a reaction cannot happen on a certain site, then $k_{fwd,j}^{(m)} = k_{rev,j}^{(m)} = 0$. We further define the net rate of reaction *j* on site *m* as:

$$R_j^{(m)} = R_{fwd,j}^{(m)} - R_{rev,j}^{(m)} . \tag{80}$$

The coverage profiles over the investigated surfaces can now be obtained by solving a system of ordinary differential equations (ODEs) written as

$$\frac{dq_i^{(m)}}{dt} = \sum_{j=1}^{N_R} v_{ij} R_j^{(m)} \ , \tag{81}$$

where N_R is the total number of (reversible) reactions. The ODEs were solved in Matlab R2017a, using the ode23s solver, which is capable of dealing with stiff equations. An important constraint that had to be satisfied is the *site conservation law*

$$\sum_{i=1}^{N_s} \sum_{m=1}^{N_{st}} x_m q_i^{(m)} = 1. \tag{82}$$

To calculate the rate constants of the reactions the following assumptions and approximations were adopted. Molecular adsorptions were assumed as non–activated events with a 2D gas as a transition state, where molecules retain translational and rotational degrees of freedom. Accordingly, the rate constants for molecular adsorptions were calculated using the Hertz–Knudsen equation assuming a sticking coefficient equal to unity (eq. (83)):[196]

$$k_{ads} = \frac{A_{st}}{\sqrt{2 \cdot \pi \cdot m_i \cdot k_B \cdot \mathrm{T}}}, \tag{83}$$

where m_i is the mass of molecule *i*; *T* is the temperature; and A_{st} is the effective area of the adsorption site. The pressure of gas phase–species is omitted in eq. (83) because it is explicitly taken into account in eq. (78) and eq. (79). The rate constants for surface reactions and desorption events were calculated using the Eyring equation:

$$k_{j^{+}/_{-}} = \frac{k_B \mathrm{T}}{h} \frac{\mathrm{Q}^{\mathrm{TS}}}{\mathrm{Q}^{\mathrm{IS}}} \exp\left(-\frac{E_a}{k_b \mathrm{T}}\right), \tag{84}$$

where h is the Planck's constant; Q^{TS} and Q^{IS} are the partition functions of the transition and initial states, respectively. The rate constants of surface reactions were calculated using the harmonic approximation, and therefore frustrated translations and rotations of surface species were treated as vibrations; under these circumstances, the partition function of an adsorbed state (either initial or transition state) is equal to the vibrational partition function (q_{vib}):

$$Q \approx q_{vib} = \prod_{k=1}^{S} \frac{e^{-\hbar\omega_k / 2k_b T}}{1 - e^{-\hbar\omega_k / k_b T}}, \tag{85}$$

where S is the number of vibrational modes; ω_k is the angular frequency of the k^{th} normal mode of vibration; and $\hbar$ is the reduced Planck's constant.

The net rates for N_2 and N_2O are calculated as follows:

$$R_{N_2,net} = \sum_{m=1}^{N_{st}} R_{\mathrm{R}\,3,net}^{(m)}, \tag{86}$$

$$R_{N_2O,net} = \sum_{j=R5}^{R7} \sum_{m=1}^{N_{st}} R_{j,net}^{(m)}, \tag{87}$$

where $R_{j,net}^{(m)}$ is the net reaction rate of j on site m. Finally, the contribution of each elementary step to the total reaction rate was quantified using Campbell's degree of rate control (DRC) – (see eq. (88)):[197,198]

$$X_{RC,j}^{(m)} = \frac{k_j^{(m)}}{R_{N_2,net}} \left(\frac{\partial R_{N_2,net}}{\partial k_j^{(m)}}\right)_{K_\ell^{(n)}, k_{\ell\neq j}^{(n\neq m)}} = \left(\frac{\partial \ln R_{N_2,net}}{\partial \ln k_j^{(m)}}\right)_{K_\ell^{(n)}, k_{\ell\neq j}^{(n\neq m)}}, \tag{88}$$

where $X_{RC,j}^{(m)}$ is the DRC coefficient for reaction j on site m; $R_{N_2,net}$ is the net reaction rate for the production of N_2 (eq. (86)) on site m (eq. (80)); $K_\ell^{(n)}$ is the equilibrium constant of reaction ℓ=1,…,N_R on site m = 1,…,N_{st}; $k_{\ell\neq j}^{(n\neq m)}$ are the rate constants for all other steps than j that take place on either Cu*

or Ni* (the site other than *m*). The larger the absolute value of $X_{RC,j}^{(m)}$ the larger the influence of that reaction step to the overall reaction rate; also when $X_{RC,j}^{(m)} > 0$, the reaction is rate–limiting, whereas for $X_{RC,j}^{(m)} < 0$ the reaction is an inhibition step.

6.2. Results and discussion

6.2.1. Adsorption of N_2O on Ni/Cu dilute alloy surfaces

N_2O is a linear molecule ($C_{\infty V}$ symmetry) with an N─N bond between a central N atom (N_c) and a terminal N atom (N_t), and an N_c─O bond. The optB86b–vdW-computed N─O and N─N bond lengths are 1.20 Å and 1.14 Å, respectively, and these values are in excellent agreement with the experimentally determined bond distances (~1.18 Å and ~1.13 Å for N─O and N─N, respectively).[199] Gas–phase nitrous oxide is a harmful by–product of industrial processes (e.g. nitric acid production), and its catalytic decomposition has been investigated over many transition metals, including Rh,[200] Cu,[178] Ru,[201] Pd,[202] Fe,[203] Ni,[204] Pt,[176] PdAu,[205] and PdCu.[206] Here, we begin by examining the adsorption of nitrous oxide on Cu(111), Ni/Cu(111) SAA and Ni_2Cu(111) surfaces, but also on our "benchmarking surface" Rh(111). It is known that N_2O* may adopt a number of different adsorption geometries upon its interaction with metal surfaces.[177,202] Accordingly, we identify six stable adsorption geometries, out of which one is linear and perpendicular to the surface, whilst in the other five, N_2O* undergoes considerable distortion compared to N_2O in the gas phase. These structures are denoted as: *η1*–(N_t{top}), *η2*–f(N_t{bridge},N_c{top}), *η2*–h(N_t{bridge},N_c{top}), *η2*–(N_t{top},N_c{top}), *η2*–(N_t{top},O{top}), and *η2*–(N_t{hcp},O{top}); their side and top views are shown in Figure 32 (a) – (f). From those adsorption structures, *η1*–(N_t{top}) is the only one where N_2O* is bonded to the catalytic surfaces through only one atom. Regarding the *η2* structures, we note that the adopted geometries in *η2*–f(N_t{bridge},N_c{top}) and *η2*–h(N_t{bridge},N_c{top}) are virtually identical. The only difference is that in the former, nitrous oxide lies over an fcc hollow site, while in the latter it lies over an hcp site. Moreover, the *η2*–(N_t{top},O{top}) structure is known to be the

precursor state for adsorbed N_2 and atomic oxygen.[177] Since we will be referring often to the *η1*–(N_t{top}), *η2*–f(N_t{bridge},N_c{top}) and *η2*–(N_t{top},O{top}) structures throughout this paper, we adopt the following abbreviations for them: *η1*, *η2NbNt* and *η2NtOt*, respectively.

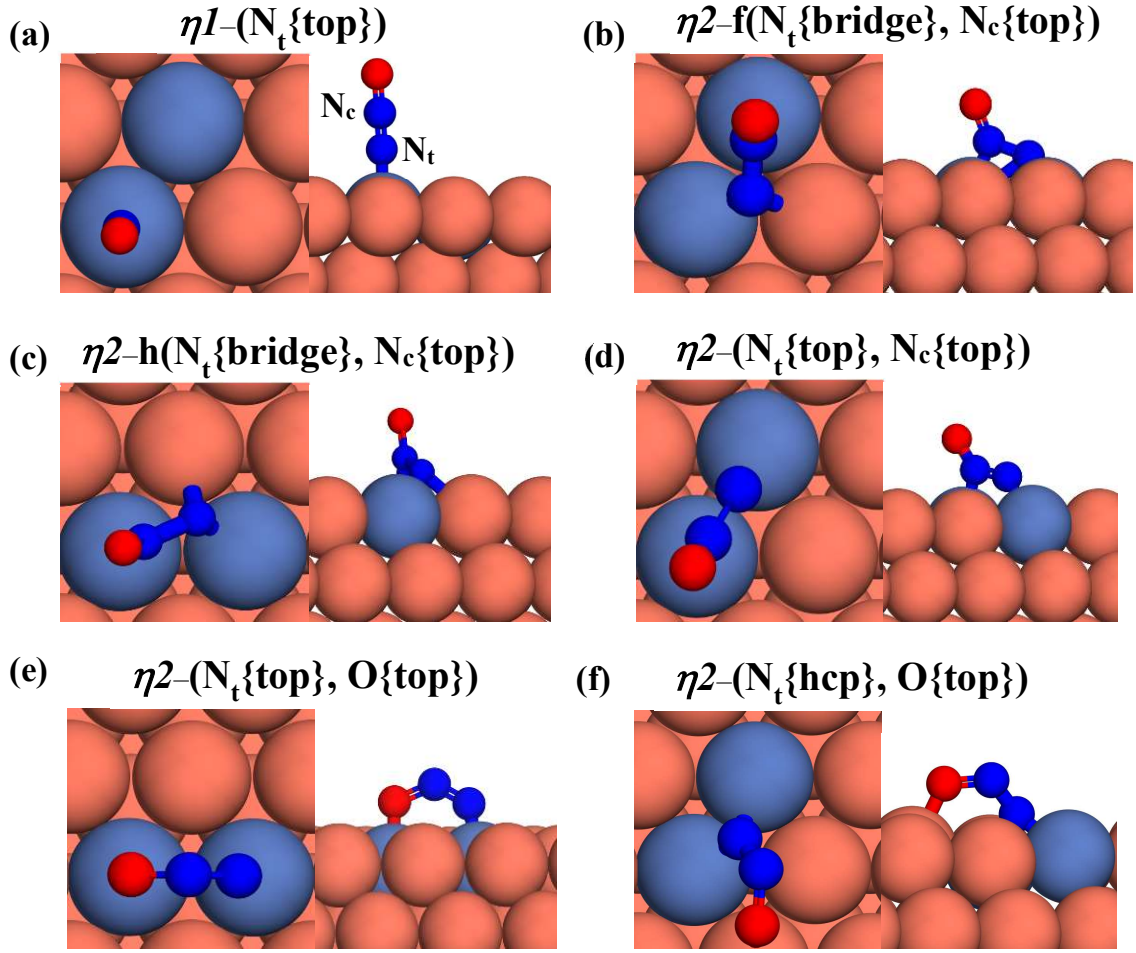

Figure 32. Top and side views of (a) *η1*–(N_t{top}); (b) *η2*–f(N_t{bridge},N_c{top}); (c) *η2*–h(N_t{bridge},N_c{top}); (d) *η2*–(N_t{top},N_c{top}); (e) *η2*–(N_t{top},O{top}) and (f) *η2*–(N_t{hcp},O{top}) adsorption structure. On the side view of (a) we highlight the terminal (N_t) and central (N_c) nitrogen atoms. Ni, Cu, N and O atoms are shown in purple, orange, blue and red, respectively. The adsorption geometries are shown over $Ni_2Cu(111)$, but they are representative for all surfaces.

The computed adsorption energies for the considered geometries, along with the N─O ($d_{N\text{-}O}$) and N─N ($d_{N\text{-}N}$) bond distances are summarised in Table 2. We note that there are two most preferred N_2O* adsorption structures on Rh(111): the *η2NbNt* mode ($E_{ads}(N_2O)$ = -0.83 eV), and the equally stable *η2*–h(N_t{bridge},N_c{top}); in the latter, N_2O* adopts the same structure as *η2NbNt,* but over an hcp hollow site (Table 2). This type of adsorption can be considered as a weak chemisorption

because: (1) the geometry of N_2O* deviates noticeably from the gas–phase geometry; and (2) because the N─N bond is considerably elongated ($d_{N\text{-}N}$ = 1.14 Å and 1.35 Å for gas-phase N_2O and *η2NbNt* N_2O*, respectively). The following most stable adsorption structures are the *η1* and *η2NtOt* with $E_{ads}(N_2O)$ = -0.71 eV and $E_{ads}(N_2O)$ = -0.72 eV, respectively. The former structure can be characterised as a strong physisorption owing to the unaffected geometry and bond lengths of *η1* N_2O* as compared to gas–phase N_2O.

The activation of the N─N bond in the *η2NbNt* structure can be elucidated by careful examination of the electronic structure of this geometry (Figure A9).[177] Our DOS analyses indicate that in *η2NbNt* the *2π* and *3π* orbitals of N_2O* become broader as a result of their interaction with the metal states, whilst the same is not true for the *η1* structure where the same orbitals appear rather localised (Figure A9). The broadening of the *3π* orbitals is indicative of electron back–donation, which in turn leads to the activation of the N─N bond. This result is in qualitative agreement with the work of Paul et al.[177] where the authors, by means of DFT calculations using the PW91 functional, found that the *η2NbNt* and *η1* are ca. equally stable on Rh(111) ($E_{ads}(N_2O)$ = -0.35 eV and $E_{ads}(N_2O)$ -0.39 eV, respectively). Moreover, our calculations suggest that N_2O* is bound stronger by ca. 0.5 eV on Rh(111) compared to the work of Paul et al.[177] This, however, should come as no surprise as recent studies by Ishikawa and Tateyama have shown that the inclusion of dispersion forces in DFT calculations may increase the binding strength of loosely bound adsorbates of the NO + CO reaction (i.e. N_2O*, CO_2*) by as much as 0.7 eV.

We proceed by investigating the adsorption of N_2O* over Cu(111) and the Cu–based alloy surfaces. We find that N_2O* interacts weakly with Cu(111) (Table 2), and that the most stable adsorption geometries thereon are *η2*–(N_t{hcp},O{top}) and *η1* for which $E_{ads}(N_2O)$ = -0.25 eV and -0.21 eV, respectively. This small binding strength suggests that N_2O* desorption from the Cu(111) surface will be likely happening before its decomposition, thereby reducing the selectivity of this surface toward N_2 during the NO + CO reaction. This observation is in line with previous studies,[178]

and is discussed in greater detail in the next section. Furthermore, adsorption in the *η2NtOt* configuration is exothermic with $E_{ads}(N_2O)$ = -0.19 eV, while the rest of the *η2* adsorptions are endothermic (Table 2).

Table 2. Adsorption energies (in eV) and bond distances (in Å) for the different N_2O* adsorption geometries over the investigated surfaces. The adsorption energies and bond distances that correspond to the most stable adsorption structure(s) for each surface are shown in bold. A dash indicates either that the adsorption structure is not stable on the specific surface or that it is not a minimum on the potential energy surface (i.e. there was an imaginary frequency in the vibrational analysis). For comparison: $d_{N\text{-}N}$ = 1.14 Å and $d_{N\text{-}O}$ = 1.20 Å for gas N_2O.

Adsorption Structure	Property	Rh(111)	Cu(111)	Ni/Cu(111) SAA	Ni_2Cu(111)
η1–(N_t{top}) (denoted as ***η1***)	$E_{ads}(N_2O)$	-0.71	-0.21	**-0.70**	-0.68
	$d_{N\text{-}O}$	1.20	1.20	**1.20**	1.21
	$d_{N\text{-}N}$	1.15	1.15	**1.15**	1.15
η2–f(N_t{bridge},N_c{top}) (denoted as ***η2NbNt***)	$E_{ads}(N_2O)$	**-0.83**	+0.15	-0.43	**-0.74**
	$d_{N\text{-}O}$	**1.22**	1.23	1.23	**1.23**
	$d_{N\text{-}N}$	**1.35**	1.29	1.29	**1.31**
η2–h(N_t{bridge},N_c{top})	$E_{ads}(N_2O)$	**-0.83**	+0.15	-0.41	-0.73
	$d_{N\text{-}O}$	**1.22**	1.23	1.23	1.23
	$d_{N\text{-}N}$	**1.36**	1.29	1.28	1.30
η2–(N_t{top},N_c{top})	$E_{ads}(N_2O)$	-0.72	+0.27	–	-0.62
	$d_{N\text{-}O}$	1.25	1.23	–	1.24
	$d_{N\text{-}N}$	1.26	1.22	–	1.25
η2–(N_t{top},O{top}) (denoted as ***η2NtOt***)	$E_{ads}(N_2O)$	-0.71	-0.19	-0.53	-0.68
	$d_{N\text{-}O}$	1.33	1.28	1.30	1.32
	$d_{N\text{-}N}$	1.20	1.19	1.20	1.20
η2–(N_t{hcp},O{top})	$E_{ads}(N_2O)$	–	-0.25	-0.44	-0.75
	$d_{N\text{-}O}$	–	1.30	1.31	1.32
	$d_{N\text{-}N}$	–	1.27	1.25	1.27

Interestingly, we note that the presence of a small amount of Ni on the surface layer of Cu(111) brings about drastic changes with regard to the binding strength of N_2O* (Table 2). Thus, the most stable adsorption geometry on the Ni/Cu(111) SAA surface is *η1* ($E_{ads(N_2O)}$ = -0.70 eV), where the N_t atom of N_2O* interacts closely with the isolated Ni atom. By contrast, the *η2NbNt* and *η2*–(N_t{hcp},O{top}) are the most favourable adsorption modes for $Ni_2Cu(111)$, with $E_{ads(N_2O)}$ = -0.74 eV and $E_{ads(N_2O)}$ = -0.73 eV,respectively. Crucially, the corresponding adsorption processes are about 0.5 eV more exothermic than the *η1* and *η2*–(N_t{hcp},O{top}) modes on Cu(111), thereby highlighting the potential of the Ni/Cu dilute alloys for the decomposition of N_2O*. With this in mind, we examine the latter reaction over Cu(111) and the Cu–based surfaces.

6.2.2. N_2O* formation and activation on Cu–based surfaces – the "conventional" reaction path

In order to verify the reliability of our data, we first perform calculations in relation to the activation of N_2O* on the Rh(111) surface, and compare our results to those reported in previous theoretical works. The computed reaction pathway for the decomposition of N_2O* to either N_2* + O* or NO* + N* is displayed in Figure A10 in Appendix III. In this "conventional" reaction pathway the transformation of NO* + N* to N_2* + O* proceeds via the *η1* adsorption structure (Figure A10), and our computed activation barriers are congruent with previously calculated values. For example, Paul et al.[177] reported an activation barrier of 0.34 eV for the transformation of the *η2NtOt* structure to the *η1* structure; this number is in good agreement with our computed barrier (E_a = 0.38 eV from state (4) to state (3) in Figure A10). Another example is the required barrier for the decomposition of the *η2NbNt* (state (1) in Figure A10) structure to NO* + N*. The values for this work and ref. [177] are 0.36 eV and 0.41 eV, respectively. Consequently, we use our computational setup and study the decomposition of N_2O* on Cu(111), Ni/Cu(111) SAA and $Ni_2Cu(111)$ surfaces.

Figure 33 (a) shows the "conventional" decomposition pathway for Cu(111), where the *η1* structure "connects" the NO* + N* and N_2* + O* states. During the NO + CO reaction, the

combination of NO* and N* species may result in the formation of N_2O*, which ideally should be decomposed to N_2* + O*. Once formed, N_2O* adopts the *η2NbNt* structure, and starting from this geometry on Cu(111) (state (1) in Figure 33 (a)), we realise that the formation of N_2* and O* is thermodynamically and kinetically favoured over the formation of NO* and O*. In particular, the decomposition of *η2NbNt* N_2O* to NO* + O* requires the traversing of a barrier of 0.94 eV, while the three barriers to be traversed for the formation of N_2* + O* are only 0.14 eV, 0.06 eV and 0.06 eV. Yet, we conjecture that Cu(111) will be susceptible to the production of N_2O during the NO + CO reaction. This is because of the following reasons: (1) N_2O* can be formed from NO* and N* species with a relatively small kinetic barrier of 0.44 eV (Figure 33 (a)); once N_2O* is formed from NO* and N* in the *η2NbNt* structure (state (1) in Figure 33 (a)), its desorption is the most probable scenario (Table 2); and (3) even in the *η1* and *η2NtOt* geometries, N_2O* binds weakly on Cu(111) and its desorption will be proceeding at considerable rates even at moderate reaction temperatures.

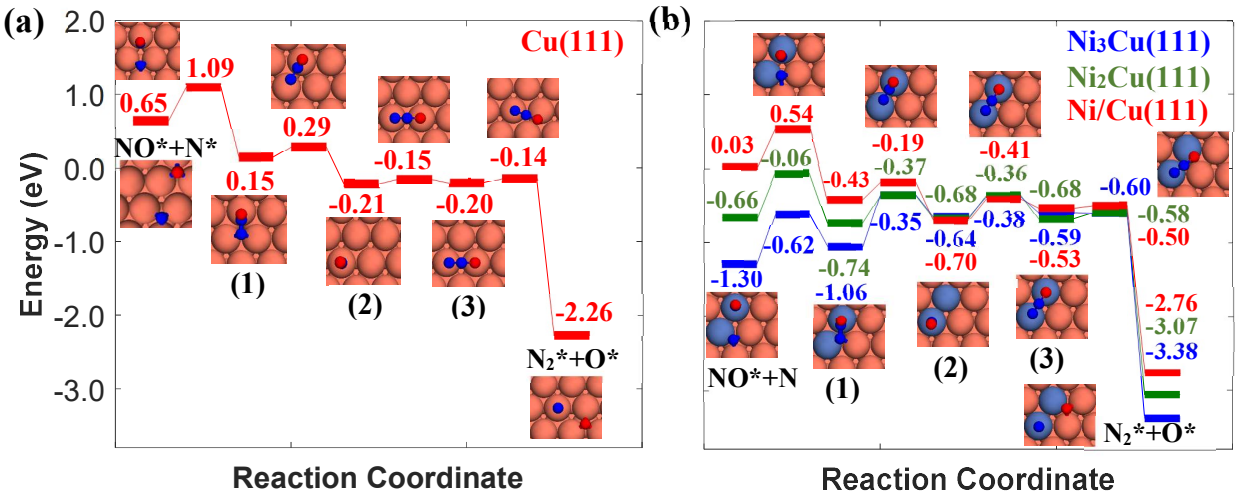

Figure 33. Reaction path for the decomposition of N_2O* to NO* + N* or N_2* + O* over (a) Cu(111) surface; (b) Ni/Cu(111) SAA, $Ni_2Cu(111)$ and $Ni_3Cu(111)$ surfaces. The numbering of the adsorbed configurations of N_2O is as follows: (1) *η2NbNt*, (2) *η1* and (3) *η2NtOt*. The zero level corresponds to infinitely separated (and thus non–interacting) N_2O molecule and clean slab. States without any labelling are transition states. Side views of the different states are shown in Appendix III (Figure A13). Ni, Cu, O and N atoms are shown in purple, orange, red and blue, respectively.

On the contrary, we find that the decomposition of N_2O* may be significantly promoted by embedding one or two Ni atoms on Cu(111), thereby forming a single atom alloy or a dilute alloy

surface. The computed desorption energies for *η2NbNt* N_2O* (state (1) in Figure 33 (b)) on Ni/Cu(111) SAA and Ni_2Cu(111) are 0.43 eV and 0.74 eV, respectively. By considering this adsorption structure as the starting point, we note that the transformation of N_2O* to structure *η1* (i.e. state (2)) and *η2NtOt* (i.e. state (3)), and the decomposition of the latter to N_2* + O would generally traverse small barriers, which are always less than 0.30 eV and 0.40 eV for Ni/Cu(111) SAA and Ni_2Cu(111), respectively. Thus, *η2NbNt* N_2O* (state (1)) would prefer to decompose to N_2* + O*, than desorb to the gas phase.

The exothermic adsorption of *η2NbNt* N_2O* (i.e. the first adopted structure after N_2O* formation from NO* and N*) will, to certain extent, prevent the N_2O* desorption to the gas phase. This will increase the probability of "trapping" N_2O* to the catalyst surface and therefore the probability for its decomposition. Moreover, even stronger *η2NbNt* N_2O* binding should be expected on Ni–Ni dimers and Ni single atoms that are embedded on more open surfaces than the densely packed (111) and on under–coordinated sites that can be found in catalytic nanoparticles.

Another point that merits consideration is that the selectivity toward the decomposition products (NO* + N* or N_2* + O*) can be altered by tuning the size of the Ni cluster. To better illustrate this point, we present the corresponding N_2O* decomposition pathway over a Cu(111) with an embedded Ni trimer (Ni_3Cu(111) in Figure 33 (b)). Interestingly, the kinetic barrier for the formation of the *η2NbNt* geometry (state (1) in Figure 33 (b)) from NO* and N* increases monotonically at increasing size of the Ni cluster (E_a = 0.51 eV, 0.60 eV and 0.68 eV for Ni/Cu(111) SAA, Ni_2Cu(111) and Ni_3Cu(111), respectively). The opposite is true for the reverse reaction (i.e. *η2NbNt* N_2O* to NO* + N*) for which E_a = 0.97 eV, 0.68 eV and 0.44 eV for Ni/Cu(111) SAA, Ni_2Cu(111) and Ni_3Cu(111), respectively. This result underlines the importance of developing ways to control the architecture of dilute alloy surfaces.

6.2.3. N_2O formation and activation on Cu–based surfaces – an alternative reaction path

Besides the "conventional" route for the decomposition of N_2O* (Figure 33), we have identified an alternative reaction pathway which, to the best of our knowledge, has not been reported

before. This path exists only on Cu(111) and on the Ni/Cu dilute alloy surfaces. The decomposition of N_2O* to N_2* + O* happens without transformation to the *η1* structure as in the conventional pathway. In contrast, in this pathway the two decomposed states (i.e. NO* + N* and N_2* + O*) are "connected" *via* an *η2*-(N_t{fcc},O{top}) adsorption structure (this is as Figure 32 (f) but over an fcc site; the two adsorption structures exhibit the same binding strength – $E_{ads(N_2O)}$ = -0.74 eV for $Ni_2Cu(111)$). After performing a number of test simulations, we could not identify the same path on Rh(111), and this might explain why it was not reported in previous studies.[177]

For all the Cu–based surfaces, Figure 34 shows that *η2NbNt* N_2O* is formed in the same way as in the reaction path of Figure 33. Then the *η2NbNt* N_2O* rotates around the axis of the N─N bond, thereby bringing the more electronegative O closer to the surface. Interestingly, once O is closer to the Ni/Cu(111) SAA, the N─O bond is immediately cleaved and the kinetic barrier for this process is only 0.23 eV (Figure 34 (b)). The ease by which the N─O is broken over the Ni/Cu SAA surface may be associated with the sharp and narrow distribution of the electron density of the single Ni atom close to the Fermi level (see section 5.2.1), and it is expected that back–donation to the *3π* antibonding orbital of N_2O* enables the facile activation of the N─O bond.

By contrast, the decomposition of N_2O* to N_2* and O* is taking place through the *η2*–(N_t{fcc},O{top}) geometry (state (2) and (3) in Figure 34 (a) and (c), respectively) over Cu(111) and $Ni_2Cu(111)$. The intervening barriers between the *η2NbNt* and N_2* + O* states are small (≤ 0.23 eV). Irrespective of these low kinetic barriers, Cu(111) is still expected to be prone to releasing N_2O* to the gas phase given the generally weak N_2O*–Cu(111) interaction (Figure 34 (a)). The same is not true for $Ni_2Cu(111)$ where the N_2O* desorption energy is in the range of 0.65 eV – 0.74 eV, while the kinetic barriers that lead to N_2* + O* are between 0.06 eV and 0.23 eV (Figure 34 (c)). Given the similar energetics between the pathway of Figure 34 and the "conventional" one, we conclude that both of them need to be considered in the reaction mechanism of the NO + CO reaction. Importantly,

the existence of alternative N_2O^* decomposition paths may provide an explanation of the high selectivity to N_2 exhibited by dilute Cu–based alloys.[42]

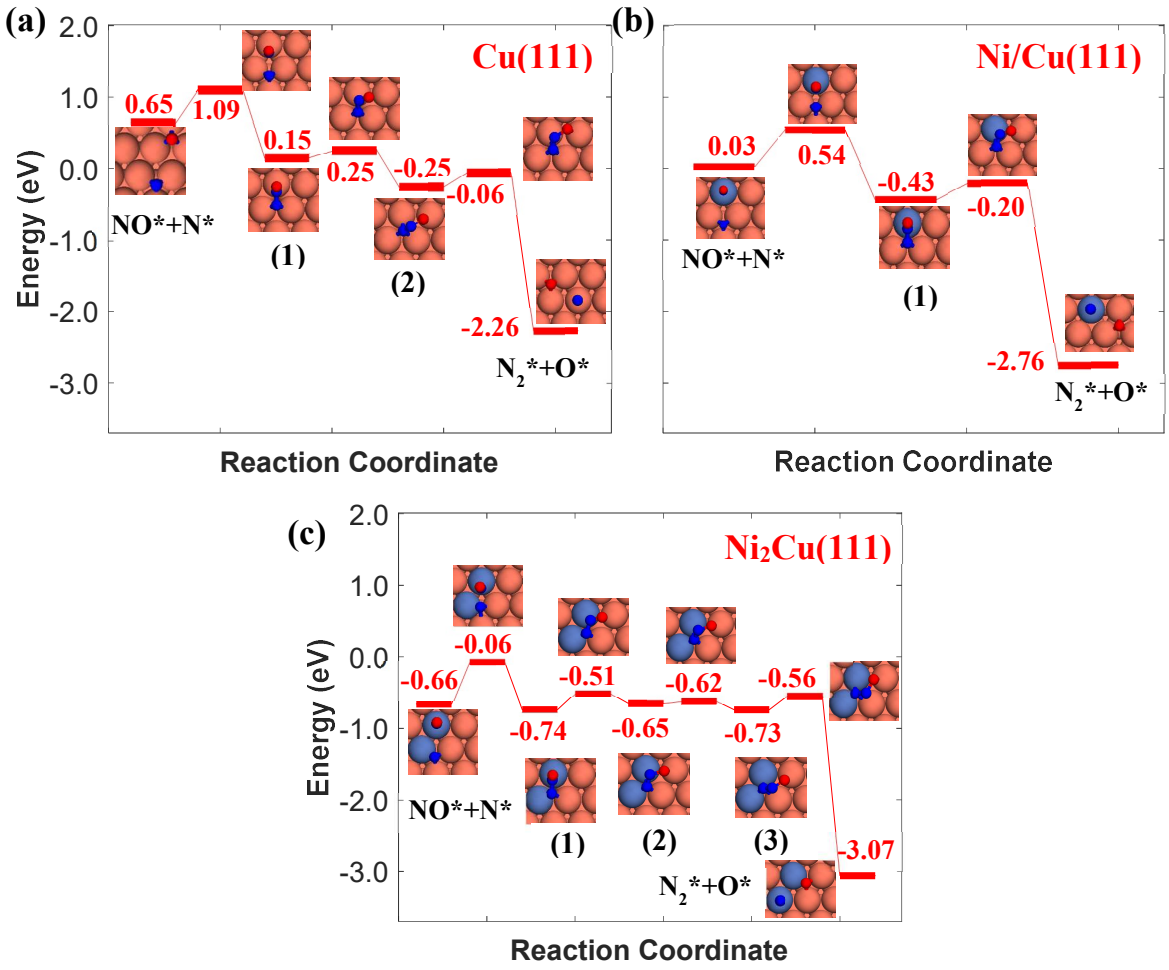

Figure 34. A second reaction path for the decomposition of N_2O^* on (a) Cu(111); (b) Ni/Cu(111) SAA and (c) $Ni_2Cu(111)$. State (1) corresponds to a *η2NbNt* structure in all panels. The *η2*–(N_t{fcc},O{top}) structure is state (2) and state (3) in panels (a) and (c), respectively. The zero level corresponds to infinitely separated (and thus non–interacting) N_2O molecule and clean slab. States without any labelling are transition states. Side views of the different states are shown in the Appendix III (Figure A14). Ni, Cu, O and N atoms are shown in purple, orange, red and blue, respectively.

6.2.4. N_2O formation and activation on Cu–based surfaces through the formation of $(NO)_2^*$

Thus far, the formation of nitrous oxide was assumed to proceed through the coupling of NO* and N* species (Figure 33 and Figure 34). NO* is of course the product of the molecular adsorption of gas–phase nitric oxide. On the other hand, the existence of N* species implies prior scission of the

N─O bond. In general, low–index coinage metal surfaces exhibit large kinetic barriers for the direct dissociation of NO* (E_a = 1.57 eV for Cu (111) and (100), and E_a > 2.5 eV for Ag and Au (111) and (100) surfaces) – (see Figure 27), thereby being ineffective at activating the N─O bond of NO*. Yet, they are known to be active for the reduction of NO, which is mainly converted to N_2O. The activity of coinage metal surfaces is ascribed to the formation of NO* dimer species (i.e. $(NO)_2$*) whose N─O bonds are more easily activated than those of monomeric NO*.[42,178,207–209] This species is formed owing to van der Waals interactions between neighbouring NO* species,[210] and may be observed even at relatively low NO* coverages over Cu(111).[211] On the contrary, our calculations indicate that NO* is adsorbed as a monomer on Rh(111) and this is corroborated by near edge X–ray absorption fine structure spectroscopy.[212]

The most energetically favoured adsorption structure of NO* on Cu(111) is an N–down geometry where the N─O bond axis is perpendicular to the surface, and N is above an fcc hollow site ($E_{ads(NO)}$ = -1.55 eV).[46] A stable NO dimer is formed when two NO* species are adsorbed on adjacent fcc sites (NO* + NO* state in Figure 35 (a)). We note that in the relaxed geometry of this state, the O atoms of the neighbouring nitric oxide adspecies are slightly tilted towards each other (Figure 35 (a)). The thermodynamic stability of this configuration has been confirmed by other DFT studies, as well as in scanning tunnelling microscopy experiments.[210,211] The two neighbouring NO* species can be converted to N_2O* (with an *η1* structure) and O* (see state (1) in Figure 35 (a)). This is happening *via* a transition state where one of the two NO* adsorbates bends down to the Cu(111) surface, while the other is slightly lifted (Figure 35 (a)). Once *η1* N_2O* is formed, its decomposition occurs in the same way as in Figure 33 (a), namely through the formation of the *η2NtOt* structure. We note that the structure of the $(NO)_2$* transition state, and the computed barrier for the scission of the N─O bond *via* the $(NO)_2$* precursor (E_a = 0.84 eV) are in excellent agreement with the DFT calculations by Bogicevic and Hass (E_a = 0.82 eV),[178] thereby furnishing further evidence for the reliability of our calculations.

We continue by investigating the same reaction pathway over the Ni/Cu(111) SAA and $Ni_2Cu(111)$ surfaces. Our calculations show that the formation of N_2O* *via* the dimerization route is indeed possible over small Ni clusters. In contrast to Cu(111), on these dilute alloys $(NO)_2$* adopts a flat geometry parallel to the surfaces in the transition state, and the computed kinetic barriers are 1.27 eV and 1.30 eV for Ni/Cu(111) SAA and $Ni_2Cu(111)$, respectively (Figure 35 (a) and (b)). These values are higher than the computed barrier for Cu(111) – (E_a = 0.84 eV), and this may be attributed to the extra energy cost required for bending down both NO* species. Nevertheless, they are lower than or equal to the corresponding kinetic barriers for the direct dissociation of NO* (E_a = 1.47 eV and 1.30 eV for Ni/Cu(111) SAA and $Ni_2Cu(111)$, respectively).[46] Therefore, the formation and decomposition of N_2O* through dimerization is another pathway that should be included in the reaction mechanism of the NO + CO reaction over the Cu–based alloy surfaces.

To elucidate the effect of the Ni cluster size to the formation rate of *η1* N_2O* and O* *via* the $(NO)_2$* intermediate, we perform additional calculations for the $Ni_3Cu(111)$ surface (Figure A12). On this surface, we compute E_a = 1.77 eV and E_a = 1.37 eV for the splitting of the N─O bond *via* dimerization and *via* the direct NO* dissociation, respectively. Additionally, we note that on Ni dimers and trimers the formed *η1* N_2O* can be transformed to the *η2NtOt* (state (3) in Figure 35 (c) for Ni_2Cu), and decompose to N_2* + 2O* only after O* spillover to Cu(111). The barrier for O* diffusion from a mixed hollow site to a Cu hollow site over $Ni_2Cu(111)$ (from state (1) to state (2) in Figure 35 (c)) is 0.61 eV. Therefore, this extra energy cost in conjunction with the large kinetic barrier for the scission of the N─O bond of $(NO)_2$* render the decomposition of N_2O* through the dimerization pathway less likely on Ni clusters with more than two Ni atoms.

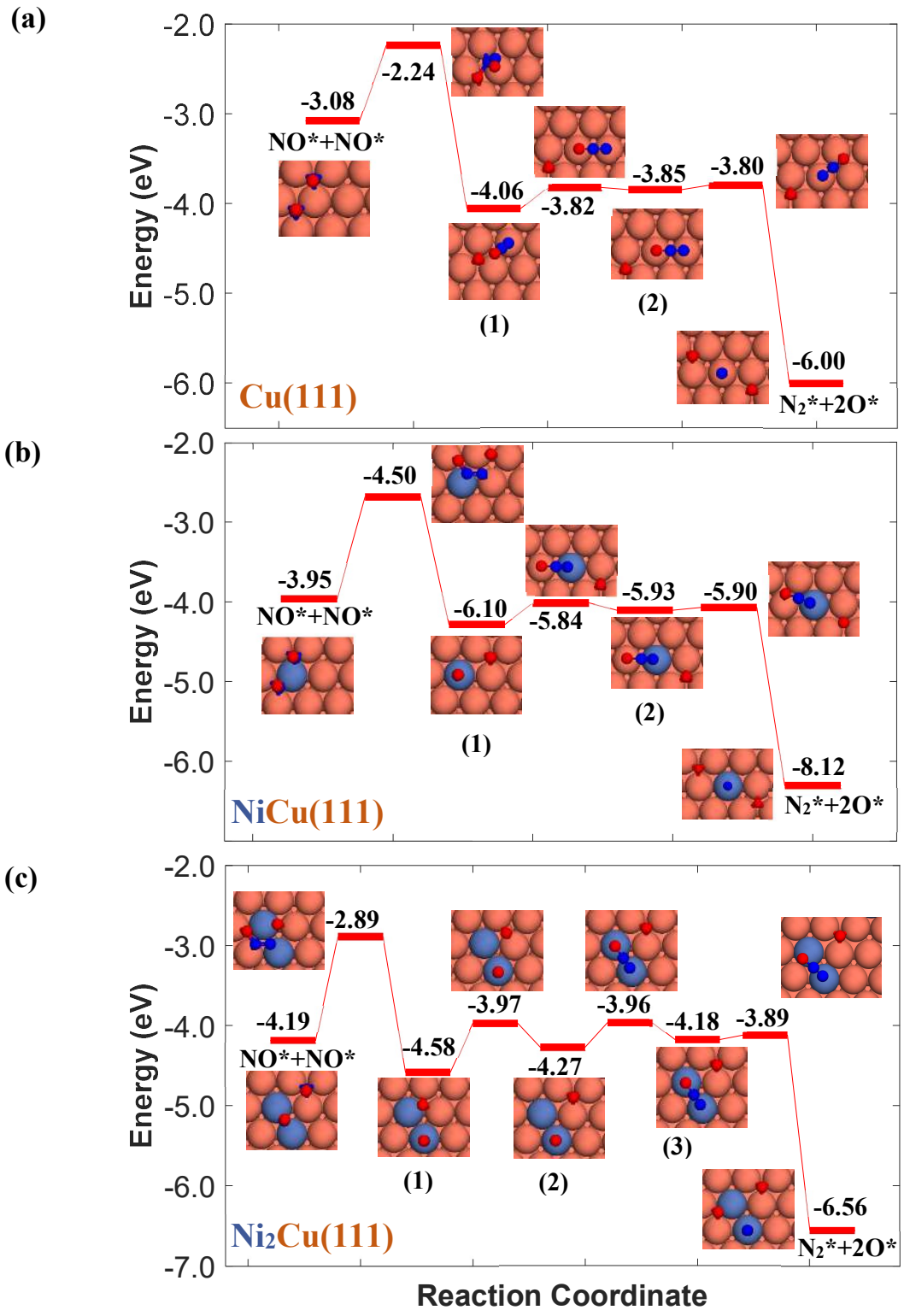

Figure 35. Reaction pathway for the formation and decomposition of N_2O* *via* $(NO)_2$* for (a) Cu(111); (b) Ni/Cu(111) SAA; and (c) $Ni_2Cu(111)$. The zero level corresponds to two non–interacting gas–phase NO molecules and a clean slab. States without any labelling are transition states. Side views of the different states are shown in the Appendix III (Figure A15). Ni, Cu, O and N atoms are shown in purple, orange, red and blue, respectively.

6.2.5. The microkinetics of the NO + CO reaction over Ni/Cu dilute alloys

Using the computed energetics for the decomposition of N_2O* in conjunction with previous results for the formation of N_2*, CO* oxidation and NO* decomposition over Ni/Cu surfaces (see chapter 5), we parameterise a microkinetic model for the NO + CO reaction. Our studies include one site type for Cu(111) and Rh(111) surfaces, and two site types for the bimetallic surfaces (see section 6.1). The goal is a preliminary assessment of the catalytic performance of the Ni/Cu dilute alloys and a comparison to Cu(111) and Rh(111). Accordingly, the microkinetic simulations are performed in the absence of adsorbate–adsorbate interactions, whose effects in the catalytic performance of the Cu–based surfaces is part of future research. Regarding the bimetallic surfaces, we assume that Ni* species (single atoms or dimers) can be occupied by one adspecies (e.g. CO*), which can react with another adspecies on a Cu site (e.g. O*) and form a product on the Ni site (e.g. CO_2*). Such events are treated as reactions that take place on the dopant site, and follow the energetics computed over the Ni site of the Ni/Cu surfaces (Appendix III). On the contrary, the Cu(111) energetics are used if the reaction involves two adspecies that are both on Cu sites (Appendix III). Despite their simplicity, such microkinetic models are sometimes capable of capturing the salient features of experimental trends,[213] providing mechanistic insights, [214] and aiding in the identification of the active site during catalysis.[215,216]

The NO + CO reaction mechanism is composed of 16 reversible reaction steps, shown in Table 3 along with their forward and reverse barriers. For all simulations the total pressure is set to 16.0 Torr with $P_{NO} = P_{CO} = 8.0$ Torr, thereby replicating the experimental conditions of Belton and co–workers. [217] At this point, we note that the dissociative desorption of O_2 and the formation of NO_2* are reactions through which O* may be removed from the surface and they could be included in the microkinetic model. However, both of them exhibit very high kinetic barriers, and on this basis are excluded from the reaction mechanism. For example, the computed barrier for the O_2* association reaction on Cu(111) is 2.10 eV, while the barrier for the reverse process is just 0.16 eV (see Figure A16 in

Appendix III); these values are is in reasonable agreement with former DFT calculations.[218] Along the same lines, we find that the dissociation of NO_2* to NO* + O* is significantly more facile than its formation and its desorption (see Figure A17 in Appendix III)).

We first simulate the NO + CO reaction on Rh(111). The *total* coverages of the surface species and the DRC analysis for this surface are shown in Figure 36 (a). The coverage profiles reveal that the catalyst surface is saturated with NO* species up to temperatures of 1000 K. Under these conditions, the high surface coverage gives rise to steric hindrance effects, which prevent the dissociation of NO*. This behaviour has been reported in the experimental work of Herman et al., and is in qualitative agreement with the fact that Rh(111) is catalytically active only at temperatures higher than 625 K.[217] Moreover, our model predicts that surface sites are freed up by NO adspecies only at T > 1000 K; this high "T threshold" can be attributed to (1) the absence of the repulsive NO* – NO* in our microkinetics (see Figure A11 in Appendix III); and (2) the very strong NO* – Rh(111) interaction predicted by the optB86b–vdW functional. In particular, NO* – NO* interactions may contribute to the reduction of the surface coverage, and in turn, this will generate free sites whereon the dissociation of NO* can happen at lower temperatures than those predicted by our model.[219,220] Regarding the second point, we find that the most stable adsorption site for NO* on Rh(111) is hcp, in line with previous computational and experimental works.[174,221,222] However, we compute E_{ads}(NO) = -2.85 eV, which is larger than the PW91 values of Mavrikakis et al.[174] (-2.39 eV – 2 × 2 cell) and of González et al.[221] (-2.62 eV – 3 × 3 cell). Unfortunately, at coverages of 0.11 ML, like in our DFT calculations, accurate experimental measurement of E_{ads}(NO) is challenging because of the tendency of NO* to dissociate on Rh(111).[174]

The reduction of the NO* surface coverage gives rise to the formation of N* and O* at T > 1000 K. The accumulation of N* species in the temperature range of 1000 K – 1200 K, is associated with the inefficiency of Rh(111) in forming *η2NbNt* N_2O* (R9, E_a = 1.50 eV) and N_2* (R16, E_a = 1.85 eV) – (Table 3). Both reaction steps are rate–limiting with a positive DRC coefficient ($0.19 \leq X_{DRC,R9} \leq 0.30$) between 1100 K and 1300 K (Figure 36 (a)). Along the same lines, the build–up of O* is

ascribed to the moderate activation barrier for the CO* oxidation reaction (E_a = 1.17 eV – R14 in Table 3), which is the only reaction that exhibits a reasonable activation barrier for the removal of O* from the surface.

Table 3. Reaction mechanism for the NO + CO reaction, and the corresponding forward (E_{fwd}) and reverse (E_{rev}) barriers (in eV). All reactions are treated as reversible, and dashes mean that the corresponding reaction does not take place on the catalyst surfaces. R1–R7 correspond to molecular adsorptions/desorptions; R8–R16 are surface reactions from which R10 and R11 are N_2O* transformation reactions.

		Rh(111)		Cu(111)		Ni/Cu(111) SAA		Ni_2Cu(111)	
Reaction & Reaction Number		E_{fwd}	E_{rev}	E_{fwd}	E_{rev}	E_{fwd}	E_{rev}	E_{fwd}	E_{fwd}
$NO_{(g)}$ + *↔ NO*	(R1)	0.00	2.87	0.00	1.55	0.00	2.10	0.00	2.65
$CO_{(g)}$ + *↔ CO*	(R2)	0.00	2.20	0.00	0.78	0.00	1.51	0.00	1.71
$N_{2(g)}$ + *↔ N_2*	(R3)	0.00	0.79	0.00	0.15	0.00	0.79	0.00	0.77
$CO_{2(g)}$ + *↔ CO_2*	(R4)	0.00	0.27	0.00	0.30	0.00	0.28	0.00	0.37
$N_2O_{(g)}$ + *↔ N_2O* *η2NbNt*	(R5)	0.00	0.83	0.00	0.00	0.00	0.43	0.00	0.74
$N_2O_{(g)}$ + *↔ N_2O* *η2NtOt*	(R6)	0.00	0.68	0.00	0.19	0.00	0.53	0.00	0.68
$N_2O_{(g)}$ + *↔ N_2O* *η1*	(R7)	0.00	0.72	0.00	0.20	0.00	0.70	0.00	0.68
NO* + * ↔ N* + O*	(R8)	1.42	2.03	1.57	1.43	1.47	1.43	1.30	1.24
NO* + N*↔ N_2O* *η2NbNt* + *	(R9)	1.50	0.40	0.44	0.94	0.51	0.45	0.60	0.68
N_2O* *η2NbNt* ↔ N_2O* *η1*	(R10)	0.46	0.30	0.14	0.56	0.24	0.50	0.37	0.31
N_2O* *η1* ↔ N_2O* *η2NtOt*	(R11)	0.24	0.40	0.06	0.05	0.29	0.12	0.32	0.32
N_2O* *η2NtOt* +*↔N_2*+O*	(R12)	0.07	2.54	0.05	2.12	0.03	2.26	0.09	2.48
N_2O**η2NbNt* +*↔ N_2* + O*	(R13)	—	—	0.19	2.20	0.23	2.56	0.23	2.51
CO* + O* ↔ CO_2* + *	(R14)	1.17	0.41	0.48	1.22	0.71	0.60	0.88	0.48
NO* + NO* ↔ N_2O* *η1* + O*	(R15)	—	—	0.84	1.82	1.27	1.60	1.30	1.69
N* + N* ↔ N_2*	(R16)	1.85	2.14	0.64	3.6	0.88	3.40	0.62	2.81

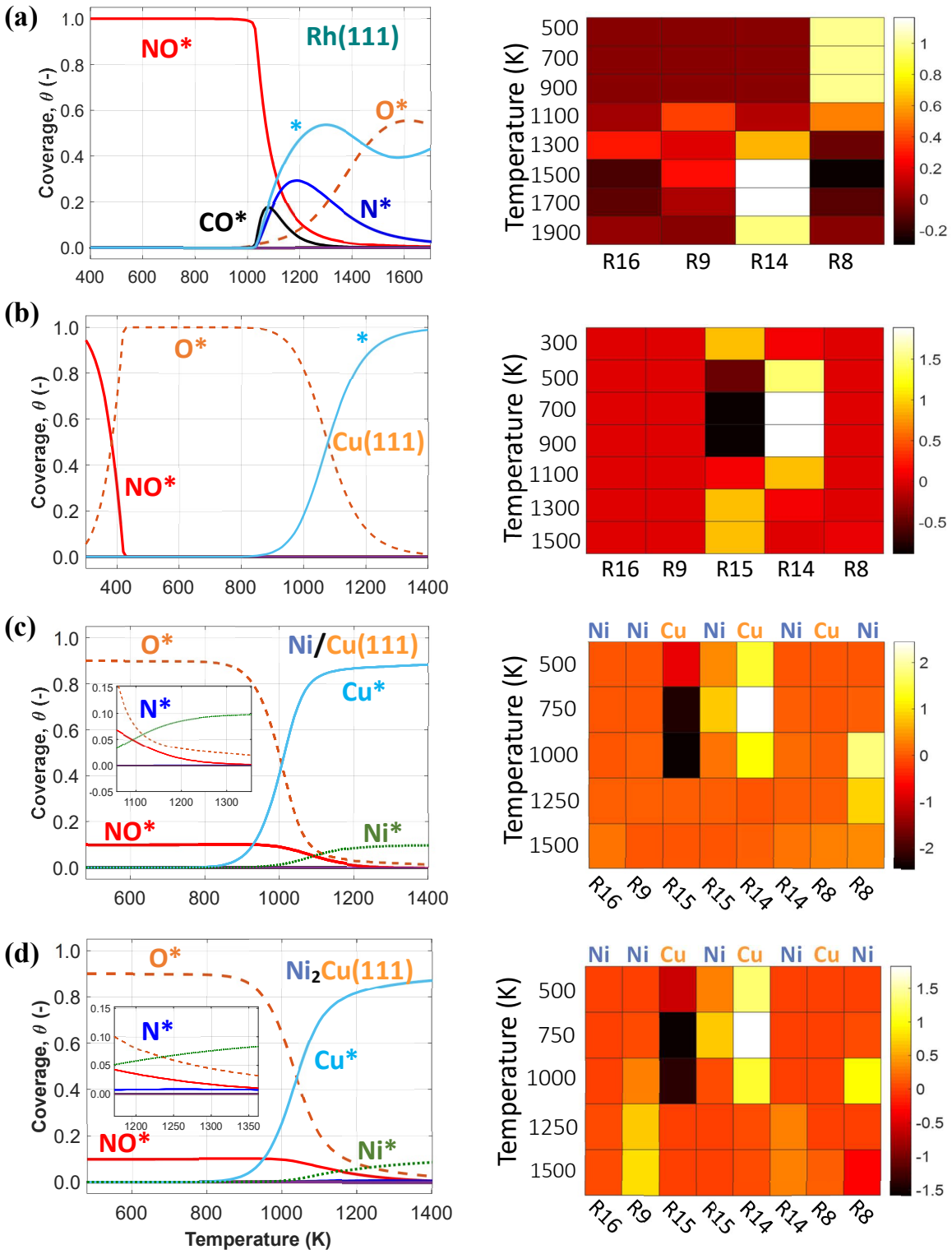

Figure 36. Total coverage (eq. (76)) profiles and DRC coefficients (X_{RC}) for the NO + CO reaction steps for (a) Rh(111); (b) Cu(111); (c) Ni/Cu(111) SAA; and (d) $Ni_2Cu(111)$. X_{RC} values are presented at various temperatures by means of heatmaps; the site whereon the reaction occurs is shown on the top of the heatmaps for the bimetallic surfaces.

The corresponding coverage profiles and DRC analysis for Cu(111) are displayed in Figure 36 (b). Cu(111) exhibits rather different behaviour than Rh(111). In particular, at T < 350 K all surface sites are occupied by NO*, but at T > 350 K there is a sharp increase in the coverage of the O* species. This sharp transition is attributed to the activation of the N─O bond *via* the NO* dimerization reaction (E_a = 0.84 eV) – (R15 in Table 3), which converts 2NO* to O* and *η1* N_2O*. The catalyst surface remains fully covered by O* within the temperature range of 420 K – 900 K. Accordingly, our DRC analysis shows that under these conditions, the oxidation of CO* controls the reaction rate, and that the NO* dimerization is an inhibiting step as it adds more O* onto the surface (Figure 36 (b)).

The last two coverage profiles shown in Figure 36 (panels (c) and (d)) are those for the Ni/Cu alloy surfaces. These surfaces contain a total of 10,000 sites, out of which 9,000 are Cu sites (Cu*) and 1,000 are Ni sites (Ni*). The coverage profiles are very similar on both cases, and indicate that Cu* sites are covered with O* up to ca. 900 K (similar to Cu(111)), while Ni* sites are poisoned by NO*. A disparity between the two surfaces is seen between 1000 K and 1500 K, where we observe a small build–up of N* over $Ni_2Cu(111)$ only (Figure 36 (c) and (d)). The presence of N* on the latter surface is indicative of the direct NO* dissociation (R8, E_a = 1.30 eV – Table 3), which happens to a smaller extent on the SAA surface (R8, E_a = 1.47 eV – Table 3). Markedly, the N* accumulation remains at low levels thanks to the efficiency of $Ni_2Cu(111)$ in forming N_2* and *η2NbNt* N_2O*(Table 3). The latter can either decompose to N_2* + O* (R10, R11, R12 and R13) or desorb (R5).

Next, we examine the activity and selectivity to N_2 of the four surfaces. The latter metric is computed as

$$S_{N_2/N_2O} = \frac{R_{N_{2,net}}}{R_{N_{2,net}} + R_{N_2O,net}}, \tag{89}$$

where $R_{N_{2,net}}$ and $R_{N_2O,net}$ are the net reaction rates for N_2 and N_2O, respectively (see eq. (86) and eq. (87)).

Figure 37 displays the activity plots for the studied surfaces, where the catalytic rate is provided by the computed turnover frequency TOF at various temperatures. The observed trend for Rh(111) (Figure 37 (a)) can be rationalised based on the corresponding coverage plot (Figure 36 (a)). As seen in Figure 37 (a), the activity of Rh(111) is low below 950 K owing to the high NO* coverage, which hinders the direct NO* dissociation (Figure 36 (a)). On the contrary, for T > 950 K there is an increase in the catalytic activity. Initially the rate of N_2O production is greater than that of N_2, and only at T > 1200 K the two production rates become equal (Figure 37 (a)).

Similarly to Rh(111), the catalytic activity of Cu(111) can be explained from the coverage profile plot in Figure 36 (b). For this surface, low (i.e. 300 K – 500 K) and high (i.e. 500 K – 1400 K) temperatures can be discussed separately. Between 300 K and 420 K, we observe that the catalytic activity increases steadily (see Figure A18 in Appendix III), and the surface transitions from a NO*–rich phase to an O*–rich phase. As discussed earlier, this transition is associated with the dimerization reaction (R15 in Table 3), which consumes NO*, releases N_2O and yields O*. At ca. 420 K, there is a sharp reduction in the catalytic activity (Figure A18), and this is the result of the poisoning of Cu(111) by O* species. The surface remains in the poisoned state for temperatures up to ca. 700 K, where the removal of O* species happens efficiently and the dimerization reaction begins to take place again at considerable rates (see Figure 37 (b) and the heatmap in Figure 36 (b)). Finally, for T > 1000 K there is a decrease in the catalytic activity (Figure 37 (b)) because under these conditions, the gaseous state of the reactants is preferred over adsorption on the catalytic surface. Throughout the investigated temperature range, the production rate of N_2O is far greater than the production rate of N_2, and this is attributed to the inability of Cu(111) to directly dissociate NO* as well as to the weak binding of the $\eta 1$ N_2O* produced by the dimerization reaction.

On the other hand, enhanced catalytic activity can be achieved when Ni* species are present in Cu (111) (Figure 37 (c) and (d)). Remarkably, the production rate of N_2 is considerably larger on

Ni/Cu(111) SAA than on Cu(111) and even more so on $Ni_2Cu(111)$, where the N_2 and N_2O production rates become equal beyond 1000 K.

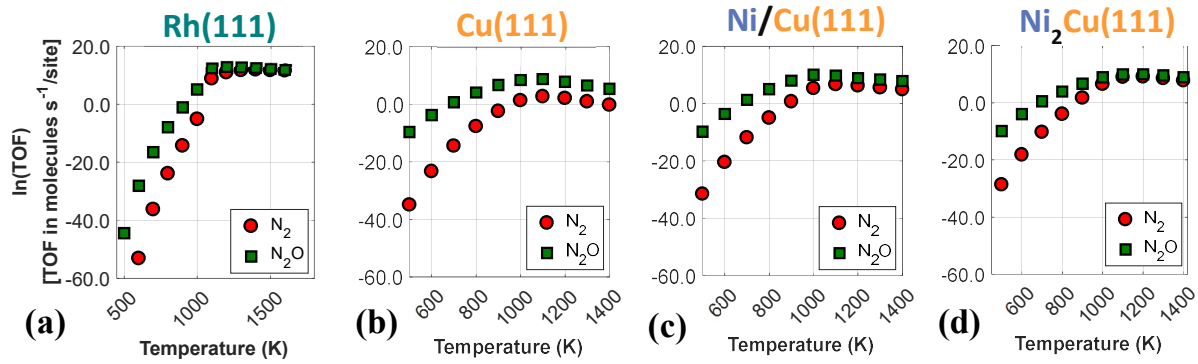

Figure 37. Rates of production of nitrogen–containing products for (a) Rh(111); (b) Cu(111); (c) Ni/Cu(111) SAA; and (d) $Ni_2Cu(111)$.

Given the importance of S_{N_2/N_2O}, this chapter concludes with an investigation on this metric, followed by suggestions for further improvements in this regard. Regarding Rh(111), our microkinetic model predicts that the main nitrogen–containing product from Rh(111) at T < 1000 K is N_2O, whilst the production of N_2 exhibits a substantial increase beyond 1100 K (Figure 38 (a)). The latter temperature corresponds to the point where the surface sites are freed up (Figure 36 (b)), and the dissociation of NO* is enabled. Notably, this trend is qualitatively in line with the reactor experiments of Peden et al.[223] on Rh(111). The experiments showed that Rh(111) exhibits poor selectivity to N_2 for reaction temperatures up to 700 K; yet, the authors observed a sharp increase in S_{N_2/N_2O} at temperatures higher than that.

The same analysis for Cu(111) reveals that this surface is indeed susceptible to the formation of N_2O (Figure 38 (a)). We find that the main way of forming N_2O* (in *η1* structure) on Cu(111) is via the formation of the $(NO)_2$* intermediate followed by N─O activation (R15). This is in line with molecular beam / infrared spectroscopy studies on other Cu low–index surfaces.[207] The *η1* N_2O* can go through one of the following paths: (1) desorb directly (E_a = 0.21 eV); (2) transform to *η2NtOt* N_2O* (E_a = 0.06 eV) and either desorb (E_a = 0.20 eV) or dissociate to N_2* + O* (E_a = 0.05 eV); (3)

transform to *η2NbNt* N_2O* (E_a = 0.56 eV) and desorb spontaneously. Therefore, N_2O* can easily undergo transformations over Cu(111), but in every new state there is a high probability for desorption, thereby explaining the poor N_2 selectivity of this surface.

Interestingly, the catalytic behaviour Ni/Cu(111) SAA and Ni_2Cu(111) appears to be more similar to Rh(111), which is well established for the NO + CO reaction, than to Cu(111), which is the host metal (Figure 38 (a)). In more precise terms, it is observed that on each of the dilute alloy surfaces the selectivity to N_2 remains low at T < 900 K but increases sharply at higher temperatures similarly to Rh(111). S_{N_2/N_2O} for both Ni/Cu(111) SAA and Ni_2Cu(111) exhibits an interesting behaviour by which it first increases for T > 900 K and then decreases at 1200 K.

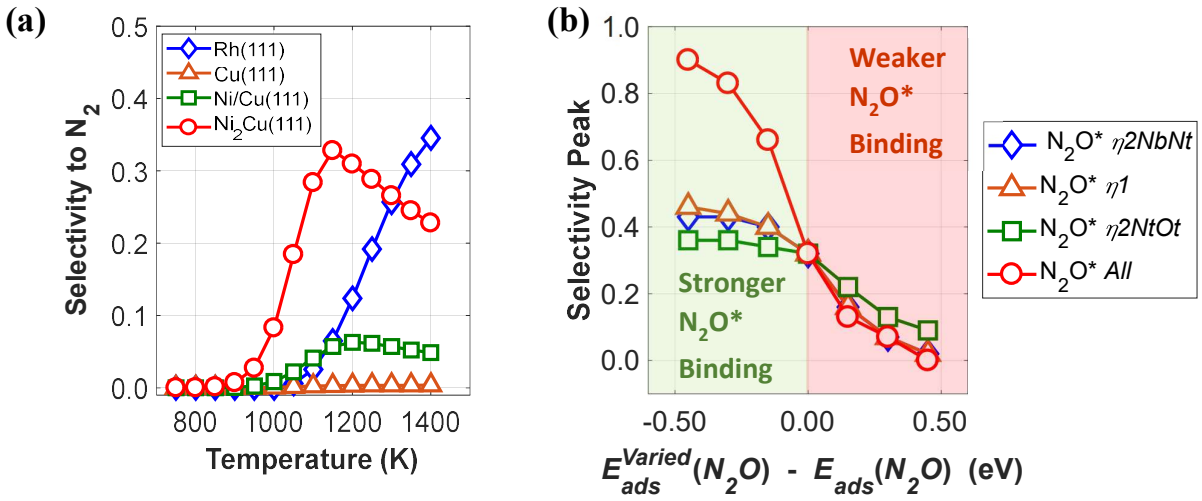

Figure 38. (a) Selectivity to N_2 for Cu(111), Rh(111) and the Ni/Cu alloys. (b) Maximum of the N_2 selectivity peak at various N_2O* adsorption energies. Values on the right correspond to smaller N_2O* binding strength on Ni* than the DFT–computed (red shade); Values on the left correspond to larger N_2O* binding strength on Ni* than the DFT–computed (green shade). In the simulations of panel (b) only the desorption energy of N_2O* was varied, whilst all the other kinetic barriers were kept fixed at their DFT–computed values.

To shed light on this behaviour, we have carried out additional microkinetic simulations for Ni_2Cu(111) where the activation barrier of one of the following events on Ni* is assigned with a very large value (e.g. 2.5 eV): (1) NO* direct dissociation (R8); (2) N_2* formation (R16); (3) NO* dimerization (R15); and (4) *η2NbNt* N_2O* formation (R9). In doing so, we record how the selectivity peak responds to the obstruction of the aforementioned events (see Figure A19 in the Appendix III).

We determine that the selectivity spike in the two bimetallic surfaces is associated with the direct dissociation of NO* and the formation of *η2NbNt* N_2O*, which could subsequently decompose to N_2* + O* (see Appendix III). Therefore, it is the ability of Ni/Cu alloys to form and process *η2NbNt* N_2O* that gives rise to the selectivity peak in Figure 38 (a). The selectivity to N_2 enters a downturn because at T > 1200 K, there is a rise in the N_2O* desorption rate. On the other hand, the formation of N_2 on Rh(111) is solely relying on the direct dissociation of NO* and such a selectivity spike is not observed (Figure 38 (a)). Accordingly, the higher intensity of the N_2 selectivity peak on $Ni_2Cu(111)$ than on Ni/Cu(111) SAA can be explained by: (1) the higher concentration of N* species on $Ni_2Cu(111)$ owing to its better ability to dissociate NO* as compared to Ni/Cu(111) SAA (see Table 3 and Figure 36 (d)); (2) the generally stronger interaction between N_2O* and $Ni_2Cu(111)$ than that between N_2O* and Ni/Cu(111) SAA (Table 3), noting that strong interaction will favour the decomposition of N_2O* over its desorption.

Finally, we explore the effect of the N_2O* binding strength on the height of the selectivity peak on $Ni_2Cu(111)$ by performing a sensitivity analysis with respect to $E_{ads}(N_2O)$ – (Figure 38 (b)). Remarkably, the adsorption energy of N_2O* appears to have a great impact upon the N_2 selectivity at 1100 K – 1200 K (Figure 38 (b)). For example, shifting the adsorption energy of all N_2O* adsorption structures to more negative values by 0.15 eV and 0.30 eV (i.e. stronger binding) results to an increase in the maximum of the peak by 0.31 (from 0.33 to 0.67) and 0.52 (from 0.33 to 0.85), respectively. We conjecture that binding strengths of this magnitude may be provided by sites on more open low-index surfaces (e.g. (100) and (110)) but also on stepped surfaces, and if this is true, the presence of such sites will contribute dramatically to the N_2 selectivity at low temperatures. Therefore, this result underscores the potential of well–engineered dilute Ni/Cu alloys for the NO + CO reaction and creates motivation for further investigations.

6.3. Concluding remarks

DFT calculations and microkinetic modelling have highlighted the potential of highly dilute Ni/Cu for the decomposition of N_2O* and the NO + CO. These materials are attractive because they are composed of abundant and inexpensive metals. Interestingly, our results pointed out that the size of the dopant cluster is critical to the catalytic performance of the dilute alloy. As demonstrated, the selectivity of the N_2O* decomposition can be tuned by changing the size of the dopant clusters. On this basis, we proceed by exploring ways to control the size of dopant surface species.

Chapter 7

7. On the surface restructuring of highly dilute alloys under vacuum and reactive conditions: a DFT study

Our attention now turns to defining ways by which one can modify/control size and configuration of dopant clusters on coinage metal surfaces. Given that catalytic surfaces interact with gas–phase species during reaction, it is natural to investigate the morphological response of dilute alloys under reactive conditions. According to our discussion in 1.5, CO is capable of causing morphological changes to alloy catalysts owing to the strong CO*–metal interactions, and this molecule is ubiquitous in industrial chemistries. Therefore, in this chapter, we use DFT and explore restructuring events (e.g. aggregation and segregation) that are induced by CO*. *The contents of this chapter have been published in J. Phys. Chem. C 2019, 123, 9128−9138 and J. Chem. Phys. 153, 244702 (2020)*.

7.1. Computational details

DFT calculations were performed using VASP version 5.4.1.[150,151] The valence electrons were treated explicitly and the core ionic potentials were modelled using PAW method.[152] A plane–wave basis set was employed and the kinetic energy cutoff was set to 400 eV. Calculations were performed under the generalised gradient approximation using the revised Perdew–Burke–Ernzerhof (RPBE) exchange–correlation functional.[224] This functional has been specifically designed to improve upon over–binding issues, particularly tailored to the chemisorption of CO.[225] Moreover, binding energies calculated with RPBE have already been shown to be in good agreement to those experimentally acquired on SAA surfaces.[67] Under–coordinated (211) edges were modelled using a four-layer (3 × 1) slab where the two bottom–most layers were fixed at the corresponding RPBE lattice constant and the remaining ones were allowed to fully relax. The low–index (100) facet was modelled by a five–layer (3 × 3) slab, where the two bottom-most layers were fixed and others were allowed to fully relax. Periodic images in the z–direction were separated by a 10 Å vacuum in both cases, and the first Brillouin zones of the (211) step and (100) facets were sampled with a 6 × 5 × 1 and a 7 × 7 × 1 Monkhorst–Pack k–point mesh, respectively. In all cases, we used the RPBE–calculated equilibrium lattice constants of the coinage metal host (3.64 Å, 4.23 Å and 4.22 Å for Cu, Ag and Au, respectively). Electronic self–consistency was assured up to a tolerance of 10^{-7} eV and the Hellmann–Feynman forces acting on all ions that are free to move were relaxed to less than 10^{-2} eV/Å. The adsorption energy of *m* CO molecules ($E_{ads}(mCO)$) was computed according to eq. (90):

$$E_{ads}\left(m\mathrm{CO}\right) = E_{tot}^{m\mathrm{CO}+slab} - E_{tot}^{slab} - mE_{tot}^{\mathrm{CO}_{(g)}}, \tag{90}$$

where $E_{tot}^{m\mathrm{CO}+slab}$ is the DFT total energy of *m CO* molecules co–adsorbed on a slab, E_{tot}^{slab} is the DFT total energy of the clean slab, and $E_{tot}^{\mathrm{CO}_{(g)}}$ the DFT total energy of a CO molecule in the gas phase.

The segregation energy (ΔE_{seg}), denoting the enthalpic preference for a dopant atom to reside in the bulk versus in the surface layer of the host material, is given by eq. (91):

$$\Delta E_{seg} = E_{tot,Bulk} - E_{tot,SAA}\,, \tag{91}$$

where $E_{tot,Bulk}$ is the DFT total energy of the dopant atom immersed in the 3rd layer of the slab (Figure 39) and $E_{tot,SAA}$ is the DFT total energy of the clean slab with the dopant atom in the surface layer (Figure 39). Negative values of ΔE_{seg} imply a preference of the dopant to segregate into the bulk, whereas positive values indicate preference for segregation to the surface layer.

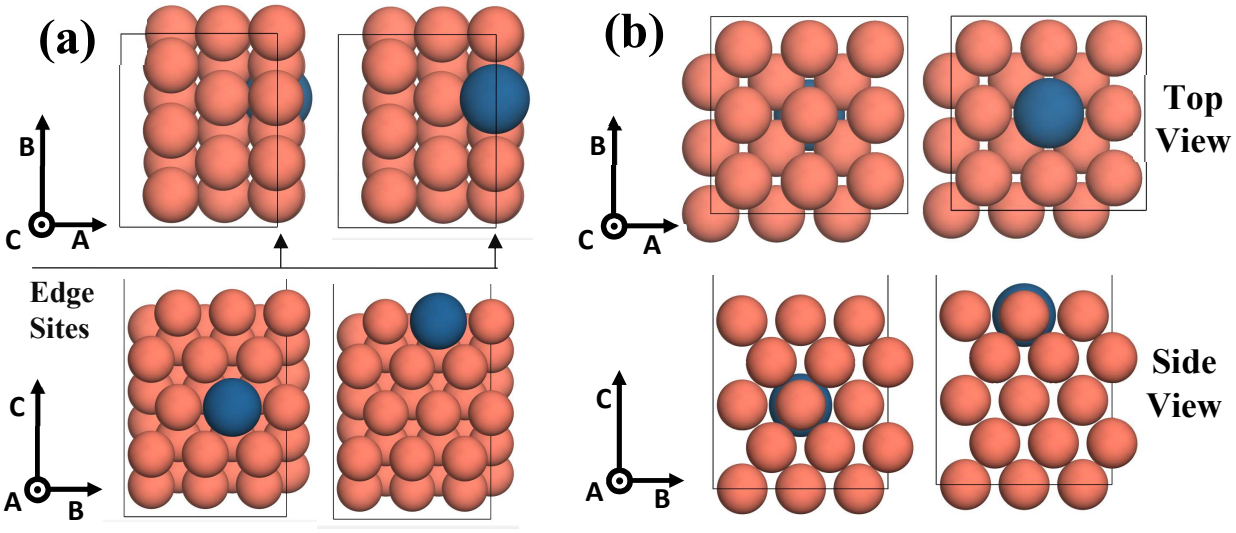

Figure 39. (a) Figures in the first row show the top view of the (211) slab with the dopant atom (blue) being immersed in the 3rd layer of the host matrix (orange) – (top–left figure) and then being placed on the top layer (top–right figure). Figures in the second row show the side view of the same slabs; (b) figures in the first row show the top view of the (100) slab with the dopant atom (blue) being immersed in the 3rd layer of the host matrix (orange) – (top–left inset) and then being placed on the top layer (top–right inset). Figures in the second row show the side view of the same slabs. In the schematics of the axes the symbol ⊙ denotes an arrow pointing from the page towards the reader.

The CO–induced segregation energy ΔE_{seg}^{CO} (see supplementary information of ref. 67) is given by eq. (92):

$$\Delta E_{seg}^{CO} = \Delta E_{seg} + \{E_{ads}^{host}(\mathrm{CO}) - E_{ads}^{SAA}(\mathrm{CO})\}\,, \tag{92}$$

where $E_{ads}^{host}(\mathrm{CO})$ and $E_{ads}^{SAA}(\mathrm{CO})$ are the adsorption energies of one CO* molecule on the pure host material and SAA, respectively.

The aggregation energy (ΔE_{agg}), denoting the thermodynamic preference for the formation of clusters (dimers and trimers) from isolated dopant atoms, is given by eq. (93):

$$\Delta E_{agg} = E_{tot}(n) + (n-1)\cdot E_{tot}(host) - n\cdot E_{tot}(SAA), \quad (93)$$

where $E_{tot}(n)$, $E_{tot}(host)$ and $E_{tot}(SAA)$ are the DFT total energies of an alloy with a cluster of *n* dopant atoms, the pure host material and the SAA, respectively. According to eq. (93), $\Delta E_{agg} < 0$ indicates a preference for the dopant atoms to cluster on the surface. Conversely, $\Delta E_{agg} > 0$ implies a thermodynamic preference for the SAA phase.

A CO molecule can induce aggregation if its adsorption energy on an n–mer dopant island ($E_{ads}^{n-mer}(\mathrm{CO})$) is more negative than on the SAA ($E_{ads}^{SAA}(\mathrm{CO})$), such that positive values of ΔE_{agg} may be offset. It follows that the CO–induced aggregation energy ($\Delta E_{agg}^{m\times \mathbf{CO}}(n)$) is expressed as:

$$\Delta E_{agg}^{m\times CO}(n) = \Delta E_{agg}(n) - \{m\cdot E_{ads}^{SAA}(\mathrm{CO}) - E_{ads}^{n-mer}(m\mathrm{CO})\}, \quad (94)$$

where *m* represents the number of CO molecules adsorbed on the *n–mer* dopant island.

7.2. Results and discussion

7.2.1. CO Adsorption on SAA (211) and (100) Surfaces

The dominant facets on fcc metal NPs are the low index (111) and (100), and these are linked by edge sites (se e.g. Figure 1). Previous works modelled the adsorption of CO* to SAA and pure metal (111) surfaces. This chapter expands the investigations to the (211) and (100) facets, thereby examining the vast majority of sites being found on commonly encountered NP geometries (e.g. cuboctahedral and octahedral). To model under–coordinated edge sites, one can employ a (211) step, whereon sites with coordination number equal to seven can be found. Edge sites exhibit distinct electronic environments as compared to lower index facets and are of great interest in catalysis because of their high reactivity.[103,142] Although these sites are often highly active[148,226] and can make a notable contribution to the overall catalytic rate, they are also known for their susceptibility to poisoning (e.g.

CO and sulphur poisoning).[148] This is the result of their very strong interaction with certain adsorbates, which bind tightly to these sites leading to their deactivation.[143]

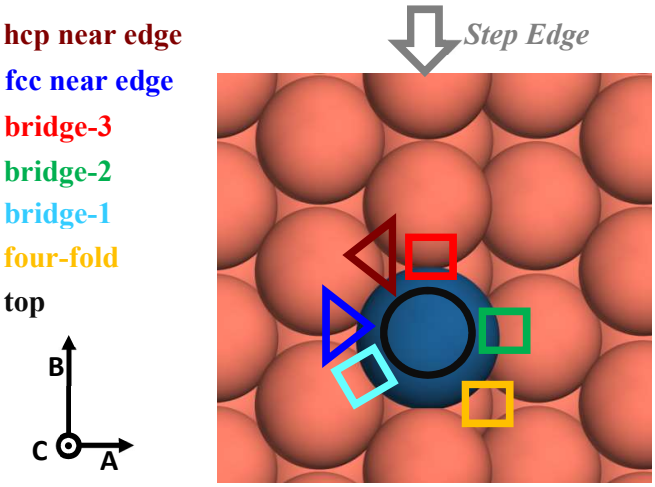

Figure 40. Top view of the (211) surface, showing the sites whereon the adsorption of CO was tested. This includes: three bridge sites (i.e. bridge–1, bridge–2 and bridge–3), a four–fold near edge site, two three–fold near edge sites (i.e. hcp near edge, fcc near edge) and the dopant (blue) top site. Host metal atoms shown in orange.

Using the RPBE XC functional and the computational setup described in the previous section, we study the adsorption of CO* to (211) SAA surfaces and pure metal surfaces. Previous theoretical studies, which employed RPBE as the XC functional (see ref. 67), demonstrate excellent agreement between simulated and experimentally obtained temperature programmed desorption (TPD) data for various pure metal (111) and SAA (111) surfaces (including, Pd/Cu(111), Pt/Cu(111), Pd/Au(111) and others), with a mean absolute error in the CO* binding energy of 0.05 eV. Herein, we present calculations for the adsorption energy of CO (E_{ads}(CO)) on fifteen (211) SAA surfaces, including Pt–, Pd–, Rh–, Ir– and Ni–doped Ag(211), Au(211) and Cu(211). E_{ads}(CO), is computed on seven different adsorption sites, which are on or proximal to the edge of SAA and pure metal (211) surfaces (Figure 40). We determine that in all SAA (211) surfaces the most stable adsorption site is the top dopant site and the corresponding E_{ads}(CO) values are plotted in Figure 41 (a). In the same figure, we also plot E_{ads}(CO) on the most stable adsorption site of (211) pure metal surfaces (e.g. Pt(211), Pd(211), Cu(211) etc.), which can be either the edge top site or the edge bridge site (bridge–3 in Figure 40), depending on the metal.

For Cu(211) E_{ads}(CO) = -0.70 eV, which is in reasonable agreement with experimentally determined value (E_{ads} (CO) ≈ -0.61 ± 0.01 eV).[227] We also find that DFT is consistent with infrared reflection absorption (IRA) spectroscopy,[228] predicting that adsorbed CO is considerably more stable on top sites over the Ir(211) surface (E_{ads} (CO) = -2.14 eV). Furthermore, according to our results the most stable adsorption site on the Rh(211), Pd(211), Pt(211) and Ni(211) surfaces is the edge two–fold site (bridge–3 in Figure 40), whereon E_{ads}(CO) = -1.75 eV, -1.64 eV, -1.75 eV and -1.55 eV, respectively. Interestingly, the two–fold edge site is marginally more stable than the top edge on Pt(211), where we calculate E_{ads}(CO) = -1.75 eV and -1.74 eV, respectively. This marginal difference of E_{ads}(CO) on these two sites is also reported in studies that combine theory and experiment.[229] Finally, the CO adsorption strength is significantly lower on (211) coinage surfaces (i.e. Cu(211), Au(211) and Ag(211)) compared to that of the PGMs (i.e. Pt(211), Pd(211), Rh(211), and Ir(211)) and Ni(211) – (Figure 41 (a)) , testament to the much higher poisoning susceptibility of the latter over the former.

Some SAAs bind CO with an intermediate strength as compared to the coinage metals and PGMs. Interestingly however, the adsorption strength of CO* on Ir and Rh SAAs is enhanced compared to pure Rh(211) and Ir(211). The calculated E_{ads}(CO) values on Rh/Ag(211), Rh/Au(211), Ir/Ag(211) and Ir/Au(211) are -2.08 eV, -1.93 eV, -2.64 eV and -2.52 eV, respectively (compared to -1.75 eV and -2.14 eV on pure Rh(211) and Ir(211), respectively). On the other hand, the CO* adsorption strength on Pt and Pd(211) SAA surfaces is significantly reduced compared to that on pure Pt(211) and Pd(211). For example the binding strength of CO* on Pt/Cu(211) is weaker by ca. 0.27 eV compared to Pt(211), while the corresponding reduction between Pd/Au(211) and Pd(211) is about 0.60 eV. It follows that these two alloys will be more resistant to CO poisoning relative to the monometallic PGM edges. Indeed, Pd/Au and Pt/Cu SAAs have been shown to exhibit high resistance to poisoning, whilst performing highly selective hydrogenations.[39] Our results suggest that Pt/Ag, Pt/Au, Pd/Cu and Pd/Ag SAAs also have the potential to exhibit high CO* tolerance and a previous screening study has

suggested that they are also of interest for use as hydrogenation catalysts, thanks to facile H_2 activation and subsequent H spillover.[45]

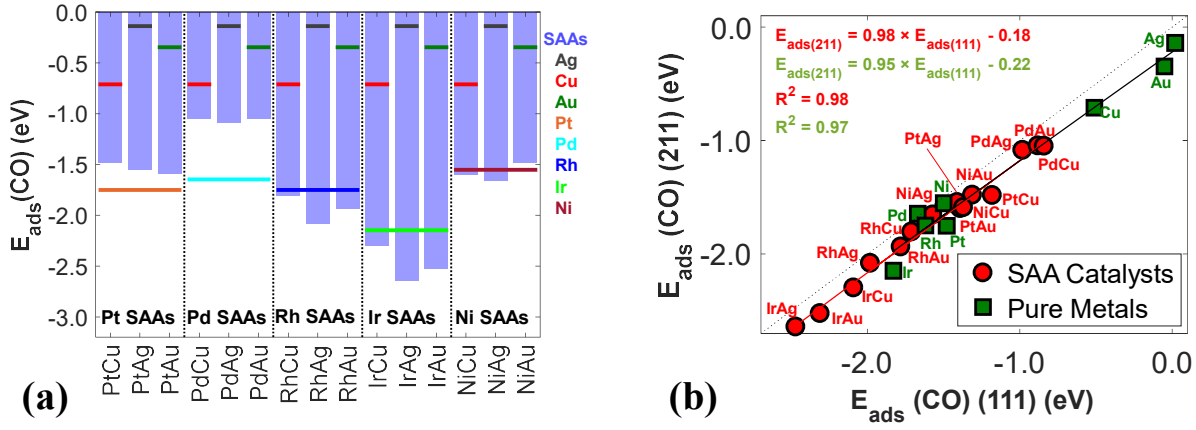

Figure 41. (a) The bars show adsorption energies of CO* (E_{ads}(CO)) on the most stable sites of SAA (211) surfaces. E_{ads}(CO) for (211) pure metal surfaces are shown by coloured lines [Ag (black), Cu (green), Au (red), Pt (orange), Pd (cyan), Rh (blue), Ir (light green) and Ni (burgundy)]; (b) linear correlation between E_{ads}(CO) (211) and E_{ads}(CO) (111) for SAAs (red) and pure metals (green). Regression lines and equations are shown, with the corresponding coefficients of determination (R^2) and the parity line (dashed black line).

Briefly comparing to a previous work on the (111) surface,[67] we plot E_{ads}(CO) (211) versus E_{ads} (CO) (111) in Figure 41 (b) and make the general observation that the binding strength of CO* on the (211) edge is consistently greater than that on the (111) facet for both the pure metal catalyst and SAAs. Importantly, there is a strong correlation between E_{ads}(CO) (211) and E_{ads}(CO) (111) (Figure 41 (b)), with CO* binding being systematically stronger on the (211) SAA surfaces by 0.18 eV on average, compared to (111) SAA surfaces. The same is true for the pure metal catalysts examined, for which the binding strength of CO* on (211) is greater than that on (111) by approximately 0.2 eV. This result is in line with the surface (211) atoms having a lower coordination number than those on (111) (7 versus 9, respectively).

In a similar manner to the study on the (211) edge, we consider the adsorption behaviour of CO* on (100) SAA and pure metal surfaces, whereon surface atoms have a coordination number of 8. DFT calculated E_{ads}(CO) on (100) SAA and pure metal surfaces are plotted in Figure 42 (a), and these values (e.g. E_{ads}(CO) for Cu(100) and Ni(100)) are in agreement with other DFT using RPBE and experimental studies.[230,231]

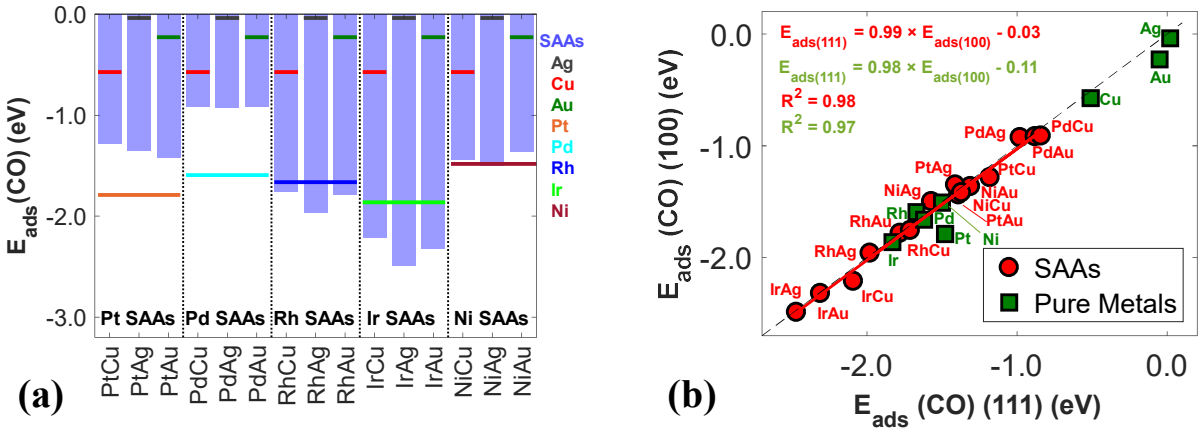

Figure 42. (a) The bars show adsorption energies of CO (E_{ads}(CO)) on the most stable sites of SAA (100) surfaces. E_{ads}(CO) for pure (100) metals are shown by coloured lines [Ag (black), Cu (green), Au (red), Pt (orange), Pd (cyan), Rh (blue), Ir (light green) and Ni (Burgundy)]; (b) linear correlation between E_{ads}(CO) (100) and E_{ads}(CO) (111) for SAAs (red) and pure metals (green). Regression lines and equations are shown, with the corresponding coefficients of determination (R^2) and the parity line (dashed black line).

Interestingly, trends of the CO* adsorption energy are similar to those observed on the (211) edges, though binding of CO on the (100) facet is in general weaker (Figure 42 (a)). As with the (211) edges, CO* binds very strongly on Ir and Rh (100) SAAs, whereon the adsorption is more exothermic than on pure Ir and Rh (100) surfaces. This trend holds on (211), (100) and (111),[67] and it follows that Ir and Rh SAA nanoparticles will be more susceptible to CO poisoning, and therefore inappropriate for applications that require high CO poisoning resistance (e.g. steam reforming). However, using the CO* binding strength as an indicator/descriptor of reactivity, Rh and Ir SAAs are likely to be promising catalysts for breaking strong chemical bonds that cannot be activated by other SAAs. Indeed, previous calculations and chapter 5 have shown that Rh SAAs in general exhibit some of the lowest activation barriers for numerous reactions (e.g. C─H activation and N─O scission).[45]

As with adsorption on the (211) edge, E_{ads}(CO) (100) is strongly correlated with E_{ads}(CO) (111) (Figure 42 (b)) for both SAA and pure metal surfaces. In particular, for pure metals we find the relative binding strength across the different surfaces to decrease as follows: (211) > (100) > (111), which, according to our results suggests that an increase in the coordination number by 1 corresponds to ca. 0.10 eV decrease in the binding strength. This trend is in line with the findings of a previous work on

various Pt and Au surfaces,[9] and also in agreement with the *d* band model which suggests broadening of the *d* band upon increasing coordination number and therefore weaker binding (see section 1.2).

On the other hand, despite the different coordination numbers of the surface atoms on SAA (100) and (111) facets, the adsorption energies calculated thereon are very similar (i.e. E_{ads}(CO) (100) ≈ E_{ads}(CO) (111)), as most of the SAA data points lie on the parity line (Figure 42 (b)). We postulate that the similarities in CO* adsorption behaviour of SAA (111) and (100) surfaces is the result of a lack of charge mixing between the dopant atom and the coinage metal atoms, which makes the former behave more like an isolated site rather than part of a well–delocalised surface state (see chapter 5). Consequently, the available electron densities for adsorbate binding are similar for dopant atoms in both facets and hence is the CO* binding strength.[43] The binding strength of CO* on the SAA surfaces follows the order (211) > (100) ≈ (111).

7.2.2. Surface segregation studies

Now that the adsorption of CO* on SAAs has been investigated, we move on by assessing the capability of CO* in inducing catalyst restructuring. The enthalpic preference of a dopant atom to reside on the surface layer or in the bulk matrix of the host metal is quantified by the segregation energy, ΔE_{seg}. ΔE_{seg} are computed for fifteen binary alloys, always relative to the SAA phase. Based on eq. (91), when $\Delta E_{seg} > 0$ there will be a thermodynamic preference for the dopant atom to segregate to the surface in favour of the SAA phase. On other hand, when $\Delta E_{seg} < 0$ there will be a preference of segregation into the bulk matrix of the coinage metal host such that the dopant atom is submerged therein. To compute ΔE_{seg} values, one has to perform two calculations for each binary alloy on (100) and (211) facets: first, with one dopant atom in the top layer of the slab (Figure 39), forming a SAA and second, with the isolated dopant immersed in the bulk matrix of the coinage metal (Figure 39). The results presented in this and the following sections provide information on the thermodynamic stability of the different investigated structures, but neglect entropic and kinetic effects which are important under experimental conditions. Such effects are considered in chapter 8 and in section 7.2.4.

The computed ΔE_{seg} are displayed in a parity manner in Figure 43. In the absence of any adsorbates on the surface, $\Delta E_{seg} < 0$ for almost all the (211) and (100) binary alloys. Therefore, in the majority of cases, the dopant atom has a thermodynamic preference for segregation into the bulk of the coinage metal (Figure 43). Exceptions to this observation are Pd/Cu(211) and Pd/Cu(100), for which ΔE_{seg} are slightly positive (0.07 eV and 0.06 eV, respectively), and this is attributed to the fact that Pd and Cu atoms have very similar surface energies on (211) and (100) surfaces.[232] The trends in the segregation of dopant metal atoms in SAA (211) and (100) surfaces are very similar to those on the (111) facet. The only difference is Pt/Cu SAA, where $\Delta E_{seg} > 0$ on (111),[67] whereas we find $\Delta E_{seg} < 0$ on (100) and (211).

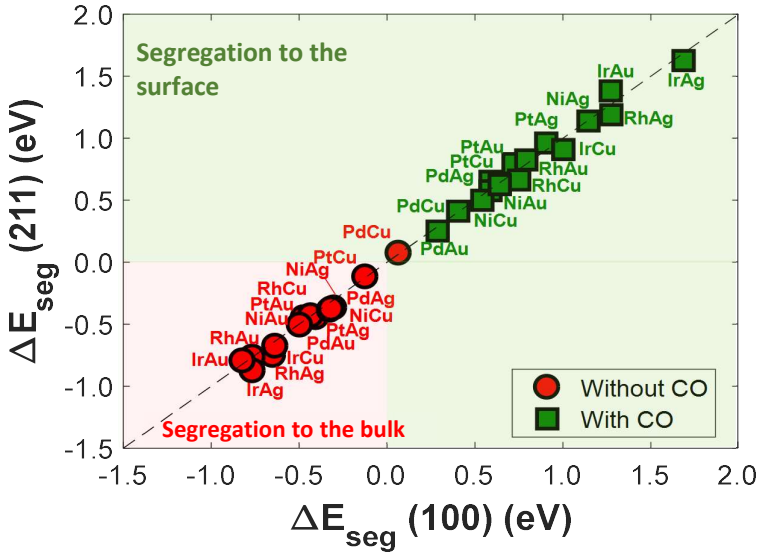

Figure 43. Calculated ΔE_{seg} for fifteen binary alloys in the absence of CO* (red circles) and in the presence of CO* (green squares). Segregation of the dopant atom to the surface is favoured in the area highlighted in green. The opposite is true in the area highlighted in red.

The thermodynamic preference for the dopant to submerge into the bulk matrix of the coinage metal may be reversed by the presence of a potent adsorbate (e.g. CO*).[55] Indeed, adsorbates that interact strongly with metal atoms usually enrich the surface of bimetallic catalysts with those metal atoms.[233] Thus, the possibility of inducing segregation through CO adsorption is next evaluated. In the presence of an adsorbed CO molecule, the CO–induced segregation energy is found from eq. (92). The obtained results indicate that the adsorption of CO* will induce segregation of the dopant to the surface

for every binary alloy as $\Delta E_{seg}^{CO} > 0$ in both (211) and (100) surfaces (Figure 43). It follows that the relative adsorption strength of CO* on the SAAs is sufficiently greater than on the pure coinage metals, overcoming any negative ΔE_{seg} and making ΔE_{seg}^{CO} always positive (see eq. (92)).

Interestingly, it is noted that the most positive ΔE_{seg}^{CO} values are calculated for those binary alloys that showed the most negative ΔE_{seg} on both (100) and (211) surfaces under vacuum conditions (e.g. Ir/Ag, Rh/Ag). These "reactive" dopants (i.e. Rh and Ir) have significantly higher surface energies, as well as smaller lattice constants than Ag.[232] This difference in the lattice constants introduces strain effects, thereby reducing further any electronic overlap between dopant and coinage atoms.[213] In turn, the accumulated electron density on the Ir and Rh atom sites could be mitigated either by an increase in the coordination number (i.e. immerse into the bulk of the coinage metal), or by coupling with a CO* molecule. Similarly, one may explain why those SAAs exhibiting less negative ΔE_{seg} under vacuum conditions yield relatively small positive values of ΔE_{seg}^{CO}. For example the surface energies of Pd and Ag are not significantly different[232] and the same holds for their RPBE lattice constants (4.00 and 4.23 for Pd and Ag, respectively). In turn, for Pd/Ag we find a slightly negative ΔE_{seg} and a relatively small positive value of ΔE_{seg}^{CO}.

7.2.3. Surface aggregation studies

We continue by presenting a study on the restructuring of the surface layer of SAAs. To this end, we investigate the surface aggregation of dopant atoms on highly dilute alloys, in the presence versus in the absence of CO*. The aggregation energy (ΔE_{agg}) for thirteen bimetallic alloys are computed using eq. (93). ΔE_{agg} quantifies the preference of dopant atoms to form aggregates and clusters, such as dimers, trimers and islands from a dispersed SAA phase. In this case, we explicitly considered "small" dopant clusters like those considered in chapters 5 and 6 (i.e. dimers and trimers). The presence of only small clusters is based on the assumption that dopant atom loadings at the limit

of high dilution will be less than 1 % and therefore, entropic forces will make the formation of larger aggregates less likely for miscible metal combinations.[36,234,235]

We examined different dopant dimer configurations on (100) and (211) surfaces (Figure 44). On the (211) step, there is a dimer that is formed by neighbouring dopant atoms on the edge. On the (100) surface we considered two dimers, with the dopant atoms being either 1NN or second nearest neighbours (2NN) (Figure 44). Under vacuum conditions, it is determined that most Cu–based alloys have a strong thermodynamic preference for dispersion to the SAA phase ($\Delta E_{agg} > 0$) on both (211) and (100) surfaces (Figure 44 (a)); this is in good agreement with other theoretical and experimental works and indeed our previous work on the (111) facet.[34,235–237] The SAA phase is also thermodynamically favoured for most of Au– and Ag–based alloys under vacuum conditions. Yet, we compute $\Delta E_{agg} < 0$ on Ir/Cu(100), Ir/Cu(211), Ir/Ag(211) and Ir/Ag(100), where there is clear thermodynamic propensity for forming edge and (100) 1NN dimers. The presence of strong Ir–Ir interactions in dimer configurations is also evidenced by the smaller relaxed distance between adjacent Ir atoms in dimers, as compared to adjacent atoms in pure Ir metal surfaces. For example, we find an Ir–Ir distance of 2.46 Å on the (211) dimer of Ir/Ag, whilst the corresponding Ir-Ir distance on pure Ir(211) is 2.75 Å. However, when the two Ir atoms are arranged in a 2NN dimer on (100) the distance between them is greater than that in the 1NN (100) dimer, and we compute $\Delta E_{agg} > 0$ for the 2NN dimer (Figure 44 (a)). For example, on Ir/Cu(100) the relaxed distances between dopants of 1NN and 2NN dimers are 2.53 Å and 3.18 Å, respectively, and ΔE_{agg} = -0.08 eV and +0.09 eV, respectively. Finally, in some cases $\Delta E_{agg} \approx 0.0$ eV (e.g. Rh/Ag(211), Rh/Au(211)). One would expect that when accounting for entropic effects in these cases, and those with slightly negative ΔE_{agg}, will result in dopant atom dispersion.

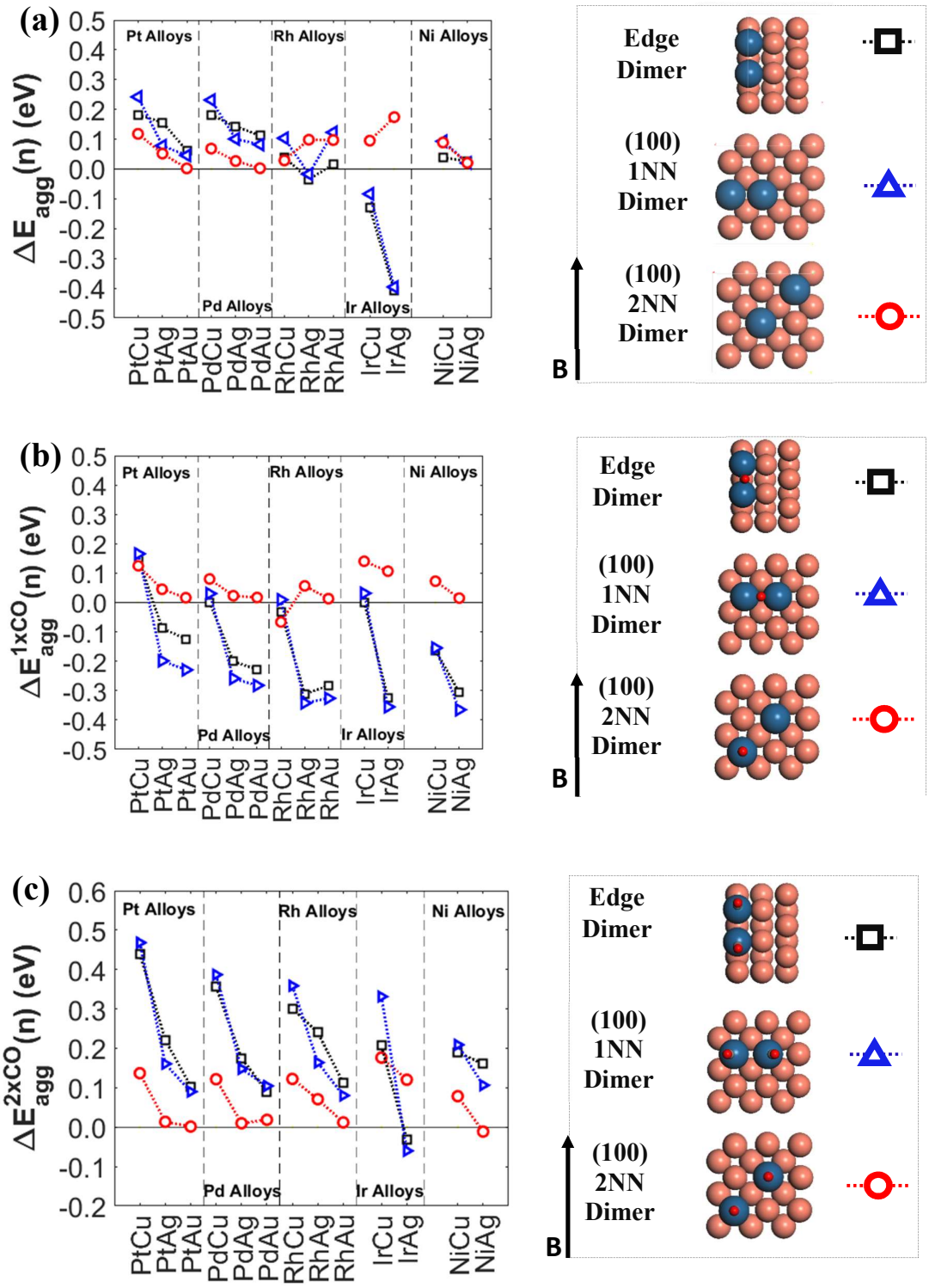

Figure 44. Aggregation energies (ΔE_{agg}) for dimers relative to the SAA phase of Ni, Pd, Pt, Rh and Ir doped into the (100) and (211) surfaces with (a) no adsorbed CO molecule; (b) 1 adsorbed CO molecule; and (c) 2 adsorbed CO molecules. The legends next to each plot show dimer configurations in the relaxed state. Therein carbon, coinage metal, dopant metal and oxygen atoms are represented by grey, orange, blue and red spheres, respectively.

Finally, the aggregation behaviour of the same binary alloys is studied in the presence of CO*, exploring the idea of controlling the size of dopant ensemble by tuning P_{CO}.[55,238] First, we simulate "low P_{CO}" conditions, whereby full saturation of all dopant atoms in the dimer configurations is not possible. To capture representative configurations for such conditions, we performed DFT calculations with only one CO adsorbed on the most stable adsorption site on the edge, (100) 1NN and (100) 2NN aggregates. In all alloys, the most stable site for CO* adsorption on the (100) 2NN dimer is a dopant top site. By contrast, the most stable adsorption site on edge and (100) 1NN dimers is the two–fold bridge site between two adjacent dopant atoms, with the exception of Ir/Cu and Ir/Ag alloys, where the top dopant site is the most stable.

Using the corresponding adsorption energy values ($E_{ads}^{n-mer}(CO)$), where *n–mer* corresponds to a dimer in this case, we calculate $\Delta E_{agg}^{1\times CO}$ (Figure 44 (b)). The main observation is that all Ag– and Au–based alloys show a thermodynamic preference to forming (1NN) aggregates on the (100) facet and (211) edges in the presence of CO*. This is also true for Ni/Cu, where dispersion of Ni atoms was preferred under vacuum conditions (Figure 44 (a)). The same trend has been observed upon C_2H_2 adsorption on Ni/Cu(111).[239] We find that the type of the most stable adsorption site is crucial to the stability of the aggregate phase versus the SAA phase. In particular, the formation of (100) 1NN and edge dimers is promoted on the binary alloys where CO* prefers the two–fold site in–between adjacent dopant atoms (e.g. Pt/Ag, Pt/Au, Pd/Ag etc.). When bound to two neighbouring dopants, CO* interacts with both dopants, thereby keeping them together by forming a stable dimer. Quite the contrary is observed when CO* is more stable on the top dopant site, which is true for Ir/Ag and Ir/Cu (100) 1NN and edge dimers, as well as on (100) 2NN dimers of all the binary alloys. Under these circumstances, CO* interacts strongly with the atom where it is adsorbed and tends to isolate it from the neighbouring dopant. For example, under vacuum conditions the formation of (100) 1NN and edge dimers was favoured on Ir/Cu(211) and Ir/Cu(100) ($\Delta E_{agg}^{1\times CO}$ = -0.13 eV and -0.08 eV, respectively, as shown in Figure 44 (a)). In contrast to all other cases, addition of a CO* on these configurations, brought about

slight preference for the SAA phase ($\Delta E_{agg}^{1\times CO}$ = +0.01 eV and +0.03 eV, respectively, as shown in Figure 44 (b)) instead of further promoting the formation of aggregates.

To simulate higher CO* coverages, a 2nd CO* is included in our DFT calculations, with both adsorbates placed on the two dopant top sites. The underlying assumption is that the P_{CO} in a surface science experiment will be high enough so that the dopant atoms are covered with CO* (partially or fully), but also low enough so that the host coinage metal is free of CO*. This would be possible due to the significant difference between adsorption energies on each metal atom within the alloy. In this case, the CO*–CO* lateral interactions become prominent and force the dispersion of the dopant atoms on the (211) and (100) coinage metal surfaces. In particular, the SAA phase is strongly preferred over the dimer phase under full CO dopant coverage conditions (Figure 44 (c)) in agreement with calculations on the (111) facet.[67] The formation of (100) 1NN and edge dimers is rarely thermodynamically favoured, with the only exception being Ir/Ag. For this particular system, there is a slight preference for aggregation with $\Delta E_{agg}^{2\times CO}$ = -0.06 eV and -0.03 eV for (100) 1NN and edge dimers, respectively. These $\Delta E_{agg}^{2\times CO}$ values are, however, close to zero. They are significantly less negative than the corresponding ΔE_{agg} obtained under vacuum (i.e. -0.40 eV and -0.41 eV, respectively), and so when subjected to entropic forces may result in dispersion (see chapter 8).

Interestingly, the number of CO* molecules bound to dopant cluster has little effect on the thermodynamic preference for forming (100) 2NN aggregates. In the presence of a single CO* adsorbed on these configurations, the stable adsorption site is the dopant top site for all binary alloys, so aggregation cannot be promoted. This could be enabled, however, using larger adsorbates that are also bidentate (e.g. C_2H_2) or chelating.[239] In addition to the weak interactions between dopant atoms of the (100) 2NN dimer, we find that CO*–CO* interactions are also small given the large distance between the dopant atoms. This is reflected by the relaxed geometry of the two CO* molecules, which remain sharply vertical to the dopant top sites (see bottom inset in the legend of Figure 44 (c)).

Finally, aggregation for trimer configurations, in the presence versus in the absence of CO*, is analysed in a similar manner and the results are presented in Appendix IV (Figure A20). Aggregation energies, ΔE_{agg}, are calculated under vacuum conditions, and in the presence of 1 × CO, 2 × CO and 3 × CO.

7.2.4. Case study on Rh/Cu SAA: theory and experiments

The previous sections presented an extensive study in relation to the thermodynamic stability of the SAA phase over various bimetallic surfaces. According to the aggregation calculations, for the vast majority of the investigated bimetallic alloys there is a preference for atomic dispersion by the dopants under vacuum conditions. Indeed, the formation of the SAA phase has been experimentally confirmed for many systems, and one of them is Rh/Cu.[240] Under the supervision of Prof. Charles Sykes, Yicheng Wang prepared three low–index Rh/Cu SAA surfaces ((111), (100) and (110)), which were then imaged by means of STM under ultra–high vacuum (UHV) conditions – (Figure 45).[241] Alloying occurred under identical conditions over the three single crystals, and the thermodynamic stability of the SAA phase was confirmed by a series of STM images. This is congruent with our DFT predictions, which underline the enthalpic preference of Rh atoms to be isolated under vacuum (Figure 44 (a)).

A peculiar feature though is that on the Cu(111) surface Rh atoms are densely packed close to the step edge region of the crystal. The same is not observed for (110) and (100) surfaces, where Rh atoms are randomly distributed, thereby forming a uniform SAA phase. This interesting observation hints that the alloying mechanism differs on surfaces with different geometries, but also that kinetic effects might be pronounced under realistic conditions. Consequently, the observed behaviour cannot be explained by our DFT calculations that disregard the kinetics of surface processes that occur upon alloying.

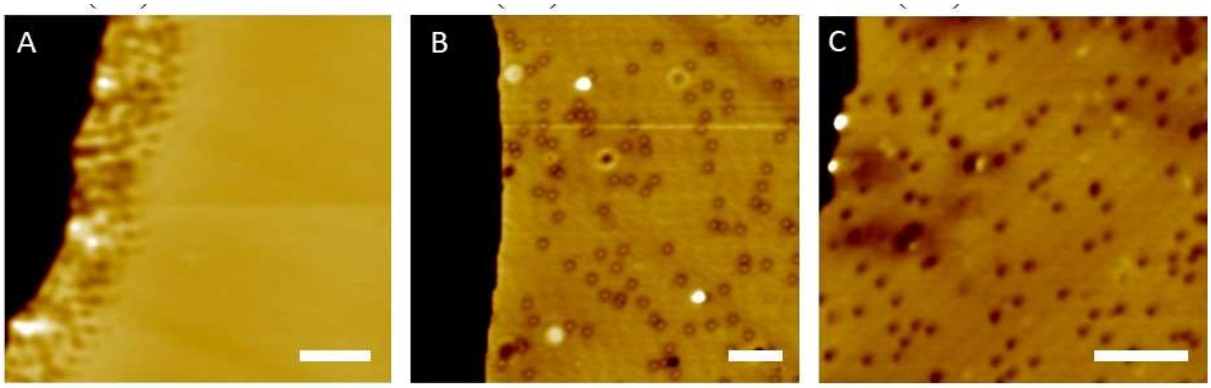

Figure 45. STM images of 0.01 ML RhCu SAAs. (A) RhCu(111) where dense brims of Rh appear in the regions above step edges; Rh atoms appear as depressions. (B) RhCu(100) in which isolated Rh atoms can be seen alloyed throughout the terrace. (C) RhCu(110) in which isolated Rh atoms are also seen alloyed throughout the terraces. Typical imaging conditions: 300 mV and 300 pA. The scale bars are 5 nm. All SAA surfaces were prepared via Rh deposition on Cu held at 380 K followed by cooling to 80 K for STM imaging. *STM images acquired by Yicheng Wang from Sykes group at Tufts University*. *The figure was prepared by Yicheng Wang.*

In order to clarify the disparate behaviour of the three facets, we performed DFT calculations that provide the kinetic barriers for different types of Rh diffusion. Our computational investigations included three types of diffusion. The first is known as *hopping diffusion*, where an Rh adatom is visualised as a hard sphere, which slides over a corrugated plane (i.e. the surface) – (Figure 46 (a)). The second is diffusion *via exchange*, that is often the prevailing one on more open surfaces.[242] In this case, a Rh adatom, which is adsorbed on a hollow site, displaces a neighbouring Cu atom from the surface, and the latter atom becomes the "new adatom" (Figure 46 (b)). The last diffusion mechanism is diffusion *via* an existing vacancy in the host material. This *vacancy–mediated exchange* diffusion first requires the formation of a vacancy on Cu, and then this vacancy is filled by the Rh adatom (Figure 46 (c)). The computational setup that was used for these calculations is slightly different than the one described in the beginning of the chapter, and a short description is given in Appendix IV.

Figure 46 (a) shows that simple Rh adatom hopping is significantly more facile on the Cu(111) surface ($E_{a,fcc\rightarrow hcp}$ = 0.23 eV or $E_{a,hcp\rightarrow fcc}$ = 0.06 eV) surface than on Cu(100) – ($E_{a,(100)}$ = 0.90 eV) and Cu(110) – ($E_{a,(110)}$ = 0.37 eV). It should be noted that the reported hopping barrier for Cu(110) in Figure 46 (a) involves Rh hopping along the rows of the Cu(110) surface (see Appendix IV). Also computed is the corresponding barrier for Rh hopping across these rows, but this is a large kinetic barrier (1.82

eV). This high value implies that diffusion across the rows will be highly unlikely *via* hopping, in qualitative agreement with previous works.[243]

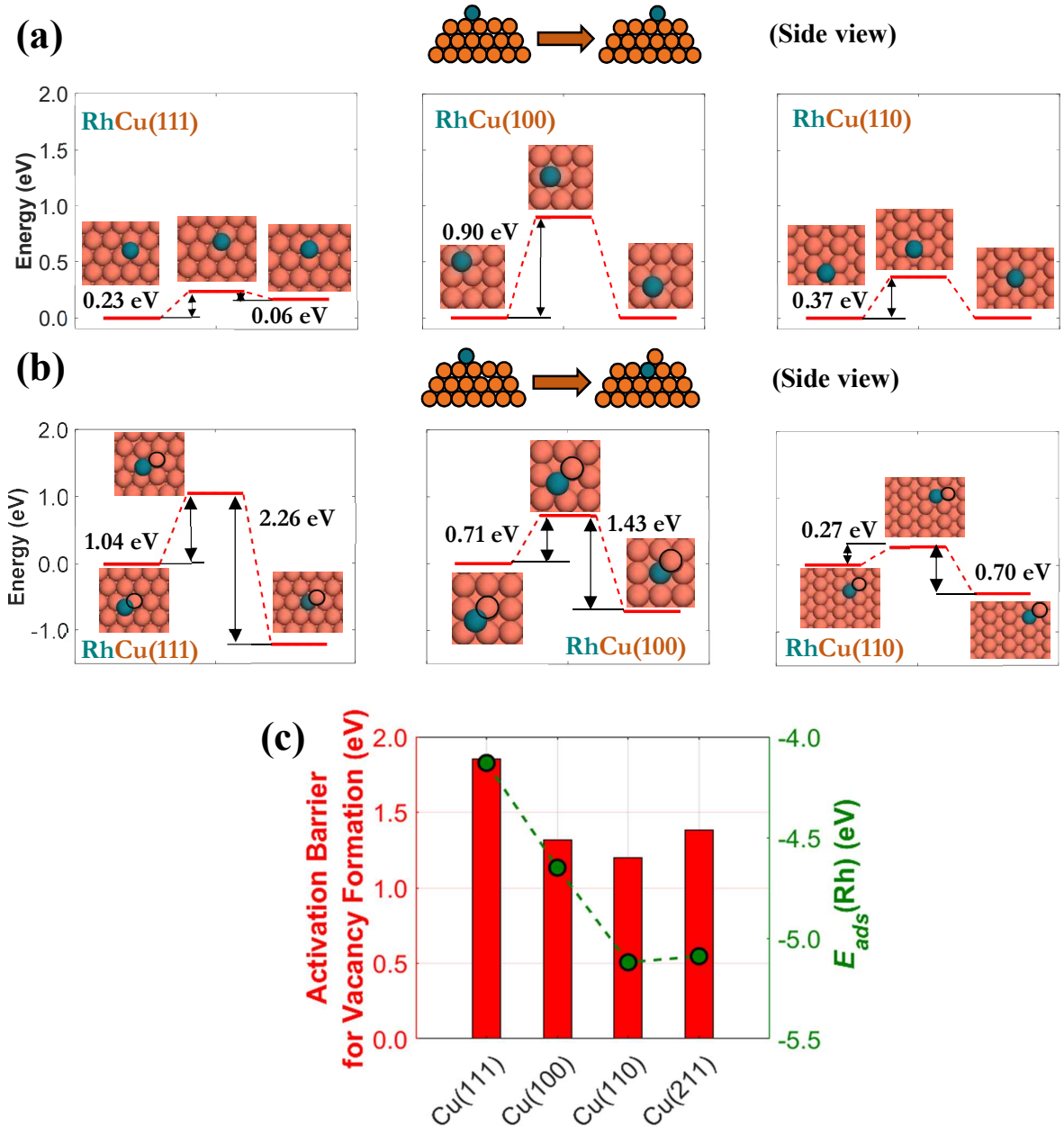

Figure 46. DFT–computed kinetic barriers for (a) Rh hop diffusion; and (b) atomic exchange for the three investigated low–index surfaces. A side view representation of the different alloying steps is given above each panel, where we only show states that correspond to a minimum in the PES. Cu and Rh atoms are shown in orange and teal, respectively. Cu atoms that participate in an event are annotated by black circles. (c) Energy cost for vacancy formation on pure Cu surfaces and adsorption energies of an Rh adatom on the most stable adsorption site of the same surfaces.

Regarding to the atomic exchange, we find that this process proceeds in a similar manner on the three Cu surfaces: the Rh adatom is initially adsorbed on a hollow site; in the transition state a Cu

atom is “lifted–up” by the adatom and a “Rh–Cu dimer” is formed above a surface vacancy; in the final state Rh is integrated into the Cu host surface, while the lifted–up Cu atom ends up as an adatom over a mixed hollow site (Figure 46 (b)). Contrary to the previously discussed hop diffusion (Figure 46 (a)), atomic exchange events are much more easily activated on the open Cu(100) – ($E_{a,(100)}$ = 0.71 eV) and Cu(110) – ($E_{a,(110)}$ = 0.27 eV) surfaces as compared to Cu(111), where $E_{a,(111)}$=1.04 eV. As a result, the computed barriers in Figure 46 (a) and Figure 46 (b) indicate that the predominant alloying mechanism toward the SAA phase will be different among the three low–index surfaces, and begins to explain the observed disparate distribution of Rh atoms over these three surfaces (Figure 45). In particular, Figure 46 (a) and (b) corroborate that Rh atoms which land on Cu(111) will be able to diffuse *via* hopping across the surface before they experience the appropriate alloying sites (e.g. step edges) that enables them to integrate into the Cu host surface. By contrast, Rh integration *via* direct atomic exchange into the terraces of the Cu host will be more favorable on Cu(100) and Cu(110) than hopping. This allows Rh adatoms to incorporate easily and directly in the terraces, and therefore form a uniform and well–dispersed SAA phase over the entire single crystal surface (Figure 45).

The critical step in relation to the vacancy–mediated diffusion is the formation of a vacancy on the Cu crystal. Figure 46 (c) displays the barriers for this process on pure Cu(111), Cu(100) and Cu(110) surfaces. The energy cost for vacancy formation is also computed on the (211) surface, which models the step, and its close vicinity, in Figure 45 (A). The principal observation is that the formation of vacancies are much more facile on the more open Cu (100) and Cu(110), and the stepped Cu(211) surfaces than on the densely packed Cu(111). Therefore, the high concentration of Rh atoms in the vicinity of step edges of Cu(111) – (Figure 45 (A)) may be explained by the following four factors: (i) the fast Rh adatom hopping on Cu(111) – (Figure 46 (a)); (ii) the higher susceptibility of the region near the step towards the formation of vacancies as compared to the densely packed (111) plane (Figure 46 (c)); (iii) the relatively easy integration of a Rh adatom into an existing vacancy on the Cu(111) surface (not shown) and (iv) the high stability of a Rh atom embedded in the Cu(111) host surface (see

the first inset in Figure 46 (a). The significantly stronger binding of Rh adatoms on Cu(211) as compared to Cu(111) is the force that drives these species on the area near the step (Figure 46 (c)).

Finally, it is interesting that although DFT predicts Rh atoms will tend to segregate to the bulk of Cu (Figure 43), the STM images reveal that Rh atoms mostly remain on the top layer. This is, however, the result of the kinetic trapping of Rh atoms on the surface layer because of the very large barriers for segregation to the bulk (E_a = 2.0 eV and 1.80 eV for Rh/Cu(111) and Rh/Cu(100), respectively (see Figure A21 in Appendix IV).

7.3. Concluding remarks

In summary, we examined the surface aggregation and surface segregation of dopant atoms on dilute alloys surfaces by means of DFT calculations. For the majority of the investigated systems, the dopant atoms prefer to form a well–dispersed phase under vacuum conditions, while this trend may be reversed, and clustering may occur, by exposing the surface to CO. The following chapter is also dedicated to the surface restructuring of dilute alloy surfaces, but this is studied by means of an alternative approach that combines DFT calculations and Monte Carlo simulations.

Chapter 8

8. Engineering the surface architecture of highly dilute alloy under reactive conditions

The presented DFT calculations in chapter 7 are useful in that they reveal whether there is an enthalpic preference by dopants to form clusters or to disperse into isolated atoms over the host metal surface. However, this approach does not account for important effects that are present in experiments, such as the CO* coverage, temperature, and configurational entropy effects. This chapter presents an alternative approach, which handles the aforementioned effects, and can be used for sampling the thermodynamically most favourable dopant configurations. This approach relies on lattice–based Monte Carlo (MC) simulations, which are parameterised from DFT calculations, and is employed to examine the surface architecture of Pd/Au(111), Pd/Ag(111), Pt/ Cu(111), Rh/Cu(111), Ir/Ag(111), and Ni/Cu(111) under both vacuum and reactive conditions. Interestingly, the results of our MC simulations suggest that fine–tuning of the surface architecture of highly dilute alloys may be possible by exposing the surface to different CO partial pressures. *The contents of this chapter have been published in ACS Catal. 2020, 10, 1224−1236.*

8.1. Computational details

Density functional theory calculations. The DFT calculations were performed using VASP, and exchange and correlation effects were treated by the RPBE exchange–correlation energy functional.[224] Spin polarized calculations were performed only for the Ni/Cu surfaces. The core ionic electrons were treated using PAW potentials and the valence electronic wave functions were expanded by means of plane waves with an energy cutoff of 400 eV. We modelled the FCC (111) slab using a five–layer p(3 × 3) unit cell. We expect that the presence of a small number of dopant atoms on the surface layer of the alloy surface is unlikely to bring about a change to the lattice constant of the host metal. Therefore, the two bottom–most layers were kept fixed at the corresponding RPBE lattice constant of the host metal (3.64, 4.23, and 4.22 Å for Cu, Ag, and Au, respectively) and the three top–most layers were allowed to relax during ionic optimisation. The Brillouin zone was sampled with a 13 × 13 × 1 Monkhorst–Pack k–point mesh and the Hellmann–Feynman forces on all atoms that are free to move were relaxed to less than 10^{-2} eV/Å. To aid with convergence, we employed the smearing scheme of Methfessel and Paxton with a width of 0.10 eV. The adsorption energy of *m* CO molecules ($E_{ads}(m\cdot CO)$) was computed according to eq. (90).

The DFT–computed formation energies, which are used for the fitting of the CEs (see next subsections), are defined with respect to the DFT total energy of CO gas and the corresponding SAA catalyst, as follows:

$$E_f = E_{tot}\left(n+m\cdot CO\right)+\left(n-1\right)\cdot E_{tot}\left(host\right)-n\cdot E_{tot}\left(SAA\right)-m\cdot E_{tot}^{CO(g)}, \tag{95}$$

where $E_{tot}\left(n+m\cdot CO\right)$, $E_{tot}\left(host\right)$, $E_{tot}\left(SAA\right)$ and $E_{tot}^{CO(g)}$ are the DFT total energies of an alloy surface with a cluster of *n* dopant atoms and *m* CO adspecies, the pure host material and a single dopant atom in the surface layer of the host material, respectively. According to eq. (95), the formation energy of an adsorbate–free SAA surface is zero. Along these lines, the SAA configuration and the CO molecule in the gas phase are used as a reference and therefore the formation energy of any other configuration

is relative to their energies. Negative and positive values of E_f indicate, respectively, geometries with higher and lower stability than the SAA geometry with gas CO. Vibrational frequencies were computed within the harmonic approximation using a finite difference displacement of 0.02 Å. Based on the attained vibrational frequencies of CO in the chemisorbed state, we computed zero–point energy corrected pre–exponential factors for the desorption of CO*.

Monte Carlo simulations. On–lattice Monte Carlo (MC) simulations were performed within the GT framework,[116,126] as implemented in *Zacros* (version 2.0).[137] The MC calculations were performed within the grand canonical ensemble with a fixed CO chemical potential (calculated from P_{CO}) and a constant number of dopant/host atoms in each simulation. We performed MC simulations with various dopant loadings (1, 2, 3 and 4%) under vacuum conditions, as well as at various P_{CO} for dopant loadings of 4 %. In the latter calculations, we investigate partial pressures of CO that result in CO* dopant fractional coverages (Ω_{CO}) in the range of $0.0 \leq \Omega_{CO} \leq 1.0$, and we define this quantity as

$$\Omega_{CO} = \frac{N_{CO*}}{N_{Dopant}}, \tag{96}$$

where N_{CO*} is the number of adsorbed CO molecules on the dopant metal atoms and N_{Dopant} is the total number of dopant atoms. As a result of the weak interactions between CO* and the Au(111), Cu(111) and Ag(111) surfaces and the low P_{CO} employed in all simulations, the CO* coverage on the host metal atoms was negligible; however, CO adsorption and CO* diffusion on host metal sites were explicitly taken into account in our MC model (see the following paragraphs).

The simulation lattice contained three different site types, atop, threefold and bridge. The binding strength of CO* on fcc and hcp threefold sites surrounded by dopant atoms is very similar.[67] Therefore, we simplified the MC lattice by using only the fcc threefold site energies to treat both sites, referring to these throughout the text as "threefold". To minimise any finite lattice size effects,[103] we performed preliminary lattice size testing (see Figure A22 in Appendix V). On the basis of our tests, we employed lattices with a total number of sites of 19,200 (3,200 atop sites) and 7,500 (1,250 atop

sites) for the simulations under vacuum conditions and in the presence of CO, respectively, as there were no notable lattice size effects in either case (see Figure A22 in Appendix V). A representative lattice structure used in our simulations is shown in Figure 47. Each top site is connected with 18 sites, including the closest 6 atop sites, 6 bridge sites and 6 threefold sites (Figure 47). For example, the atop site shown in black in Figure 47 is connected with all the surrounded sites shown in green. Moreover, each bridge site is connected with 8 neighbouring sites: the closest 2 threefold sites, 4 bridge sites and 2 atop sites. Finally, each threefold site is connected with the closest 3 atop sites and 3 bridge sites (Figure 47).

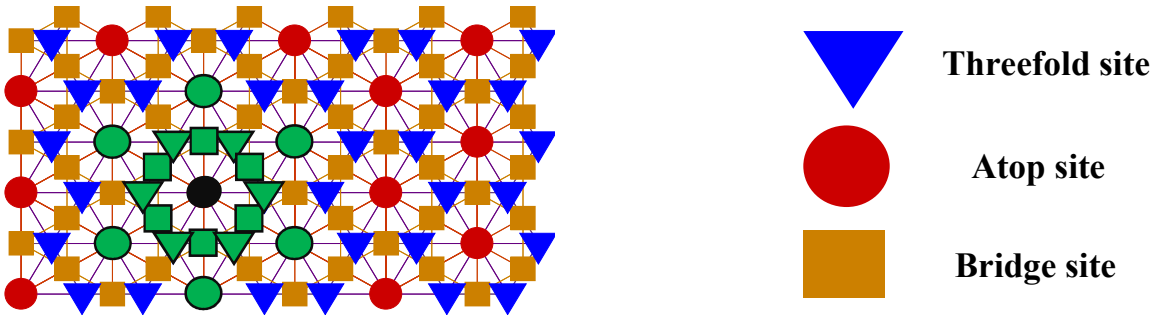

Figure 47. Lattice employed in MC simulations. Three site types are considered: atop (shown as red circles), threefold (shown as blue triangles) and bridge (shown as orange squares). The sites that are connected with the atop site shown as black circle are shown in green.

In order to capture both the state of CO* adlayer and that of the alloy surface with our model, we adopt the following conventions: atop sites are always covered by one of the following four species: a bare dopant atom (i.e. not covered by CO*), a bare host atom (i.e. not covered by CO*), a CO*–covered dopant atom or a CO*–covered host atom. Importantly, the last species appears only on Au– and Ag–based alloys, where CO* can adsorb in all the host metal site types; these are atop, bridge and threefold. By contrast, the adsorption of CO on Cu atop site on the Cu(111) surface is significantly less stable than on Cu–Cu bridge and threefold fcc site (E_{ads} (CO) of -0.51 eV, -0.48 eV and -0.35 eV for threefold, bridge and atop sites, respectively) and therefore the adsorption and diffusion of CO on Cu atop sites are excluded from our MC model. In addition, bridge or threefold sites can be either vacant or occupied by CO*. This gives rise to 5 species that are considered for the Cu–based alloys in

our MC simulations: dopant atom, host atom, CO*–threefold, CO*–bridge, CO*–top dopant. Along the same lines, there are 6 species considered for Au– and Ag–based: dopant atom, host atom, CO*–threefold, CO*–bridge, CO*–top dopant and CO*–top host.

We allowed for several state–to–state events to occur on the lattice during the MC simulation including: i) swaps of atop surface species (e.g. dopant metal atoms, host metal atoms and dopant atoms with a CO* molecule attached); ii) CO* diffusions from one site to another; and iii) CO adsorption on different site types (Figure 48). We consider 17 state–to–state events in total (Figure 48), from which only the adsorptions/desorptions of CO* are actual elementary events. In contrast, the rates of CO* diffusion events and species swaps are set to be much faster than CO* adsorption/desorption so that stationary conditions are reached efficiently in the simulation. In any case, given enough simulation time, the system would sample the most thermodynamically favourable surface configurations, in line with the objective of our study, which did not aim at resolving the kinetics of the host–dopant atom swaps.

CO adsorption events are treated as non–activated, and we compute the kinetic constant of CO adsorption (or equivalently the pre–exponential factor) using the 2D gas model (see eq. (83)). The rate constant for the desorption of CO* is calculated using the Eyring equation as derived from harmonic transition state theory:

$$k_{des} = \frac{Q_{vib,\mathrm{CO}_{(g)}} \cdot Q_{transl,\mathrm{CO}_{(g)}} \cdot Q_{rot,\mathrm{CO}_{(g)}}}{Q_{vib,\mathrm{CO}^*}} \cdot \frac{k_B \cdot T}{h} \cdot \exp\left(\frac{\Delta E_{ads}}{k_B \cdot T}\right), \tag{97}$$

where $Q_{vib,\mathrm{CO}_{(g)}}$, $Q_{transl,\mathrm{CO}_{(g)}}$ and $Q_{rot,\mathrm{CO}_{(g)}}$ are the vibrational, translational and rotational partition functions of a CO molecule in the gas phase, ΔE_{ads} is the adsorption energy and Q_{vib,CO^*} is the vibrational partition function for a CO molecule, which is chemisorbed on the alloy surface.

We highlight that the actual values of k_{ads} and k_{des} are not important, as we are not interested in the kinetics; yet, their ratio has to be correctly calculated, because it is directly related to the chemical potential of gas CO. Thus, based on the equations above and those presented in chapter 3 (see eq. (43)

– eq. (49)), we find the ratio of the forward over the reverse pre–exponentials for all the CO adsorption events (reactions 12–17 in Figure 48). The use of these pre-exponential ratios in our calculations ensures their thermodynamic consistency.

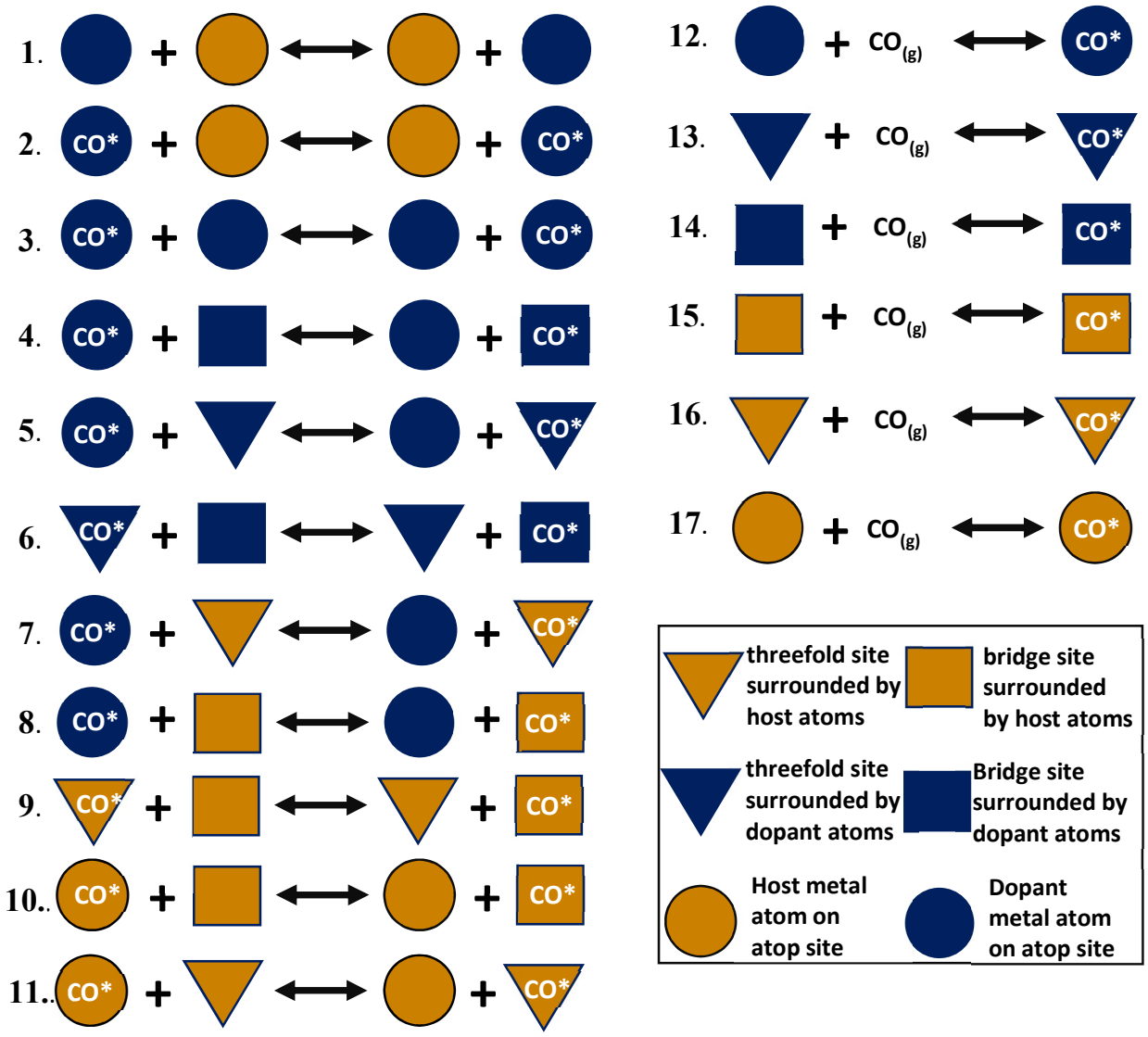

Figure 48. Schematics of the microscopic processes included in the reaction mechanism of the MC simulations. Processes 1–3 correspond to swaps of surface species; processes 4–11 are diffusions of CO and processes 12–17 are CO adsorptions on the different site types. Dopant and host metal atoms are shown as blue and orange circles, respectively. Bridge sites surrounded by dopant and host metal atoms are shown as blue and orange squares, respectively; similarly for threefold sites but with triangle symbols. Adsorbed CO is denoted as CO*. We note that all the microscopic processes are included in the reaction mechanism of Au– and Ag–based alloys. For Cu–based alloys the adsorption of CO on Cu atop sites is omitted and therefore processes 10, 11 and 17 are not included in the reaction mechanism.

Along the same lines, the thermodynamically consistent pre–exponential ratios of CO* diffusion events (reactions 4 – 11 in Figure 48) were calculated on the basis of a thermodynamic cycle (see Appendix V), which includes CO adsorption to one site type, then diffusion of CO* from this site type to another site type and finally desorption of CO* from the latter site.

In all simulations, the MC lattice was initialised without any CO* species adsorbed on the surface. Each atop site was occupied by either a dopant or a host atom, and the dopant loading remained constant at all times. We consider several surface aggregates, referred to as surface species from here on, including isolated dopant atoms (i.e. monomers), contiguous dopant dimers and trimers, but also island species that contain more than 3 dopant atoms. The system was allowed to reach stationary conditions, detected by having a constant average number of surface species and Ω_{CO} over a time–window. Under these circumstances, the lattice state was frequently sampled and the average fractional coverage of a particular surface dopant atom species k (single atoms, dimers, trimers, …), $\overline{Y_k}$, was computed using eq. (98):

$$\overline{Y_k} = \frac{1}{N_{MC,conf}} \sum_{i=1}^{N_{MC,conf}} Y_{k,i} = \frac{1}{N_{MC,conf}} \sum_{i=1}^{N_{MC,conf}} \left(\frac{N_{k,i}}{N_{tot,i}} \right), \qquad k \in \{Monomers, Dimers, Trimers, ...\} \quad (98)$$

where $Y_{k,i}$ is the fraction of dopant species k in snapshot i, $N_{MC,conf}$ is the number of lattice snapshots taken under stationary conditions, $N_{k,i}$ is the number of dopant species k in snapshot i and $N_{tot,i}$ is the total number of species detected in snapshot i. It follows that the number of dopant atoms (N_D), which is constant in each simulation, is linked to the fractions of the dopant species as shown in eq. (99):

$$N_D = N_{tot} \cdot \sum_{m=1}^{D_{\max}} Y_m \cdot m \,, \quad (99)$$

where N_{tot} is the total number of species in a particular snapshot, Y_m is the fraction of species with m dopant atoms and D_{max} is the number of dopant atoms contained in the largest species existing on the alloy surface. To simplify the analysis, we will lump together any species larger than trimers into a class of species referred to as *islands*.

Cluster expansion Hamiltonians. We have performed an approximate total of 240 DFT calculations with various dopant and CO* arrangements on the alloy surfaces in this study. Using this DFT dataset, we have fitted a CE for each alloy system,[118] enabling the fast computation of the energy of arbitrarily complex configurations formed on the MC lattice during simulation. The CE method was recently implemented in the GT–KMC framework by Nielsen et al.[116] and within this formalism, the energy, $H(\sigma)$, of a configuration σ is expanded in "clusters" or "figures". These clusters represent single– to multi–body terms with a certain energy contribution to the total energy of a lattice configuration, $H(\sigma)$, which is given by eq. (58).

We again note that an exact CE can in principle be built by incorporating a very large number of clusters in the energetics model. Yet, the calculation of the ECI parameters for such a large number of incorporated clusters would require an impractically large number of DFT calculations. In addition, it is known that the inclusion of an excessive number of terms in the CE gives rise to overfitting issues.[20,108] A common practice in order to overcome these challenges is to truncate the CE, by choosing an appropriate small set of energetic clusters, based on which one can accurately compute the energy of any on–lattice adsorbate configuration. After fitting the truncated CE, its performance is assessed by statistical measures such as the LOOCV score (see section 3.5), which indicates the predictive capacity of the CE.

In our CEs, we consider explicitly the spatial arrangement of dopant and host atoms in the lattice top sites, as well as CO* as an adsorbate (surface species). This adsorbate can be bound to dopant top sites, bridge sites formed by two neighbouring dopant atoms (dimer), threefold sites surrounded by a dopant triangle (trimer) and to the most stable adsorption sites on the host (111) surfaces. The latter sites correspond to bridge and threefold sites on Cu(111) surfaces and atop, bridge and threefold sites on Au(111) and Ag(111) surfaces.[67] Our DFT calculations show that the adsorption of CO* on mixed sites (i.e. bridge sites between a dopant atom and a host metal atom or threefold sites between 2 dopant atoms and 1 host) is not stable. This is in agreement with earlier DFT–based studies[51]

and high–resolution electron energy–loss spectroscopy (HREELS) works, which for example corroborate that CO adsorption can be stable on mixed Ni–Cu bridge sites only at high CO* coverages and temperatures lower than 130 K.[244] Accordingly, it is ensured that CO* adsorption is not stable on mixed sites by assigning a high ECI value to clusters formed by CO* and a mixture of dopant and host metal atoms (see Figure A25 in Appendix V). This value is 10.0 eV, which is appropriate for the temperature range of our studies, since it is much larger than $k_B \cdot T$ at all temperatures considered.

In our CEs, we consider terms with a different number of dopant atoms in various geometries (see Figure A25 in Appendix V). Furthermore, we include several two–body CO*–CO* interaction terms in the energetics (CO adspecies are adsorbed on different site types) with up to 2nd nearest neighbour interaction range. Figure 49 shows the parity between the DFT–computed formation energies of the geometries in our DFT datasets sets and the CE–predicted formation energies. Moreover, Table 4 shows the number of figures included in the CE of each alloy, the number of DFT geometries used to fit each CE, the root–mean square (RMS) errors between the DFT–computed and CE–predicted formation energies, as well as the calculated *CV* scores. We briefly note that the *CV* score and the RMS errors are normalised with respect to the number of top sites (Table 4).

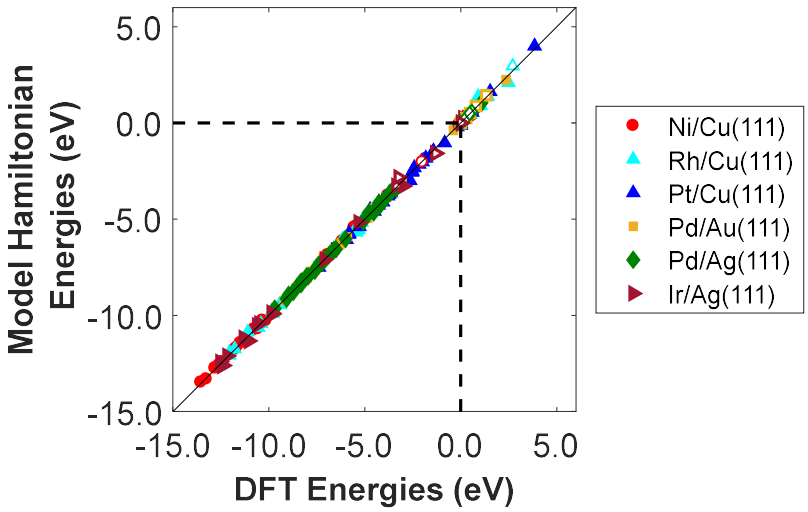

Figure 49. Parity between the DFT–computed and the CE–predicted formation energies of the geometries included in the DFT datasets of all investigated alloys. Open symbols represent the formation energy of clean geometries (i.e. geometries without CO adsorbed)**.** Positive energy values correspond to geometries of lower stability than the SAA geometry. The dashed lines indicate the formation energy of the SAA geometry, which is used as a reference.

Table 4. Tabulation of the details of the CEs for each investigated surface in the present work.

Surface	Figures included in the CE	Number of DFT Geometries	Root-mean square between DFT and CE (meV/site)	*CV* score (meV/site)
Ni/Cu(111)	19	42	10.0	2.7
Rh/Cu(111)	20	36	24.0	8.0
Pd/Ag(111)	20	42	9.0	3.0
Pd/Au(111)	20	46	10.0	3.2
Pt/Cu(111)	19	35	17.0	6.5
Ir/Ag(111)	19	41	31.0	9.7

8.2. Results and discussion

We investigate the surface aggregation of dopant atoms over a number of (111) highly dilute alloy surfaces. Simulations are performed under vacuum conditions (P_{CO} = 0), as well as in the presence of gas CO at different concentrations (i.e. various P_{CO}). In the latter case, the chemical potential of CO is such that the CO* dopant fractional coverage, Ω_{CO}, is within the range of 0.0 – 1.0 (see eq. (96)), whilst the host metal remains almost free of chemisorbed CO during simulation.

8.2.1. Surface aggregation of dopant atoms under vacuum conditions

We first use our MC model to investigate the effect of the dopant loading on surface aggregation under vacuum conditions. We study (111) surfaces of various dopant loadings within the range of 1 – 4 % at 350 K. Dopant loadings within this range are typically found in SAA catalysts employed in experimental studies.[34,234,245] SAA catalysts are prepared by methods whereby the dopant atoms are deposited on the surface of the host metal (galvanic replacement for NP synthesis[39] and vapour deposition in surface science).[34] Accordingly, we assume that the barrier for diffusion of dopant atoms from the surface layer to the bulk is sufficiently large so that dopant atoms will be kinetically trapped on the surface of the catalyst under vacuum conditions and not segregate into the bulk of the alloy (see section 7.2.4 and Figure A21). Indeed, we note that a number of SAAs are kinetically stable as extended surfaces and NPs, despite having a thermodynamic preference for dopant atom segregation

into the bulk.[67,125,234,246] Sykes and co–workers have highlighted the importance of the temperature under which the dopant deposition happens;[247] they studied the Pd/Cu(111) structure showing that only when Pd deposition occurs at high temperatures (e.g. 500 K), there is a significant fraction of Pd atoms segregating into the subsurface layer of the alloy.[247] Conversely, when Pd deposition took place at 350 K the vast majority of Pd atoms remained on the surface layer. Along the same lines, HREELS studies have shown that on Ni/Cu(111) surfaces, segregation of Ni atoms into the bulk takes place only when Ni deposition occurs at temperatures higher than 475 K.[248] Finally, under reactive conditions, and particularly in the presence of CO*, dopant atoms are generally very stable on the surface layer of highly dilute alloys as a result of the strong CO*–dopant interactions.

In addition, we assume that the deposition of the dopant onto the host metal surface occurs at high enough temperatures so that dopant atoms are mixed in the matrix of the host metal, thereby forming a surface alloy. According to the pioneering work of Garfunkel and co–workers,[248] deposition of Ni on Cu(111) surfaces within the temperature range of 375 – 475 K inhibits the formation of Ni 2D and 3D islands on (top of) the host surface, and also prevents the segregation of Ni into the bulk of the alloy.

Figure 50 shows the results of our MC simulations under vacuum conditions for all the alloys under investigation. A general observation is that within the examined range of 1 – 4 %, there is a small effect of the dopant loading on the surface aggregation. In particular, we simulate a clear thermodynamic preference toward the SAA phase for Pd/Au(111), Pt/Cu(111), and Rh/Cu(111) surfaces for all the considered dopant loadings (Figure 50 (c), (e) and (f), respectively). For all these cases > 0.99. Our calculations are in good agreement with combined surface science and theoretical studies on the Pt/Cu(111) system,[249] where the SAA phase was found to prevail at Pt coverages lower than 6 % of the monolayer. Along the same lines, our simulations are corroborated further by H_2 activation studies on Pd/Au(111) alloys, which have revealed a tendency of Pd atoms to be dispersed at Pd coverages less than 0.05 ML,[234] as well as by recent theoretical works.[250,251] Finally, the same

trend has been suggested by recent DFT studies, in which the aggregation energies (ΔE_{agg}) for the formation of dimer and trimer species for all the aforementioned alloys were found to favour the SAA phase under vacuum.[67]

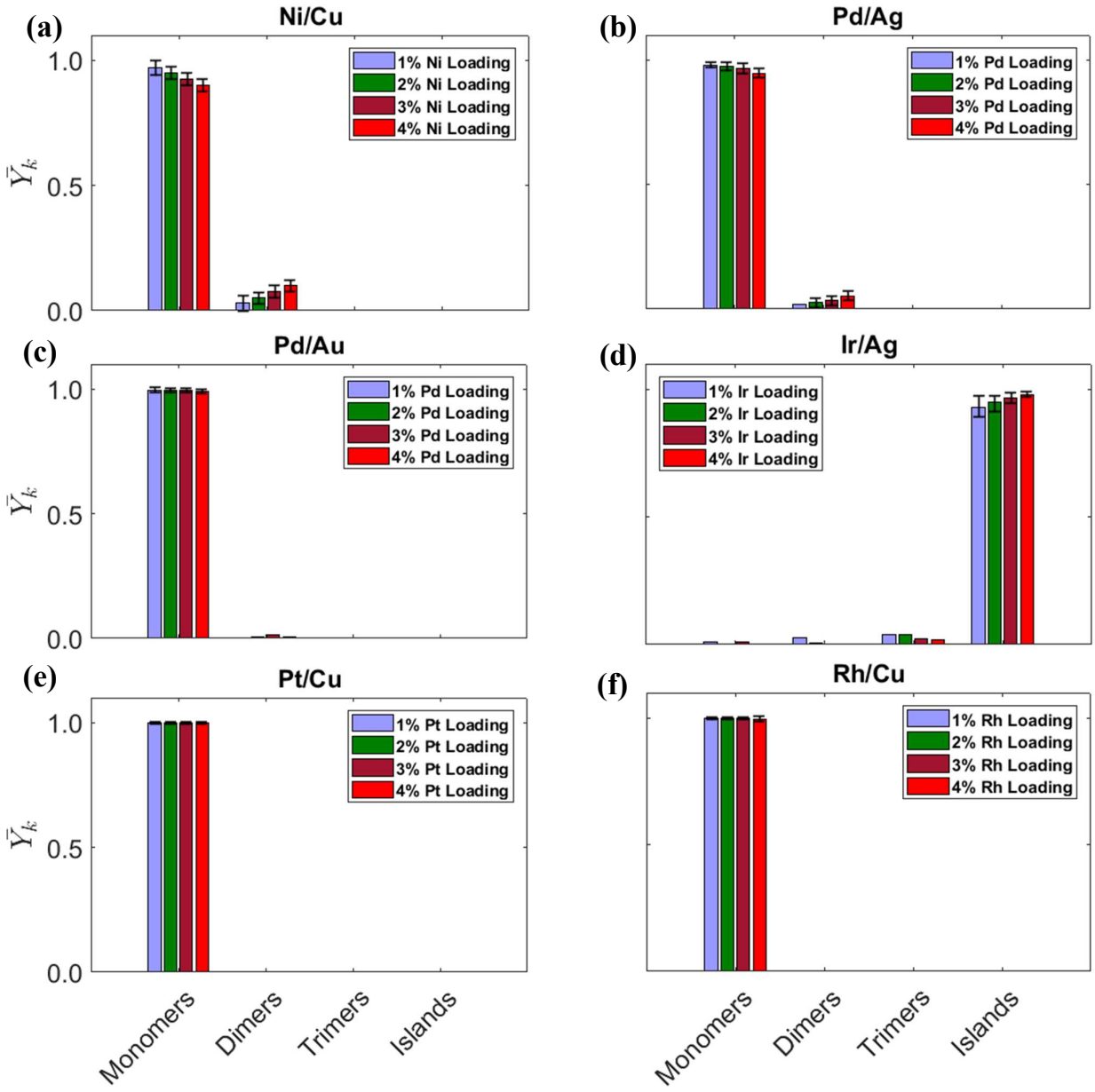

Figure 50. Fractions of surface species at 350 K under vacuum conditions and at different dopant loadings for (a) Ni/Cu(111); (b) Pd/Ag(111); (c) Pd/Au(111); (d) Ir/Ag(111); (e) Pt/Cu(111) and (f) Rh/Cu(111). The error bars are ± one standard deviation.

Conversely, the effect of dopant loading on the surface aggregation is somewhat important on the Pd/Ag(111) and more so on the Ni/Cu(111) surface (Figure 50 (a) and (b)). More specifically, for

Pd/Ag(111) and Ni/Cu(111) surfaces and at 1% PGM loading, we compute a small fraction of dimers of 0.02 and 0.03, respectively (Figure 50 (a) and (b)). However, these dimer fractions are considerably larger at 4 % dopant loading, where = 0.06 and 0.10 for Pd/Ag(111) and Ni/Cu(111), respectively (Figure 50 (a) and (b)). Both cases are quite interesting, as they exhibit a behaviour that could not have been predicted by DFT calculations alone. For instance, under vacuum conditions, the DFT–computed ΔE_{agg} for dimer clusters on the Ni/Cu(111) surface is -0.01 eV.[67] This value is almost zero suggesting that, enthalpically, the SAA phase and the formation of Ni dimers will be almost equally favoured. Yet, our MC simulations suggest that Ni atoms tend to be dispersed (i.e. > 0.85) and that there is only a small fraction of dimers, which becomes larger at increasing Ni coverage. This is attributed to configurational entropy contributions to the free energy of the system, which become increasingly more important at higher temperatures, as those reached under experimental conditions. Similar conclusions hold for the case of Pd/Ag. We point out that these effects of coverage, temperature, and entropy are explicitly considered in our MC simulations, but are not accounted for in DFT calculations, thereby highlighting the value of MC approaches in elucidating the behaviour of such alloys.

Finally, we find that the enthalpic preference for the formation of Ir aggregates on the Ir/Ag(111) surface is sufficiently high, such that there are no isolated Ir atoms thereon. Indeed, previous DFT studies have highlighted the high thermodynamic stability of dopant aggregates (e.g. for Ir triangular trimers ΔE_{agg} = -0.90 eV).[67] Yet, the present MC approach enables us to upscale these previous investigations, thereby showing that Ir aggregates with more than three Ir atoms dominate over the Ir/Ag(111) surface (Figure 50 (d)).

8.2.2. Surface aggregation of dopant atoms in the presence of CO*

CO chemisorption is, in general, more stable on hollow sites of dopant aggregates (i.e. dimers and trimers) than on their atop sites (see chapter 7). Yet, Ir alloys do not exhibit this behaviour; in these alloys, CO adsorption is very stable on the atop sites of Ir trimers and Ir–Ir species (see chapter 7). A CO molecule adsorbed on the hollow site of a dopant cluster can bring about the trapping of the

dopant atoms in neighbouring positions, thereby providing an enthalpic driving force for surface aggregation. In contrast, at high CO* dopant coverage, lateral interactions between CO adspecies will inhibit aggregation.

The ability of CO* to induce or inhibit surface aggregation in bimetallic alloys has been highlighted by MD and DFT,[51,252,253] whilst electronic factors of the surface aggregation of Pd atoms on Pd/Cu(111) surfaces were discussed by Kasai and co-workers.[254] With this in mind, we explore the effect of CO* coverage, Ω_{CO}, on the surface aggregation of dopant atoms on each of the (111) highly dilute alloy surfaces in this study. P_{CO} is varied such that Ω_{CO} takes values in the range of 0.0 – 1.0, and such that the host metal atoms remain almost CO*–free. The dopant loading is kept fixed at 4 % in all the simulations presented in this section. We report Ω_{CO} and $\overline{Y_k}$ at different values of a normalised pressure, P_N (Figure 51 (a) – (f)), which we define as:

$$P_N = \frac{P_{CO}}{P_{CO,max}}, \tag{100}$$

where P_{CO} is the applied partial pressure of CO and $P_{CO,max}$ is the partial pressure of CO for which Ω_{CO} assumes a value close to unity. Therefore, P_N = 1.0 corresponds to dopant atoms approximately fully covered by CO* (i.e. one CO* adspecies per dopant atom) and P_N values close to zero correspond to CO*–free dopant atoms (i.e. vacuum conditions).

We note that for almost all the alloys there is a general thermodynamic preference toward the SAA phase at low P_N (i.e. low Ω_{CO}) – (Figure 51 (a), (b), (c), (e) and (f)). An exception to this is Ir/Ag(111), where we observe that for $\Omega_{CO} < 0.28$, Ir atoms aggregate to form islands (Figure 51 (d)). Moreover, the SAA phase is also favoured on all the alloy surfaces at P_N values close to unity (Figure 51 (a) – (f)), corresponding to almost one CO adspecies per dopant atom ($\Omega_{CO} \rightarrow 1$). Under these circumstances, repulsive CO*–CO* lateral interactions tend to break dopant clusters apart by overcoming any attractive dopant–dopant interactions, thereby promoting the formation of the SAA phase.

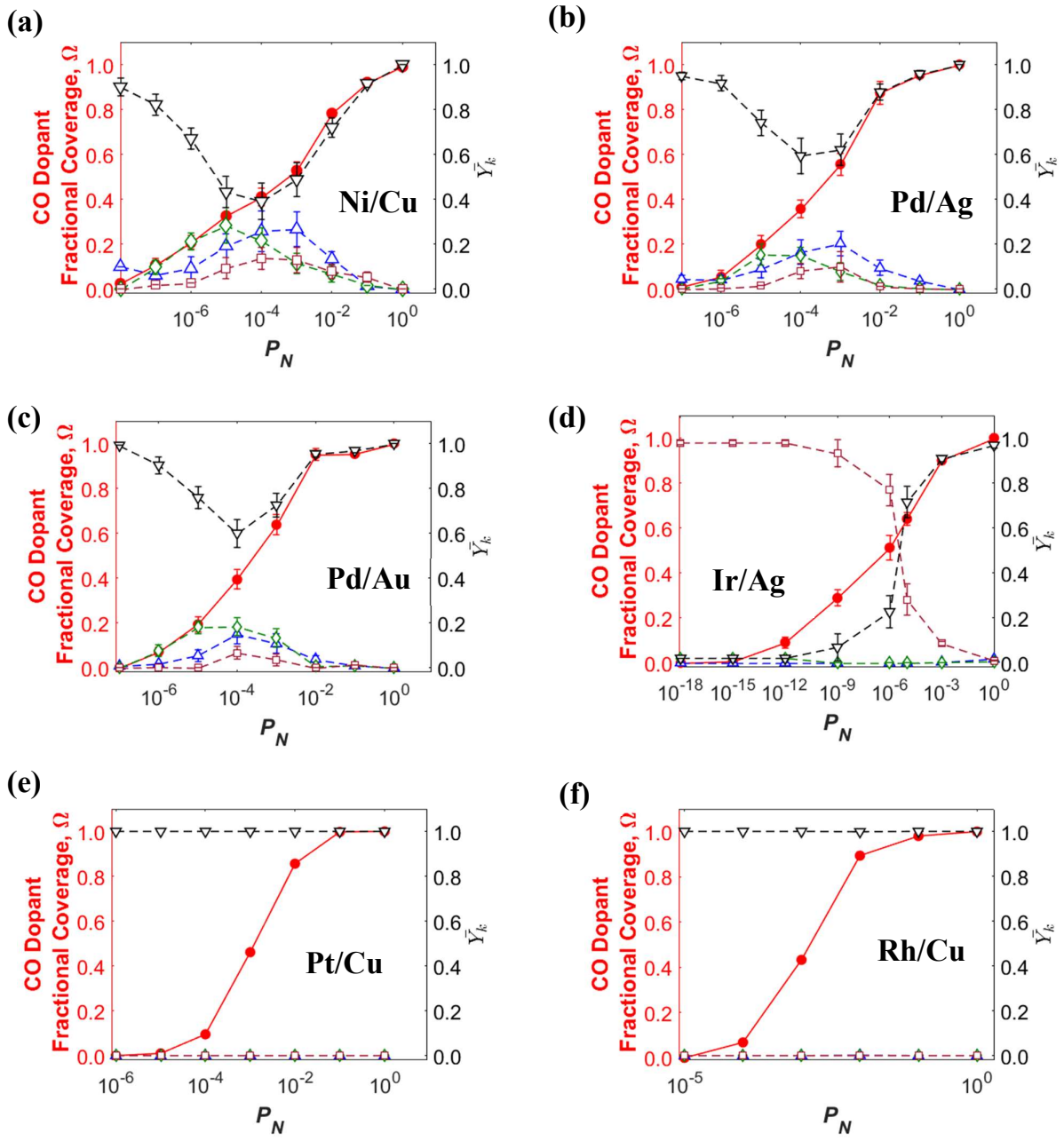

Figure 51. Fractions of surface species at 350 K at different values of the normalised pressure, P_N, for (a) Ni/Cu(111); (b) Pd/Ag(111); (c) Pd/Au(111); (d) Ir/Ag(111); (e) Pt/Cu(111) and (f) Rh/Cu(111). The left y–axis (red) shows the CO dopant fractional coverage, while the right y–axis (black) shows the fraction of different surface species. The dopant loading is 4 % in all cases and the error bars are ± one standard deviation.

On the other hand, we realise that surface aggregation is induced at intermediate CO dopant fractional coverages on Ni/Cu(111), Pd/Ag(111) and Pd/Au(111) surfaces (Figure 51 (a) – (c)). The MC results suggest that dopant dimer and trimer as well as island species are present in significant fractions on the aforementioned surfaces for $0.20 \leq \Omega_{CO} \leq 0.80$. Moreover, the tendency of Ni atoms

to form clusters is particularly pronounced as compared to Pd atoms on Pd/Ag(111) and Pd/Au(111). This high tendency for Ni surface aggregation on Ni/Cu(111) alloys in the presence of CO is in qualitative agreement HREELS studies, but also with very recent reflection adsorption infrared spectroscopy studies.[248,255] Thus, on Ni/Cu(111) at $\Omega_{CO} \approx 0.41$ we compute a relatively low fraction of monomers of approximately 0.39. Interestingly, in all three aforementioned cases the fraction of isolated monomers is minimal at a CO* dopant fractional coverage of approximately 0.40.

Within the range $0.20 \leq \Omega_{CO} \leq 0.80$ there is also a noteworthy phase transition between $\overline{Y_{dimers}}$ and $\overline{Y_{trimers}}$, thereby indicating that one could favour the formation of a particular ensemble of dopant clusters by adjusting P_{CO}. For example, for the three aforementioned alloys, the highest possible fraction of trimers at 350 K is for $0.20 \leq \Omega_{CO} \leq 0.40$. At $\Omega_{CO} \approx 0.2$ the fractions of dopant trimer clusters on Ni/Cu(111), Pd/Ag(111) and Pd/Au(111) are 0.21, 0.15 and 0.18, respectively, whilst the corresponding fractions of dopant dimers are 0.10, 0.09 and 0.06, respectively. By contrast, it is evident that the formation of dimers is promoted for $0.40 < \Omega_{CO} \leq 0.80$ and at $\Omega_{CO} \approx 0.6$, where the computed dimer fractions are in most cases larger than the corresponding trimer fractions and are 0.26, 0.20 and 0.11 for Ni/Cu(111), Pd/Ag(111) and Pd/Au(111), respectively (Figure 51 (a) – (c)).

The DFT–computed ΔE_{agg} for triangular trimer clusters on Ni/Cu(111), Pd/Ag(111) and Pd/Au(111) at $\Omega_{CO} = 0.33$ are -0.36 eV, -0.29 eV and -0.34 eV, respectively. These values are significantly more negative than the corresponding ΔE_{agg} for dimer clusters which are -0.15 eV, -0.14 eV and -0.14 eV for Ni/Cu(111), Pd/Ag(111) and Pd/Au(111), respectively. Accordingly, one would expect that trimer species will dominate over dimer and monomer species. However, our MC simulations (Figure 51 (a) – (c)) reveal that at similar Ω_{CO} (i.e. $0.20 < \Omega_{CO} < 0.30$) the fraction of monomer species is always larger than 0.52, being larger than both between $\overline{Y_{dimers}}$ and $\overline{Y_{trimers}}$. This result highlights the importance of coverage, configurational entropy and temperature effects, which can lead to the substantial population of states that are not the most enthalpically favoured.

Ir atoms in the Ir/Ag(111) surface have a high tendency to form islands at $\Omega_{CO} < 0.28$ (Figure 51 (d)). However, these Ir islands become gradually smaller for higher P_{CO} (i.e. Ω_{CO}), and the SAA phase is "enforced" for Ω_{CO} larger than 0.6. Contrary to the case of Ni/Cu(111), Pd/Ag(111) and Pd/Au(111) alloys, we observe a relatively sharp transition from a phase where island species prevail on the surface to a phase where dopant atoms are isolated and occupied by CO*. During this transition there is very limited, if any, formation of small Ir clusters (e.g. dimers and trimers), and the absence of these small dopant clusters can be attributed to: (1) the more energetically favoured adsorption of CO* on atop sites of Ir clusters as compared to hollow sites; and (2) the very low stability of the SAA phase at low and intermediate CO dopant fractional coverages.

Finally, we study the effect of Ω_{CO} into the restructuring of Rh/Cu(111) and Pt/Cu(111) alloy surfaces (Figure 51 (e) and (f)). DFT studies indicate that these alloys have a very strong enthalpic preference for the SAA phase, independently of the CO dopant fractional coverage. In addition, the high stability of the SAA phase in Rh/Cu(111) and Pt/Cu(111) is underscored in recent works, which focus on Cu–based highly dilute alloys.[236] Indeed, the formation of dopant clusters in Rh/Cu and Pt/Cu is enthalpically unfavourable even in the presence of multi–dentate species (i.e. species that bind to more than one site upon adsorption) such as ethylene (C_2H_2).[239] These results are further supported by our MC simulations, where we find that within the range of $0.0 \leq \Omega_{CO} \leq 1.0$ the fraction of monomer species is always 1.0. Yet, we point out that Rh/Cu and Pt/Cu SAA catalysts are promising toward the efficient catalysis of numerous chemistries of practical interest, and in some cases the formation of contiguous dopant sites may deteriorate their performance for certain applications. A typical example of such a reaction is the selective hydrogenation of 1,3–butadiene to butenes over Pt/Cu alloys, where the formation of large Pt clusters, at high Pt loadings (≈ 30 %), diminishes the selectivity toward butene in favour of butane.[170]

8.2.3. CO influence on the surface morphology of dilute alloy surfaces: experimental evidence

Prof. Maria Flytzani–Stephanopoulos, Prof. Charles Sykes and their groups at Tufts University have explored the possibility of influencing the surface morphology of Pd/Au dilute alloys by exposing them to CO. In particular, Mengyao Ouyang prepared Pd/Au NPs supported on SiO_2 based on sequential reduction, and then used CO–DRIFTS to probe the catalyst surface under different CO* coverages.[256] During the CO–DRIFTS experiment, the catalyst was exposed to 0.1 bar of CO gas and the surface coverage was manipulated by changing the temperature (Figure 52).

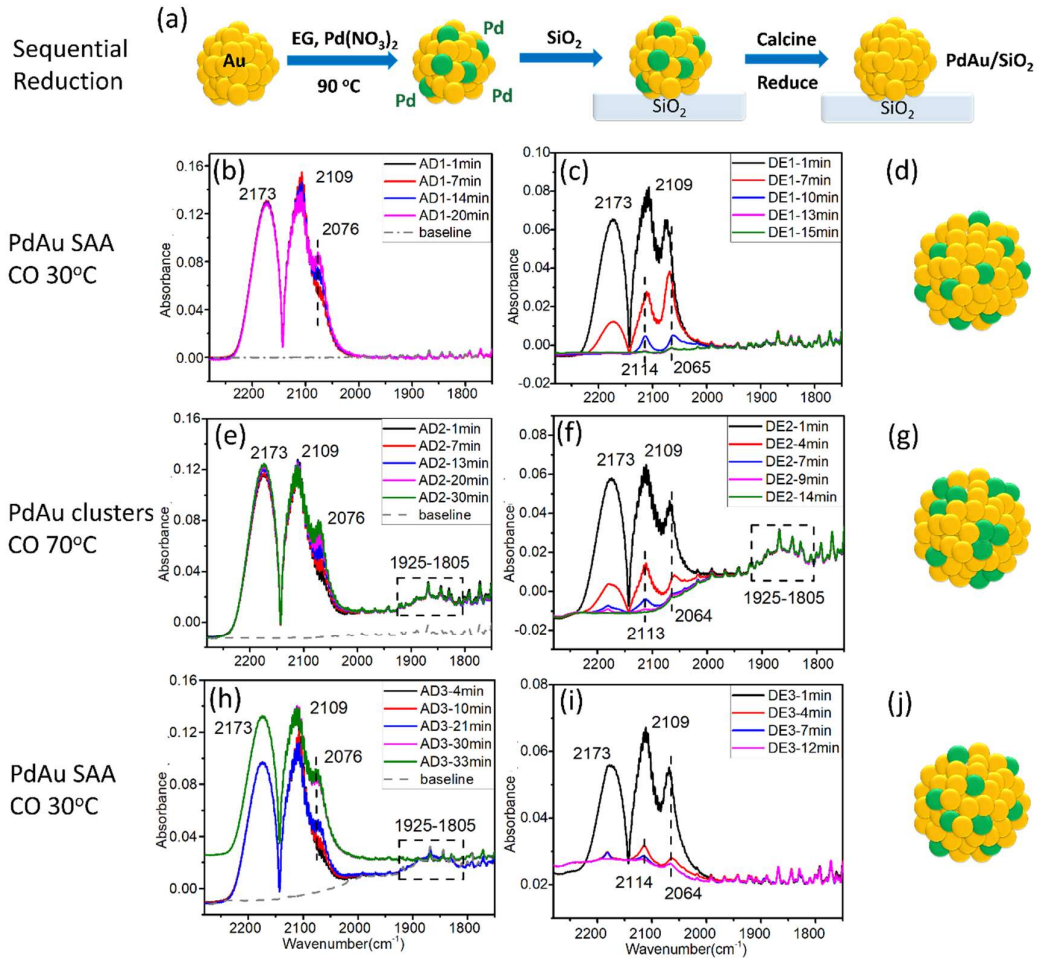

Figure 52. (a) Schematic illustration of $PdAu/SiO_2$ synthesis in which the final reduction step leads to migration of Pd to the interior of the NPs. Proposed structure and CO–DRIFTS results of $Pd_{0.02}Au_{0.98}$ /SiO_2 sample sequentially at 30°C (b) (c) (d), 70°C (e) (f) (g), 30°C (h) (i) (j) during 10% CO/He adsorption (P_{CO} = 0.1 bar) and desorption process. Prior to the experiment, the sample was reduced at 200°C in 5% H_2/He for 1 h in situ. The annotation in the upper right box means CO adsorption (AD) process and He purge process (DE) during some time in each step. *The experiments and analysis were conducted by Mengyao Ouyang – Tufts Nanocatalysis & Energy Laboratory. The figure was reprinted from ref.* [256].

Interestingly, there were stark differences in the retrieved DRIFTS spectra under different conditions, thereby indicating that the catalyst transitioned between the SAA phase and a phase, which was rich in Pd clusters. Upon CO adsorption at 30 ^{o}C, the CO–DRIFTS spectra exhibited three peaks at 2173 cm^{-1}, 2109 cm^{-1} and 2076 cm^{-1} from which the first is assigned to gaseous CO, the second to gaseous CO and CO* adsorbed on under–coordinated sites of Au, and the third to linear CO* adsorbed on Pd top (Figure 52 (b)). The gradual increase of the CO* Pd top peak shows that CO* is causing the segregation of subsurface Pd to the top (Figure 52 (b)) owing to the strong CO*–Pd interaction.[256]

On the contrary, once the adsorption of CO happened at 70 ^{o}C, besides the aforementioned peaks, an additional peak appeared between 1925 cm^{-1} and 1805 cm^{-1} (Figure 52 (e)). The latter peak has been previously assigned to CO* adsorbed on hollow Pd sites,[49,257] thus revealing the formation of Pd clusters at higher temperatures (and therefore lower CO* coverages). Markedly, this is in qualitative agreement with our MC results (Figure 51 (c)), which support that at high CO* coverage Pd atoms tend to be atomically dispersed, while a reduction in CO* coverage can induce surface aggregation. The Pd clusters remained on the surface even after CO* desorption (Figure 52 (f)), and disappeared only after exposure again to CO at 30 ^{o}C followed by CO* desorption (Figure 52 (i)).[256]

To test our computational approach, we performed MC simulations that replicate the conditions of the experiments of Ouyang et al. Under the same conditions (i.e. P_{CO} = 0.1 bar, T = 70 ^{o}C) our model predicted that Pd atoms are fully covered by CO*, and therefore the SAA phase is predominant on the alloy surface. As the quantitative reproduction of the interaction between CO* and metal surfaces is a great challenge for DFT,[258,259] we carried out sensitivity analysis to understand the effect of the binding strength of CO* on the population of different Pd clusters (i.e. Pd monomers, Pd-Pd dimers and Pd trimers) – (see Figure A26 in Appendix V). It appears that DFT overestimates the CO* binding energy as evidenced by (i) the absence of Pd aggregates for the experimental conditions of 70 ^{o}C and P_{CO} = 0.1 bar; and (ii) the systematically lower vibrational frequencies for CO chemisorption on Pd atoms and aggregates in the Pd/Au(111) surface. In particular, the computed

vibrational frequencies of CO* on Pd top, Pd–Pd bridge and threefold sites are 2018 cm^{-1}, 1859 cm^{-1} and 1755 cm^{-1}, respectively, which are lower than the corresponding experimental values (i.e. 2076 cm^{-1}, within 1925-1950 cm^{-1} and below 1900 cm^{-1} for Pd top, bridge and threefold respectively), thereby indicating that the binding strength of CO* is, in every case, overestimated by DFT. In view of this, in our model we used a CO binding energy which is lower than the DFT computed one by 0.2 eV; equivalently an adsorption energy shifted by +0.2 eV, which is the widely accepted error of DFT. This value reproduces substantial populations of Pd aggregates, in line with experimental data for the aforementioned conditions (Figure 53). Given the highly intricate structure of the supported catalyst and also the intrinsic DFT error, this result is encouraging and furnishes evidence that our *ab initio* MC approach is reliable.

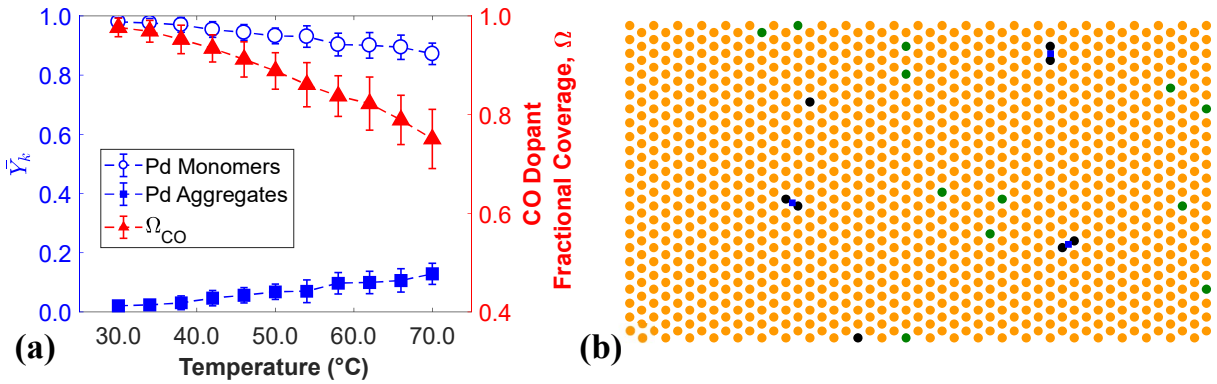

Figure 53. (a) $\overline{Y_k}$ and Ω_{CO} at temperatures within the range of 30 – 70°C for E_{ads}(CO) on Pd surface species that are shifted by +0.2 eV as compared to the DFT–predicted values; P_{CO} = 0.1 bar for all calculations. (b) Representative MC snapshot at 70°C that shows that the majority of Pd aggregates are Pd–Pd dimers. Pd, Au and Pd atoms covered by CO are shown in black, yellow and green, respectively. Bridge sites amid Pd atoms covered by CO are shown in blue. The error bars in panel (a) are ±1 standard deviation.[256]

8.3. Concluding remarks

This chapter presented an *ab initio* Monte Carlo approach that, in contrast to DFT calculations alone, accounts for coverage, configurational entropy and temperature effects. The approach was applied under both reactive and vacuum conditions and was used to study the surface architecture of different dilute alloy surfaces including Pt/Cu(111), Rh/Cu(111), Ni/Cu(111), Pd/Au(111),

Pd/Ag(111) and Ir/Ag(111). Our simulations revealed that different alloys may respond differently when exposed to a reactive environment, and provided "guidelines" on how one may pre–treat these surfaces toward a particular surface architecture. Future works may be dedicated to the incorporation of the kinetics of surface restructuring events (e.g. atomic swapping) in the presented approach, thereby leading to sophisticated dynamic models for the restructuring of dilute alloy surfaces.

Chapter 9

9. Concluding remarks and future work

9.1. Main contributions of this Thesis

This Thesis explored the effects of the adlayer structure and surface morphology on the catalytic activity of materials that exhibit intricate behaviour. These materials can be pure metals, whose performance may be subject to strong adsorbate–adsorbate interactions, or bimetallic alloys, whose surface morphology may be manipulated at will under reactive conditions. Given their rich features, such materials often deviate from established conceptual models (e.g. *d* band model) and can be effectively studied by means of sophisticated computational methods like DFT and KMC, whose underpinning were given in chapters 2 and 3.

Chapter 4 discussed that lateral interactions affect the structure of the adsorbate layer over catalytic surfaces. To demonstrate that, we employed KMC simulations incorporating BEP relations and CE Hamiltonians to model the oxidation of NO on Pt(111). These simulations suggested that the inclusion of interactions of different range and complexity gives rise to disparate adsorbate layer structures and catalytic rate predictions. This result has important implications on two aspects: first, it demonstrates that in systems with an ordered adsorbate overlayer, the strong correlation in the adlayer can lead to interesting effects, whereby the geometry of the domain alone can strongly influence the kinetics. This was clearly demonstrated by the 3–Fig. CE and 8–Fig. CE simulations on periodic lattices, which yield significant differences in TOF between commensurate and non–commensurate lattices; second, the accuracy with which the CE is fitted to density functional theory data can have a decisive effect on the physics reproduced by KMC simulations, even at the qualitative level. Note that all CEs had been fitted to the same DFT data. The only difference was the truncation level, including up to 1NN interactions in the 3–Fig. CE and up to 3NN interactions in the 5–Fig. CE. For this system, a CE with only 1NN interactions leads to TOF values that are very different from those of more accurate CEs, and our detailed analysis explained the origin of such deviations.

Next, we focused on bimetallic alloys like highly dilute and single atom alloys. Chapter 5 investigated the behaviour of typically structure sensitive reactions on a number of SAA(111) and SAA(100) surfaces. In this regard, DFT calculations revealed that isolated dopant atoms show disparate reactivity when are exposed to different coordination environments. Remarkably, however, (dissociation) reactions that exhibit substantial structure sensitivity on PGM surfaces, revealed a "reduced" structure–insensitive on (111) and (100) SAA and coinage metal surfaces. This is a finding with far–reaching implications for future single–crystal and catalysis studies where the activation of chemical bonds is of central importance (e.g. the RDS). In more precise terms, this result implies that studies over the (111) SAA facet may give insight into the behaviour of the (100) SAA facet, and vice versa, thereby accelerating the development and design of optimal SAA catalysts.

Besides SAAs, we also delved into highly dilute alloy surfaces whereon the dopant atoms form small clusters like dimers and trimers. Our screening studies in chapter 5 showed that the performance of Ni_2Cu and Ni_3Cu with respect to association and dissociation reactions, which are important to emission control catalysis, is similar (or even better in some cases) to those of well–established pure metals in heterogeneous catalysis (e.g. Rh, Pt and Pd). Ni/Cu alloys are attractive from a practical standpoint because of their low cost and the abundance of the constituent metals.

Along these lines, we proceeded by studying the decomposition of N_2O* and the NO + CO reactions over the aforementioned surface in chapter 6. Regarding the former reaction, on Cu–based surfaces we identified three different pathways, two of which could not be identified over Rh(111). The existence of these reaction paths provides alternative routes for the decomposition of N_2O* on Ni/Cu dilute alloys, and renders these materials promising for this reaction. Additionally, our microkinetic analysis of the NO + CO reaction underscored that the addition of a small number of Ni atoms on Cu surfaces brings about substantially improved catalytic performance as compared to a pure Cu catalyst, and comparable performance to Rh, thus highlighting the potential of Ni/Cu dilute alloys for emission control catalysis.

Another noteworthy point that emerged from our discussion in chapter 6 was that the selectivity of the N_2O* decomposition reaction could be altered by changing the size of the Ni cluster. In particular, larger Ni clusters (i.e. more than two atoms) appeared to favour the formation of NO* + N*, while smaller clusters favoured the formation of N_2* + O*. This result demonstrated the importance of defining ways to control and manipulate the surface architecture of highly dilute alloys.

Accordingly, chapters 7 and 8 were dedicated to this topic, and presented an *ab initio* MC approach that is capable of highlighting the thermodynamically most stable configurations of dopant atoms on coinage metal surfaces. Using this MC approach, the restructuring of dilute alloy surfaces could be modelled under both vacuum and reactive conditions, and its reliability was verified by experiments. In this Thesis, the reactive atmosphere was modelled by the addition of CO in the gas phase, which was in contact with the catalytic surface. Our results pointed out that in some cases, extensive dopant aggregation can be achieved upon exposure to CO chemical potentials that result in CO* dopant fractional coverages between 0.2 and 0.8 (e.g. Pd/Au(111), Pd/Ag(111) and Ni/Cu(111)). On the same surfaces, the formation of the SAA phase was favoured at high fractional coverages thanks to the repulsive interactions between CO* adsorbed on neighbouring dopant atoms. By contrast, on other surfaces (e.g. Pt/Cu(111) and Rh/Cu(111)), irrespective of P_{CO}, the aggregation of dopant atoms was not possible. Markedly, our *ab initio* MC approach can be readily applied to other bimetallic combinations and adsorbate species, thus serving as a proof–of–principle for the design of bespoke ensembles that can optimise catalytic performance for reactions of practical interest.

9.2. Further research opportunities

The conducted research herein has generated avenues for future research, and so this Thesis is completed with a brief mention in this regard. Future research activities may further our understanding on the performance of Ni/Cu dilute alloys in relation to emission control catalysis. To this end, the first step could be to model the NO + CO reaction by employing KMC simulations combined with BEP

relations and CEs (i.e. the approach presented in chapter 4). Under these circumstances, we will account for adsorbate–adsorbate interactions, thereby building accurate kinetic models.

Another point that merits consideration and could be part of future research is the identification of the active site for the NO + CO reaction on Ni/Cu dilute alloy catalysts. To achieve that, other commonly exposed facets (e.g. (100), (110), (211)), besides the densely packed (111), have to be investigated, and ideally the results should be compared with experimental data. This approach has been established by Mavrikakis and co–workers and has turned out to be successful.[216] Moreover, it is known that under conditions relevant to catalysis, Cu–based catalysts undergo oxidation that results in the formation of a Cu_2O layer on the catalyst surface. The Cu_2O phase has been found to promote the oxidation of CO*,[260] but also the dissociation of NO*.[261] Therefore, studies on the effects of this oxide structure in the catalysis of the NO + CO chemistry could be another topic for future research.

Finally, the ultimate goal would be to build KMC models that account for surface restructuring and reaction simultaneously. These models would provide "*in–situ"* information on how a catalytic surface is restructured when exposed to adsorbates, and on how this restructuring influences the reaction kinetics. Such models would be able to deal with the high complexity of surface reactions, and unveil aspects thereof that will be critical for the development of promising catalytic materials.

Appendix I

- *ECI parameters for the CE of the NO oxidation*

Table A1. Energetic contribution parameters used in this study in Lattice-gas Hamiltonian form and in meV.[116]

Figure	3–Figure CE	5–Figure CE	8–Figure CE
H_0/N_L	-27	45	9
Point	-1200	-1580	-1374
1NN	300	260	156
2NN		84	56
3NN		84	12
4NN			28
5NN			28
6NN			
7NN			
8NN			
1-1-3			64

- *Formation of 2 x 1 O* domains for 8-Fig. CE models*

Figure A1 shows a lattice snapshot from KMC simulation for μ_{O^*} = -0.577 eV and ca. 0.39 ML coverage. We observe domains of 2 × 1 O* order.

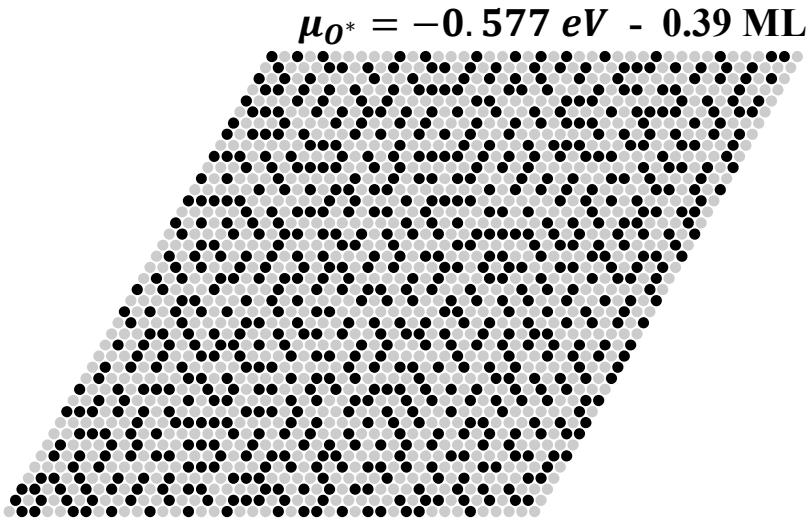

Figure A1. Representative lattice snapshots from KMC simulation at 480 K of an 8–Fig. CE energetics model adlayer structure of a 42 × 42. O* adatoms are represented by black circles and empty sites by grey circles. y_{O_2} = 0.1 bar, P_{NO2}/P_{NO} = 54.5.

- *Formation of anti-phase boundaries*

To understand the cause of the adlayer disruption by anti-phase boundaries we examine two small, periodic lattices (Figure A2 (a) and (b)). The lattice periodicity means that sites lying on lattice edges are connected to others located on opposite sides of the cell. For instance, in Figure A2 (a) site 6 of the 6 × 6 lattice is connected to sites 5, 11 and 12 as well as sites 36, 31 and 1. Similarly, site 5 of the 5 × 5 lattice (Figure A2 (b)) neighbours sites 4, 10 and 9 as well as sites 25, 21 and 1. The 1st nearest neighbours of the sites located in the top left corner of each lattice, are shown in the areas enclosed by the dashed hexagons (Figure A2).

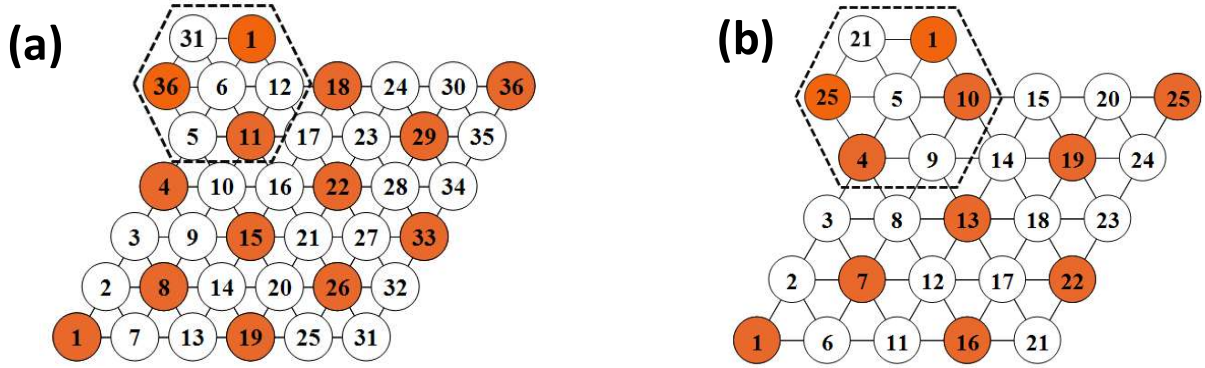

Figure A2. (a) A 6×6 commensurate lattice with the adsorbates (orange circles) organised in ° structure. (b) A 5×5 non–commensurate lattice where the ° is disrupted, as exemplified on the left top corner. White circles depict vacant sites and both lattices are periodic.

Starting from occupied site number 1, we organise adsorbates in the ° structure on both lattices (this is the structure used as the initial configuration of each simulation). On the 6×6 lattice, whose number of sites is divisible by three, we observe that the ° structure is preserved in the area of the dashed hexagon in Figure A2 (a). The adlayer structure is in this case commensurate to lattice size. In more general terms, if **A** and **B** are unit cell vectors of the simulation lattice, then there exist integers z_1, z_2, z_3 and z_4, and unit cell vectors of the adlayer structure **a**, **b**, such that $\mathbf{A} = z_1\,\mathbf{a} + z_2\,\mathbf{b}$ and $\mathbf{B} = z_3\,\mathbf{a} + z_4\,\mathbf{b}$. Thus, no disruption is induced during simulation. On the contrary, Figure A2 (b) shows that defect structures emerge, e.g. around site 5 etc.; the stable ° structure cannot "develop" in this lattice, as is the case of all lattices with dimensions not divisible by 3. The strong repulsions between O* adspecies in 3-Fig.

CE energetics model force adsorbates in the defective regions to rearrange, resulting in the emergence of anti-phase boundaries

Appendix II

- *K-point convergence testing*

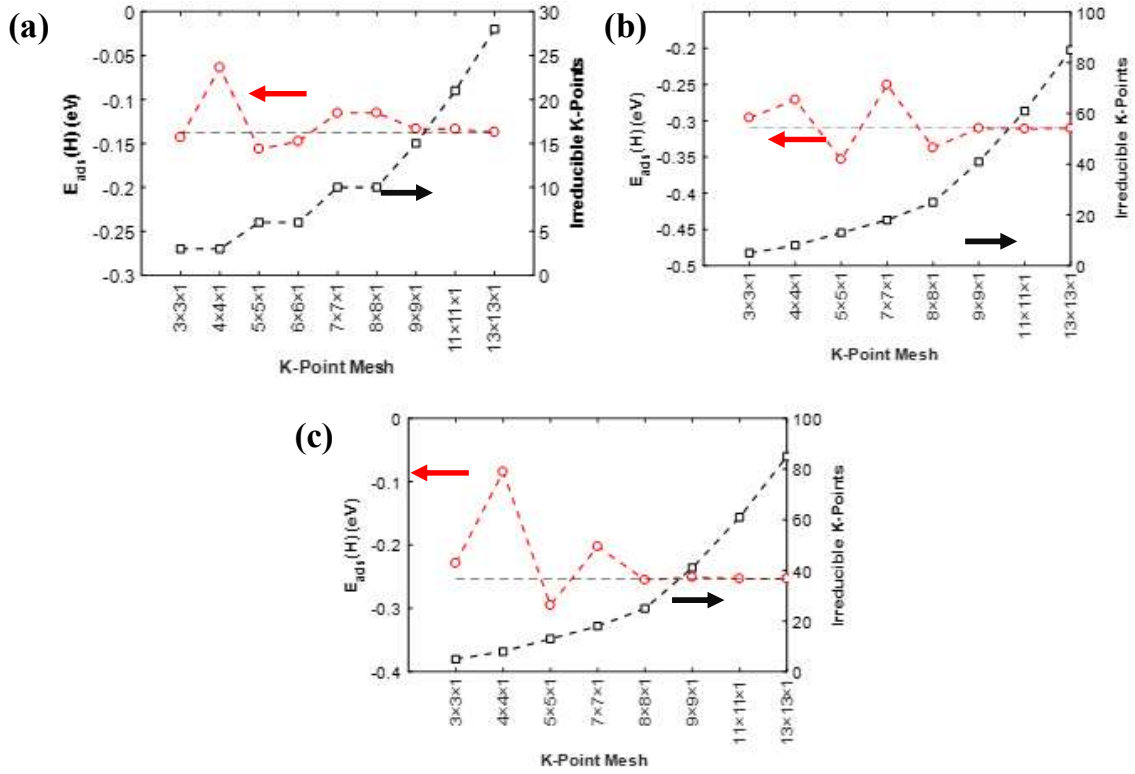

Figure A3. K–point convergence test for a H adatom on (a) a 4–fold site on Cu(100); (b) a mixed bridge site on a Pt/Cu(100) SAA surface, and (c) a dopant top site of the latter surface.

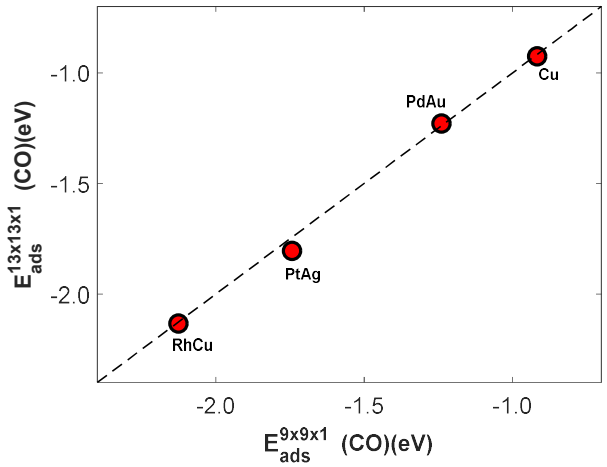

Figure A4. Parity between the adsorption energies of CO computed with 9 × 9 × 1 and 13 × 13 × 1 k-meshes. CO is chemisorbed on the top dopant sites of the single atom alloy surfaces and on a top site on the Cu(111) surface.

- *Computed Adsorption energies*

Table A2. Adsorption energies of NO on the top dopant site on SAA surfaces and on the most stable site of pure metal surfaces.

Catalytic Surface	$E_{ads}(N_2)$ (111) (eV)	$E_{ads}(N_2)$ (100) (eV)
NiAg	-2.30	-2.35
NiAu	-2.13	-2.32
NiCu	-2.09	-2.25
PdAg	-1.18	-1.24
PdAu	-1.13	-1.30
PdCu	-1.06	-1.21
PtAg	-1.38	-1.47
PtAu	-1.36	-1.58
PtCu	-1.22	-1.42
RhAg	-2.58	-2.68
RhAu	-2.44	-2.66
RhCu	-2.31	-2.48
Au	-0.85	-0.58
Ag	-0.62	-0.68
Cu	-1.55	-1.61
Pt	-2.25	-2.70
Rh	-2.85	-2.87
Ni	-2.84	-2.99
Pd	-2.62	-2.40

Table A3. Adsorption energies of N_2 on the top dopant site on SAA surfaces and on the most stable (i.e. atop) site of pure metal surfaces.

Catalytic Surface	$E_{ads}(N_2)$ (111) (eV)	$E_{ads}(N_2)$ (100) (eV)
NiAg	-0.93	-0.97
NiAu	-0.85	-0.93
NiCu	-0.79	-0.89
PdAg	-0.38	-0.42
PdAu	-0.40	-0.46
PdCu	-0.32	-0.41
PtAg	-0.39	-0.43
PtAu	-0.45	-0.52
PtCu	-0.28	-0.39
RhAg	-1.07	-1.08
RhAu	-0.97	-1.00
RhCu	-0.90	-0.93
Au	-0.17*	-0.16*
Ag	-0.15*	-0.16*
Cu	-0.15	-0.30
Pt	-0.45	-0.70
Rh	-0.79	-0.80
Ni	-0.65	-0.79
Pd	-0.48	-0.61

* physisorption: N_2 is far above the top layer of the surface.

Table A4. Adsorption energies of O on the top dopant site on SAA surfaces and on the most stable site of pure metal surfaces.

Catalytic Surface	E_{ads}(O) (111) (eV)	E_{ads}(O) (100) (eV)
NiAg	-1.12	-1.25
NiAu	-0.47	-0.65
NiCu	-0.83	-0.99
PdAg	0.13	0.04
PdAu	0.56	0.45
PdCu	0.32	0.21
PtAg	-0.28	-0.33
PtAu	0.03	-0.17
PtCu	-0.08	-0.30
RhAg	-0.98	-1.27
RhAu	-0.64	-0.96
RhCu	-0.74	-1.02
Au	-0.20	-0.20
Ag	-0.60	-1.05
Cu	-1.90	-3.20
Pt	-1.52	-1.06
Rh	-2.28	-2.30
Ni	-2.47	-2.94
Pd	-1.49	-1.46

- *Correlation plots between adsorption energy and d band centre*

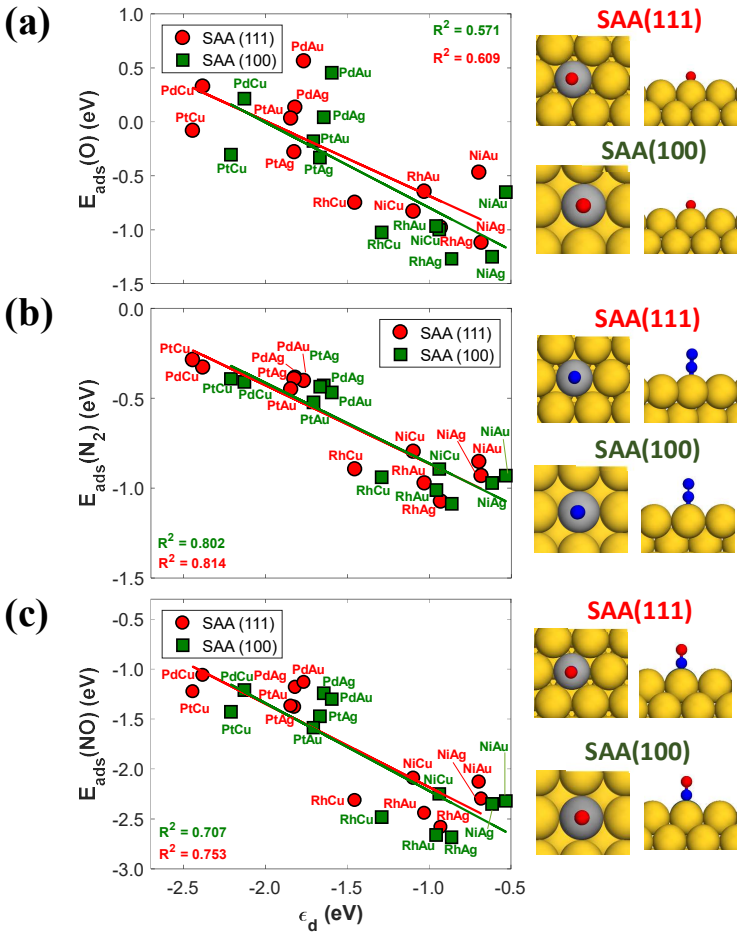

Figure A5. Linear correlation between the adsorption energy of (a) O*; (b) N_2* and (c) NO* on the dopant top site of several SAA surfaces and ε_d. Regression lines are shown with the corresponding coefficients of determination (R^2). N, O, dopant and host atoms are shown in blue, red, grey and yellow, respectively.

- *Effective activation barrier*

The concept of the effective activation barrier is illustrated in Figure A6 where we show how the barrier predicted by the dimer method ($E_{a,\ predicted}$) and the reported effective barriers ($E_{a,\ effective}$) are calculated. The dissociation of NO on Cu–based and platinum group metal (100) surfaces is an example of a system with a potential energy surface that resembles the one shown in Figure A6. More specifically, NO is initially adsorbed perpendicularly on a mixed bridge or a fourfold site (Most stable IS in Figure A6). Then, it tilts toward the surface, and ends up in an adsorption structure where the molecule is parallel to the surface (Meta–stable IS in Figure A6). The reported effective barriers are always defined with respect to the most stable IS.

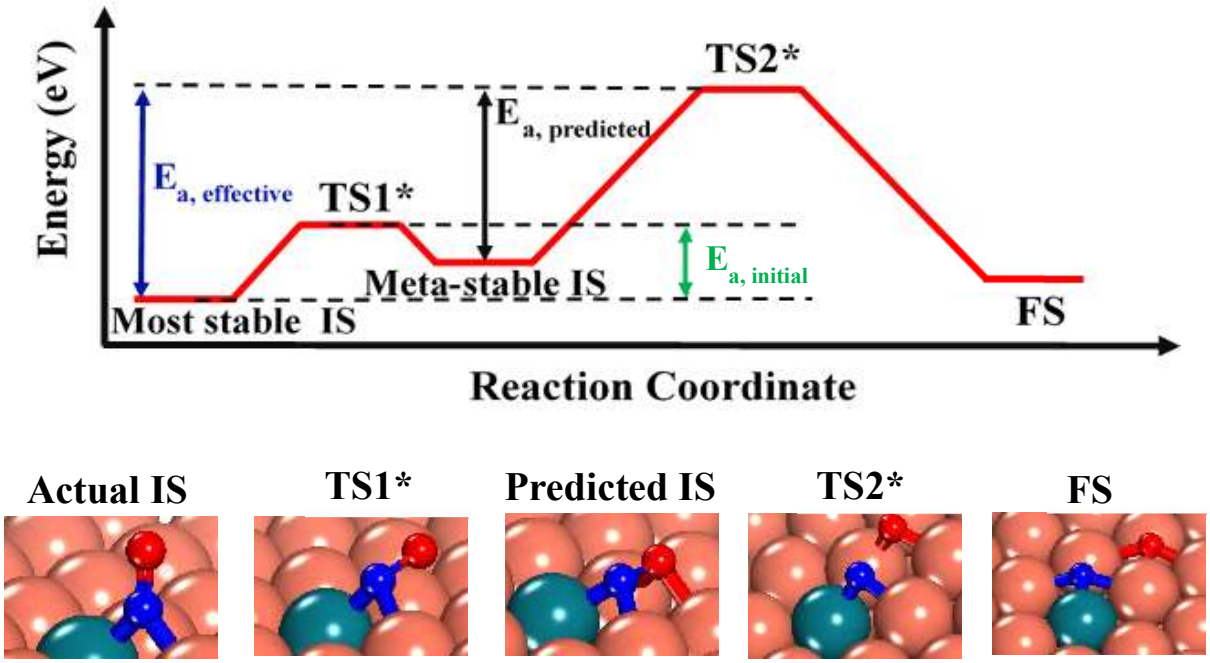

Figure A6. Illustration and definition of predicted and effective activation barriers. The effective activation barrier is always calculated with respect to the energetically most stable IS. The insets at the bottom of the figure show the corresponding structures of the presented potential energy surface for the dissociation of NO. O, N, Cu and dopant metal atoms are shown in red, blue, orange and green, respectively.

- *Computed barriers for CO oxidation*

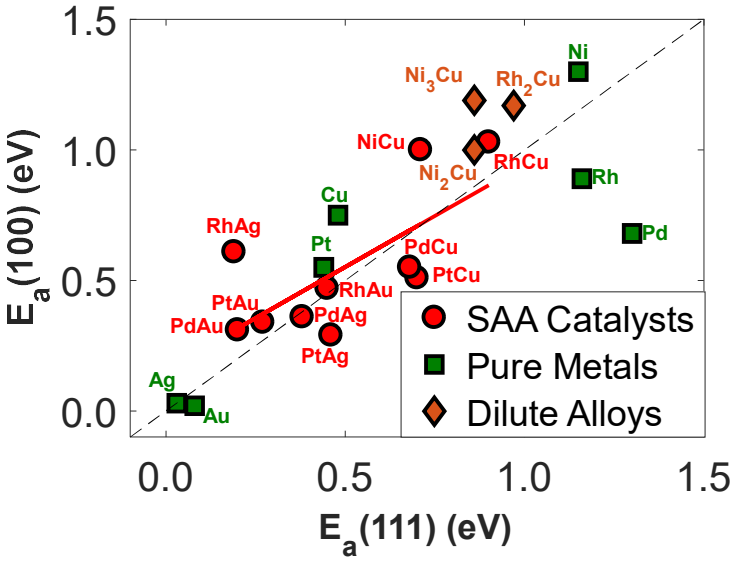

Figure A7 E_a(100) and E_a(111) parity for SAA surfaces (red circles), pure metal surfaces (green squares) and Ni clusters on Cu (orange diamonds) for the catalytic CO oxidation. The black dashed line represents the parity line.

- *Desorption energies*

Table A5. Summary of adsorption energies of NO on the most stable adsorption site of Ni dimers and trimers embedded on Cu surfaces. The most stable adsorption sites are hollow bridge and threefold sites for Ni dimers and trimers, respectively, and NO is perpendicular to the surface.

Alloy Surface	E_{ads}(NO) (111) (eV)	E_{ads}(NO) (100) (eV)
Ni_2Cu	-2.65	-2.86
Ni_3Cu	-3.07	-3.09
Cu	-1.55	-1.61
Ni	-2.84	-2.99

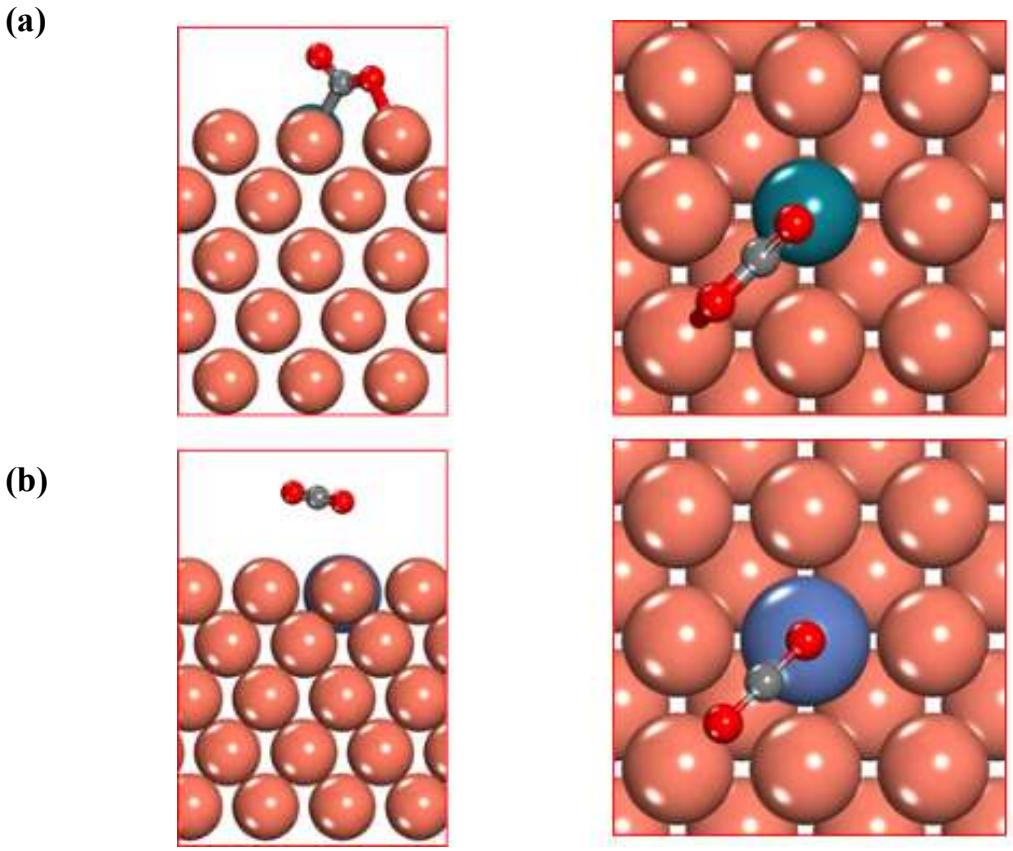

Figure A8. (a) The side and top views of the η^2–(atop, atop) CO_2 adsorption structure on a Rh/Cu(100) SAA surface. (b) The side and top views of the CO_2 physisorbed structure on a Ni/Cu(100) SAA surface. O and C atoms are shown in red and grey, respectively. Ni, Rh and Cu atoms are shown in purple, green and orange, respectively.

Table A6. Summary of CO_2 adsorption energies for the physisorbed and η^2–(atop, atop) structures on the Ni cluster (111) surfaces.

Catalyst Surface	$E_{ads}(CO_2)$ (eV) Physisorbed Structure	$E_{ads}(CO_2)$ (eV) "Bent" Structure (η^2-(atop, atop))
$Ni_2Cu(111)$	-0.26	**-0.37**
$Ni_3Cu(111)$	-0.27	**-0.43**
$Ni_2Cu(100)$	-0.26	**-0.65**
$Ni_3Cu(100)$	-0.27	**-0.87**

Appendix III

- *Electronic structure analyses of N_2O adsorption modes*

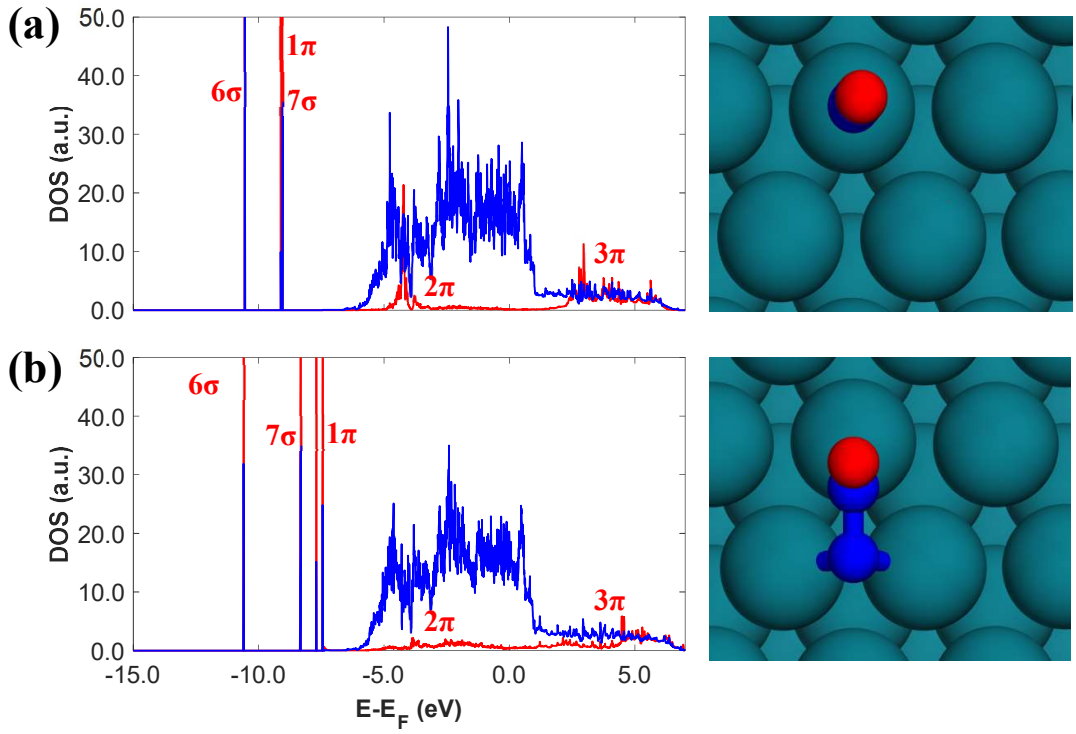

Figure A9. Projected density of states for (a) the *η1*–(N$_t${top}) and (b) the *η2*–h(N$_t${bridge}, N$_c${top}) on Rh(111). The red line is the N_2O contribution and the blue line is the metal contribution (only Rh surface atoms). The relaxed adsorption structures are shown on the right of each panel. Rh, O and N atoms are shown in dark green, red and blue.

- *N_2O formation and decomposition on Rh(111)*

Figure A10 shows the reaction path for the decomposition of N_2O to either NO* + N* or N_2* + O*. The energies presented are referenced to a non–interacting N_2O molecule in the gas–phase and a clean Rh(111) slab. For an accurate comparison of our results to the work of Paul et al.,[177] all the energies presented include the zero point energy (ZPE) correction, which can be introduced by calculating the energy of an adsorbed state as

$$E_{DFT,s} = E_{DFT}^{Slab+N_2O} - E_{DFT}^{Slab} - E_{DFT}^{N_2O_{(g)}} + \hbar\left(\sum_{i=1}^{9}\frac{w_i}{2} - \sum_{i=1}^{3}\frac{w_{N_2O,i}}{2}\right), \quad (101)$$

where $E_{DFT,s}$ is the energy of a state s; $E_{DFT}^{Slab+N_2O}$, E_{DFT}^{Slab} and $E_{DFT}^{N_2O_{(s)}}$ are the DFT energies for a Rh(111) slab whereon N_2O is adsorbed, clean Rh(111) slab and a gas-phase N_2O molecule; $\hbar$ is the reduced Planck

constant; $\omega_{N_2O,i}$ is the the angular frequency of the i^{th} mode of gas-phase N_2O and ω_i is the angular frequency of the i^{th} mode of N_2O in an adsorbed state.

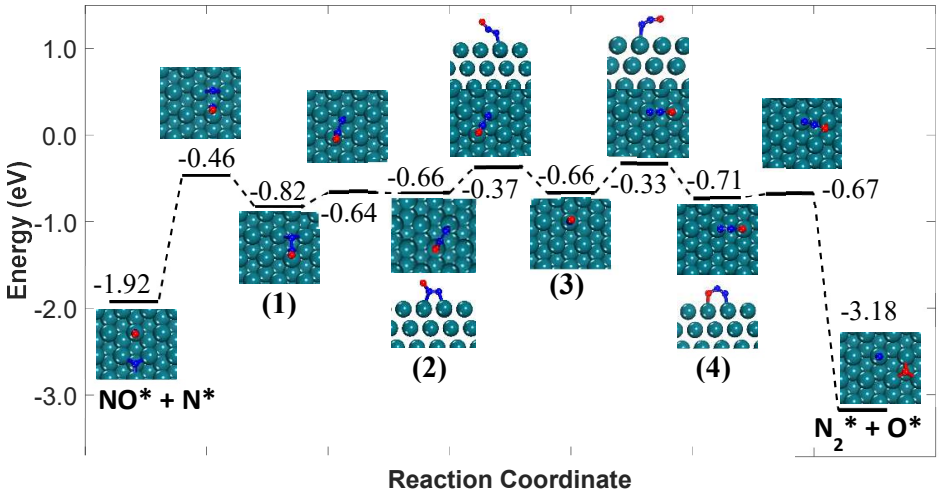

Figure A10. Reaction path for the decomposition of N_2O* either to NO* + N*or to N_2* + O*. The energy values are ZPE–corrected. The numbering of the adsorbed configurations of N_2O is as follows: (1) *η2*–f(N_t{bridge},N_c{top}), (2) *η2*–(N_t{top},N_c{top}), (3) *η1*–(N_t{top}) and (4) *η2*–(N_t{top},O{top}). Rh, O and N atoms are shown in dark green, red and blue, respectively.

- *N_2O formation and decomposition on Rh(111)*

To demonstrate the NO* – NO* repulsive interactions, we plot the average adsorption energy of NO* over Rh(111) for different NO* surface coverages. As seen, at increasing surface coverage the NO* binding strength diminishes (i.e. less exothermic adsorption).

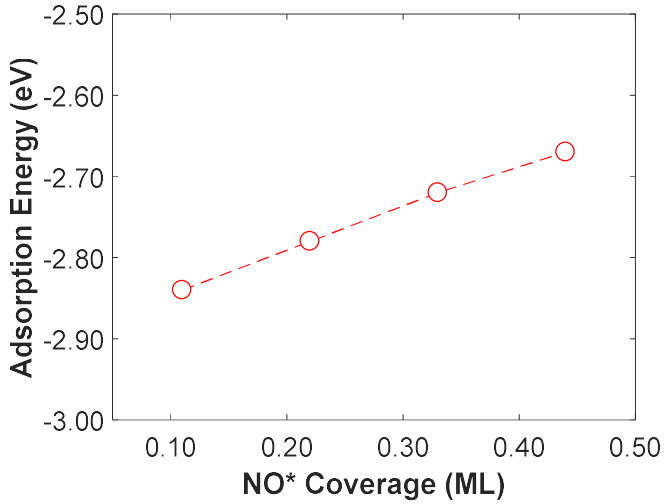

Figure A11. Average adsorption of NO* for various coverages.

- *N_2O* formation via $(NO)_2$* on $Ni_3Cu(111)$*

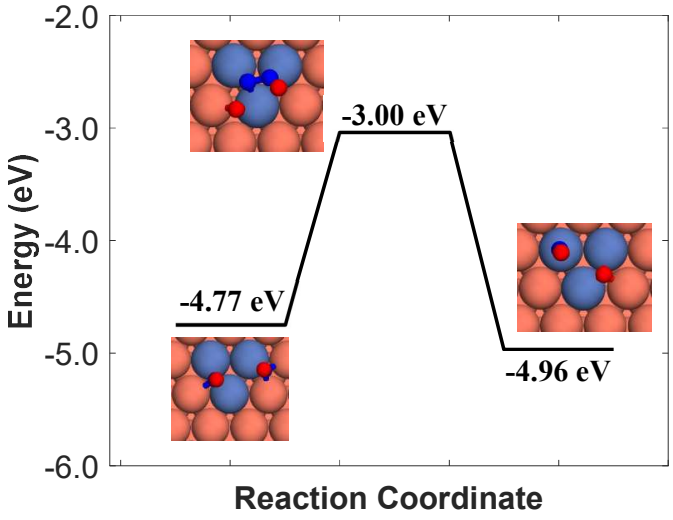

Figure A12. N_2O* formation via $(NO)_2$* on $Ni_3Cu(111)$.

- *Side views of the states within the N_2O* formation and decomposition reaction pathways*

The following figures show the side view of the different states that are involved in the N_2O* formation/decomposition pathways (see Figure 32, Figure 33 and Figure 34 in the main text). The images are for the $Ni_2Cu(111)$ surface, but in the vast majority of cases they are representative for all the Cu–based surfaces.

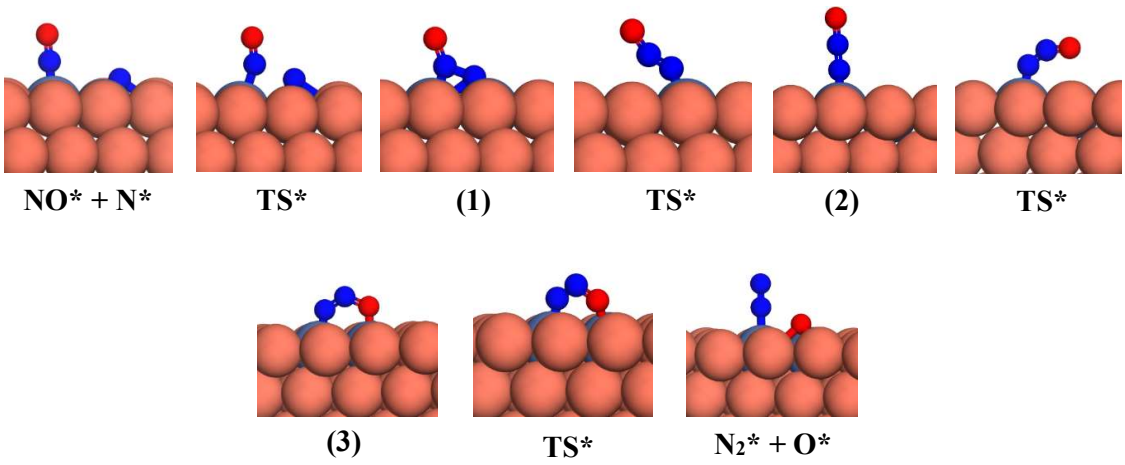

Figure A13. Side views of the states in Figure 33 (B) of the main text. Ni, Cu, O and N atoms are shown in purple, orange, red and blue, respectively.

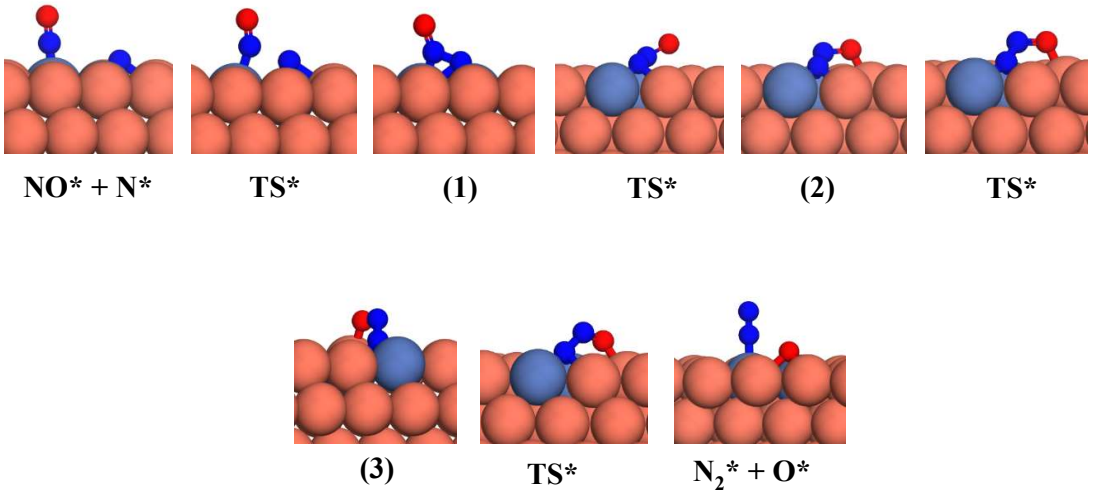

Figure A14. Side views of the states in Figure 34 (C) of the main text. Ni, Cu, O and N atoms are shown in purple, orange, red and blue, respectively.

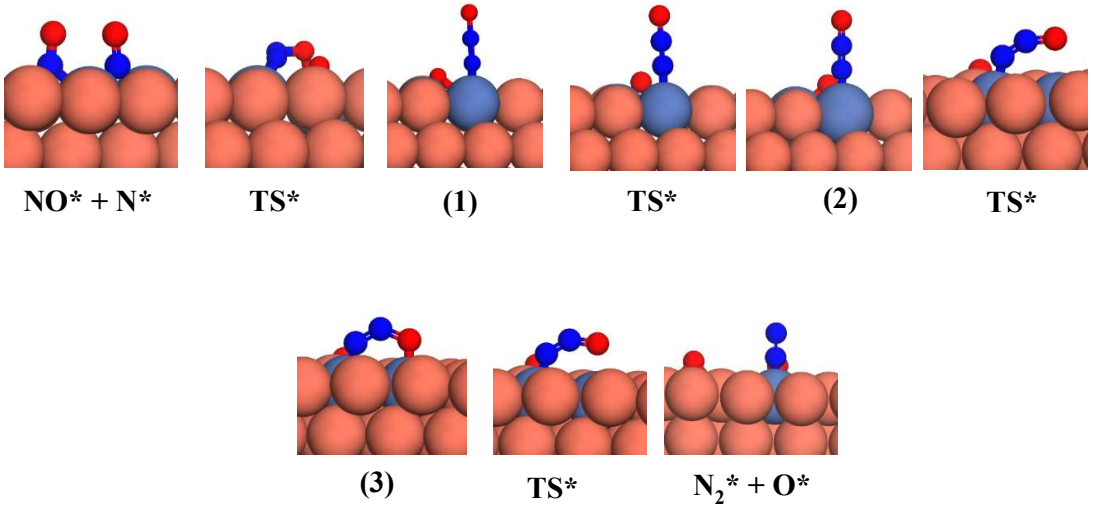

Figure A15. Side views of the states in Figure 35 (C) of the main text. Ni, Cu, O and N atoms are shown in purple, orange, red and blue, respectively.

- *O_2* association and NO_2* formation*

Figure A16 shows the initial, transition and final states for the formation of O_2* from two O* adatoms. Also shown are the computed DFT energies for each structure.

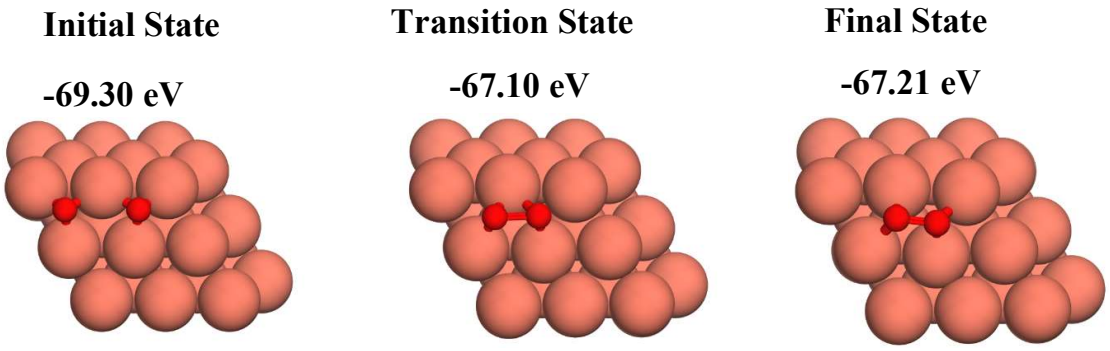

Figure A16. Top view of initial, transition and final states for the formation of O_2* on Cu(111). Cu and O atoms are shown in orange and red, respectively.

Regarding the NO_2* formation, we find that on Cu–based the forward barrier is always larger than 0.70 eV, while the reverse barrier (i.e. NO_2* dissociation) is always smaller than 0.30 eV. Our data indicates that the formation of NO_2* is neither kinetically nor thermodynamically favoured. The most stable final state for all the three surfaces is the so–called μ–N,O–nitrito adsorption mode, whose stability is experimentally confirmed on other coinage metal surfaces.[262] We also compute the adsorption energies of NO_2* in the μ-N,O-nitrito structure on the Cu-based surfaces (Table A6). The obtained values imply that even if NO_2* is formed on the surface its dissociation will be dramatically more favourable than its desorption, thereby corroborating our reaction mechanism, which does not take into account the formation of NO_2*.

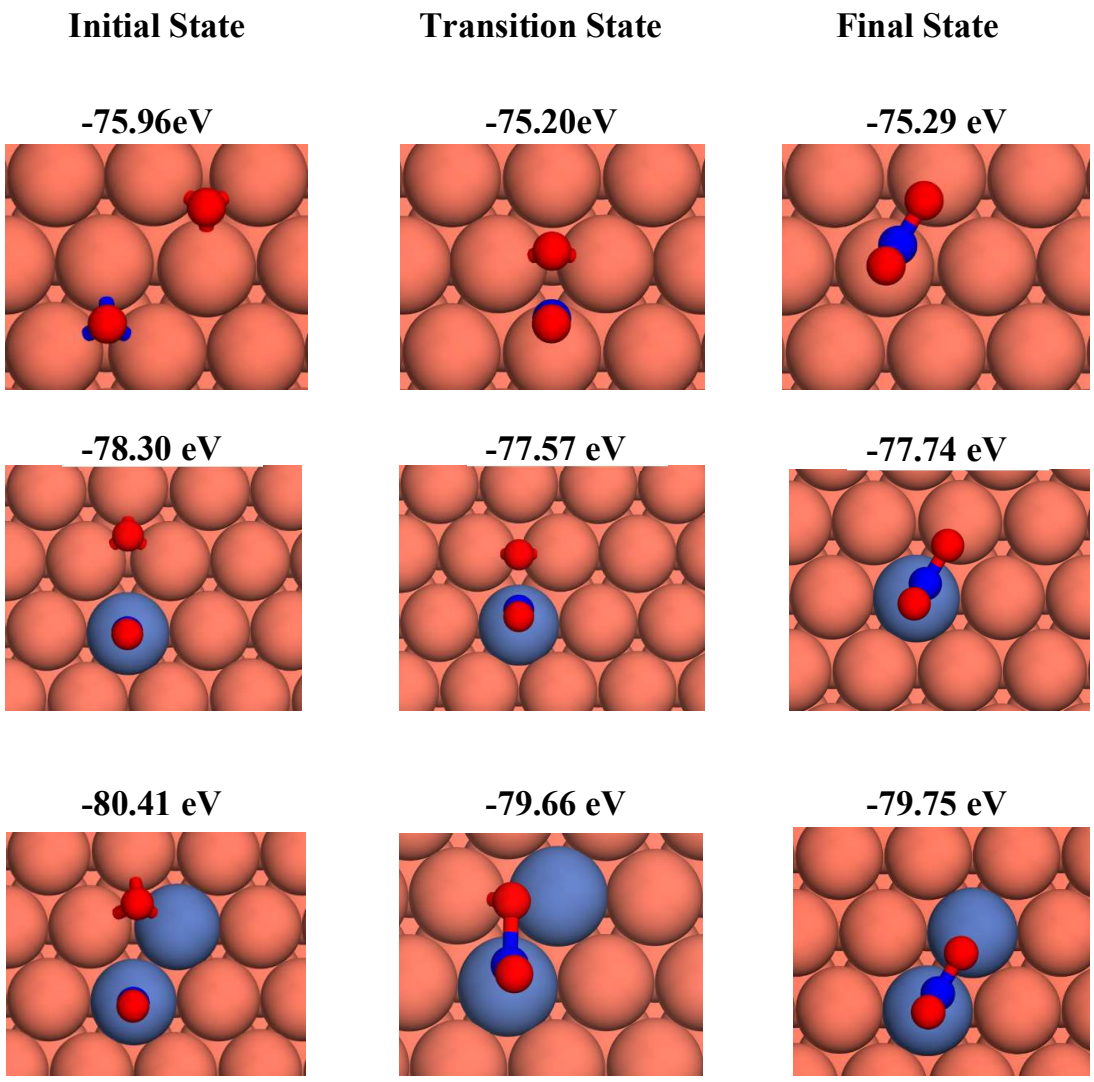

Figure A17. Top view of initial, transition and final states for the formation of NO_2* on Cu(111), Ni/Cu(111) SAA and Ni_2Cu(111) surfaces. Ni, Cu, O and N atoms are shown in purple, orange, red and blue, respectively.

Table A7. Adsorption energies for NO_2* in μ–N,O–nitrito adsorption structure on Cu-based surfaces. Note that the gas–phase calculation for $NO_{2(g)}$ was spin–polarised.

Surface	$E_{ads}(NO_2)$
Cu(111)	-1.70 eV
Ni/Cu(111) SAA	-2.10 eV
$Ni_2Cu(111)$	-2.30 eV

- *Activity plot for Cu(111) at "low temperatures"*

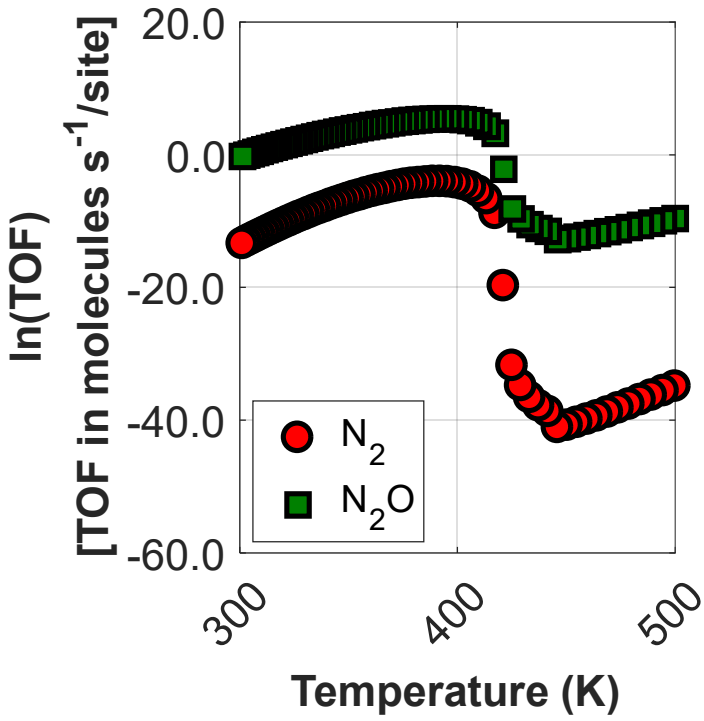

Figure A18. Activity of Cu(111) within the temperature range of 300 K – 500 K (low–temperature range).

- *Explanation for the selectivity peak on Ni/Cu bimetallic alloys*

Figure A19 (a) and (b) shows that the selectivity peak of $Ni_2Cu(111)$ is unaffected by changes to the activation barrier to the formation of N_2* (R16 in Table 3 in chapter 6) and the dimerization reaction (R15 in Table 2 in chapter 6) on Ni*. On the contrary, the peak (which appears between 950 K and 1400 K) disappears upon increasing the activation barrier for the formation of N_2O* (R9 in Table 2 in chapter 6) and NO* dissociation (R8 in Table 2 in chapter 6) reactions on Ni*. Therefore, the selectivity spike for Ni/Cu SAA and Ni_2Cu in Figure 38 (a) is associated only with the latter two reactions.

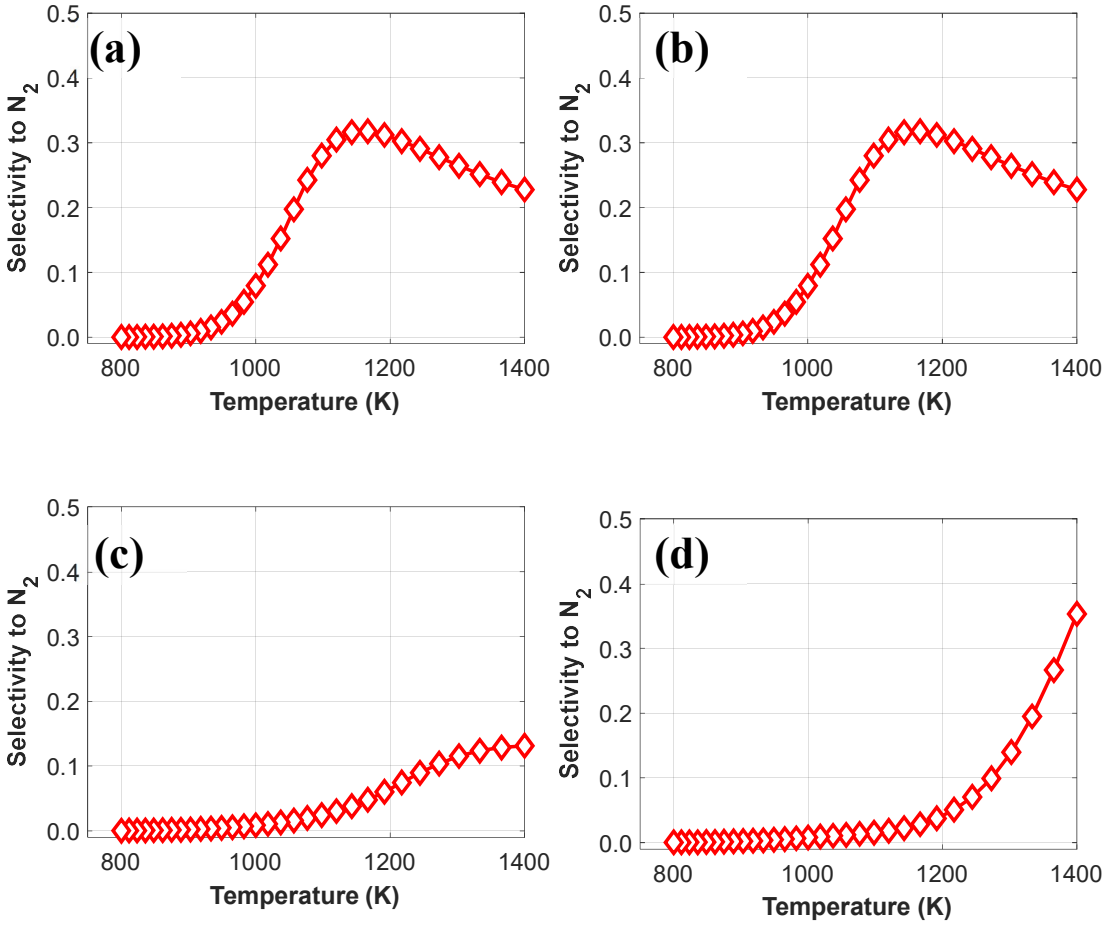

Figure A19. Predicted selectivity to N_2 after setting a large activation barrier (i.e. 2.5 eV) for (a) the formation of N_2* on Ni*; (b) the dimerization reaction on Ni*; (c) the direct dissociation of NO* on Ni*; and (d) the formation of N_2O* on Ni*

- *Sites involved in surface reactions over Ni/Cu bimetallic alloys*

Several elementary events in our microkinetic model involve two sites, which may be of different type on the Ni/Cu bimetallic alloys. On the latter surfaces, the two–site reactions (see Table 3) can happen either on Cu sites, where the reactants and products are on Cu*, or on pair of sites that include both Ni* and Cu*. Table A7 tabulates the two–site events of the NO + CO reaction along with the site types whereon the reactant and product adspecies are adsorbed in our model.

Table A8. Two-site events and sites where reactant and product species are adsorbed. The adsorption sites (i.e. either Ni*or Cu*) are shown in bold. Also in bold are the reaction numbers, which correspond to the numbers shown in Table 2 in the main text. Empty sites are denoted as Ni* or Cu*. For occupied sites, the adsorbate is specified followed by the site type in parenthesis.

Reaction	Reactant 1	Reactant 2	Product 1	Product 2
NO* + * ↔ N* + O* **(R8)**	NO* (**Ni***)	**Cu***	N* (**Ni***)	O* (**Cu***)
NO* + N*↔ N_2O* *η2NbNt* + * **(R9)**	NO* (**Ni***)	N* (**Cu***)	N_2O* *η2NbNt* (**Ni***)	**Cu***
N_2O* *η2NtOt* + * ↔ N_2* + O* **(R12)**	N_2O* *η2NtOt* (**Ni***)	**Cu***	N_2* (**Ni***)	O* (**Cu***)
N_2O* *η2NbNt* + * ↔ N_2* + O* **(R13)**	N_2O* *η2NbNt* (**Ni***)	**Cu***	N_2* (**Ni***)	O* (**Cu***)
CO* + O* ↔ CO_2* + * **(R14)**	CO* (**Ni***)	O* (**Cu***)	CO_2* (**Ni***)	**Cu***
NO* + NO* ↔ N_2O* *η1* + O* **(R15)**	NO* (**Ni***)	NO* (**Cu***)	N_2O* *η1* (**Ni***)	O* (**Cu***)
N* + N* ↔ N_2* + * **(R16)**	N* (**Ni***)	N* (**Cu***)	N_2* (**Ni***)	**Cu***

Appendix IV

- *Surface aggregation studies – dopant trimers*

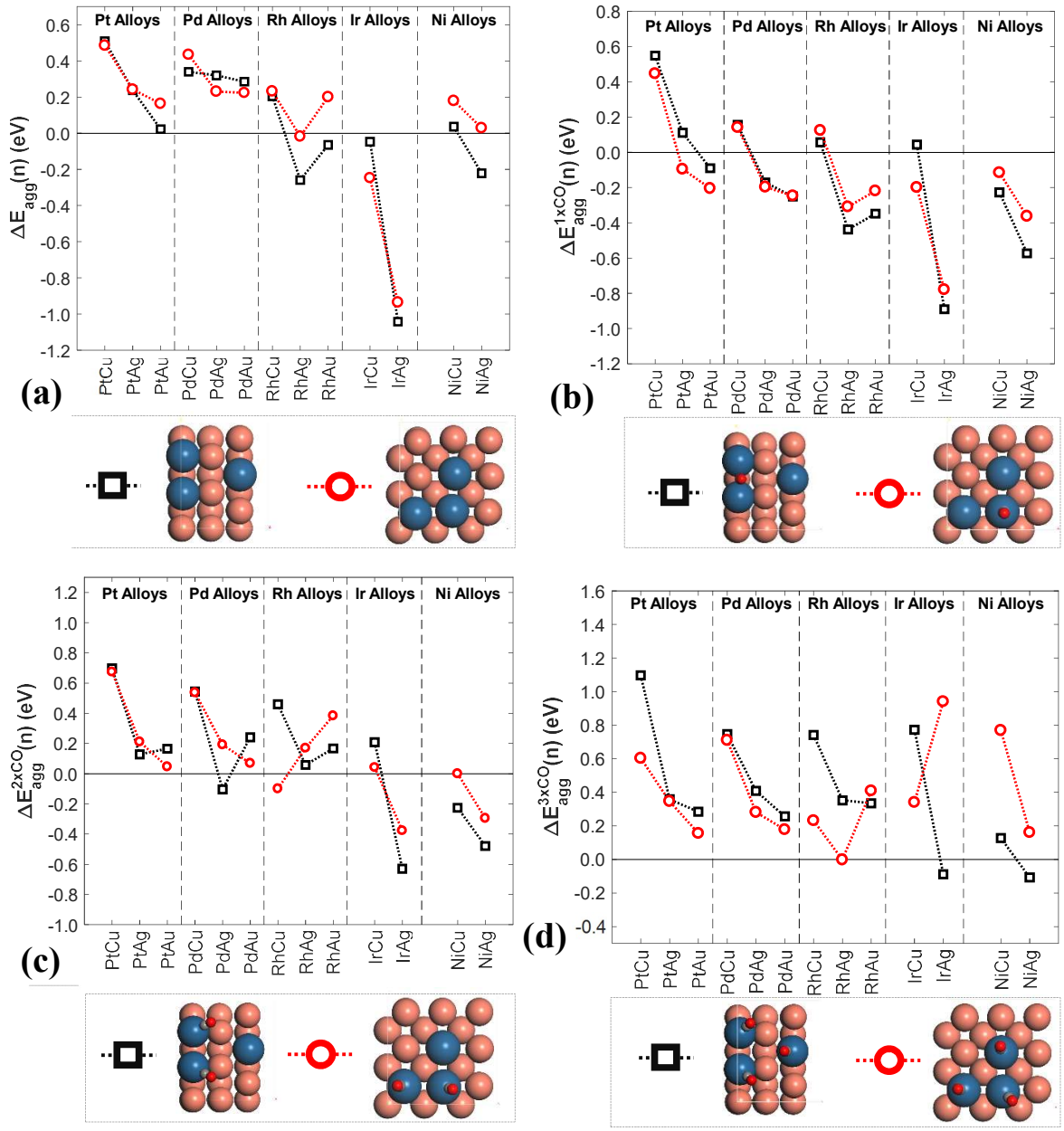

Figure A20. Aggregation energies (ΔE_{agg}) for trimers relative to the SAA phase of Ni, Pd, Pt, Rh and Ir doped into the (100) and (211) surfaces of the group 11 metals with (a) no adsorbed CO molecule; (b) 1 adsorbed CO molecule; (c) 2 adsorbed CO molecules and (d) 3 adsorbed CO molecules. The legend below each plot, show dimer configurations in the relaxed state; therein carbon, coinage metal, dopant metal and oxygen atoms are represented by grey, orange, blue and red spheres, respectively.

- *Computational setup for Rh diffusion*

To describe the exchange and correlation effects, we employed the PBE functional. Using this functional, we computed a lattice constant for Cu of 3.63 Å, which is in excellent agreement with previous works and in reasonable agreement with the experimental value of 3.59 Å.[263] The electronic wave function was converged to 10^{-7} eV and the Hellman–Feynman forces were relaxed to less than 10^{-2} eV $Å^{-1}$. The low-index SAA Rh/Cu(111), Rh/Cu(100), Rh/Cu(110) and Rh/Cu(211) surfaces were modeled by a 4–layer p(4 × 4), 4-layer p(4 × 4), 8–layer p(4 × 4) and a 4–layer p(4 × 1) cell, respectively. Some (110) surfaces, like Au(110) and Pt(110), undergo a transition towards the energetically favored (1 × 2) missing row reconstruction geometry.[264–266] Cu(110), however, is not known to be prone to such a reconstruction, and therefore our DFT calculations focus on an ideal (1 × 1) geometry.[267] The bottom two layers of the (111), (100) and (211) surfaces were fixed at the PBE–computed Cu lattice constant, while the top two layers and any Rh or Cu adatom thereon, were allowed to relax during geometry optimization. For the (110) surface, the bottom four layers were fixed at the Cu lattice constant and the top four ones were allowed to relax. The following Monkhorst–Pack k–point meshes were used to sample the Brillouin zones of the considered surfaces: 4 × 4 × 1 k–point mesh for the (111) surface, 4 × 4 × 1 for (100), 3 × 4 × 1 for (110) and 5 × 4 × 1 for the (211) surface. Finally, transition states were identified with the dimer method, and vibrational analyses were performed in order to verify that each of the located transition states was a 1st order saddle point in the PES.

.

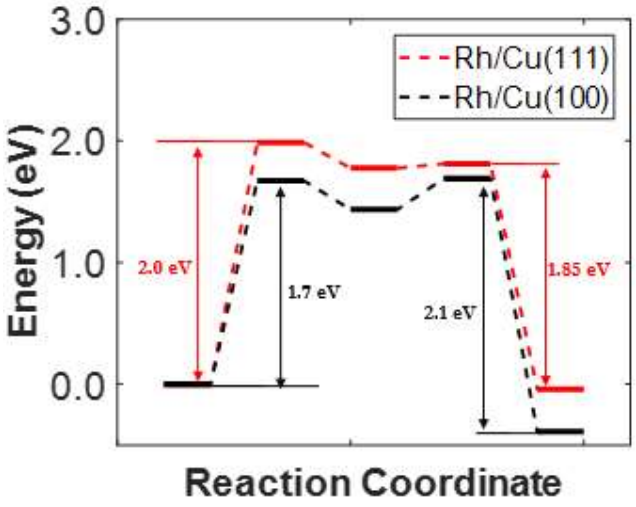

Figure A21. Computed barriers for segregation of Rh to the bulk of Rh/Cu(100) and Rh/Cu(111) surfaces.

Appendix V

- *Lattice size testing*

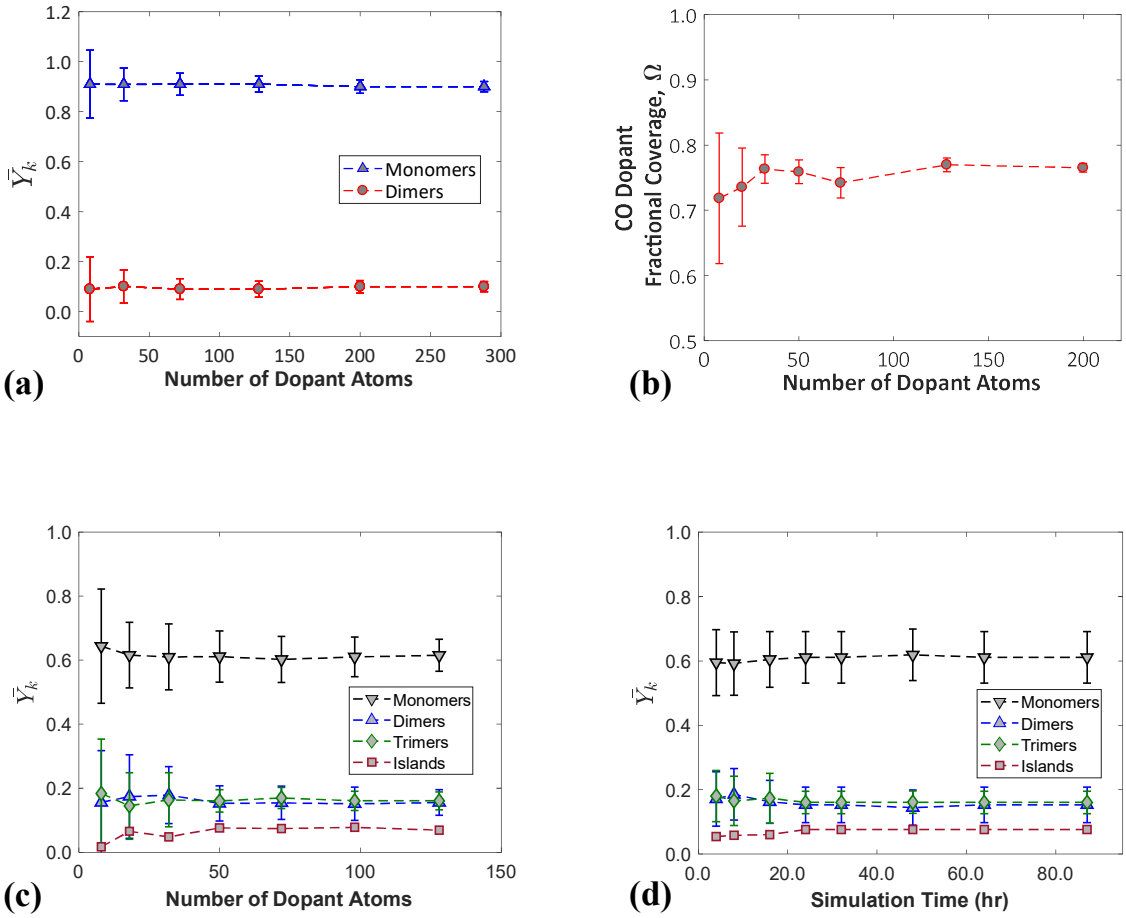

Figure A22. (a) Lattice size testing performed on the Ni/Cu(111) alloy under vacuum conditions and for 4% Ni loading. (b) Lattice size testing performed on the Ni/Cu(111) alloy in the presence of CO at $P_N = 0.01$ (for the definition of P_N see the main text) and for 4 % Ni loading. (c) Lattice size testing performed on the Pd/Ag(111) alloy in the presence of CO and $P_N = 10^{-4}$. Note that at this CO pressure the induced aggregation is maximum (see the main text). (d) Walltime testing on the Pd/Ag(111) alloy in the presence of CO and $P_N = 10^{-4}$. The error bars in all panels are ± one standard deviation.

- *Pre-exponentials for CO* diffusion – Thermodynamic consistency*

The total difference in free energy of a multistep thermodynamic process where the initial and final states are identical is

$$\Delta F_{tot} = \Delta F_{12} + \Delta F_{23} + ... + \Delta F_{n1} = 0, \tag{102}$$

where F is a free energy and ΔF_{12}, ΔF_{23} and ΔF_{n1} are the differences of free energies between states 1 and 2, states 2 and 3 and states n and 1, respectively. An example of such a multistep process is shown in Figure A10: a gas-phase CO molecule binds to the bridge site of a dopant dimer (reaction 1→2); this is followed by a CO* diffusion to an atop site (reaction 2→3) and subsequently by a desorption (reaction 3→1) that brings the system to its initial state 1. The equilibrium constant for the 1→2 step will be

$$K_{12} = \frac{A_{1\to 2}}{A_{2\to 1}} \cdot \frac{\exp\left(-\frac{E_{1\to 2}}{k_B \cdot T}\right)}{\exp\left(-\frac{E_{2\to 1}}{k_B \cdot T}\right)} = \frac{A_{1\to 2}}{A_{2\to 1}} \cdot \exp\left(-\frac{\Delta E_{\mathrm{rxn},1\to 2}}{k_B \cdot T}\right), \tag{103}$$

where $E_{1\to 2}$ and $E_{2\to 1}$ are the activation barriers of the 1→2 and 2→1 reactions, respectively, T is the temperature, $A_{1\to 2}$ and $A_{2\to 1}$ are the pre-exponent factors of the 1→2 and 2→1 reactions, respectively, k_B is Boltzmann's constant, and $\Delta E_{\mathrm{rxn},1\to 2}$ is the energy difference between the initial and final states. The right-hand-side of equation (103) is

$$\frac{A_{1\to 2}}{A_{2\to 1}} \cdot \exp\left(-\frac{\Delta E_{\mathrm{rxn},1\to 2}}{k_\mathrm{B} \cdot T}\right) = \frac{Q_\mathrm{prod}}{Q_\mathrm{reac}} \cdot \exp\left(-\frac{\Delta E_{\mathrm{rxn},1\to 2}}{k_\mathrm{B} \cdot T}\right) = \exp\left(-\frac{\Delta F_{12}}{k_\mathrm{B} \cdot T}\right), \tag{104}$$

where Q_prod and Q_reac are the partition functions of the initial and final state and

$$\ln\left(\frac{A_{1\to 2}}{A_{2\to 1}}\right) - \frac{\Delta E_{\mathrm{rxn},1\to 2}}{k_\mathrm{B} \cdot T} = -\frac{\Delta F_{12}}{k_\mathrm{B} \cdot T} \quad \Rightarrow$$

$$\Rightarrow \Delta F_{12} = \Delta E_{\mathrm{rxn},1\to 2} - k_\mathrm{B} \cdot T \cdot \ln\left(\frac{A_{1\to 2}}{A_{2\to 1}}\right). \tag{105}$$

Similarly, we write

$$\Delta F_{23} = \Delta E_{\mathrm{rxn},2\to3} - k_{\mathrm{B}} \cdot T \cdot \ln\left(\frac{A_{2\to3}}{A_{3\to2}}\right), \tag{106}$$

$$\Delta F_{31} = \Delta E_{\mathrm{rxn},3\to1} - k_{\mathrm{B}} \cdot T \cdot \ln\left(\frac{A_{3\to1}}{A_{1\to3}}\right). \tag{107}$$

By replacing equations, and into equation (102) we find

$$\Delta F_{\mathrm{tot}} = \Delta E_{\mathrm{rxn,tot}} - k_{\mathrm{B}} \cdot T \cdot \left(\ln\left(\frac{A_{3\to1}}{A_{1\to3}}\right) + \ln\left(\frac{A_{2\to3}}{A_{3\to2}}\right) + \ln\left(\frac{A_{1\to2}}{A_{2\to1}}\right)\right) = 0 \cdot \tag{108}$$

Since the final and initial states are identical (i.e. a CO molecule in gas phase), $\Delta E_{\mathrm{rxn,tot}}$ =0, and therefore

$$\underbrace{\frac{A_{1\to2}}{A_{2\to1}}}_{\substack{Pre-exponential \\ Ratio\,1}} \times \underbrace{\frac{A_{2\to3}}{A_{3\to2}}}_{\substack{Pre-exponential \\ Ratio\,2}} \times \underbrace{\frac{A_{3\to1}}{A_{1\to3}}}_{\substack{Pre-exponential \\ Ratio\,3}} = 1. \tag{109}$$

The pre-exponential ratios 1 and 3 in eq. (109) involve the pre-exponential factors of the CO adsorption and desorption from and to an atop site and a bridge site; these ratios are obtained from first principles (see chapter 8). Once the aforementioned pre-exponential ratios are computed, we calculate the diffusion pre-exponential ratio (pre-exponential ratio 2) by means of eq. (109). In this way, we assure the thermodynamic consistency of our MC calculations.

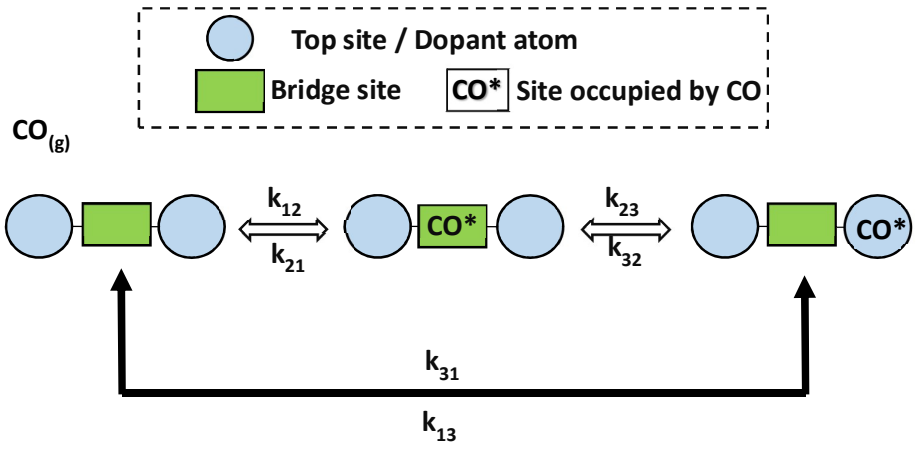

Figure A23. A typical example of multistep process with the same initial and final states

- *Figures included in the CE and ECIs*

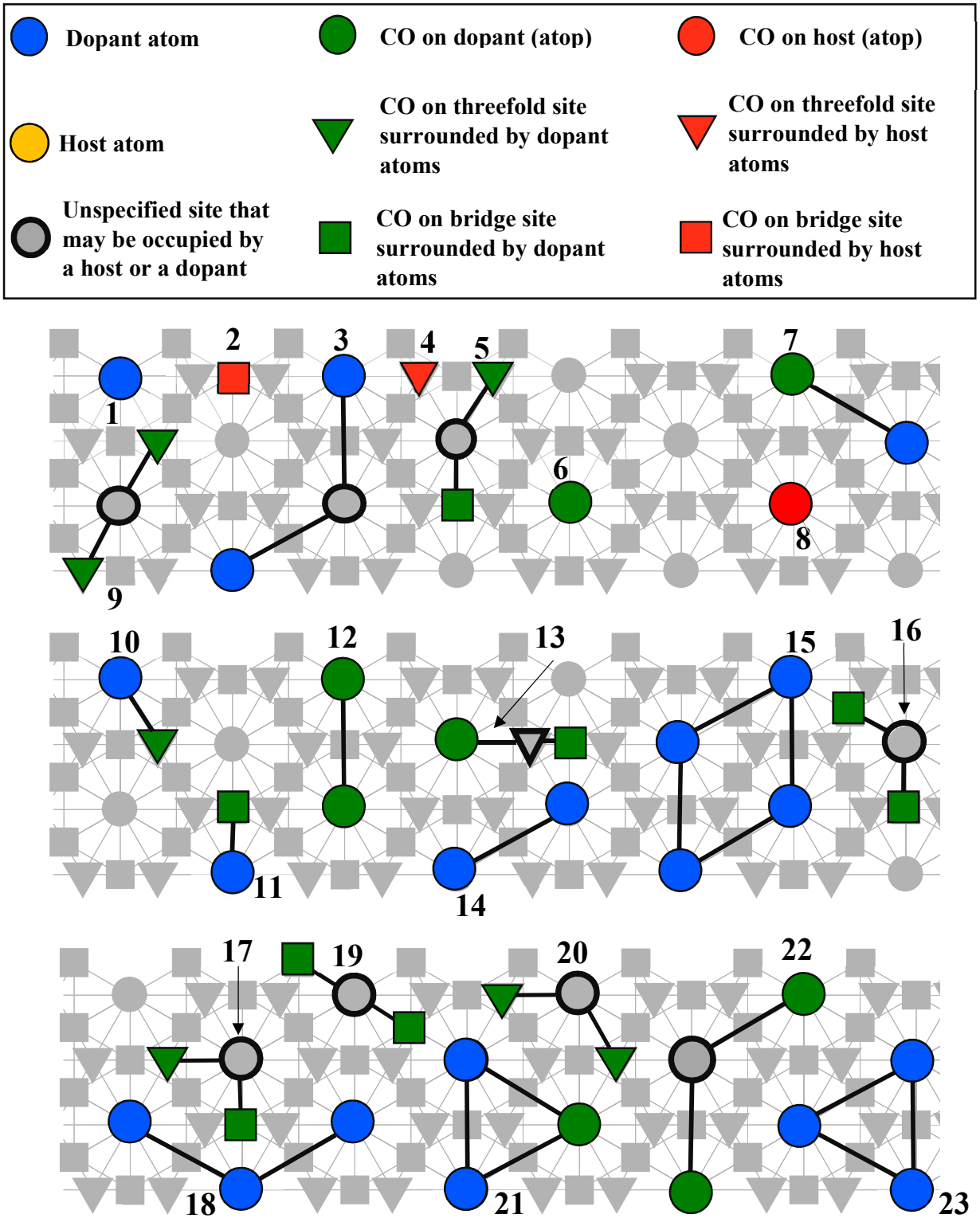

Figure A24. All different figures that may be included in the cluster expansions (CEs) of the investigated alloys. Note that the CO adsorbates on the host bridge sites and on the dopant bridge sites are represented by one species in the CE, but we use two different colours for clarity in the figure above. Thus, in the simulation, the "extra stability" of CO on dopant bridge is modelled by attractive interactions of cluster 11, respectively.

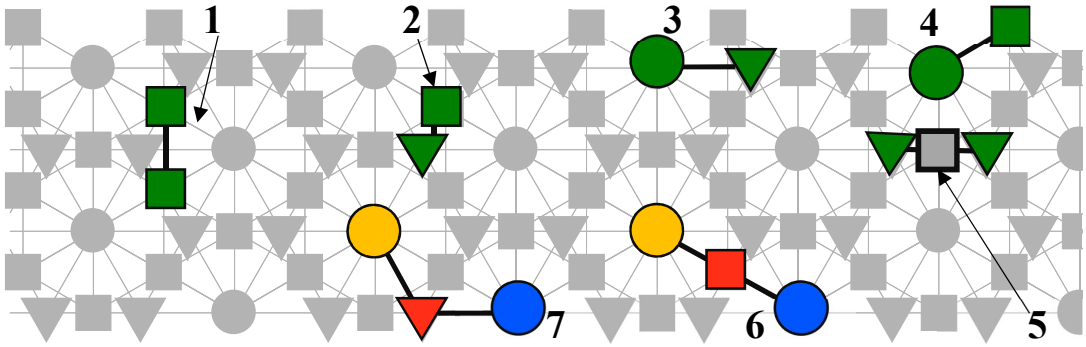

Figure A25. Unstable configurations whose formation is eliminated in the MC simulations for all alloys by assigning a large effective cluster interaction parameter of 10.0 eV. Patterns 6 and 7 represent mixed bridge and threefold adsorption sites.

Table A9. ECI parameters and their graph multiplicities (GM). This table shows which clusters were used in the cluster expansion of each of the investigated alloys along with the corresponding ECI and GM. The cluster numbering is shown in Figure A24. A dash indicates that the specific cluster was not used in the specific case.

Pattern	Ni/Cu(111)		Rh/Cu(111)		Pt/Cu(111)		Pd/Au(111)		Pd/Ag(111)		Ir/Ag(111)	
	GM	ECI (eV)	GM	ECI (eV)	GM	ECI (eV)	GM	ECI (eV)	GM	ECI (eV)	GM	ECI (eV)
1	1	-0.002	1	0.01	1	-0.02	1	-0.005	1	-0.01	1	-0.01
2	1	-0.44	1	-0.44	1	-0.44	1	-0.03	1	-0.04	1	-0.03
3	-	-	2	-0.01	2	0.03	2	-0.01	2	0.01	2	-0.02
4	1	-0.48	1	-0.49	1	-0.49	1	-0.05	1	0.07	1	-0.04
5	2	0.18	2	0.29	2	0.34	2	0.12	2	0.22	-	-
6	1	-1.33	1	-1.65	1	-1.15	1	-0.87	1	-0.96	1	-2.4
7	-	-	2	0.31	2	0.22	2	0.04	2	0.06	2	-0.13
8	-	-	-	-	-	-	1	-0.02	1	0.01	1	-0.01
9	2	0.05	-	-	-	-	2	0.05	2	-0.003	2	-0.65
10	1	-0.42	1	-0.42	1	-0.19	1	-0.47	1	-0.49	1	0.04
11	1	-0.54	1	-0.59	1	-0.30	1	-0.53	1	-0.61	1	0.01
12	2	0.11	2	0.33	2	0.36	2	0.11	2	0.16	2	0.08
13	2	0.38	2	0.53	2	0.56	2	0.21	2	0.26	2	0.75
14	2	0.01	2	0.10	2	0.19	2	0.08	2	0.03	2	-0.41
15	-	-	-	-	-	-	-	-	-	-	4	-0.18
16	2	0.19	2	0.26	2	0.25	2	0.19	2	0.25	2	0.29
17	1	0.38	1	0.50	-	-	1	0.23	-	-	-	-
18	-	-	2	-0.03	-	-	-	-	-	-	2	0.20
19	2	0.08	2	-0.06	2	0.06	2	0.03	2	0.11	2	0.29
20	2	0.24	-	-	-	-	2	0.12	2	0.12	-	-
21	-	-	6	-0.05	6	-0.06	6	-0.02	6	-0.03	-	-
22	-	-	2	0.02	2	0.05	-	-	-	-	-	-
23	-	-	-	-	6	0.005	-	-	-	-	6	0.41

- *Sensitivity analysis on CO* binding strength over Pd clusters on Pd/Au dilute alloys*

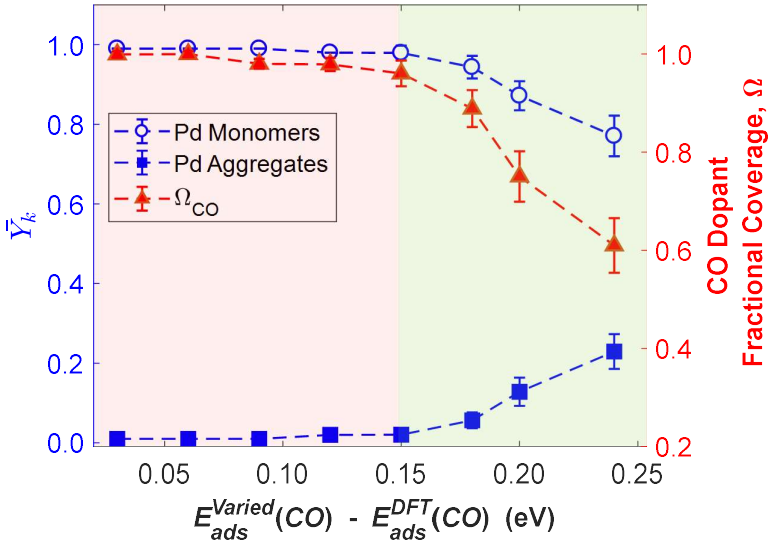

Figure A26. Fractions of surface Pd species () and CO dopant fractional coverage (Ω_{CO}) at various smaller binding energies than the DFT-computed value and at 70ºC and P_{CO} = 0.1 bar. Almost no Pd aggregates are observed in the red-shaded region, whereas such aggregates are present in the green-shaded. The error bars are ±1 standard deviation.

References

[1] I. Chorkendorff, J.W. Niemantsverdriet, K. Kakaei, M.D. Esrafili, and A. Ehsani, in *Concepts Mod. Catal. Kinet.* (Wiley-VCH Verlag GmbH & Co. KGaA, Weinheim, FRG, 2003), pp. 1–21.

[2] B. Hammer and J.K. Norskov, Nature **376**, 238 (1995).

[3] B. Hammer and J.K. Nørskov, in *Adv. Catal.* (2000), pp. 71–129.

[4] B. Hammer, Y. Morikawa, and J.K. Nørskov, Phys. Rev. Lett. **76**, 2141 (1996).

[5] H. Xin and S. Linic, J. Chem. Phys. **132**, 221101 (2010).

[6] J.K. Nørskov, F. Studt, F. Abild-Pedersen, and T. Bligaard, in *Fundam. Concepts Heterog. Catal.*, First Edit (John Wiley & Sons, Inc, Hoboken, NJ, USA, 2014), pp. 114–137.

[7] A. Ruban, B. Hammer, P. Stoltze, H.. Skriver, and J.. Nørskov, J. Mol. Catal. A Chem. **115**, 421 (1997).

[8] T. Bligaard, J.K. Nørskov, S. Dahl, J. Matthiesen, C.H. Christensen, and J. Sehested, J. Catal. **224**, 206 (2004).

[9] T. Jiang, D.J. Mowbray, S. Dobrin, H. Falsig, B. Hvolbæk, T. Bligaard, and J.K. Nørskov, J. Phys. Chem. C **113**, 10548 (2009).

[10] M. Mavrikakis, B. Hammer, and J.K. Nørskov, Phys. Rev. Lett. **81**, 2819 (1998).

[11] J.R. Kitchin, J.K. Nørskov, M.A. Barteau, and J.G. Chen, J. Chem. Phys. **120**, 10240 (2004).

[12] J.K. Nørskov, F. Studt, F. Abild-Pedersen, and T. Bligaard, in *Fundam. Concepts Heterog. Catal.* (John Wiley & Sons, Inc, Hoboken, NJ, USA, 2014), pp. 97–113.

[13] J. Greeley, I.E.L. Stephens, A.S. Bondarenko, T.P. Johansson, H.A. Hansen, T.F. Jaramillo, J. Rossmeisl, I. Chorkendorff, and J.K. Nørskov, Nat. Chem. **1**, 552 (2009).

[14] M.G. Evans and M. Polanyi, Trans. Faraday Soc. **34**, 11 (1938).

[15] J.K. Nørskov, F. Studt, F. Abild-Pedersen, and T. Bligaard, in *Fundam. Concepts Heterog. Catal.* (John Wiley & Sons, Inc, Hoboken, NJ, USA, 2014), pp. 85–96.

[16] C. Wu, D.J. Schmidt, C. Wolverton, and W.F. Schneider, J. Catal. **286**, 88 (2012).

[17] Y. Ouyang, L. Shi, X. Bai, Q. Li, and J. Wang, Chem. Sci. **11**, 1807 (2020).

[18] Z.-J. Zhao, S. Liu, S. Zha, D. Cheng, F. Studt, G. Henkelman, and J. Gong, Nat. Rev. Mater. **4**, 792 (2019).

[19] B.W.J. Chen, L. Xu, and M. Mavrikakis, Chem. Rev. acs. chemrev.0c01060 (2020).

[20] D.J. Schmidt, W. Chen, C. Wolverton, and W.F. Schneider, J. Chem. Theory Comput. **8**, 264 (2012).

[21] C.G.M. Hermse and A.P.J. Jansen, in *Catal. Vol. 19*, edited by J.J. Spivey and K.M. Dooley (Royal Society of Chemistry, London, 2006), pp. 109–163.

[22] J. Méndez, S.H. Kim, J. Cerdá, J. Wintterlin, and G. Ertl, Phys. Rev. B **71**, 085409 (2005).

[23] V.P. Zhdanov, Surf. Sci. Rep. **12**, 185 (1991).

[24] D.Y. Murzin, Ind. Eng. Chem. Res. **44**, 1688 (2005).

[25] S. Ovesson, B.I. Lundqvist, W.F. Schneider, and A. Bogicevic, Phys. Rev. B - Condens. Matter Mater. Phys. **71**, 1 (2005).

[26] R.B. Getman, W.F. Schneider, A.D. Smeltz, W.N. Delgass, and F.H. Ribeiro, Phys. Rev. Lett. **102**, 076101 (2009).

[27] R.B. Getman, Y. Xu, and W.F. Schneider, J. Phys. Chem. C **112**, 9559 (2008).

[28] K. Frey, D.J. Schmidt, C. Wolverton, and W.F. Schneider, Catal. Sci. Technol. **4**, 4356 (2014).

[29] F. Besenbacher, I. Chorkendorff, B.S. Clausen, B. Hammer, A.M. Molenbroek, J.K. Nørskov, and I. Stensgaard, Science (80-.). **279**, 1913 (1998).

[30] N. Takehiro, P. Liu, A. Bergbreiter, J.K. Nørskov, and R.J. Behm, Phys. Chem. Chem. Phys. **16**, 23930 (2014).

[31] P. Liu and J.K. Nørskov, Phys. Chem. Chem. Phys. **3**, 3814 (2001).

[32] H. Li, K. Shin, and G. Henkelman, J. Chem. Phys. **149**, 174705 (2018).

[33] R.T. Hannagan, G. Giannakakis, M. Flytzani-Stephanopoulos, and E.C.H. Sykes, Chem. Rev. **120**, 12044 (2020).

[34] G. Kyriakou, M.B. Boucher, A.D. Jewell, E. a Lewis, T.J. Lawton, A.E. Baber, H.L. Tierney, M. Flytzani-Stephanopoulos, and E.C.H. Sykes, Science (80-.). **335**, 1209 (2012).

[35] J. Liu, F.R. Lucci, M. Yang, S. Lee, M.D. Marcinkowski, A.J. Therrien, C.T. Williams, E.C.H. Sykes, and M. Flytzani-Stephanopoulos, J. Am. Chem. Soc. **138**, 6396 (2016).

[36] H.L. Tierney, A.E. Baber, J.R. Kitchin, and E.C.H. Sykes, Phys. Rev. Lett. **103**, 246102 (2009).

[37] J. Liu, J. Shan, F.R. Lucci, S. Cao, E.C.H. Sykes, and M. Flytzani-Stephanopoulos, Catal. Sci. Technol. **7**, 4276 (2017).

[38] J. Shan, J. Liu, M. Li, S. Lustig, S. Lee, and M. Flytzani-Stephanopoulos, Appl. Catal. B Environ. **226**, 534 (2018).

[39] M.D. Marcinkowski, M.T. Darby, J. Liu, J.M. Wimble, F.R. Lucci, S. Lee, A. Michaelides, M. Flytzani-Stephanopoulos, M. Stamatakis, and E.C.H. Sykes, Nat. Chem. **10**, 325 (2018).

[40] X. Zhang, G. Cui, H. Feng, L. Chen, H. Wang, B. Wang, X. Zhang, L. Zheng, S. Hong, and M. Wei, Nat. Commun. **10**, 5812 (2019).

[41] C.J. Wrasman, A. Boubnov, A.R. Riscoe, A.S. Hoffman, S.R. Bare, and M. Cargnello, J. Am.

Chem. Soc. **140**, 12930 (2018).

[42] F. Xing, J. Jeon, T. Toyao, K. Shimizu, and S. Furukawa, Chem. Sci. **10**, 8292 (2019).

[43] H. Thirumalai and J.R. Kitchin, Top. Catal. **61**, 462 (2018).

[44] M.T. Greiner, T.E. Jones, S. Beeg, L. Zwiener, M. Scherzer, F. Girgsdies, S. Piccinin, M. Armbrüster, A. Knop-Gericke, and R. Schlögl, Nat. Chem. **10**, 1008 (2018).

[45] M.T. Darby, R. Réocreux, E.C.H. Sykes, A. Michaelides, and M. Stamatakis, ACS Catal. **8**, 5038 (2018).

[46] K.G. Papanikolaou and M. Stamatakis, Catal. Sci. Technol. **10**, 5815 (2020).

[47] M.T. Darby, M. Stamatakis, A. Michaelides, and E.C.H. Sykes, J. Phys. Chem. Lett. **9**, 5636 (2018).

[48] F. Maroun, F. Ozanam, O.M. Magnussen, and R.J. Behm, Science (80-.). **293**, 1811 (2001).

[49] K. Luo, T. Wei, C.-W. Yi, S. Axnanda, and D.W. Goodman, J. Phys. Chem. B **109**, 23517 (2005).

[50] F. Gao, Y. Wang, and D.W. Goodman, J. Phys. Chem. C **114**, 4036 (2010).

[51] H.C. Ham, J.A. Stephens, G.S. Hwang, J. Han, S.W. Nam, and T.H. Lim, J. Phys. Chem. Lett. **3**, 566 (2012).

[52] H.Y. Kim and G. Henkelman, ACS Catal. **3**, 2541 (2013).

[53] Y. Wang, L. Cao, N.J. Libretto, X. Li, C. Li, Y. Wan, C. He, J. Lee, J. Gregg, H. Zong, D. Su, J.T. Miller, T. Mueller, and C. Wang, J. Am. Chem. Soc. **141**, 16635 (2019).

[54] M. Qiu, H. Tao, Y. Li, Y. Li, K. Ding, X. Huang, W. Chen, and Y. Zhang, Appl. Surf. Sci. **427**, 837 (2018).

[55] A.J. McCue and J.A. Anderson, J. Catal. **329**, 538 (2015).

[56] A.Y. Stakheev, N.S. Smirnova, P. V. Markov, G.N. Baeva, G.O. Bragina, A. V. Rassolov, and I.S. Mashkovsky, Kinet. Catal. **59**, 610 (2018).

[57] E. Vignola, S.N. Steinmann, A. Al Farra, B.D. Vandegehuchte, D. Curulla, and P. Sautet, ACS Catal. **8**, 1662 (2018).

[58] S. Divi and A. Chatterjee, J. Phys. Chem. C **120**, 27296 (2016).

[59] K. Yuge, A. Seko, A. Kuwabara, F. Oba, and I. Tanaka, Phys. Rev. B **74**, 174202 (2006).

[60] B.C. Han, A. Van der Ven, G. Ceder, and B. Hwang, Phys. Rev. B **72**, 205409 (2005).

[61] F. Tao, M.E. Grass, Y. Zhang, D.R. Butcher, J.R. Renzas, Z. Liu, J.Y. Chung, B.S. Mun, M. Salmeron, and G.A. Somorjai, Science (80-.). **322**, 932 (2008).

[62] S. Zafeiratos, S. Piccinin, and D. Teschner, Catal. Sci. Technol. **2**, 1787 (2012).

[63] K.G. Papanikolaou, M.T. Darby, and M. Stamatakis, ACS Catal. **10**, 1224 (2020).

[64] G.A. Somorjai and M.A. Van Hove, Prog. Surf. Sci. **30**, 201 (1989).

[65] B. Zhu, G. Thrimurthulu, L. Delannoy, C. Louis, C. Mottet, J. Creuze, B. Legrand, and H. Guesmi, J. Catal. **308**, 272 (2013).

[66] Y. Yao and D.W. Goodman, Phys. Chem. Chem. Phys. **16**, 3823 (2014).

[67] M.T. Darby, E.C.H. Sykes, A. Michaelides, and M. Stamatakis, Top. Catal. **61**, 428 (2018).

[68] W. Kohn and L.J. Sham, Phys. Rev. **140**, A1133 (1965).

[69] M. Born and R. Oppenheimer, Ann. Phys. **389**, 457 (1927).

[70] P. Coppens, Annu. Rev. Phys. Chem. **43**, 663 (1992).

[71] P. Hohenberg and W. Kohn, Phys. Rev. **136**, B864 (1964).

[72] K. Burke and L.O. Wagner, Int. J. Quantum Chem. **113**, 96 (2013).

[73] E. Engel and R.M. Dreizler, *Density Functional Theory* (Springer Berlin Heidelberg, Berlin, Heidelberg, 2011).

[74] L.G. Verga and C.-K. Skylaris, in *Front. Nanosci.*, 1st ed. (Elsevier Ltd., 2018), pp. 239–293.

[75] J. Wellendorff, K.T. Lundgaard, A. Møgelhøj, V. Petzold, D.D. Landis, J.K. Nørskov, T. Bligaard, and K.W. Jacobsen, Phys. Rev. B **85**, 235149 (2012).

[76] P.A.M. Dirac, Math. Proc. Cambridge Philos. Soc. **26**, 376 (1930).

[77] Peter Atkins and Ronald Friedman, *MOLECULAR QUANTUM MECHANICS*, Fourth (OXFORD University Press, Oxford, 2005).

[78] P. Atkins and J. Paula, in *Phys. Chem. Thermodyn. Struct. Chang.*, Tenth (Oxford University Press, New York, 2014), pp. 604–650.

[79] G.I. Csonka, J.P. Perdew, A. Ruzsinszky, P.H.T. Philipsen, S. Lebègue, J. Paier, O.A. Vydrov, and J.G. Ángyán, Phys. Rev. B - Condens. Matter Mater. Phys. **79**, 1 (2009).

[80] K. Honkala, A. Hellman, I.N. Remediakis, A. Logadottir, A. Carlsson, S. Dahl, C.H. Christensen, and J.K. Nørskov, Science (80-.). **307**, 555 (2005).

[81] J.K. Nørskov, F. Studt, F. Abild-Pedersen, and T. Bligaard, in *Fundam. Concepts Heterog. Catal.* (John Wiley & Sons, Inc, Hoboken, NJ, USA, 2014), pp. 6–25.

[82] J.P. Perdew, in *AIP Conf. Proc.* (AIP, 2001), pp. 1–20.

[83] D.S. Sholl and J.A. Steckel, in *Density Funct. Theory A Pract. Introd.* (John Wiley & Sons, Inc., Hoboken, NJ, USA, 2009), pp. 209–233.

[84] M.C. Payne, M.P. Teter, D.C. Allan, T.A. Arias, and J.D. Joannopoulos, Rev. Mod. Phys. **64**, 1045 (1992).

[85] D.S. Sholl and J.A. Steckel, in *Density Funct. Theory A Pract. Introd.* (John Wiley & Sons, Inc., Hoboken, NJ, USA, 2009), pp. 49–81.

[86] G. Kresse and D. Joubert, Phys. Rev. B **59**, 1758 (1999).

[87] J.K. Nørskov, F. Abild-Pedersen, F. Studt, and T. Bligaard, Proc. Natl. Acad. Sci. **108**, 937 (2011).

[88] P.G. Moses, L.C. Grabow, E.M. Fernandez, B. Hinnemann, H. Topsøe, K.G. Knudsen, and J.K. Nørskov, Catal. Letters **144**, 1425 (2014).

[89] K.G. Papanikolaou and M. Stamatakis, in *Comput. Model. Nanomater.* (2020), pp. 95–125.

[90] S.D. Bond and B.J. Leimkuhler, Acta Numer. **16**, 1 (2007).

[91] V. Brázdová and D.R. Bowler, in *At. Comput. Simulations*, First Edit (Wiley-VCH Verlag GmbH & Co. KGaA, Weinheim, Germany, 2013), pp. 75–88.

[92] J.K. Nørskov, F. Studt, F. Abild-Pedersen, and T. Bligaard, in *Fundam. Concepts Heterog. Catal.*, First Edit (John Wiley & Sons, Inc, Hoboken, NJ, USA, 2014), pp. 47–67.

[93] Gillespie D, *Markov Processes: An Introduction for Physical Scientists* (Academic Press, San Diego, 1991).

[94] M. Dumont and P. Dufour, Comput. Phys. Commun. **41**, 1 (1986).

[95] D.T. Gillespie, J. Comput. Phys. **22**, 403 (1976).

[96] D.T. Gillespie, J. Phys. Chem. **81**, 2340 (1977).

[97] A.F. Voter, in *Radiat. Eff. Solids*, edited by K.E. Sickafus, E.A. Kotomin, and B.P. Uberuaga (Springer Netherlands, Dordrecht, 2007), pp. 1–23.

[98] A.B. Bortz, M.H. Kalos, and J.L. Lebowitz, J. Comput. Phys. **17**, 10 (1975).

[99] A. Slepoy, A.P. Thompson, and S.J. Plimpton, J. Chem. Phys. **128**, 205101 (2008).

[100] J.J. Lukkien, J.P.L. Segers, P.A.J. Hilbers, R.J. Gelten, and A.P.J. Jansen, Phys. Rev. E **58**, 2598 (1998).

[101] M.J. Hoffmann, M. Scheffler, and K. Reuter, ACS Catal. **5**, 1199 (2015).

[102] A. Chatterjee and D.G. Vlachos, J. Comput. Mater. Des. **14**, 253 (2007).

[103] K.G. Papanikolaou, M.T. Darby, and M. Stamatakis, J. Chem. Phys. **149**, 184701 (2018).

[104] G. Henkelman and H. Jónsson, J. Chem. Phys. **111**, 7010 (1999).

[105] G. Henkelman and H. Jónsson, J. Chem. Phys. **113**, 9978 (2000).

[106] G. Henkelman, B.P. Uberuaga, and H. Jónsson, J. Chem. Phys. **113**, 9901 (2000).

[107] D.S. Sholl and J.A. Steckel, in *Density Funct. Theory* (John Wiley & Sons, Inc., Hoboken, NJ, USA, 2009), pp. 131–161.

[108] A.P.J. Jansen, *An Introduction to Kinetic Monte Carlo Simulations of Surface Reactions* (Springer Berlin Heidelberg, Berlin, Heidelberg, 2012).

[109] J.M. Bray, J.L. Smith, and W.F. Schneider, Top. Catal. **57**, 89 (2014).

[110] A. Bajpai, K. Frey, and W.F. Schneider, Langmuir **36**, 465 (2020).

[111] S.P. Devarajan, J.A. Hinojosa, and J.F. Weaver, Surf. Sci. **602**, 3116 (2008).

[112] Z.-P. Liu and P. Hu, J. Am. Chem. Soc. **125**, 1958 (2003).

[113] Z.-P. Liu, P. Hu, and M.-H. Lee, J. Chem. Phys. **119**, 6282 (2003).

[114] J.K. Nørskov, F. Studt, F. Abild-Pedersen, and Thomas Bligaard, in *Fundam. Concepts Heterog. Catal.* (John Wiley & Sons, Inc, Hoboken, NJ, USA, 2014), pp. 26–46.

[115] M. Jørgensen and H. Grönbeck, ACS Catal. **7**, 5054 (2017).

[116] J. Nielsen, M. D'Avezac, J. Hetherington, and M. Stamatakis, J. Chem. Phys. **139**, 224706 (2013).

[117] L.C. Grabow, A.A. Gokhale, S.T. Evans, J.A. Dumesic, and M. Mavrikakis, J. Phys. Chem. C **112**, 4608 (2008).

[118] J.M. Sanchez, F. Ducastelle, and D. Gratias, Phys. A Stat. Mech. Its Appl. **128**, 334 (1984).

[119] S. Piccinin and C. Stampfl, Phys. Rev. B **81**, 155427 (2010).

[120] R. Drautz, R. Singer, and M. Fähnle, Phys. Rev. B **67**, 035418 (2003).

[121] S. Verma, T. Rehman, and A. Chatterjee, Surf. Sci. **613**, 114 (2013).

[122] A. Walle and G. Ceder, J. Phase Equilibria **23**, 348 (2002).

[123] S. Matera, W.F. Schneider, A. Heyden, and A. Savara, ACS Catal. **9**, 6624 (2019).

[124] A.P.J. Jansen and C. Popa, Phys. Rev. B **78**, 085404 (2008).

[125] K.G. Papanikolaou, M.T. Darby, and M. Stamatakis, J. Phys. Chem. C **123**, 9128 (2019).

[126] M. Stamatakis and D.G. Vlachos, J. Chem. Phys. **134**, 214115 (2011).

[127] M. Silverberg, A. Ben-Shaul, and F. Rebentrost, J. Chem. Phys. **83**, 6501 (1985).

[128] V.. Zhdanov and B. Kasemo, Surf. Sci. **405**, 27 (1998).

[129] M. Silverberg and A. Ben-Shaul, J. Chem. Phys. **87**, 3178 (1987).

[130] C. OLIVA, C. VANDENBERG, J. HANSNIEMANTSVERDRIET, and D. CURULLAFERRE, J. Catal. **248**, 38 (2007).

[131] A. Shayeghi, S. Krähling, P. Hörtz, R.L. Johnston, C.J. Heard, and R. Schäfer, J. Phys. Chem. C **121**, 21354 (2017).

[132] S. Díaz-Tendero, M. Alcamí, and F. Martín, Phys. Chem. Chem. Phys. **15**, 1288 (2013).

[133] E.W. Hansen and M. Neurock, J. Catal. **196**, 241 (2000).

[134] J.R. Ullmann, J. ACM **23**, 31 (1976).

[135] T. Gambu, R. Abrahams, and E. van Steen, Catalysts **9**, 310 (2019).

[136] S. Piccinin and M. Stamatakis, ACS Catal. **4**, 2143 (2014).

[137] M. Stamatakis, (2013).

[138] K. Mudiyanselage, C.-W. Yi, and J. Szanyi, J. Phys. Chem. C **113**, 5766 (2009).

[139] J.M. Hawkins, J.F. Weaver, and A. Asthagiri, Phys. Rev. B **79**, 125434 (2009).

[140] M. Stamatakis and D.G. Vlachos, Comput. Chem. Eng. **35**, 2602 (2011).

[141] G. Peng and M. Mavrikakis, Nano Lett. **15**, 629 (2015).

[142] B. Ni and X. Wang, Adv. Sci. **2**, 1500085 (2015).

[143] S.S. Mulla, N. Chen, L. Cumaranatunge, G.E. Blau, D.Y. Zemlyanov, W.N. Delgass, W.S. Epling, and F.H. Ribeiro, J. Catal. **241**, 389 (2006).

[144] H. Tang, A. Van Der Ven, and B.L. Trout, Phys. Rev. B - Condens. Matter Mater. Phys. **70**, 1 (2004).

[145] A.D. Smeltz, W.N. Delgass, and F.H. Ribeiro, Langmuir **26**, 16578 (2010).

[146] K. Lejaeghere, V. Van Speybroeck, G. Van Oost, and S. Cottenier, Crit. Rev. Solid State Mater. Sci. **39**, 1 (2014).

[147] G.A. Somorjai, Catal. Letters **7**, 169 (1991).

[148] M.P. Andersson, F. Abild-Pedersen, I.N. Remediakis, T. Bligaard, G. Jones, J. Engbæk, O. Lytken, S. Horch, J.H. Nielsen, J. Sehested, J.R. Rostrup-Nielsen, J.K. Nørskov, and I. Chorkendorff, J. Catal. **255**, 6 (2008).

[149] B. Hammer, J. Catal. **199**, 171 (2001).

[150] G. Kresse and J. Hafner, Phys. Rev. B **47**, 558 (1993).

[151] G. Kresse and J. Furthmüller, Comput. Mater. Sci. **6**, 15 (1996).

[152] P.E. Blöchl, Phys. Rev. B **50**, 17953 (1994).

[153] J. Klimeš, D.R. Bowler, and A. Michaelides, Phys. Rev. B **83**, 195131 (2011).

[154] J. Klimeš, D.R. Bowler, and A. Michaelides, J. Phys. Condens. Matter **22**, 022201 (2010).

[155] M. Dion, H. Rydberg, E. Schröder, D.C. Langreth, and B.I. Lundqvist, Phys. Rev. Lett. **92**, 246401 (2004).

[156] S. Dahl, A. Logadottir, R.C. Egeberg, J.H. Larsen, I. Chorkendorff, E. Törnqvist, and J.K. Nørskov, Phys. Rev. Lett. **83**, 1814 (1999).

[157] D. Loffreda, D. Simon, and P. Sautet, J. Catal. **213**, 211 (2003).

[158] X. Liu, L. Sun, and W.-Q. Deng, J. Phys. Chem. C **122**, 8306 (2018).

[159] A. Ishikawa and Y. Tateyama, J. Phys. Chem. C **122**, 17378 (2018).

[160] M. Daté, H. Okuyama, N. Takagi, M. Nishijima, and T. Aruga, Surf. Sci. **350**, 79 (1996).

[161] K. Tian, X.-Y. Tu, and S.-S. Dai, Surf. Sci. **601**, 3186 (2007).

[162] J.S. Villarrubia and W. Ho, J. Chem. Phys. **87**, 750 (1987).

[163] B. Hammer, Faraday Discuss. **110**, 323 (1998).

[164] D. Mei, Q. Ge, M. Neurock, L. Kieken, and J. Lerou, Mol. Phys. **102**, 361 (2004).

[165] M. Mavrikakis, L.B. Hansen, J.J. Mortensen, B. Hammer, and J.K. Nørskov, in *Transit. State Model. Catal.* (1999), pp. 245–258.

[166] M.J.P. Hopstaken and J.W. Niemantsverdriet, J. Phys. Chem. B **104**, 3058 (2000).

[167] P.B. Rasmussen, P.A. Taylor, and I. Chorkendorff, Surf. Sci. **269**–**270**, 352 (1992).

[168] H.-Y. Su, Z. Zeng, X.-H. Bao, and W.-X. Li, J. Phys. Chem. C **113**, 8266 (2009).

[169] J.K. Nørskov, T. Bligaard, B. Hvolbæk, F. Abild-Pedersen, I. Chorkendorff, and C.H. Christensen, Chem. Soc. Rev. **37**, 2163 (2008).

[170] F.R. Lucci, J. Liu, M.D. Marcinkowski, M. Yang, L.F. Allard, M. Flytzani-Stephanopoulos, and E.C.H. Sykes, Nat. Commun. **6**, 8550 (2015).

[171] A. Michaelides, Z.P. Liu, C.J. Zhang, A. Alavi, D.A. King, and P. Hu, J. Am. Chem. Soc. **125**, 3704 (2003).

[172] P.J. Feibelman, Phys. Rev. B **38**, 12133 (1988).

[173] G.A. Somorjai, J. Mol. Struct. THEOCHEM **424**, 101 (1998).

[174] M. Mavrikakis, J. Rempel, J. Greeley, L.B. Hansen, and J.K. Nørskov, J. Chem. Phys. **117**, 6737 (2002).

[175] S. Kandoi, A.A. Gokhale, L.C. Grabow, J.A. Dumesic, and M. Mavrikakis, Catal. Letters **93**, 93 (2004).

[176] R. Burch, S.T. Daniells, and P. Hu, J. Chem. Phys. **121**, 2737 (2004).

[177] J.-F. Paul, J. Pérez-Ramírez, F. Ample, and J.M. Ricart, J. Phys. Chem. B **108**, 17921 (2004).

[178] A. Bogicevic and K.C. Hass, Surf. Sci. **506**, L237 (2002).

[179] V.P. Zhdanov and B. Kasemo, Surf. Sci. Rep. **29**, 31 (1997).

[180] W.T. Wallace, Y. Cai, M.S. Chen, and D.W. Goodman, J. Phys. Chem. B **110**, 6245 (2006).

[181] K.C. Taylor, Catal. Rev. **35**, 457 (1993).

[182] C.Y. Kang, M. Taniguchi, M. Uenishi, and H. Tanaka, Chem. Lett. **41**, 822 (2012).

[183] H. Asakura, T. Onuki, S. Hosokawa, N. Takagi, S. Sakaki, K. Teramura, and T. Tanaka, Phys. Chem. Chem. Phys. **21**, 18816 (2019).

[184] K. Ueda, C.A. Ang, Y. Ito, J. Ohyama, and A. Satsuma, Catal. Sci. Technol. **6**, 5797 (2016).

[185] H. Yoshida, Y. Okabe, N. Yamashita, S. Hinokuma, and M. Machida, Catal. Today **281**, 590 (2017).

[186] K. Koizumi, H. Yoshida, M. Boero, K. Tamai, S. Hosokawa, T. Tanaka, K. Nobusada, and M. Machida, Phys. Chem. Chem. Phys. **20**, 25592 (2018).

[187] H. Yoshida, N. Yamashita, S. Ijichi, Y. Okabe, S. Misumi, S. Hinokuma, and M. Machida, ACS Catal. **5**, 6738 (2015).

[188] T. Hirakawa, Y. Shimokawa, W. Tokuzumi, T. Sato, M. Tsushida, H. Yoshida, J. Ohyama, and M. Machida, ACS Appl. Nano Mater. **3**, 9097 (2020).

[189] N. Takagi, K. Ishimura, H. Miura, T. Shishido, R. Fukuda, M. Ehara, and S. Sakaki, ACS Omega **4**, 2596 (2019).

[190] H. Yoshida, Y. Kawakami, W. Tokuzumi, Y. Shimokawa, T. Hirakawa, J. Ohyama, and M. Machida, Bull. Chem. Soc. Jpn. **93**, 1050 (2020).

[191] C.B. Jones, I. Khurana, S.H. Krishna, A.J. Shih, W.N. Delgass, J.T. Miller, F.H. Ribeiro, W.F. Schneider, and R. Gounder, J. Catal. **389**, 140 (2020).

[192] Y. Nishihata, J. Mizuki, T. Akao, H. Tanaka, M. Uenishi, M. Kimura, T. Okamoto, and N. Hamada, Nature **418**, 164 (2002).

[193] S. Hosokawa, T. Shibano, H. Koga, M. Matsui, H. Asakura, K. Teramura, M. Okumura, and T. Tanaka, ChemCatChem **12**, 4276 (2020).

[194] L. Zhang, I.A.W. Filot, Y.-Q. Su, J.-X. Liu, and E.J.M. Hensen, J. Catal. **363**, 154 (2018).

[195] K.G. Papanikolaou and M. Stamatakis, Catal. Sci. Technol. (2021) DOI: 10.1039/D1CY00011J.

[196] K.W. Kolasinski, in *Surf. Sci.* (John Wiley & Sons, Ltd, Chichester, UK, 2012), pp. 51–114.

[197] C.T. Campbell, ACS Catal. **7**, 2770 (2017).

[198] C. Stegelmann, A. Andreasen, and C.T. Campbell, J. Am. Chem. Soc. **131**, 8077 (2009).

[199] J.L. Teffo and A. Chédin, J. Mol. Spectrosc. **135**, 389 (1989).

[200] Y. Li and M. Bowker, Surf. Sci. **348**, 67 (1996).

[201] V.G. Komvokis, M. Marti, A. Delimitis, I.A. Vasalos, and K.S. Triantafyllidis, Appl. Catal. B Environ. **103**, 62 (2011).

[202] A. Kokalj, I. Kobal, and T. Matsushima, J. Phys. Chem. B **107**, 2741 (2003).

[203] S.Y. Wu, C.H. Su, J.G. Chang, H.T. Chen, C.H. Hou, and H.L. Chen, Comput. Mater. Sci. **50**, 3311 (2011).

[204] H. Orita and N. Itoh, Surf. Sci. **550**, 166 (2004).

[205] X. Wei, X.F. Yang, A.Q. Wang, L. Li, X.Y. Liu, T. Zhang, C.Y. Mou, and J. Li, J. Phys. Chem. C **116**, 6222 (2012).

[206] K. Kim, S. Baek, J.J. Kim, and J.W. Han, Appl. Surf. Sci. **510**, (2020).

[207] W.A. Brown, R.K. Sharma, D.A. King, and S. Haq, J. Phys. Chem. **100**, 12559 (1996).

[208] Y. Wang, D. Zhang, Z. Yu, and C. Liu, J. Phys. Chem. C **114**, 2711 (2010).

[209] Z.P. Liu, S.J. Jenkins, and D.A. King, J. Am. Chem. Soc. **126**, 7336 (2004).

[210] T.N. Pham, Y. Hamamoto, K. Inagaki, D.N. Son, I. Hamada, and Y. Morikawa, J. Phys. Chem. C **124**, 2968 (2020).

[211] A. Shiotari, S. Hatta, H. Okuyama, and T. Aruga, J. Chem. Phys. **141**, 134705 (2014).

[212] I. Nakai, H. Kondoh, T. Shimada, R. Yokota, T. Katayama, T. Ohta, and N. Kosugi, J. Chem. Phys. **127**, 024701 (2007).

[213] J.K. Nørskov, F. Studt, F. Abild-Pedersen, and T. Bligaard, in *Fundam. Concepts Heterog. Catal.* (John Wiley & Sons, Inc, Hoboken, NJ, USA, 2014), pp. 68–84.

[214] L.C. Grabow and M. Mavrikakis, ACS Catal. **1**, 365 (2011).

[215] S. Li, S. Singh, J.A. Dumesic, and M. Mavrikakis, Catal. Sci. Technol. **9**, 2836 (2019).

[216] S. Bhandari, S. Rangarajan, and M. Mavrikakis, Acc. Chem. Res. **53**, 1893 (2020).

[217] G.S. Herman, C.H.F. Peden, S.J. Schmieg, and D.N. Belton, Catal. Letters **62**, 131 (1999).

[218] Y. Xu and M. Mavrikakis, Surf. Sci. **494**, 131 (2001).

[219] A.C. Lausche, A.J. Medford, T.S. Khan, Y. Xu, T. Bligaard, F. Abild-Pedersen, J.K. Nørskov, and F. Studt, J. Catal. **307**, 275 (2013).

[220] J. Schumann, A.J. Medford, J.S. Yoo, Z.J. Zhao, P. Bothra, A. Cao, F. Studt, F. Abild-Pedersen, and J.K. Nørskov, ACS Catal. **8**, 3447 (2018).

[221] S. González, C. Sousa, and F. Illas, J. Catal. **239**, 431 (2006).

[222] H.J. Borg, J.F.C.J.M. Reijerse, R.A. Van Santen, and J.W. Niemantsverdriet, J. Chem. Phys. **101**, 10052 (1994).

[223] C.H.F. Peden, D.N. Belton, and S.J. Schmieg, J. Catal. **155**, 204 (1995).

[224] J.P. Perdew, K. Burke, and M. Ernzerhof, Phys. Rev. Lett. **77**, 3865 (1996).

[225] B. Hammer, L.B. Hansen, and J.K. Nørskov, Phys. Rev. B **59**, 7413 (1999).

[226] F. Abild-Pedersen, J. Greeley, and J.K. Nørskov, Catal. Letters **105**, 9 (2005).

[227] S. Vollmer, G. Witte, and C. Wöll, Catal. Letters **77**, 97 (2001).

[228] I. Nakamura, K. Suzuki, a. Takahashi, M. Haneda, H. Hamada, and T. Fujitani, J. Vac. Sci. Technol. A Vacuum, Surfaces, Film. **25**, 1143 (2007).

[229] S.C. Creighan, R.J. Mukerji, A.S. Bolina, D.W. Lewis, and W.A. Brown, Catal. Letters **88**, 39 (2003).

[230] K.M. Gameel, I.M. Sharafeldin, A.U. Abourayya, A.H. Biby, and N.K. Allam, Phys. Chem. Chem. Phys. **20**, 25892 (2018).

[231] J.C. Trac Y, J. Chem. Phys. **56**, 2748 (1972).

[232] J.-M. Zhang, F. Ma, and K.-W. Xu, Appl. Surf. Sci. **229**, 34 (2004).

[233] I. Chorkendorff and J.W. Niemantsverdriet, *Concepts of Modern Catalysis and Kinetics* (Wiley-VCH Verlag GmbH, Weinheim, 2003).

[234] F.R. Lucci, M.T. Darby, M.F.G. Mattera, C.J. Ivimey, A.J. Therrien, A. Michaelides, M. Stamatakis, and E.C.H. Sykes, J. Phys. Chem. Lett. **7**, 480 (2016).

[235] F.R. Lucci, T.J. Lawton, A. Pronschinske, and E.C.H. Sykes, J. Phys. Chem. C **118**, 3015 (2014).

[236] Q. Fu and Y. Luo, J. Phys. Chem. C **117**, 14618 (2013).

[237] A. Bach Aaen, E. Lægsgaard, A.. Ruban, and I. Stensgaard, Surf. Sci. **408**, 43 (1998).

[238] F. Gao, Y. Wang, and D.W. Goodman, J. Phys. Chem. C **113**, 14993 (2009).

[239] K. Yang and B. Yang, Phys. Chem. Chem. Phys. **19**, 18010 (2017).

[240] R.T. Hannagan, D.A. Patel, L.A. Cramer, A.C. Schilling, P.T.P. Ryan, A.M. Larson, V. Çınar, Y. Wang, T.A. Balema, and E.C.H. Sykes, ChemCatChem **12**, 488 (2020).

[241] Y. Wang, K.G. Papanikolaou, R.T. Hannagan, D.A. Patel, T.A. Balema, L.A. Cramer, P.L. Kress, M. Stamatakis, and E.C.H. Sykes, J. Chem. Phys. **153**, 244702 (2020).

[242] L.T. Roling and M. Mavrikakis, Nanoscale **9**, 15005 (2017).

[243] L. Hansen, P. Stoltze, K.W. Jacobsen, and J.K. Nørskov, Phys. Rev. B **44**, 6523 (1991).

[244] E. Garfunkel, M. Yu, S. Yang, and X. Feng, J. Vac. Sci. Technol. A Vacuum, Surfaces, Film. **7**, 1579 (1989).

[245] G.X. Pei, X.Y. Liu, A. Wang, A.F. Lee, M.A. Isaacs, L. Li, X. Pan, X. Yang, X. Wang, Z. Tai, K.

Wilson, and T. Zhang, ACS Catal. **5**, 3717 (2015).

[246] J. Shan, N. Janvelyan, H. Li, J. Liu, T.M. Egle, J. Ye, M.M. Biener, J. Biener, C.M. Friend, and M. Flytzani-Stephanopoulos, Appl. Catal. B Environ. **205**, 541 (2017).

[247] H.L. Tierney, A.E. Baber, and E.C.H. Sykes, J. Phys. Chem. C **113**, 7246 (2009).

[248] S. Yang, M. Yu, G. Meigs, X.H.H. Feng, and E. Garfunkel, Surf. Sci. **205**, L777 (1988).

[249] A.J. Therrien, A.J.R. Hensley, M.D. Marcinkowski, R. Zhang, F.R. Lucci, B. Coughlin, A.C. Schilling, J. Mcewen, and E.C.H. Sykes, Nat. Catal. **1**, 192 (2018).

[250] H.C. Ham, G.S. Hwang, J. Han, S.W. Nam, and T.H. Lim, J. Phys. Chem. C **113**, 12943 (2009).

[251] J.A. Stephens, H.C. Ham, and G.S. Hwang, J. Phys. Chem. C **114**, 21516 (2010).

[252] G. Wang, M.A. Van Hove, P.N. Ross, and M.I. Baskes, J. Chem. Phys. **121**, 5410 (2004).

[253] J.R. Michalka and J.D. Gezelter, J. Phys. Chem. C **119**, 150611154824003 (2015).

[254] A.A.B. Padama, A.P.S. Cristobal, J.D. Ocon, W.A. Diño, and H. Kasai, J. Phys. Chem. C **121**, 17818 (2017).

[255] D.A. Patel, R.T. Hannagan, P.L. Kress, A.C. Schilling, V. Çınar, and E.C.H. Sykes, J. Phys. Chem. C **123**, 28142 (2019).

[256] M. Ouyang, K.G. Papanikolaou, A. Boubnov, A.S. Hoffman, G. Giannakakis, S.R. Bare, M. Stamatakis, M. Flytzani-Stephanopoulos, and E.C.H. Sykes, Nat. Commun. **12**, 1549 (2021).

[257] X. Xu and D.W. Goodman, J. Phys. Chem. **97**, 7711 (1993).

[258] S. Gautier, S.N. Steinmann, C. Michel, P. Fleurat-Lessard, and P. Sautet, Phys. Chem. Chem. Phys. **17**, 28921 (2015).

[259] P.J. Feibelman, B. Hammer, J.K. Nørskov, F. Wagner, M. Scheffler, R. Stumpf, R. Watwe, and J. Dumesic, J. Phys. Chem. B **105**, 4018 (2001).

[260] B. Eren, C. Heine, H. Bluhm, G.A. Somorjai, and M. Salmeron, J. Am. Chem. Soc. **137**, 11186 (2015).

[261] A.A.B. Padama, H. Kishi, R.L. Arevalo, J.L. V Moreno, H. Kasai, M. Taniguchi, M. Uenishi, H. Tanaka, and Y. Nishihata, J. Phys. Condens. Matter **24**, 175005 (2012).

[262] M.E. Bartram and B.E. Koel, Surf. Sci. **213**, 137 (1989).

[263] P. Haas, F. Tran, and P. Blaha, Phys. Rev. B **79**, 085104 (2009).

[264] K.M. Ho and K.P. Bohnen, Phys. Rev. Lett. **59**, 1833 (1987).

[265] E.C. Sowa, M.A. Van Hove, and D.L. Adams, Surf. Sci. **199**, 174 (1988).

[266] I. Matrane, M. Mazroui, R. Ferrando, M. Badawi, and S. Lebègue, Surf. Sci. **690**, 121463 (2019).

[267] J.-M. Zhang, H.-Y. Li, and K.-W. Xu, Surf. Interface Anal. **39**, 660 (2007).